

INVESTIGATIONS OF INTERFACES FOR ELECTROCHEMICAL DEVICES  
USING TUNABLE BLOCK COPOLYMER ELECTROLYTES

by  
Nora C. Buggy

© Copyright by Nora C. Buggy, 2021

All Rights Reserved

A thesis submitted to the Faculty and the Board of Trustees of the Colorado School of Mines in partial fulfillment of the requirements for the degree of Doctor of Philosophy (Chemical Engineering).

Golden, Colorado

Date \_\_\_\_\_

Signed: \_\_\_\_\_

Nora C. Buggy

Signed: \_\_\_\_\_

Dr. Andrew M. Herring  
Thesis Advisor

Golden, Colorado

Date \_\_\_\_\_

Signed: \_\_\_\_\_

Dr. Anuj Chauhan  
Professor and Department Head  
Department of Chemical and Biological Engineering

## ABSTRACT

Polymer electrolyte-based electrochemical energy conversion devices, such as electrolyzers or fuel cells, are of interest for large scale hydrogen production and conversion, respectively. Much effort has gone toward improving the anion exchange membrane (AEM), the solid polymer electrolyte which separates the anode and cathode and transports anions and water across the electrochemical device. In addition to the AEM, device performance is dictated in part by sluggish reaction kinetics that can result from poorly formed structures in the electrode catalyst layer (CL). The CL is comprised of a heterogeneous mixture of conductive supporting material, catalyst particles, and anion exchange ionomer (AEI). Electrode design can be improved by synergistically developing ionomer chemistry with fundamental knowledge of their interactions with catalysts and supporting materials. The limited work carried out in this area has focused on using platinum group metal catalysts, which can be replaced with cheaper more abundant catalysts in AEM-based devices due to the enhanced reaction kinetics realized in base. Hence, in this work, tunable block copolymer-based AEIs are developed and their interactions, structure and performance with a silver catalyst are investigated.

First, a novel polyethylene-based block copolymer AEM was developed. The polycyclooctene midblock of the ABA triblock copolymer polychloromethylstyrene-*b*-polycyclooctene-*b*-polychloromethylstyrene (PCMS-*b*-PCOE-*b*-PCMS) was hydrogenated to yield a polyethylene (PE) midblock. The new PE-based AEM had high ionic conductivity, moderate water uptake, and decent alkaline stability. Notably, the mechanical strength of the AEM improved in liquid water. X-ray scattering studies revealed that in liquid water the PE backbone rearranges to form larger crystalline domains, leading to enhanced mechanical properties.

Next, interactions between silver nanoparticles (AgNPs) and block copolymer-based ionomers were investigated. This study utilized the PCMS-*b*-PCOE-*b*-PCMS triblock copolymer precursor and ionomers derived from quaternization with trimethylamine or N-methylpiperidine. Using FTIR, interactions with AgNPs were determined to occur more strongly with the phenyl groups, vinyl groups, and the pendant quaternary ammonium cations (QACs). Changes in thermal

characteristics and crystallinity were highly dependent on the QAC, uncovering differences in the nature of the interactions between silver and trimethylammonium or methylpiperidinium.

Ionomer thin film morphology was characterized on a silver surface to model an idealized catalyst interface using grazing incidence small angle X-ray scattering. This work utilized two diblock and two triblock copolymer precursors of PCMS and polyisoprene (PIp). The morphology of the block copolymer precursor was found to align vertically to the interface, but after quaternization, the morphology became more disordered due to dipole-dipole interactions between pendant QACs. Environmental studies were used to elucidate water uptake via changes in the radius of gyration.

The final set of studies implemented a half-cell to study the kinetics of the oxygen evolution reaction (OER) on electrodes coated in a silver-ionomer ink. Optimization of the ionomer chemistry is realized through a series of backbone and QAC modifications. The best performing electrode was integrated in a water electrolyzer with the PE-based AEM developed in the first study. In the final chapter, the hypotheses and structure-property-performance relationship are revisited, and future work is proposed.

## TABLE OF CONTENTS

ABSTRACT . . . . .	iii
LIST OF FIGURES . . . . .	xi
LIST OF TABLES . . . . .	xxi
LIST OF SYMBOLS . . . . .	xxiii
LIST OF ABBREVIATIONS . . . . .	xxiv
ACKNOWLEDGMENTS . . . . .	xxvi
DEDICATION . . . . .	xxvii
CHAPTER 1 INTRODUCTION . . . . .	1
1.1 The Hydrogen Economy . . . . .	1
1.2 Fuel Cells . . . . .	2
1.3 Electrolyzers . . . . .	5
1.4 Anion Exchange Membranes . . . . .	7
1.5 Ionomers and the Enigma of the Catalyst Layer . . . . .	12
1.6 Motivation for Utilizing Silver Catalysts for ORR and OER . . . . .	17
1.7 Ionomer Thin Films: Current Understanding . . . . .	20
1.8 Existing Knowledge Gap and Associated Research Challenges . . . . .	24
1.9 Thesis Statements . . . . .	24
CHAPTER 2 A POLYETHYLENE-BASED TRIBLOCK COPOLYMER ANION EXCHANGE MEMBRANE WITH HIGH CONDUCTIVITY AND PRACTICAL MECHANICAL PROPERTIES . . . . .	27
2.1 Motivation . . . . .	27
2.2 Abstract . . . . .	27

2.3	Introduction . . . . .	29
2.4	Experimental Methods . . . . .	32
2.4.1	Materials . . . . .	32
2.4.2	Hydrogenation with <i>p</i> -Toluenesulfonyl hydrazide (TSH) . . . . .	32
2.4.3	Membrane Fabrication and Quaternization . . . . .	32
2.4.4	NMR Characterization . . . . .	33
2.4.5	Gel Permeation Chromatography (GPC) . . . . .	33
2.4.6	Fourier-Transform Infrared Spectroscopy (FTIR) . . . . .	33
2.4.7	Elemental Analysis . . . . .	33
2.4.8	Thermal Characterization . . . . .	34
2.4.9	Ion Exchange Capacity (IEC) . . . . .	34
2.4.10	IEC Alkaline Stability . . . . .	34
2.4.11	Water Uptake Measurements . . . . .	35
2.4.12	X-ray Scattering . . . . .	35
2.4.13	Transmission Electron Microscopy (TEM) . . . . .	36
2.4.14	Mechanical Properties . . . . .	36
2.4.15	Chloride and Hydroxide Ion Conductivity . . . . .	36
2.5	Results and Discussion . . . . .	37
2.5.1	Polymer Synthesis and Characterization . . . . .	37
2.5.2	Membrane Fabrication and Thermal Characterization . . . . .	40
2.5.3	Water Uptake . . . . .	45
2.5.4	Morphology . . . . .	48
2.5.5	Crystallinity . . . . .	55
2.5.6	Tensile Testing . . . . .	57

2.5.7	Ionic Conductivity . . . . .	58
2.5.8	Alkaline Stability . . . . .	59
2.6	Conclusions . . . . .	63
CHAPTER 3 INVESTIGATING SILVER NANOPARTICLE INTERACTIONS WITH QUATERNARY AMMONIUM FUNCTIONALIZED TRIBLOCK COPOLYMERS AND THEIR EFFECT ON MIDBLOCK CRYSTALLINITY . . . . .		
3.1	Motivation . . . . .	64
3.2	Abstract . . . . .	64
3.3	Introduction . . . . .	65
3.4	Experimental Methods . . . . .	67
3.4.1	Materials . . . . .	67
3.4.2	Polymer and Ag-Polymer Composite Sample Fabrication . . . . .	67
3.4.3	Fourier-Transform Infrared Spectroscopy . . . . .	67
3.4.4	Thermal Characterization and Crystallization Kinetics . . . . .	67
3.4.5	X-ray Scattering . . . . .	68
3.4.6	X-ray Photoelectron Spectroscopy . . . . .	68
3.4.7	NMR Characterization . . . . .	69
3.4.8	Gel Permeation Chromatography . . . . .	69
3.5	Results and Discussion . . . . .	69
3.6	Conclusions . . . . .	84
CHAPTER 4 DESIGNING ANION EXCHANGE IONOMERS WITH ORIENTED NANOSCALE PHASE SEPARATION AT A SILVER INTERFACE . . . . .		
4.1	Motivation . . . . .	87
4.2	Abstract . . . . .	87
4.3	Introduction . . . . .	88



4.4	Experimental Methods . . . . .	92
4.4.1	Materials . . . . .	92
4.4.2	Synthesis of PIP-SG1 . . . . .	92
4.4.3	Synthesis of diblock copolymer PIP- <i>b</i> -PCMS, Di-1 and Di-2 . . . . .	93
4.4.4	Synthesis of difunctional chain transfer agent (CTA) . . . . .	93
4.4.5	Synthesis of telechelic PIP macro-CTA . . . . .	94
4.4.6	Synthesis of triblock copolymer PCMS- <i>b</i> -PIP- <i>b</i> -PCMS, Tri-1 and Tri-2 . . . . .	94
4.4.7	Gel Permeation Chromatography (GPC) . . . . .	95
4.4.8	Nuclear Magnetic Resonance (NMR) Spectroscopy . . . . .	95
4.4.9	Transmission Electron Microscopy (TEM) . . . . .	95
4.4.10	Small Angle X-ray Scattering (SAXS) . . . . .	95
4.4.11	Preparation of Thin Film Samples . . . . .	95
4.4.12	Ellipsometry . . . . .	98
4.4.13	Grazing-Incidence Small-Angle X-ray Scattering (GISAXS) . . . . .	98
4.4.14	X-ray photoelectron spectroscopy (XPS) . . . . .	99
4.4.15	Atomic Force Microscopy (AFM) . . . . .	99
4.5	Results and Discussion . . . . .	99
4.5.1	Polymer Synthesis . . . . .	99
4.5.1.1	Diblock Copolymer Synthesis . . . . .	99
4.5.1.2	Triblock Copolymer Synthesis . . . . .	104
4.5.2	Bulk Film Morphology . . . . .	108
4.5.3	Neutral Block Copolymer Thin Film Morphology . . . . .	108
4.5.4	Ionomer Thin Film Morphology . . . . .	117
4.6	Conclusions . . . . .	132

CHAPTER 5	EVALUATING THE EFFECT OF IONOMER CHEMICAL COMPOSITION IN SILVER- IONOMER CATALYST INKS TOWARD THE OXYGEN EVOLUTION REACTION BY HALF-CELL MEASUREMENTS AND WATER ELECTROLYSIS . . . .	134
5.1	Motivation . . . . .	134
5.2	Abstract . . . . .	135
5.3	Introduction . . . . .	136
5.4	Experimental Methods . . . . .	140
5.4.1	Materials . . . . .	140
5.4.2	Gel Permeation Chromatography (GPC) . . . . .	141
5.4.3	Nuclear Magnetic Resonance (NMR) Spectroscopy . . . . .	141
5.4.4	Environmental scanning electron microscopy (ESEM) and energy dispersive spectroscopy (EDS) . . . . .	141
5.4.5	BrunauerEmmetTeller (BET) Surface Area . . . . .	141
5.4.6	Half-Cell Electrode Fabrication . . . . .	141
5.4.7	Half-Cell Experiments . . . . .	142
5.4.8	Anion Exchange Membrane (AEM) Fabrication . . . . .	143
5.4.9	Differential Scanning Calorimetry (DSC) . . . . .	143
5.4.10	Ionic Conductivity Measurements . . . . .	143
5.4.11	Small-angle X-ray Scattering (SAXS) . . . . .	144
5.4.12	Membrane Electrode Assembly (MEA) Fabrication . . . . .	144
5.4.13	Single-Cell Electrolyzer Testing . . . . .	145
5.5	Results and Discussion . . . . .	145
5.5.1	PCMS- <i>b</i> -PCOE- <i>b</i> -PCMS Triblock Copolymer Characterization . . . . .	145
5.5.2	Electrode Fabrication and Characterization . . . . .	147
5.5.3	Electrochemical Characterization: Half-Cell Experiments . . . . .	148

5.5.3.1	Comparison of Quaternary Ammonium Cation . . . . .	150
5.5.3.2	Comparison of Ink Dilution . . . . .	157
5.5.3.3	Comparison of Partial Hydrogenation at Ni Foam Interface . . . . .	159
5.5.4	Performance Demonstration in AEM electrolyzer . . . . .	162
5.5.4.1	PIp- <i>ran</i> -PCMS Characterization . . . . .	162
5.5.4.2	AEM Characterization . . . . .	164
5.5.4.3	AEM Electrolyzer Performance . . . . .	165
5.6	Conclusions . . . . .	168
CHAPTER 6 CONCLUSIONS AND RECOMMENDATIONS . . . . .		170
6.1	Summary and Conclusions . . . . .	170
6.2	Recommendations for Future Work . . . . .	177
REFERENCES . . . . .		181
APPENDIX COPYRIGHT PERMISSIONS . . . . .		229

## LIST OF FIGURES

Figure 1.1	Schematic of an anion exchange membrane fuel cell using hydrogen as fuel. . . . 4
Figure 1.2	Schematic of an anion exchange membrane water electrolyzer. . . . . 5
Figure 1.3	Bibliometric analysis of the publications for AEMFCs and AEMWEs from 1990-present. “Fuel cell” or “electrolyzer”, along with “anion exchange membrane” were used as search terms. This citation report was generated using Web of Science. . . . . 7
Figure 1.4	Representation of a simplified anion exchange membrane. . . . . 8
Figure 1.5	Schematic representation of different copolymers of “A” and “B” components. Top: Example of a random copolymer configuration. Middle: Example of a diblock (AB) copolymer configuration. Bottom: Example of a triblock (ABA) copolymer configuration. . . . . 8
Figure 1.6	Morphologies of phase separating block copolymer systems, including spherical (S), cylindrical (C), gyroid (G), lamellar (L), and their inverse (‘). . . . 9
Figure 1.7	Chemical structures of common anion exchange membrane cation groups. From left to right, top: pyridinium, ammonium, phosphonium, and sulfonium. Bottom: guanidinium, imidazolium. Reproduced with permission from . . . . 10
Figure 1.8	Different tethering strategies, i.e. adjacent to or on the polymer backbone, terminal ionic groups with pendant chains, tails to tethered cationic moieties, and multiple cations on a side chain. Reproduced with permission from . . . . 10
Figure 1.9	Left: Schematic of detailed anion exchange membrane device electrode depicting the heterogeneous CL and electrode structure. Right: Schematic of ionomer-coated catalyst particle highlighting the idealized interfaces between ionomer, catalyst, and supporting material, along with species transport. . . . 12
Figure 1.10	Bibliometric analysis of the publications for ORR and OER catalysis in alkaline media. “ORR” or “OER”, along with “catalysis” and “alkaline” were used as search terms. This citation report was generated using Web of Science. 18
Figure 1.11	Pourbaix diagram of silver. Reproduced with permission from . . . . . 20
Figure 1.12	Model proposed by Paul et al. for thickness-dependent Nafion <sup>®</sup> thin film morphology on SiO <sub>2</sub> substrates. Reproduced with permission from . Copyright © 2013 American Chemical Society. . . . . 22
Figure 2.1	Graphical abstract. . . . . 28

Figure 2.2	$^1\text{H}$ NMR of R2-CTA (bottom black line), telechelic PCOE with a close-up of the end-group region (middle red line) and triblock PCMS- <i>b</i> -PCOE- <i>b</i> -PCMS (top blue line). . . . .	38
Figure 2.3	GPC traces of PCOE precursor (black line) and AEM-MP, triblock copolymer PCMS- <i>b</i> -PCOE- <i>b</i> -PCMS (red line). . . . .	38
Figure 2.4	Solid-state $^{13}\text{C}$ NMR and peak assignments of PCMS- <i>b</i> -PE- <i>b</i> -PCMS. . . . .	39
Figure 2.5	FTIR spectra of the starting PCMS- <i>b</i> -PCOE- <i>b</i> -PCMS (A), the hydrogenated PCMS- <i>b</i> -PE- <i>b</i> -PCMS (B), PCMS- <i>b</i> -PE- <i>b</i> -PCMS quaternized with TMA (C) and MPRD (D). Spectra from 1800 to 650 $\text{cm}^{-1}$ is shown at a larger scale for clarity. Dotted line indicates the $\nu(\text{C-Cl})$ from benzyl chloride groups at 827 $\text{cm}^{-1}$ . . . . .	40
Figure 2.6	(a) TGA of PCMS- <i>b</i> -PE- <i>b</i> -PCMS, unquaternized. (Solid line is weight %, dotted line is derivative weight). (b) DSC traces of PCMS- <i>b</i> -PCOE- <i>b</i> -PCMS (dotted) and PCMS- <i>b</i> -PE- <i>b</i> -PCMS (solid) powder. Heating and cooling rates of 10 $^\circ\text{C min}^{-1}$ . . . . .	41
Figure 2.7	Chemical structures of triblock copolymers PCMS- <i>b</i> -PE- <i>b</i> -PCMS, shown quaternized with either MPRD or TMA. . . . .	42
Figure 2.8	TGA of PCMS- <i>b</i> -PE- <i>b</i> -PCMS quaternized with TMA (left) and MPRD (right). Onset of degradation of each cation group was 170 $^\circ\text{C}$ and 190 $^\circ\text{C}$ , respectively. (Solid line = weight %, dotted line = derivative weight). . . . .	44
Figure 2.9	DSC of all HyAEMs. Red lines represent heating cycles and blue lines represent cooling cycles, both at 10 $^\circ\text{C}/\text{min}$ . Dotted lines represent second heating/cooling cycle, often the second cooling cycle nearly overlaps the first cooling cycle. . . . .	44
Figure 2.10	Water vapor uptake and $\lambda$ at 60 $^\circ\text{C}$ from 20 – 95% RH. . . . .	46
Figure 2.11	DVS traces of all PCMS- <i>b</i> -PE- <i>b</i> -PCMS samples, where red traces refer to water uptake and blue traces to the relative humidity. (a) HyAEM-TM-130, (b) HyAEM-TM-180, (c) HyAEM-MP-130, (d) HyAEM-MP-180. . . . .	47
Figure 2.12	SAXS profiles for all HyAEMs in the dry state at ambient conditions (green squares), at 60 $^\circ\text{C}$ (red circles), at 60 $^\circ\text{C}$ and 95% RH (blue triangles), and after soaking in liquid water (purple x's). Shown stacked for clarity. . . . .	48
Figure 2.13	SAXS profiles for all HyAEMs highlighting high q region with peak from cationic clusters. All graphs set to same scale for comparison. Dry state at ambient conditions (green squares), at 60 $^\circ\text{C}$ (red circles), at 60 $^\circ\text{C}$ and 95% RH (blue triangles), and after soaking in liquid water (purple x's). . . . .	51

Figure 2.14	TEM for AEM-MP (A), AEM-MP-DT (B), HyAEM-TM-130 (C), HyAEM-MP-130 (D), HyAEM-TM-180 (E) and HyAEM-MP-180 (F). (A) and (B) were stained with OsO <sub>4</sub> and the dark contrast comes from the hydrophobic PCOE domains. The remaining specimens were stained with RuO <sub>4</sub> and the dark contrast comes from the hydrophilic cation-functionalized domains. . . . .	52
Figure 2.15	Unified Fit modeling of SAXS data of HyAEM-TM-130 dry (top left) and wet (top right) and HyAEM-MP-130 dry (bottom left) and wet (bottom right). . .	53
Figure 2.16	Unified Fit modeling of SAXS data of HyAEM-TM-180 dry (top left) and wet (top right) and HyAEM-MP-180 dry (bottom left) and wet (bottom right). . .	54
Figure 2.17	Crystal size analysis from WAXS spectra of the (110) reflection (a,b) and the (200) reflection (c,d) of the polyethylene backbone in all HyAEMs at ambient temperature (a,c) and 60 °C (b,d). . . . .	55
Figure 2.18	WAXS spectra for all HyAEMs investigated at ambient conditions, 60 °C, 60 °C and 95% RH, and after soaking in DI water. . . . .	56
Figure 2.19	Left: Arrhenius plot of OH <sup>-</sup> (blue squares) and Cl <sup>-</sup> (red circles) conductivity at 95% RH for HyAEM-MP-180. Right: ASR for HyAEM-MP-180 in OH <sup>-</sup> form (blue squares) and Cl <sup>-</sup> form (red circles). IEC = 1.7 mmol g <sup>-1</sup> , thickness = 65 μm. . . . .	58
Figure 2.20	Left: IEC stability in terms of % of IEC retained after soaking in 9 M KOH at room temperature for 1 week. PCOE and PE-based AEMs compared to a commercial standard, Fumasep FAS-50. Right: IEC stability after soaking in 1 M KOH at 80°C for 1 or 3 days, comparing HyAEM-MP-180 (solid bar) to the commercial standard (cross hatch bar). . . . .	60
Figure 2.21	FTIR results for HyAEM-MP-180 before and after degradation in 9 M KOH. . .	60
Figure 2.22	<sup>1</sup> H NMR and assignments for the small molecule degradation product of HyAEM-MP-180 in 9 M KOH. . . . .	61
Figure 2.23	Possible degradation pathways of HyAEM-MP-180 in 9 M KOH. . . . .	62
Figure 3.1	Graphical abstract. . . . .	65
Figure 3.2	Structure of triblock copolymer PCMS- <i>b</i> -PCOE- <i>b</i> -PCMS, shown quaternized with either TMA or MPRD. . . . .	70
Figure 3.3	Small-angle X-ray scattering of TB, TB-MP, and TB-TM at dry, ambient conditions. Spectra are offset for clarity. . . . .	71

Figure 3.4	<p>Normalized FT-IR ATR spectra are given in the bottom inset of each figure for TB (a,b), TB-TM (c,d), and TB-MP (e,f) with pure polymer samples shown by red lines and silver-polymer composites shown by blue lines. Regions of interest, 4000–2700 <math>\text{cm}^{-1}</math> (a,c,e) and 1800–650 <math>\text{cm}^{-1}</math> (b,d,f) are shown for clarity. In the top inset of each figure, the IR intensity differences are calculated by subtracting the spectra of the pure polymer samples from those of the silver composites. Areas where the silver composites had a higher intensity are filled in green, and lower intensity are filled in red. All axes are set to same scale for comparison. . . . .</p>	72
Figure 3.5	<p>TGA curves (a-c) and derivative weight plots (d-f) for TB (a,d), TB-TM (b,e), and TB-MP (c,f). Pure polymer samples are shown by red lines and silver-polymer composites are shown by blue lines. . . . .</p>	75
Figure 3.6	<p>Stacked DSC heating (top) and cooling (bottom) traces for TB (left), TB-TM (middle), and TB-MP (right). 10°C/min heating and cooling rate. Red traces refer to the pure polymer sample and blue traces refer to the polymer cast with 10 wt% silver. Solid lines represent the 1st heating/cooling cycle, and dotted lines represent the 2<sup>nd</sup>–4<sup>th</sup> scans which were identical in all cases. Traces are offset for clarity. . . . .</p>	75
Figure 3.7	<p>X-ray photoelectron spectroscopy of silver nanopowder, calibrated at 284.8 eV and measured at 284.7 eV, including survey spectrum (a), Ag 3d (b) and Ag MNN (c). Fitting of the Ag 3d and Ag MNN peaks indicate partial oxidation of the silver nanoparticle surface . . . . .</p>	76
Figure 3.8	<p>Thermal characteristics obtained from DSC scans for TB (a,d), TB-TM (b,e), and TB-MP (c,f). PP = pure polymer, Ag = silver-polymer composite. (1) refers to 1st DSC scan, (2–4) refers to 2<sup>nd</sup>–4<sup>th</sup> DSC scans, which were identical. Melting and crystallization temperatures are shown in (a-c), enthalpy of melting and crystallization shown in (d-f). The relative crystallized fraction <math>X(t)</math> versus time shown in (g). . . . .</p>	77
Figure 3.9	<p>Jeziorny plots for TB (a), TB-TM (b), and TB-MP (c), where red lines show pure polymer samples and blue lines show polymer-silver composites. Note that no crystallization exotherm was noted for TB-TM-Ag, therefore it was excluded from this analysis. Inset figures highlight areas fit to determine the Avrami exponent and rate parameter from the slope and intercept, respectively, of the linear region, typically from <math>X(t) = 0.2-0.8</math>. <math>r^2</math> of linear fit is also provided in each inset. . . . .</p>	80
Figure 3.10	<p>WAXS spectra (a-c) and area under the curve analysis (d-f) for TB (a,d), TB-TM (b,e), and TB-MP (c,f). For WAXS spectra, pure polymer samples are shown by red lines and silver-polymer composites are shown by blue lines. Area under the curve was normalized to the pure triblock backbone for comparison. PP: pure polymer, Ag: silver-polymer composite. The enthalpy of melting, <math>\Delta H_m</math>, corresponding to the degree of crystallinity from the first melt cycle from DSC, is also shown in (d-f) for comparison. . . . .</p>	82

Figure 3.11	Wide angle X-ray scattering detector images, confirming no anisotropy in scattering and validating use of azimuthal averaging to obtain 2D spectra in main text. Note that the bright spot in bottom right region is from the mica window and did not affect further analysis. . . . .	83
Figure 3.12	Pie charts depicting the relative fraction of the area under the curve of each crystalline reflection derived from WAXS experiments. The purple slice (peak 1 in the main text) and the green slice (peak 3 in the main text) correspond to the area under the (010) and (110) reflections of the triclinic crystalline structure, respectively. The blue slice (peak 2 in the main text) corresponds to the (110) reflection of the monoclinic structure. . . . .	84
Figure 4.1	Graphical abstract. . . . .	88
Figure 4.2	Synthesis of difunctional RAFT CTA . . . . .	94
Figure 4.3	High resolution core-level spectra of the Ag (top) and O (bottom) regions of the silver-coated silicon substrates. The peak position the Ag $3d_{3/2}$ and $3d_{5/2}$ peaks as well as the Ag0 loss features indicates the silver surface and film is not heavily oxidized and most of the Ag is metallic . Further, the O 1s deconvolution shows a minuscule amount of oxygen that could be attributed to AgO which we speculate is at the interface between the native $\text{SiO}_2$ layer and the metallic Ag film. . . . .	96
Figure 4.4	5x5 $\mu\text{m}$ AFM height (left) and phase (right) image of a Ag-coated silicon substrate, confirming a thin uniform layer of Ag was deposited on the silicon wafer by thermal evaporation . . . . .	97
Figure 4.5	Setup for vapor quaternization reaction of thin films. (a) glass lid, (b) tall glass bottom, (c) glass stage, (d) polymer thin film on substrate, (e) reactant liquid, (f) reactant vapor. . . . .	97
Figure 4.6	Synthesis of diblock copolymer PIP- <i>b</i> -PCMS, Di-1 and Di-2. . . . .	100
Figure 4.7	GPC of PIP-SG1 and Di-1 (top) and PIP-SG1 and Di-2 (bottom). . . . .	102
Figure 4.8	$^1\text{H}$ NMR and corresponding labeled chemical structure of Di-1 and Di-2. . . . .	103
Figure 4.9	GPC of Tri-1 and Tri-2. . . . .	104
Figure 4.10	(A) $^1\text{H}$ NMR and (B) ESI mass spectra of difunctional CTA. The sodium ion adduct of the molecule was detected in positive ionization mode, with $m/z$ of $\sim 457$ u/e ( $M_w = M_{w,CTA} + M_{w,Na}$ ) . . . . .	105
Figure 4.11	$^1\text{H}$ NMR and corresponding labeled chemical structure of Tri-1 and Tri-2. . . . .	106
Figure 4.12	Synthesis of triblock copolymer PCMS- <i>b</i> -PIP- <i>b</i> -PCMS, Tri-1 and Tri-2. . . . .	107



Figure 4.13	SAXS of $\sim 50$ $\mu\text{m}$ films of Di-1 (a), Di-2 (b), Tri-1 (c) and Tri-2 (d). . . . .	109
Figure 4.14	TEM of Di-1 (a), Di-2 (b), Tri-1 (c), and Tri-2 (d). Dark domains are PIP selectively stained with $\text{OsO}_4$ . Scale bars are all 100 nm. . . . .	109
Figure 4.15	Scattering of Di-1-30 (left) and Tri-1-30 (right) on plain silicon substrates. No distinct scattering features are noted. . . . .	110
Figure 4.16	2D GISAXS images for Di-1, Di-2, Tri-1 and Tri-2 of the 30, 45 and 60 nm samples. Horizontal linecuts are compared for the 30 nm (red), 45 nm (yellow) and 60 nm (blue) thin films. Linecut traces are offset for clarity. . . .	111
Figure 4.17	AFM height (a,c) and phase (b,d) images of Di-1 (1), Di-2 (2), Tri-1 (3), and Tri-2 (4) 30 nm samples on Ag substrates. $1 \times 1$ $\mu\text{m}$ (a,b) and $500 \times 500$ nm (c,d) images are shown. Scale bars all represent 200 nm. In height images, bright contrast represents PIP domains. In phase images, dark regions correspond to PIP domains. . . . .	113
Figure 4.18	$1 \times 1$ $\mu\text{m}$ AFM height (left) and phase (right) image of Di-1-30 on plain silicon. Both height and phase image show less distinct ordering and separation of the surface morphology. Bright domains in the height image and darker regions in the phase image correspond to PIP . . . . .	113
Figure 4.19	Domain size distributions determined from AFM images for Di-1 (a), Di-2 (b), Tri-1 (c) and Tri-2 (d). . . . .	114
Figure 4.20	20 nm samples of Di-1, Di-2, Tri-1 and Tri-2 (from top to bottom). Left column shows 2D GISAXS images, right column shows azimuthal linecuts taken at angles varying from $0$ - $90^\circ$ . . . . .	115
Figure 4.21	Annealing experiment for Tri-1-30. Top shows GISAXS images during heating and cooling. Bottom left shows horizontal line cuts from heating images, bottom right shows horizontal line cuts from cooling images. . . . .	116
Figure 4.22	Horizontal linecuts from 2D GISAXS images. Red traces are from ambient conditions, blue traces were taken at $60^\circ\text{C}$ and 95% RH. . . . .	118
Figure 4.23	Di-1-TMA GISAXS 2D images at ambient conditions (top row) and $60^\circ\text{C}$ 95% RH (bottom row). From left to right: 30 nm, 45 nm and 60 nm samples. . .	119
Figure 4.24	Di-1-MPRD GISAXS 2D images at ambient conditions (top row) and $60^\circ\text{C}$ 95% RH (bottom row). From left to right: 30 nm, 45 nm and 60 nm samples. .	119
Figure 4.25	Tri-1-TMA GISAXS 2D images at ambient conditions (top row) and $60^\circ\text{C}$ 95% RH (bottom row). From left to right: 30 nm, 45 nm and 60 nm samples. .	120
Figure 4.26	Tri-1-MPRD GISAXS 2D images at ambient conditions (top row) and $60^\circ\text{C}$ 95% RH (bottom row). From left to right: 30 nm, 45 nm and 60 nm samples. .	120

Figure 4.27	Unified Fit Modeling for Di-1-TMA. (a) Di-1-30-TMA, dry. (b) Di-1-30-TMA, 60 °C and 95% RH. (c) Di-1-45-TMA, dry. (d) Di-1-45-TMA, 60 °C and 95% RH. (e) Di-1-60-TMA, dry. (f) Di-1-60-TMA, 60 °C and 95% RH. . . . .	121
Figure 4.28	Unified Fit Modeling for Di-1-MPRD. (a) Di-1-30-MPRD, dry. (b) Di-1-30-MPRD, 60 °C and 95% RH. (c) Di-1-45-MPRD, dry. (d) Di-1-45-MPRD, 60 °C and 95% RH. (e) Di-1-60-MPRD, dry. (f) Di-1-60-MPRD, 60 °C and 95% RH. . . . .	122
Figure 4.29	Unified Fit Modeling for Tri-1-TMA. (a) Tri-1-30-TMA, dry. (b) Tri-1-30-TMA, 60 °C and 95% RH. (c) Tri-1-45-TMA, dry. (d) Tri-1-45-TMA, 60 °C and 95% RH. (e) Tri-1-60-TMA, dry. (f) Tri-1-60-TMA, 60 °C and 95% RH. . . . .	123
Figure 4.30	Unified Fit Modeling for Tri-1-MPRD. (a) Tri-1-30-MPRD, dry. (b) Tri-1-30-MPRD, 60 °C and 95% RH. (c) Tri-1-45-MPRD, dry. (d) Tri-1-45-MPRD, 60 °C and 95% RH. (e) Tri-1-60-MPRD, dry. (f) Tri-1-60-MPRD, 60 °C and 95% RH. . . . .	124
Figure 4.31	Surface plots illustrating the correlation between film thickness and relative humidity on the radius of gyration for Di-1-TMA, Di-1-MPRD, Tri-1-TMA, and Tri-1-MPRD (from left to right). A global color scale to the right is provided for comparison of the radius of gyration across all samples investigated. . . . .	127
Figure 4.32	Comparison of horizontal and vertical linecuts for Di-1-TMA and Di-1-MPRD, at dry (red traces) and 60 °C and 95% RH (blue traces). . . . .	129
Figure 4.33	Comparison of horizontal and vertical linecuts for Tri-1-TMA and Tri-1-MPRD, at dry (red traces) and 60 °C and 95% RH (blue traces). . . . .	130
Figure 4.34	Percent change in $R_g$ with hydration for Di-1-TMA samples (a), Di-1-MPRD samples (b), Tri-1-TMA samples (c) and Tri-1-MPRD samples (d). . . . .	131
Figure 5.1	Graphical abstract. . . . .	135
Figure 5.2	Diagram of an anion exchange membrane (AEM) water electrolysis cell, including detailed interfaces of the Ni foam and carbon paper porous transport layers (PTLs) and catalyst layers (CLs). . . . .	136
Figure 5.3	GPC of PCMS- <i>b</i> -PCOE- <i>b</i> -PCMS used to calculate $M_n$ , $M_w$ and PDI. . . . .	146
Figure 5.4	$^1\text{H}$ NMR of PCMS- <i>b</i> -PCOE- <i>b</i> -PCMS used to calculate the degree of polymerization (DP) and ion exchange capacity (IEC). . . . .	146
Figure 5.5	$\text{N}_2$ isotherm of pristine nickel foam substrate, used to calculate the BET surface area. . . . .	147

Figure 5.6	SEM images of pristine nickel foam (a,b) and representative as-deposited Ag-ionomer catalyst ink on Ni foam (c,d). . . . .	148
Figure 5.7	Cross-sectional diagram of the FlexCell <sup>®</sup> half-cell electrochemical measurement apparatus. . . . .	149
Figure 5.8	iR corrected LSVs (a), double layer capacitance (b), and Tafel Plots at low (c) and high (d) overpotential comparing PC-TM-25 and PC-MP-25. . . . .	150
Figure 5.9	Nyquist impedance plots of EIS performed at OCV to determine the high frequency intercept, i.e. the solution resistance, used for iR correction. (a) shows full impedance spectra, (b) shows the high frequency intercepts for clarity. . . . .	151
Figure 5.10	Ni Foam Double Layer Capacitance. . . . .	151
Figure 5.11	Tafel plots of Ni foam at low (a,c) and high (b,d) overpotentials, showing results with no iR correction (a,b) and 100% iR correction (c,d). . . . .	152
Figure 5.12	CV scans performed at 10, 20, 30 and 50 mV dec <sup>-1</sup> between 1.12 and 1.22 V, used to calculate $C_{dl}$ . . . . .	153
Figure 5.13	LSV comparing all samples investigated, no iR correction. . . . .	154
Figure 5.14	Tafel slopes from LSVs with no iR correction for PC-TM-25 and PC-MP-25 at low (a) and high (d) current densities, for PC-TM-100 and PC-MP-100 at low (b) and high (e) current densities, and PE-TM-100 and PE-MP-100 at low (c) and high (f) current densities. . . . .	154
Figure 5.15	iR corrected LSVs (a), double layer capacitance (b), and Tafel Plots at low (c) and high (d) overpotential comparing PC-TM-100 and PC-MP-100. . . . .	158
Figure 5.16	Mass activity (per gram Ag catalyst) comparing all samples investigated, with iR correction (a) and without iR correction (b). . . . .	159
Figure 5.17	DSC of PCMS- <i>b</i> -PCOE- <i>b</i> -PCMS coated Ni foam sample after partial hydrogenation to PE under H <sub>2</sub> (g). Heating and cooling rates at 10 °C min <sup>-1</sup> . . . . .	160
Figure 5.18	iR corrected LSVs (a), double layer capacitance (b), and Tafel Plots at low (c) and high (d) overpotential comparing PE-TM-100 and PE-MP-100. . . . .	161
Figure 5.19	GPC of PIP- <i>ran</i> -PCMS used to calculate $M_n$ , $M_w$ and PDI. . . . .	163
Figure 5.20	<sup>1</sup> H NMR of PIP- <i>ran</i> -PCMS used to calculate the degree of polymerization (DP) and ion exchange capacity (IEC). . . . .	163

Figure 5.21	SAXS of the AEM fabricated from Tuffbrane™ at ambient, dry conditions and immersed in liquid water. Porod slope of 2 indicates a particle symmetry of randomly distributed lamellae. . . . .	164
Figure 5.22	Polarization curves for AEM electrolyzers EL-PE-TM and EL-PE-MP in 1 M K <sub>2</sub> CO <sub>3</sub> (a) or DI H <sub>2</sub> O (b) at 50 °C with iR correction. 60% iR correction was used for polarization curves in 1 M K <sub>2</sub> CO <sub>3</sub> and 100% iR correction was used for polarization curves in DI H <sub>2</sub> O. . . . .	165
Figure 5.23	Polarization curves for AEM electrolyzers EL-PE-TM and EL-PE-MP in 1 M K <sub>2</sub> CO <sub>3</sub> (a) or DI H <sub>2</sub> O (b) at 50 °C with no iR correction. . . . .	166
Figure 5.24	Nyquist impedance plots of EIS performed at OCV to determine the HFR for iR correction and calculation of the ASR. (a) shows all electrolyzer cells, (b) shows EL-PE-TM and EL-PE-MP in 1M K <sub>2</sub> CO <sub>3</sub> , and (c) shows EL-PE-TM and EL-PE-MP in DI H <sub>2</sub> O. . . . .	166
Figure 5.25	Voltage degradation of EL-PE-MP electrolyzer. The current density of the cell was held constant at 500 mA cm <sup>-2</sup> for a duration of 5 h. . . . .	167
Figure 6.1	Bibliometric analysis the publications for OER catalysts at neutral pH. “Oxygen evolution reaction” and “neutral pH”, along with each catalyst were used as search terms. This citation report was generated using Web of Science. . . . .	178
Figure 6.2	Reaction scheme showing the hydrogenation of PCMS- <i>b</i> -PIp- <i>b</i> -PCMS to PCMS- <i>b</i> -PMB- <i>b</i> -PCMS. . . . .	179
Figure A.1	Permission to reproduce Figure 1.7 from [45]. . . . .	229
Figure A.2	Permission to reproduce Figure 1.8 from [78]. . . . .	230
Figure A.3	Permission to reproduce Figure 1.11 from [165]. . . . .	231
Figure A.4	Permission to reproduce Figure 1.12 from [189]. . . . .	232
Figure A.5	Permission to reproduce Chapter 2 from [102]. . . . .	232
Figure A.6	Permission to reproduce Chapter 3 from [395]. . . . .	233
Figure A.7	Permission received to reproduce co-authored journal articles, either published or in review, from Yifeng Du. . . . .	233
Figure A.8	Permission received to reproduce co-authored journal articles, either published or in review, from Mei-Chen Kuo. . . . .	234
Figure A.9	Permission received to reproduce co-authored journal articles, either published or in review, from Jacob S. Wilkinson. . . . .	234

Figure A.10	Permission received to reproduce co-authored journal articles, either published or in review, from Ivy Wu. . . . .	235
Figure A.11	Permission received to reproduce co-authored journal articles, either published or in review, from Kayla A. Ahrens. . . . .	235
Figure A.12	Permission received to reproduce co-authored journal articles, either published or in review, from Ryan J. Gasvoda. . . . .	236
Figure A.13	Permission received to reproduce co-authored journal articles, either published or in review, from James M. Crawford. . . . .	237
Figure A.14	Permission received to reproduce co-authored journal articles, either published or in review, from Ria Ghosh. . . . .	238
Figure A.15	Permission received to reproduce co-authored journal articles, either published or in review, from Morgan S. Ezell. . . . .	239
Figure A.16	Permission received to reproduce co-authored journal articles, either published or in review, from Sumit Agarwal. . . . .	240
Figure A.17	Permission received to reproduce co-authored journal articles, either published or in review, from Moises A. Carreon. . . . .	241
Figure A.18	Permission received to reproduce co-authored journal articles, either published or in review, from Soenke Seifert. . . . .	242
Figure A.19	Permission received to reproduce co-authored journal articles, either published or in review, from E. Bryan Coughlin. . . . .	243

## LIST OF TABLES

Table 2.1	Elemental analysis of PCMS- <i>b</i> -PE- <i>b</i> -PCMS triblock backbone hot pressed at 130 °C and 180 °C, HyAEM-TM-130 and HyAEM-MP-130. Calculated values shown in parenthesis. For quaternized membranes, calculated values are based on theoretical IEC obtained from NMR. . . . .	42
Table 2.2	Descriptions and Ion Exchange Capacities of All Anion Exchange Membranes Studied . . . . .	43
Table 2.3	Thermal Characterization from DSC . . . . .	45
Table 2.4	Water Uptake and $\lambda$ from DVS . . . . .	46
Table 2.5	Liquid Water Uptake, $\lambda$ , and Dimensional Swelling . . . . .	47
Table 2.6	Radius of Gyration, Porod Slope, and Bragg Spacing obtained from Unified Fit Modeling of SAXS Profiles . . . . .	50
Table 2.7	Mechanical Properties of Dry and Wet Films . . . . .	57
Table 3.1	Chemical Composition of PCMS- <i>b</i> -PCOE- <i>b</i> -PCMS base copolymer . . . . .	69
Table 3.2	FT-IR ATR Vibrational Mode Assignments and Observations from AgNP Interactions . . . . .	73
Table 3.3	Summary of Parameters from Jeziorny-Modified Avrami Crystallization Kinetics Analysis . . . . .	81
Table 4.1	Chemical composition and bulk morphology of diblock copolymer PIP- <i>b</i> -PCMS and triblock copolymer PCMS- <i>b</i> -PIP- <i>b</i> -PCMS . . . . .	101
Table 4.2	Domain Spacing of Neutral Block Copolymers Determined from GISAXS $q^*$ . . . . .	111
Table 4.3	Domain Size and Surface Coverage of Neutral Block Copolymers Determined from AFM . . . . .	112
Table 4.4	Unified Fit Model Parameters for Di-1-TMA Samples. . . . .	125
Table 4.5	Unified Fit Model Parameters for Di-1-MPRD Samples. . . . .	125
Table 4.6	Unified Fit Model Parameters for Tri-1-TMA Samples. . . . .	126
Table 4.7	Unified Fit Model Parameters for Tri-1-MPRD Samples. . . . .	126

Table 5.1	Chemical Composition and Ion Exchange Capacity of PCMS- <i>b</i> -PCOE- <i>b</i> -PCMS from GPC and NMR. . . . .	146
Table 5.2	Surface elemental composition for Ni foam and Ag-ionomer coated Ni foam, from EDS. . . . .	148
Table 5.3	Summary of Ag-ionomer inks used in this work. . . . .	149
Table 5.4	Summary of Electrokinetic Parameters from iR Corrected LSVs fit to Tafel Equation. . . . .	152
Table 5.5	Summary of Electrokinetic Parameters from LSVs with no iR correction fit to the Tafel Equation. . . . .	155
Table 5.6	Summary of OER Performance Parameters from iR Corrected LSVs. . . . .	156
Table 5.7	Summary of OER Performance Parameters from LSVs with no iR correction. . . . .	157
Table 5.8	Chemical Composition and Ion Exchange Capacity of PCMS- <i>b</i> -PCOE- <i>b</i> -PCMS from GPC and NMR. . . . .	163
Table 5.9	Ionic Conductivity of the AEM fabricated from Tuffbrane™ in Liquid Water. . . . .	164
Table 5.10	Area Specific Resistances (ASR) of AEM Electrolyzers in 1 M K <sub>2</sub> CO <sub>3</sub> and DI H <sub>2</sub> O. . . . .	167

## LIST OF SYMBOLS

Current density . . . . .	$j$
Domain spacing . . . . .	$d_s$
Double layer capacitance . . . . .	$C_{dl}$
Enthalpy of crystallization . . . . .	$\Delta H_c$
Enthalpy of melting . . . . .	$\Delta H_m$
Exchange current density . . . . .	$j_0$
Overpotential . . . . .	$\eta$
Porod slope . . . . .	$P$
Radius of gyration . . . . .	$R_g$
Waters per charge carrier . . . . .	$\lambda$



## LIST OF ABBREVIATIONS

Alkaline fuel cell . . . . .	AFC
Alkaline water electrolyzer . . . . .	AWE
Anion exchange ionomer . . . . .	AEI
Anion exchange membrane . . . . .	AEM
Anion exchange membrane fuel cell . . . . .	AEMFC
Anion exchange membrane water electrolyzer . . . . .	AEMWE
Area specific resistance . . . . .	ASR
Atomic force microscopy . . . . .	AFM
Benzylmethylpiperidinium . . . . .	MPRD
Benzyltrimethylammonium . . . . .	TMA
Catalyst layer . . . . .	CL
Cyclic voltammetry . . . . .	CV
Degree of polymerization . . . . .	DP
Differential scanning calorimetry . . . . .	DSC
Dynamic vapor sorption . . . . .	DVS
Electrochemical impedance spectroscopy . . . . .	EIS
Gas diffusion electrode . . . . .	GDE
Gel permeation chromatography . . . . .	GPC
Grazing-incidence small-angle X-ray scattering . . . . .	GISAXS
Grazing-incidence wide-angle X-ray scattering . . . . .	GIWAXS
Hydrogen evolution reaction . . . . .	HER
Hydrogen oxidation reaction . . . . .	HOR

Ion exchange capacity . . . . .	IEC
Oxygen evolution reaction . . . . .	OER
Oxygen reduction reaction . . . . .	ORR
Perfluorinated sulfonic acid . . . . .	PFSA
Platinum group metal . . . . .	PGM
Poly(chloromethylstyrene) . . . . .	PCMS
Poly(cyclooctene) . . . . .	PCOE
Poly(ethylene) . . . . .	PE
Poly(isoprene) . . . . .	PIp
Polydispersity index . . . . .	PDI
Porous transport layer . . . . .	PTL
Proton exchange membrane . . . . .	PEM
Proton exchange membrane fuel cell . . . . .	PEMFC
Proton exchange membrane water electrolyzer . . . . .	PEMWE
Quaternary ammonium cation . . . . .	QAC
Relative humidity . . . . .	RH
Reversible addition-fragmentation chain transfer radical polymerization . . . . .	RAFT
Ring-opening metathesis polymerization . . . . .	ROMP
Silver nanoparticle . . . . .	AgNP
Small-angle X-ray scattering . . . . .	SAXS
Thermogravimetric analysis . . . . .	TGA
Transmission electron microscopy . . . . .	TEM
Water uptake . . . . .	WU
Wide-angle X-ray scattering . . . . .	WAXS

## ACKNOWLEDGMENTS

First, I would like to thank my advisor, Dr. Andrew M. Herring, for his insight, guidance, and consistent encouragement throughout my thesis work. I am grateful to have worked with such fantastic colleagues in the lab, including Mei-Chen Kuo, Ivy Wu, ChuloOong Chris Kim, Jed LaCoste, Ashutosh Divekar, and Andrew Motz, with guest appearances by Jim Horan. I was fortunate to work alongside colleagues from the University of Massachusetts Amherst, Dr. E. Bryan Coughlin and Yifeng Du, whose invaluable collaboration and insight made this thesis work possible. I would also like to thank my fellow graduate students in our department, the gentlefolk, and the tour. This would have not been possible without their support and camaraderie. I am extremely grateful for the camping trips, mountain bike rides, powder days, and white water rafting excursions that we have shared together, which made graduate school a time I will always cherish. I am incredibly lucky to have been a part of such a wonderful research group and a welcoming department.

Further, my graduate studies would not have been possible without the stimulating and positive experience I had in my undergraduate at Rowan University. I gratefully acknowledge the excellent instruction and mentorship provided by all of my undergraduate professors, with special recognition to Dr. Kevin Dahm and Dr. Zenaída Otero Gephardt, whose continued counsel, throughout my graduate education, proved invaluable. I would also like to thank the high school teachers who inspired me to pursue engineering, including Mayra Bachrach, Rebecca Allison, and Michael Dancho. The importance of quality educators, who inspire and motivate you to reach your full potential, cannot be understated.

My graduate work was graciously funded by the Army Research Office through Grant W911NF-17-1-0568. Their financial support allowed me to travel to work with our excellent beamline scientist at Argonne National Laboratory, Soenke Seifert, whose consistent espresso shots were essential for a productive beamline shift. Finally, I would like to acknowledge my family, for supporting my education and ambitions, even when it meant moving far from home. I would especially like to thank my partner Grace for her love, patience, and unwavering support throughout my graduate studies.

In loving memory of my grandmother, Hildegard Eva Louise Dimond,  
who continued to inspire me to pursue my education to the fullest  
and who undoubtedly would have been proud  
to see how far I have come.

# CHAPTER 1

## INTRODUCTION

### 1.1 The Hydrogen Economy

There is irrefutable evidence of global warming and climate change; atmospheric amounts of greenhouse gases have increased significantly over the last 200 years, and land and ocean surface temperatures have elevated over the past 100 years [1]. Anthropogenic emissions of CO<sub>2</sub> contribute the most to greenhouse gas-induced warming and come largely from the combustion of fossil fuels [2]. To mitigate the risks associated with climate change, including severe weather events, rising sea levels, melting polar ice and ocean acidification [1], alternatives to fossil fuels or renewable energy technologies are of interest.

Hydrogen could be a fundamental component of the energy transition required to combat both global warming and drawbacks of our current energy systems [3]. Utilization of hydrogen-based energy systems will ultimately deliver reliable and affordable energy, while improving the resiliency of the current energy infrastructure. Additionally, hydrogen is a cleaner energy carrier that can be used in both stationary applications and for transportation via fuel cells and hydrogen-fueled internal combustion engines [4]. Hydrogen can also be used as a sustainable energy storage medium for electricity produced from intermittent renewable sources (e.g. wind, solar) [5]. Additionally, hydrogen is a valuable industrial chemical feedstock used in the production of methanol, ammonia, and steel production [6–8].

In order for a hydrogen-based energy economy to be realized, the cost of hydrogen production from renewable energy systems needs to be reduced [9]. This can be achieved through the development and optimization of technologies that both produce and utilize hydrogen on both stationary and portable scales [10]. As of 2020, approximately 95% of hydrogen produced in the United States is via natural gas reforming, which is an unsustainable process not only because CO<sub>2</sub> is a byproduct typically emitted in the process, but the product gas stream is not pure and needs to undergo energy intensive separation processes in order to provide a high purity hydrogen product [11]. For this reason, sustainable production of hydrogen via electrolytic processes and photolytic processes (e.g. direct solar water splitting) are of interest to ultimately remove CO<sub>2</sub>

emissions from the hydrogen production process and produce a higher purity product [12]. In the transportation sector, fuel cells and battery-powered electric vehicles are positioned to reduce CO<sub>2</sub> emissions in air, land, and water transportation applications.

The remainder of this chapter will focus on two hydrogen-based technologies: fuel cells, which utilize the electrochemical conversion of hydrogen fuel into electricity and electrolyzers, which produce hydrogen fuel via the electrochemical splitting of water.

## 1.2 Fuel Cells

The fuel cell is an electrochemical energy conversion device that produces electricity directly from chemical conversion of fuels, such as hydrogen. Fuel cells can be applied to both mobile and stationary power applications. Electrochemistry is more efficient than combustion at lower temperatures, which is limited by the efficiency of the Carnot cycle [13]. The principle of fuel cell technology was first introduced by W.R. Grove in 1839, where he described a voltaic cell containing a platinum cathode immersed in nitric acid and an amalgamated zinc anode in dilute sulfuric acid [14]. While this device had incredibly low power output, it laid the groundwork for the concept of a fuel cell apparatus. Improvements were made by Jacques [15] in 1896 and Bacon [16] in 1954, who developed the first H<sub>2</sub>/O<sub>2</sub> alkaline fuel cell in liquid KOH. In the 1960's, the National Aeronautics and Space Administration (NASA) utilized alkaline fuel cells on both the Gemini (1963) and Apollo (1968) spacecrafts [17], though high costs still prevented their commercial implementation at this time. In 1966, DuPont de Nemours and Co. produced the perfluorinated sulfonic acid (PFSA) membrane Nafion<sup>®</sup>, which was originally developed for electrolysis in the chloro-alkali industry. Nafion<sup>®</sup> membranes exhibited high proton conductivity and durability in acidic media, which ultimately catalyzed further development of proton exchange membrane fuel cells (PEMFCs). Despite interest in fuel cells fading, the 1990's brought on a public awareness of global warming, which has revitalized research interests in renewable energy alternatives.

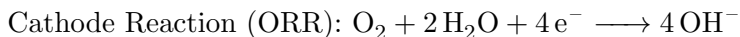
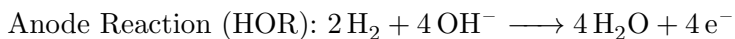
Electric vehicles are positioned to solve multiple problems, including reducing carbon emissions and local pollution levels, along with providing a lower cost by eliminating the need for rare precious metals (e.g. platinum, rhodium, and palladium) in the catalytic converter of gasoline-powered internal combustion engines. PEMFCs have captured the interest of both

researchers and industry because of their high-power density and have already been commercialized by automobile manufacturers. Notably, the Toyota Mirai and the Honda Clarity are two PEMFC-based vehicles that are currently available in the consumer market. Commercialized state of the art PEMFC technology utilizes PFSA proton exchange membranes and precious metal catalysts (typically platinum) in their applications. The use of precious metal catalysts is one of the main drawbacks to PEMFC widespread implementation; the use of platinum is both expensive and unsustainable as it is not abundant, especially for large scale power generation applications. Additionally, PFSA-based materials have negative environmental impacts as they are extremely resistant to degradation. Recently their widespread presence in drinking water was detected across the United States [18], causing some states to ban their use permanently in certain products [19]. Current PEMFC research is focused on mitigating these impacts by improving current polymer chemistry via additives, improving Pt utilization and designing new catalyst frameworks that utilize non-precious metals, and improving their durability to operate at higher temperatures [20].

Alkaline fuel cells (AFCs) use concentrated potassium hydroxide as an electrolyte solution. This type of fuel cell has been used in the majority of space missions and is still being used today for power and potable water generation [21]. Its widespread commercialization was never realized due to its limited lifetime and issues with scalability [22]. Another drawback of AFCs is the carbonation phenomena, in which carbon dioxide present in air reacts with the potassium hydroxide electrolyte to form potassium carbonate solids, which settle and clog electrodes, lowering the overall conductivity and performance of the cell until they are scrubbed from the system. Despite this drawback, electrochemistry in alkaline media is still of interest due to more facile kinetics of ORR in an alkaline media [23, 24]. This theoretically allows for the use of non-platinum group metal (PGM) catalysts such as silver, nickel, or cobalt, to achieve similar performance to PEMFCs at a reduced cost.

The anion exchange membrane fuel cell (AEMFC) is identical to the AFC in terms of how it operates; however, it utilizes an anionic solid polymer electrolyte. Utilizing a thin polymer electrolyte mitigates the need for liquid electrolytes and their associated issues, including the pumps required for liquid feeds and leaks that may occur, all while improving the power density and footprint of the device. In an AEMFC, the oxygen reduction reaction (ORR) occurs at the

cathode and the hydrogen oxidation reaction (HOR) occurs at the anode. The reactions are given below:



Oxygen reacts with water and electrons and is reduced at the cathode to produce hydroxide ions ( $\text{OH}^-$ ) which transport across the polymer electrolyte to the anode. At the anode, hydrogen flows into the fuel cell and combines with  $\text{OH}^-$  to form water and electrons. A diagram of an AEMFC is shown in Figure 1.1. Water management is particularly important in AEMFCs because it is both a product at the anode and a reactant at the cathode [25], creating a large water differential that is three times larger than in PEMFCs. This is currently being addressed through new operational strategies and cell architectures [26], in addition to optimization of the catalyst layer and AEM.

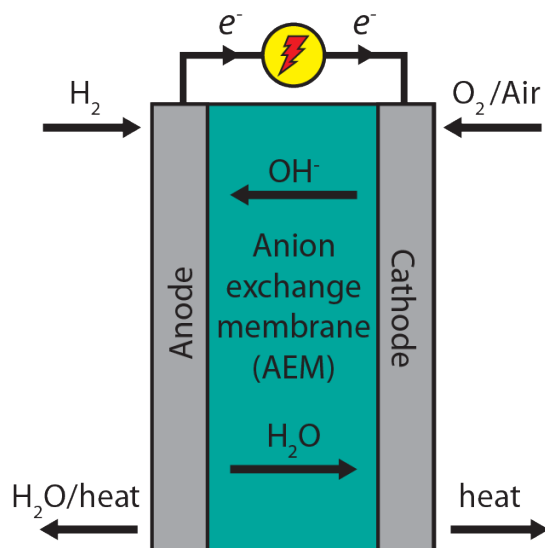


Figure 1.1 Schematic of an anion exchange membrane fuel cell using hydrogen as fuel.

The advantages of AEMFCs are similar to those of AFCs, where non-noble metal catalysts may be employed due to better kinetics of ORR at high pH. Other research suggests there is little to no fuel crossover in AEMFCs compared to PEMFCs because hydroxide ions in an AEMFC flow in the opposite direction of protons in a PEMFC and, therefore, there is less fuel crossover



due to ionic and osmotic drag across the polymer membrane [27].

### 1.3 Electrolyzers

For hydrogen to be effectively utilized by fuel cell technologies, it must first be sustainably produced. While there are many methods of producing hydrogen, including thermal, electrolytic, and photolytic processes from fossil fuels, biomass, and water [28–32], this section will focus on water electrolysis. Water is an ideal source for hydrogen production due to its wide availability, and further mitigates CO<sub>2</sub> emissions from using fossil fuel precursors. Low-temperature alkaline water electrolysis utilizing concentrated liquid KOH is considered a mature technology [33]. The two other main types are proton exchange membrane (PEM) electrolysis (considered mature on a small scale) and anion exchange membrane (AEM) electrolysis (still in R&D) [34, 35].

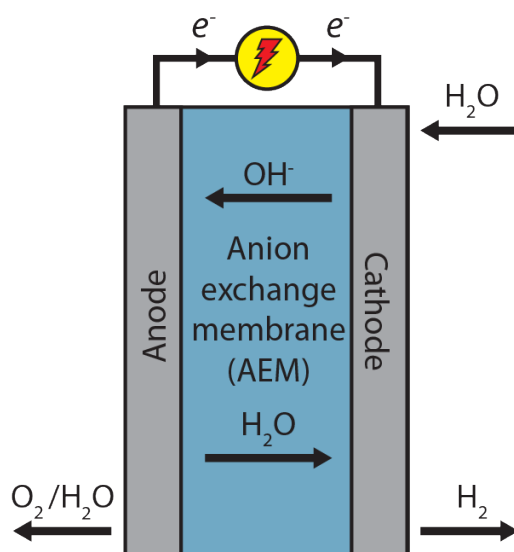


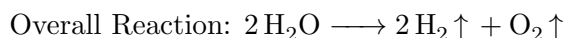
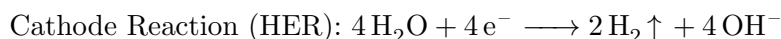
Figure 1.2 Schematic of an anion exchange membrane water electrolyzer.

Alkaline water electrolyzers (AWEs) use a liquid electrolyte, typically 30-40 wt% KOH, and nickel and cobalt-based oxide catalysts in the anode and cathode respectively [36]. The anode and cathode in this system are separated by a porous diaphragm. The main advantage of alkaline electrolysis over PEM electrolysis is the pH, where in alkaline media, non-noble metal catalysts can be utilized. The development of catalysts for the oxygen evolution reaction (OER) and hydrogen evolution reaction (HER) are well documented in both acidic and alkaline media [37–39]; however, issues related to recirculating a liquid electrolyte, e.g. electrolyte leakage, is a

disadvantage of AWEs, and the footprint of liquid systems is larger when considering scale-up. Further, the hydrogen production rate is relatively low, where operating conditions are typically  $200 \text{ mA cm}^{-2}$  at a cell voltage of  $1.8 \text{ V}$  with a conversion efficiency of  $\sim 75\%$  [40, 41].

PEM water electrolyzers (PEMWEs) utilize a proton conducting membrane and ionomer, eliminating the need for recirculating liquid electrolytes. This configuration allows for a more compact cell, where the anode and cathode are in physical contact with the non-porous PEM, also known as a zero-gap configuration. PEMWEs can operate at  $\sim 2 \text{ A cm}^{-2}$  with a conversion efficiency of  $\sim 74\%$  due to the advantages associated with the zero-gap configuration [41]. Despite the advantages in performance and footprint, PEMWEs require costly electrocatalysts including platinum and iridium oxide. Additionally, the acidic nature of these devices leads to additional requirements for corrosion-resistance of the current collectors and flow fields [42]. The high costs of these materials will likely prevent the large systems and cell stacks from widespread implementation.

AEM water electrolyzers (AEMWEs) combine the advantages of PEMWEs and AWEs by leveraging a zero-gap configuration with an alkaline environment where non-PGM catalysts can be implemented. In an AEMWE, water or alkaline liquid electrolyte (e.g. KOH,  $\text{K}_2\text{CO}_3$ ) is circulated through the cathode. In an AEMWE, the oxygen evolution reaction (OER) occurs at the anode and the hydrogen evolution reaction (HER) occurs at the cathode. The half-cell reactions are given below:



At the cathode, water is reduced to hydrogen and hydroxide ions. Hydroxide ions move across the AEM to the anode, where hydroxide ions are oxidized to produce oxygen, water, and four electrons which travel through the external circuit from anode to cathode. A schematic of an AEMWE is given in Figure 1.2.

Due to the associated low catalyst and hardware costs, interest in producing hydrogen via AEMWEs has grown in recent years. The main hurdle to scaling up this technology is durability of the AEM and anion exchange ionomers in the anode and cathode catalyst layers [43].

## 1.4 Anion Exchange Membranes

The membrane is the heart of the AEMFC or AEMWE. The bibliometric analysis in Figure 1.3 shows how publication number of AEMFC and AEMWE-related research has increased in recent years, as improvements in AEM development are realized.

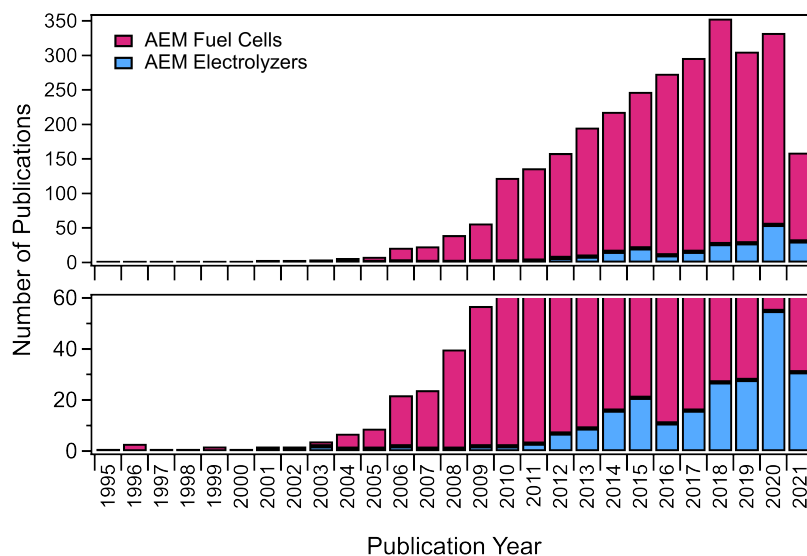


Figure 1.3 Bibliometric analysis of the publications for AEMFCs and AEMWEs from 1990-present. “Fuel cell” or “electrolyzer”, along with “anion exchange membrane” were used as search terms. This citation report was generated using Web of Science.

The AEM is tasked with selectively transporting hydroxide ions and water via functional groups in the polymer while preventing permeation of fuels, oxidants, and electrons [44, 45]. An anion exchange polymer consists of a polymer backbone with functional groups for anion exchange that are covalently bonded to the backbone (see Figure 1.4).

Required membrane characteristics include having high ionic conductivity, low fuel/oxidant crossover, low electrical conductivity, adequate water uptake, and excellent chemical and mechanical stability [46]. The ion exchange capacity (IEC) is an important membrane characteristic and refers to the number of available cationic sites on the polymer available for transporting ionic species, expressed in  $\text{mmol g}^{-1}$  or  $\text{meq g}^{-1}$  as the concentration of cationic sites per gram of polymer electrolyte. While it is important to have a high IEC, it often comes at the cost of inducing higher water uptake and can result in a loss of mechanical integrity due to

swelling. Having a high IEC can also lead to ionic clustering if there is poor phase separation or insufficient spacing between the tethered cations, which can impede ionic conductivity if the clusters cannot form a connected transport network [47].

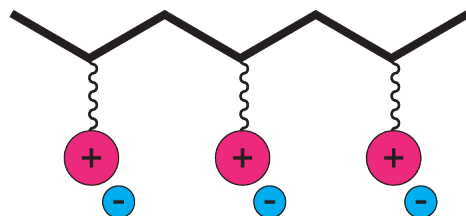


Figure 1.4 Representation of a simplified anion exchange membrane.

There are many viable polymer architectures that have been explored for use as AEMs, in contrast to PEMs which are limited by the solubility of their sulfonic acid groups. This includes random copolymers [48, 49], block copolymers [50–54], graft polymer systems [25, 55–57], and utilizing different cationic groups such as pyridinium, ammonium, phosphonium, guanidinium, imidazolium, and sulfonium [45, 58]. Copolymers are synthesized by joining two or more unique monomers, i.e. small molecules, into a polymer chain. In a random copolymer, the two monomers may appear in any order and the lengths of each block, or ratio of each monomer, are a result of the properties of each monomer and the conditions of the synthesis. The reactivity of the monomers with each other or the growing copolymer chains can be controlled by the synthesis temperature and the solvent which will all have an impact on the final composition of a random copolymer. Block copolymers have discrete segments of each monomer, as shown in Figure 1.5.

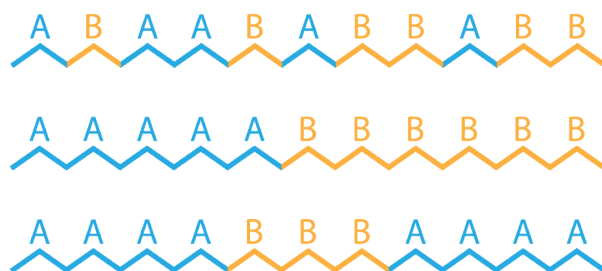


Figure 1.5 Schematic representation of different copolymers of “A” and “B” components. Top: Example of a random copolymer configuration. Middle: Example of a diblock (AB) copolymer configuration. Bottom: Example of a triblock (ABA) copolymer configuration.

In anion exchange polymers, the two monomers are typically a hydrophilic and a hydrophobic component. The hydrophilic block contains covalently bonded cationic functional groups for transporting anions, while the hydrophobic block maintains mechanical integrity of the material during water uptake and swelling. Random copolymers often exhibit a homogenous morphology due to the random distribution of hydrophilic and hydrophobic monomers [59]. While some random copolymers do exhibit ionic clustering, the clusters are randomly dispersed and lack the interconnectedness necessary for higher ionic conductivity [59, 60]. For this reason, block copolymers are of greater interest because their chemical structure tends to induce a self-assembled periodic structure (see Figure 1.6), utilizing well-defined interconnected channel networks to enhance conductivity and transport of species through the membrane. Therefore, the remainder of the introduction will focus on block copolymer-based AEMs.

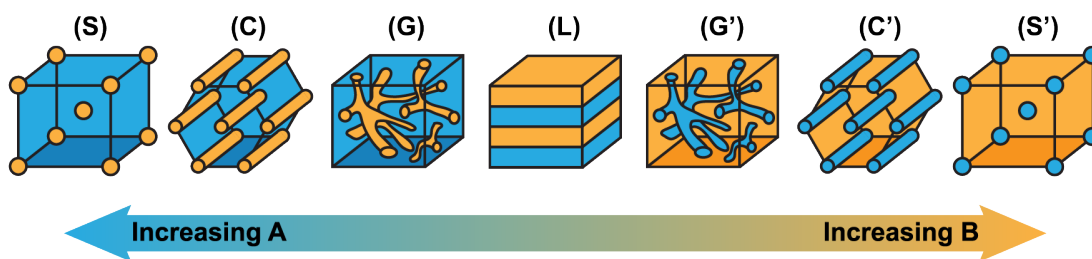


Figure 1.6 Morphologies of phase separating block copolymer systems, including spherical (S), cylindrical (C), gyroid (G), lamellar (L), and their inverse (‘).

A multitude of anion exchange polymer backbones have been reported in literature, including poly(arylene ethers) [61–64], polyphenylenes [65–68], unsaturated polypropylene and polyethylene [50, 69–71], polynorbornene [72], and many more. The main challenge in developing AEMs is balancing the ionic conductivity, which increases with IEC, with the water uptake, swelling, and mechanical stability, which all tend to worsen with increasing IEC. The high ionic conductivity of AEMs published more recently is attributed to their improvements in morphology and or creating well-defined ionic channels that promote hydroxide ion transport [73–77]. A variety of cation groups and tethering strategies have been investigated for their resiliency to hydroxide attack, shown below in Figure 1.7 and Figure 1.8.

Liu et al. investigated the effect of degree of branching in poly(arylene ether sulfone)s [78]. An improvement in hydroxide ion conductivity from  $96 \text{ mS cm}^{-1}$  to  $126 \text{ mS cm}^{-1}$  ( $80 \text{ }^\circ\text{C}$  in water) was

observed upon increasing the degree of branching compared to the linear polymer. Enhanced conductivity was attributed to the rigid branched structures creating more free volume in the material, which facilitates ion transport and provides space for water uptake in the membrane without inducing excessive swelling. Zhang et al. developed a crosslinked AEM with covalently connected cations [79]. When comparing two materials with identical IEC and water uptake, the membrane with more connected cations significantly improved the conductivity by creating a discrete ionic pathway for efficient transport.

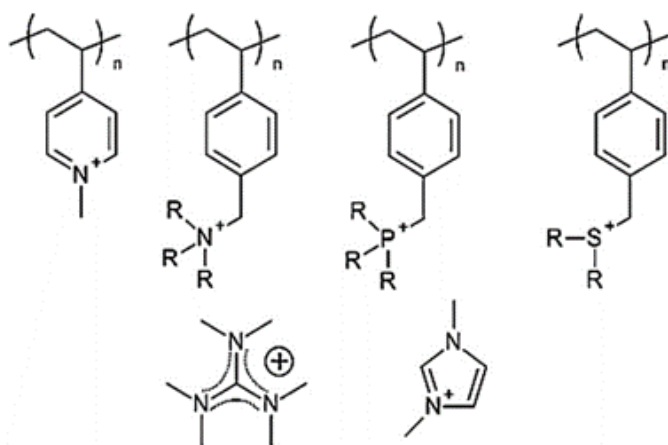


Figure 1.7 Chemical structures of common anion exchange membrane cation groups. From left to right, top: pyridinium, ammonium, phosphonium, and sulfonium. Bottom: guanidinium, imidazolium. Reproduced with permission from [45]

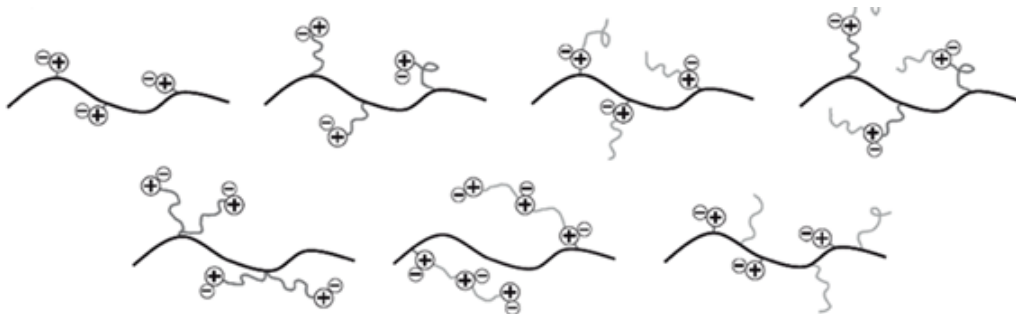


Figure 1.8 Different tethering strategies, i.e. adjacent to or on the polymer backbone, terminal ionic groups with pendant chains, tails to tethered cationic moieties, and multiple cations on a side chain. Reproduced with permission from [80].

Another major consideration when designing AEMs is chemical stability toward nucleophilic attack by hydroxide ions. Chemical degradation of the polymer backbone leads to a decrease in mechanical integrity, while various degradation mechanisms of the cationic moieties due to  $\text{OH}^-$  attack lead to lower ion conductivity and thus lessened electrochemical performance [81, 82]. These mechanisms tend to occur rapidly, especially in hotter and drier conditions, and lead to poor long-term stability for AEMs. The chemical structure of the polymer backbone and ionic groups, especially their steric hindrance, electron donating abilities, and hydration number, all play a significant role in the stability of the material and resistance to degradation mechanisms.

In 1998, Tomoi et al. first proposed improving stability by adding a long spacer chain between the quaternary nitrogen atom and the benzene ring [83]. Akiyama et al. later investigated the effect of side chain length on chemical stability of an aromatic semi-block copolymer quaternized with benzyltrimethylammonium groups [84]. After soaking in 1 M KOH at 60 °C for 1000 hours, the membrane containing a 5-carbon length side chain retained the highest percentage of its original conductivity (72%) compared to the 3-carbon length (54%) and 1-carbon length (34%) samples. This study highlights the importance of cation stability, which was improved by extending the pendant alkyl chains, and simultaneously induced a better morphology, water uptake, and mechanical integrity. Marino and Kreuer compared the alkaline stability of 26 different quaternary ammonium moieties [85]. They found the presence of benzyl-, hetero-atoms, and other electron-withdrawing groups escalated degradation mechanisms significantly and showed 5- or 6-membered aliphatic cyclic quaternary ammonium groups had exceptional stability. Much of the work following Marino and Kreuer has utilized this insight on cationic moiety stability to develop highly stable AEMs [86–90].

Much effort has gone into optimizing  $\text{OH}^-$  conductivity, mechanical integrity, and chemical stability in AEMs to be competitive with and improve the performance beyond that of PEMs. While these developments are important, research dedicated to studying anion exchange polymers as ionomers in the catalyst layer is arguably more critical to improving device performance. Small improvements in the electrode tend to have significant effects on internal resistances and reaction kinetics at the anode and cathode [91, 92]. Although research in this area is sparse, especially for AEM-based systems, researchers are now certain that these materials behave differently as thin films in the catalyst layer compared to their bulk properties.

## 1.5 Ionomers and the Enigma of the Catalyst Layer

Electrochemical device performance is strongly influenced by the structure of the catalyst layer (CL) in the electrode where the electrochemical reactions take place. The anion exchange polymer utilized as the AEM can be used in the CL, where it ideally exists as a thin film coating catalyst particles or carbon-supported catalyst particles (see Figure 1.9). The ionomer is responsible for providing  $\text{OH}^-$ , reactant, and water transport to and from reaction sites on the catalyst surface. The electrochemical reactions that take place in a fuel cell or electrolyzer take place at the interface between the electrolyte (i.e. the ionomer) and the electrode (i.e. the catalyst/conductive support which provide electrons).

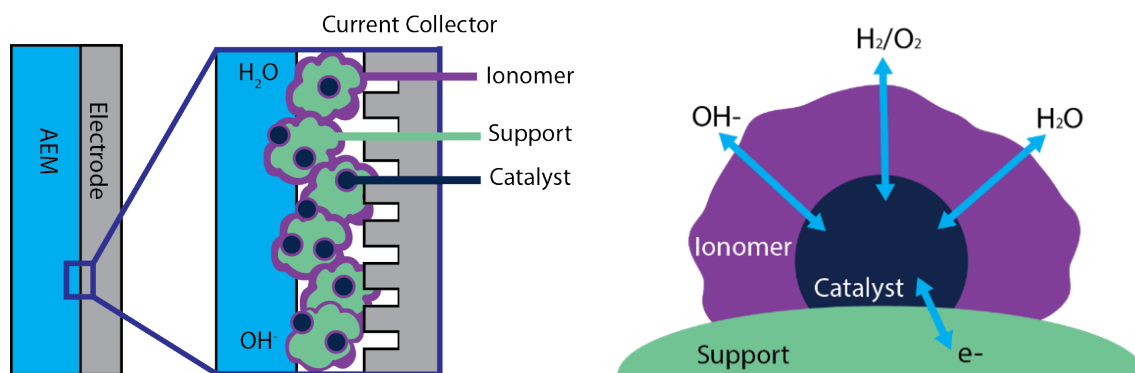


Figure 1.9 Left: Schematic of detailed anion exchange membrane device electrode depicting the heterogeneous CL and electrode structure. Right: Schematic of ionomer-coated catalyst particle highlighting the idealized interfaces between ionomer, catalyst, and supporting material, along with species transport.

The CL provides the triple-phase boundary where reactions take place. The current optimal CL microstructure is still poorly understood due to its complex multiscale, multiphase nature and is inherently difficult to examine under relevant conditions. In PEMFCs, the catalyst layer was developed empirically, and only recently are more scientific efforts being made to understand exactly how and why they work. Nafion<sup>®</sup> solubilized ionomers in simple alcohol/water mixtures were developed for commercial purposes and optimized to enable gas transport in the electrode instead of inhibiting it, while improving Pt utilization [93, 94]. Further developments in carbon-supported Pt catalysts and in catalyst ink formulations led to the electrode spraying techniques used today [95]. Most studies in this area have been performed on PEMFC CLs, with



Nafion<sup>®</sup> ionomer coated on carbon supported platinum catalysts.

Proton exchange ionomers are typically low molecular weight ion exchange polymers that can dissolve in organic solvents or be dispersed in an organic solvent/water solution. For anion exchange ionomers (AEIs), some of the ideal requirements for membranes are the same for ionomers, including high ionic conductivity, water management properties, and chemical stability in alkaline environments [46, 96]. Their design criteria differ mainly for reactant gas permeation, where membranes are designed to prevent fuel crossover, and ionomers need to promote fuel and oxygen transport to limit mass transfer resistances and facilitate the electrochemical reactions within the catalyst layer [96]. Of further differentiation, transport of water in AEMs is a function of diffusion and migration by electro-osmotic drag, whereas in the electrode, transport of water occurs entirely via diffusion and convection, which can be promoted by the addition of pore formers [97]. Ionomers are not required to form a freestanding film, so the mechanical properties are considered from a different perspective in terms of transport (e.g., water management is still critical in the electrode [98]), especially in AEMWEs [99, 100]. For this reason, ionomers or their precursor polymers are usually designed to have good solubility so that they be painted or sprayed onto a gas diffusion electrodes (GDEs) for fuel cells, or porous transport layer (PTL) substrates such as platinized titanium mesh or metal foams for electrolyzers. The electrode can then be post-processed to make the ionomer insoluble via quaternization, hydrogenation, cross-linking, or thermal annealing [47, 49, 51, 101–104].

Many studies developing new AEI chemistries tend to focus on membrane development and characterization, avoiding specifically investigating the performance of the ionomer as a thin film or in the catalyst layer of an operating device [105, 106]. The alkaline stability of AEIs had not been reported on until recently [107], where it was found the confinement effects of the AEI thin film on carbon led to a reduction in chain mobility and enhanced alkaline stability when compared to the same AEI as a powder.

In 2012, Sun et al. compared their novel styrene-ethylene/butylene-styrene (SEBS) based ionomer to a well-studied polysulfone (PSf) based ionomer [91, 108–110] in a comprehensive chemistry-morphology-performance study [111]. The SEBS based ionomers achieved 4-5x higher power density, which was attributed to a continuous hydrophilic morphology and improved dimensional stability upon water uptake compared to PSf. Improved performance was also

attributed to a reduction in charge transport resistance, determined from electrochemical impedance spectroscopy (EIS).

Shin et al. quaternized commercially available poly(vinyl alcohol) to prepare a water soluble ionomer [101]. A crosslinking agent was added to the catalyst ink and was thermally annealed after spraying to reduce dissolution of the ionomer during fuel cell testing. The ionomer content in the electrode was optimized for reaction kinetics, along with the resulting void fraction in the electrode, which affected mass transport limitations. Gupta et al. published on a SEBS block polymer with an IEC of 1.91 mmol g<sup>-1</sup> and OH<sup>-</sup> conductivity of 180 mS cm<sup>-1</sup> at 70 °C [109]. Its excellent performance as an ionomer was attributed to its higher IEC and improved water uptake and retention characteristics. The authors speculate the water permeability of the ionomer and membrane led to the performance enhancement via enhanced water management and back diffusion. Xu et al. also investigated the effect of ionomer content on the microstructure and performance of the electrode [112]. Performance was optimized by varying ionomer content, which acted to minimize charge transfer resistance and maximize electrocatalytic activity. It was also found that while increasing ionomer content excessively covered catalyst particles, it also decreased the aggregate size of the catalyst particles. This further highlights the need to balance ionomer content to optimize performance of the electrode.

The ionomer dispersion solvent has been shown to impact the electrode structure, and therefore performance, in AEMFCs [113]. Rapid evaporation of the solvent can be key to producing a mud-cracked structure with reduced transport resistances. A common issue in AEI development is the insolubility of the quaternized ionomer, which has led to the development of different processing requirements for AEM-based device electrodes compared to PEM-based device electrodes. Many researchers have reported fabricating electrodes with an unquaternized precursor polymer, and post-quaternizing the entire electrode in solution for both AEMFC [51] and AEMWE [99, 100] applications. Recent reports have shown excellent performance using a technique in which insoluble solid ionomer, catalyst and water/solvent is manually ground with a mortar and pestle to produce a texturally homogenous catalyst ink [25, 72, 114, 115].

Current research tends to focus on electrode fabrication and optimization of ionomer loading in the electrode [116–118]. While this is important, there are still limited publications on systematic ionomer chemistry developments. Switzer et al. [67] compared the fuel cell performance of two

ionomers, ATMPP and ATMPS, having identical IECs ( $1.6 \text{ meq g}^{-1}$ ) and different water uptakes (103% and 48%, respectively). They propose that the ATMPS ionomer provided a stronger catalyst-ionomer interface compared to ATMPP, which had a higher tendency to swell and likely resulted in delamination from the catalyst surface, ultimately causing poorer performance.

Zeng et al. [98] utilized an ionomer with tunable water uptake to investigate the effect on fuel cell performance. Commercially available poly(vinylbenzyltrimethylammonium) chloride was annealed to convert surface quaternary ammonium groups to tertiary amines, which are less hydrophilic. By varying the annealing time, they were able to tune the water uptake, swelling, and the hydrophilicity of the ionomer surface. Here, they speculate that increasing the water uptake of the ionomer and making the ionomer surface more hydrophilic serves to promote water removal from the catalyst surface and enhances the availability of catalyst sites, improving HOR kinetics. Their findings agreed with a previous study by Fukuta [119].

Chae et al. [120] varied the ionomer molecular weight, IEC, and alkyl chain length. The particle size of the ionomer dispersions were analyzed and correlated to EIS and AEMFC performance, finding that larger particles led to slightly worse performance and higher resistances, likely due to their high molecular weight hindering mass transport within the electrode. Additionally, the longer alkyl chain length improved AEMFC performance, mainly attributed to a decrease in IEC between the two ionomers compared ( $1.74$  vs.  $1.47 \text{ mmol g}^{-1}$ ) which likely led to improved water management in the electrode. Recently, Hassan et al. optimized the chemistry of a poly(norbornene) tetrablock copolymer by varying the IEC, molecular weight, dispersity, and water uptake to improve AEMFC peak power density by 100% from  $1.6$  to  $3.2 \text{ W cm}^{-2}$  [115]. Biancolli et al. compared the AEMFC performance of poly(ethylene-*co*-tetrafluoroethylene) (ETFE)-based AEI powders functionalized with three different cationic head-groups, including benzyltrimethylammonium, benzyl-*N*-methylpyrrolidinium, and benzyl-*N*-methylpiperidinium [121]. Benzyl-*N*-methylpiperidinium functionalized AEIs displayed the highest power outputs, in agreement with their previous work comparing AEM cationic functionalities, where they found benzyl-*N*-methylpiperidinium-functionalized AEMs showed improved alkali stability when hydrated compared to trimethylammonium-functionalized AEMs (17% vs. 30% loss in IEC in 1M KOH at  $80 \text{ }^\circ\text{C}$  for 28 days) [57].

Even more recently, a handful of studies systematically varied ionomer or membrane-ionomer combinations to determine effects on AEMWE performance. A study by Ghoshal et al. found that the perfluorinated ionomer (PFAEM-Gen 2) resulted in worse reaction kinetics, yielding higher Tafel slopes and overpotentials, likely due to interfacial effects with the cobalt catalyst utilized in this work [122]. Huang et al. optimized the ionomer in an AEMWE for water uptake and swelling for both the oxygen evolution electrode [100] and hydrogen evolution electrode [99]. In both cases, the importance of controlling the amount of water-induced swelling was highlighted. For OER at the anode, maximizing the IEC to provide high conductivity was balanced by lightly crosslinking the ionomer to reduce swelling and produce the highest-performing electrode. A hydrophobic PTFE additive provided additional water management and improved performance by substantially reducing the total charge transfer resistance. For HER at the cathode, high IEC and light crosslinking was also found to provide the best performance. In both of these studies, PGM catalysts were used, including  $\text{IrO}_2$  or  $\text{PbRuO}_x$  for OER and Pt/C, PtRu or PtNi for HER.

These studies suggest there is likely a balance in ionomer water uptake and interactions with the catalyst surface necessary to optimize fuel cell or electrolyzer performance [25, 26]; however, there is little published on the nature of interactions at the ionomer-catalyst interface. Most notably, in 2018 Maurya et al. published on an aryl ether-free polyaromatic ionomer that was designed to minimize phenyl group interactions with Pt and Pt/Ru catalysts [123]. Adsorption energies were investigated for two model compounds, one having rotatable phenyl groups and one having non-rotatable phenyl groups, on Pt and Pt-Ru surfaces. This showed non-rotatable phenyl groups had lower adsorption energies on these surfaces, and even lower affinity on Pt-Ru alloy surfaces. Infrared reflection adsorption spectroscopy was used to experimentally confirm more significant phenyl adsorption to Pt surfaces in the material with rotatable phenyl groups, and cyclic voltammetry (CV) confirmed this also significantly affected the HOR activity. Improved performance was also observed using a Pt-Ru catalyst, thus confirming that phenyl adsorption was a major contribution to poor ionomer performance and that engineering the polymer (as well as alloying the catalyst) to reduce its affinity for this adsorption significantly improved performance.

Additionally, a unique Pt microelectrode mini-cell study was performed to investigate differences between two ionomers, a benzyltrimethylammonium quaternized polyphenylene and a phenylpentamethyl guanidinium perfluorinated ionomer [124]. Effects of the ionomer backbone

and cationic groups were decoupled by obtaining HOR and ORR voltammograms using ionomer-coated Pt microelectrodes and in solutions of liquid electrolytes containing the respective cations. Reduced HOR activity was observed with the benzyltrimethylammonium cation due to potential adsorption of the cationic group, but the reaction was unhindered by the guanidinium based ionomer. Similar rotating disk electrode and density functional theory studies have shown how low coadsorption of AEI cationic moieties on palladium and platinum-based catalysts can enhance HOR activity [125, 126]. This can be achieved by modifying the AEI chemistry to interact more favorably with the catalyst surface or alloying the catalyst to interact less with the AEI. The results of this fundamental work have also been exhibited in AEMFCs utilizing Pt or PtRu catalysts with varying ionomer chemistry [127–129].

While these studies provided evidence of the significant role of,

- (i) interactions between the ionomer and catalyst;
- (ii) ionomer design regarding balancing IEC and conductivity with water uptake and swelling;  
and
- (iii) ionomer loading, catalyst loading ratio, and electrode fabrication techniques,

the majority of published work focuses on platinum and PGM catalysts. There are currently no studies of this kind on non-PGM catalysts, which are far more relevant to AEM-based devices, as the enhanced kinetics in alkaline environments and ability to utilize non-precious metal catalysts are the very motivation for developing AEMs and AEM-based devices.

## 1.6 Motivation for Utilizing Silver Catalysts for ORR and OER

The advent of AEMs with viable alkaline stability (ca. 2005 [130]) and further developments in AEMs and their applications [46] spurred interest in electrocatalysis in alkaline media (see Figure 1.10). Platinum group metals (PGMs) have had much success in acidic environments, and for this reason ORR has been extensively studied on Pt [131–134], Pt alloys [135–138], and PGMs such as Pd [139, 140], Ir [141], and Ru [24, 142]. In alkaline media, there are materials other than PGMs that are stable ORR catalysts including gold and more abundant metals such as silver or nickel [143].

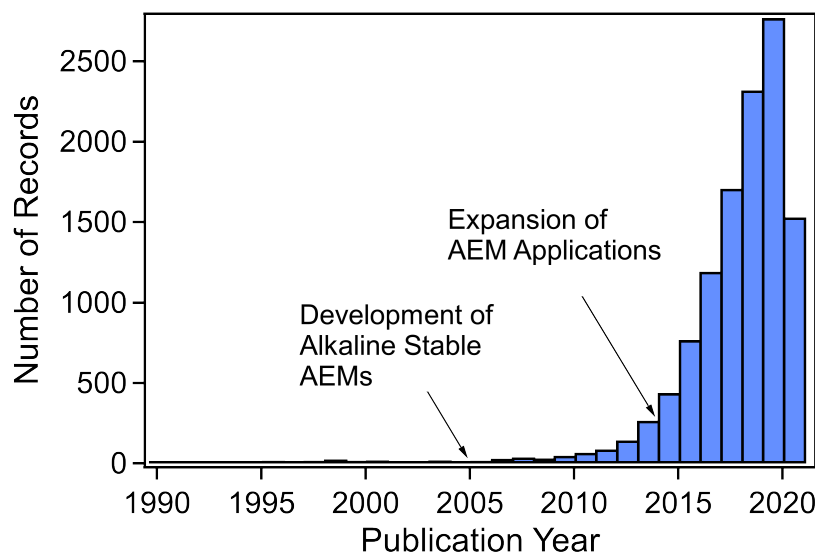


Figure 1.10 Bibliometric analysis of the publications for ORR and OER catalysis in alkaline media. “ORR” or “OER”, along with “catalysis” and “alkaline” were used as search terms. This citation report was generated using Web of Science.

Shifting from a strong acid to a strong base solution results in a negative shift in working potential range [143], leading to lower overpotentials required for ORR. This also causes a change in the local double layer at the electrode-electrolyte interface and decreases the binding energy of spectator ions, making the catalyst surface available for reactant adsorption [144]. The combined lower overpotential and reduced spectator ion binding energy provides the theoretical basis for why electrochemical reactions are more facile in alkaline media [145].

The first step in ORR is the adsorption of  $O_2$  (either dissociatively or nondissociatively) or an electron transfer [146]. Under fuel cell conditions, the cathodic ORR reaction takes place at very positive potentials, making the adsorption of neutral species like molecular  $O_2$  inhibited relative to the adsorption of intermediates such as charged superoxide radical anions ( $O_2^{\cdot-}$ ). Ramaswamy and Mukerjee investigated the fundamental reasons for better ORR kinetics on Pt in alkaline vs. acidic media, where they probed further into changes in double layer structure and reaction mechanisms [23, 147]. The authors found that the only thermodynamic advantage of ORR in base is improved stability of the hydroperoxide anion intermediate on the catalyst surface. Intermediate stability allows for the complete  $4e^-$  transfer pathway to dominate, where the final product is  $OH^-$ , as opposed to the incomplete  $2e^-$  transfer pathway, where peroxide intermediates

and radicals desorb as the final product, which can ultimately degrade the ionomer and membrane [148]. The instability of intermediates in acidic media necessitates the use of highly catalytic surfaces such as Pt, whereas in alkaline media other non-PGM catalysts are viable.

Historically, NASA developed alkaline fuel cells and found that Au-Pt alloys showed superior activity and durability compared to the original PGM catalyst used in the Apollo program [149]. More recent work has shown that Ag-Pt alloys are an equally active and durable alternative to Au, available at a lower cost [150], making Ag of more interest for AEMFCs. The ORR activity of Ag at high pH is comparable to that of Pt [151, 152] and studies of carbon-supported Ag cathodes have shown greater stability compared to Pt cathodes [151, 153], despite carbon being more susceptible to corrosion in base than in acid. The ORR mechanism on Ag in base is also similar to that on Pt, where the  $4e^-$  pathway dominates [154, 155]. Unlike Pt, Ag electrodes do not display the hysteresis effects shown in Pt electrodes due to irreversible OH and O adsorption, meaning OH adsorption on Ag is much more reversible, which is a major contributor to undesirable catalyst surface coverage [155]. Additionally, its current low cost compared to Pt ( $\$0.84 \text{ g}^{-1}$  Ag,  $\$35 \text{ g}^{-1}$  Pt) and greater abundance makes it a competitive option for an alkaline fuel cell catalyst [156, 157]. Unfortunately, very recent projections have shown that the cost of silver may be artificially low, as its availability is considered critically endangered [158]. The use of silver-based catalysts [159, 160] and porous silver electrodes [161, 162] have been demonstrated in AEMFCs.

In PEMWEs, IrO<sub>2</sub> is the benchmark PGM catalyst for OER. The cost of iridium was almost twice that of platinum ( $\$60 \text{ g}^{-1}$ ) until 2020 and will always be more expensive than Pt due to its rarity and widespread industrial use. In 2020, the COVID-19 pandemic severely disrupted the South African supply of iridium, which accounts for 81% of global iridium mine supply. This supply disruption, coupled with increasing demand for iridium by the electronics, electrochemical and automotive industries, caused the price to skyrocket to nearly  $\$230 \text{ g}^{-1}$  [163, 164]. Currently, the price of Ir remains at  $\$212 \text{ g}^{-1}$ , severely affecting the large-scale implementation of PEMWEs.

OER in alkaline media has been studied on a breadth of more abundant catalysts, including nickel-based catalysts [165–168], transition-metal (oxy)hydroxides [169], and other non-PGM metals [170, 171]. There is currently no official benchmark OER catalyst for AEMWEs, though many report utilizing Co<sub>3</sub>O<sub>4</sub>, or compare to PEMWEs by using IrO<sub>2</sub> [34, 165, 171, 172]. Silver, silver oxides and silver alloys have also been studied extensively for OER in alkaline media

[173–180]. The scope of the enclosed work will focus on silver, which is a relevant non-PGM catalyst for both AEMFC and AEMWE applications for ORR and OER respectively. For the purpose of carrying out fundamental scientific studies, the surface of silver is also more thoroughly understood and is more simple than other relevant non-PGM catalysts (e.g. nickel), as shown in the Pourbaix diagram in Figure 1.11. Future work regarding other promising catalysts will be discussed in the final chapter of this thesis.

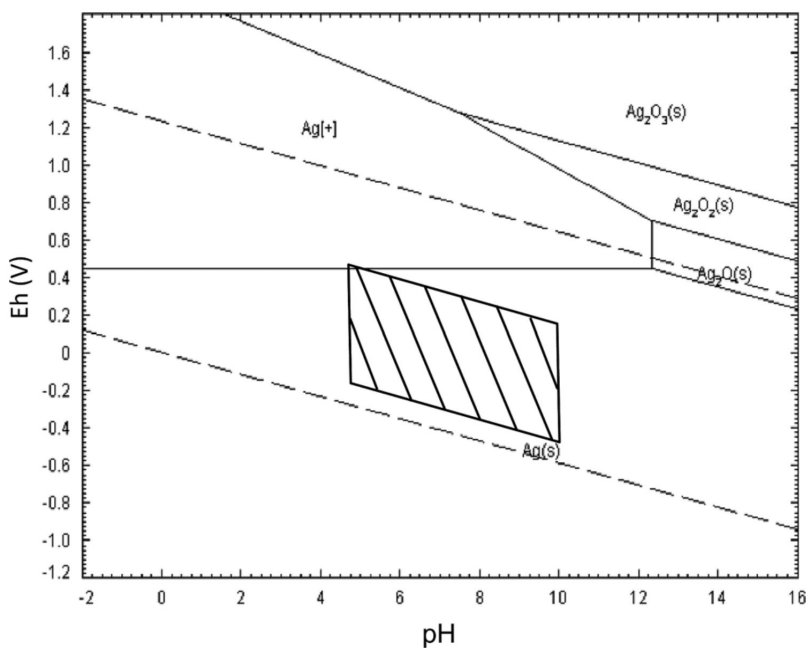


Figure 1.11 Pourbaix diagram of silver. Reproduced with permission from [181].

## 1.7 Ionomer Thin Films: Current Understanding

The thin film morphology of ionomers in the electrode is still widely unexplored, with the majority of work focusing mainly on Nafion<sup>®</sup> thin films. In PEMFCs, it is established that ionomers ideally exist as thin films (4-10 nm) covering catalyst particles [182]. By analogy, although the microstructure and thickness of ionomers in AEM-based electrodes is still speculative and likely heterogeneous at all relevant length scales, it is anticipated that they also exist as thin films in the CL, but, to date, an AEI-based catalyst layer has not been imaged. The importance of gaining a proper understanding of ionomer thin film morphology in the CL cannot be understated; it is clear that the morphology affects transport of species through ionomer thin



films, which has been shown to be crucial to optimizing the catalyst layer to improve electrochemical device performance [115, 120, 183]. Currently, it is challenging to probe the ionomer morphology in-situ under relevant device operating conditions, so typically it is studied on model flat surfaces such as polished silicon wafers or metal surfaces.

Understanding the chemistry-morphology-property relationship of ionomer thin films has already provided insight into mitigating transport resistances in the CL of PEM-based devices. In order to probe ionomer thin film characteristics, techniques such as grazing-incidence small-angle X-ray scattering (GISAXS) and wide-angle X-ray scattering (GIWAXS), ellipsometry, quartz-crystal microbalance, and thin film conductivity measurements are used to examine the thin film morphology, water uptake and ionic conductivity [183–185]. Numerous studies have shown that ionomer thin film (1-100 nm) morphology differs greatly from their bulk ( $\mu\text{m}$  scale) structure, leading to shifts in material characteristics. These changes are attributed to nano-scale confinement and surface tension effects, along with interfacial interactions between the ionomer and the thin film substrate [186, 187].

As stated previously, in the last 10 years researchers have mainly explored the morphology of Nafion<sup>®</sup> and PFSA ionomer thin films. It has been shown that interfacial interactions contribute to a thickness-dependent morphology [188, 189] which results in changes in water uptake and proton conductivity [187, 190–194]. Substrate-dependent morphologies have also been observed [187, 195, 196], where Nafion<sup>®</sup> thin films on SiO<sub>2</sub> display an isotropic structure, and on gold or platinum exhibit parallel backbone alignment relative to the substrate [197]. Other studies have shown thin films cast on substrates with hydrophilic properties (silicon and glass) absorb more water compared to films on hydrophobic substrates (graphite, Au, and ITO) [198]. This finding was further rationalized by the observed parallel morphology on hydrophobic substrates, which impedes water sorption, compared to the isotropic orientation on hydrophilic substrates, which is more favorable to water sorption [195].

Paul et al. proposed a model of the lamellar alignment of Nafion<sup>®</sup> on SiO<sub>2</sub> substrates, where ultra-thin films result in a hydrophilic surface due to surface-aligned sulfonic groups and thicker films beyond 55 nm result in a hydrophobic surface due to a disordered morphology further from the interface (see Figure 1.12) [189].

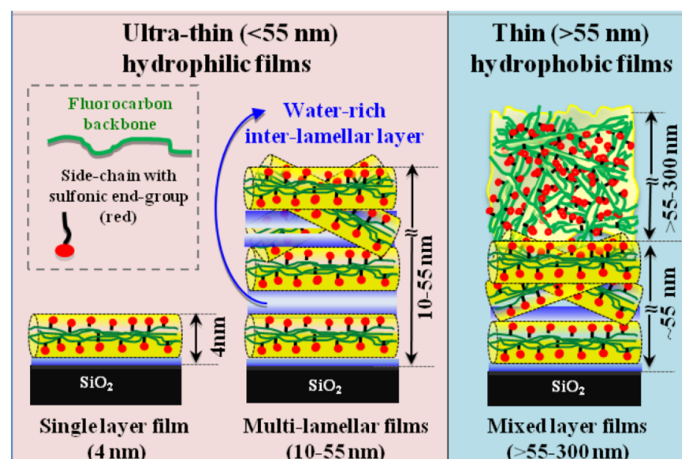


Figure 1.12 Model proposed by Paul et al. for thickness-dependent Nafion<sup>®</sup> thin film morphology on SiO<sub>2</sub> substrates. Reproduced with permission from [189]. Copyright © 2013 American Chemical Society.

Dura et al. found lamellar structures formed on SiO<sub>2</sub> substrates, but on Au and Pt they observed only a thin partially hydrated layer [196]. Mohamed et al. also found differences in how ionic clusters oriented on silicon, glassy carbon, or Pt substrates [199]. Kusoglu and Modestino have also studied the thickness-dependence of water uptake on Au substrates, finding that films thicker than 20 nm swell less than bulk films, while films thinner than 20 nm showed greater swelling due to morphological disorder [187, 192]. Additional work also investigated the effect of thermally annealing Nafion<sup>®</sup> thin films above their glass transition temperature to allow the morphology to rearrange and minimize surface energy. Paul et al. observed a decrease in water uptake and proton conductivity upon thermal annealing, though, interestingly, the phenomena was reversible by exposing the samples to water for 24 hours [185]. Abuin et al. reported a similar reduction in water uptake with annealing and confirmed the formation of crystalline domains at the substrate interface restrict swelling [195, 198].

Although ultra-thin Nafion<sup>®</sup> films have a higher water uptake, they have been shown to exhibit lower conductivity [190]. While these findings appear counterintuitive, they emphasize the discrepancies in the proton transport mechanisms occurring in Nafion<sup>®</sup> thin films and bulk membranes. The increase in activation energy of proton conductivity with decreasing film thickness was attributed to polymer confinement and morphological restructuring. Water transport has also been shown to significantly decrease in Nafion<sup>®</sup> thin films [191], where the

diffusion coefficient of water in a 20 nm thin film was found to be 7 orders of magnitude lower than that of the bulk membrane [200].

Nafion<sup>®</sup> ionomer films have also been studied using conductive-probe AFM (CP-AFM) and electrostatic force microscopy (EFM) [201–203]. Kwon et al. used CP-AFM to study a Nafion<sup>®</sup> membrane hot pressed on a carbon gas diffusion layer [204]. In this study they investigated annealing effects and found that the surface morphology shifted from cluster-like (perpendicular orientation) to chain-like (parallel orientation) with annealing and resulted in improved conductivity of the thin film. Barnes et al. also recently published a study using EFM on a Nafion<sup>®</sup> thin film adsorbed on a conductive copper surface [205]. In this study they highlighted the advantages of using a tapping-mode technique like EFM as opposed to contact-mode techniques like CP-AFM. In tapping-mode, a phase image can simultaneously be obtained during electrostatic force mapping, so softer ionic domains of the film can be directly cross-referenced with the conductive domains. This allowed them to identify non-conducting soft phases, which were labeled “dead-end channels” and did not propagate completely through to contact the copper surface. This technique gave significant insight into the connectivity and orientation of conducting channels.

Research on Nafion<sup>®</sup> thin films has provided critical insight toward understanding the PEMFC CL; however, little research has been conducted on AEI thin films. Only a limited number of AEIs have been studied as thin films, including Tokuyama A201 [206, 207], quaternized comb-shaped poly(2,6-dimethyl-phenylene oxide) (QA-PPO) [208], and commercial Fumasep<sup>®</sup> Fumion FAA-3 ionomer (FAA-3) [209]. A recent study by Luo et al. considers a variety of AEIs of different backbones and side chain chemistries, highlighting the role of ionomer chemistry in their structure and water uptake [210]. Perfluorinated polymers showed phase separation in GISAXS, while all hydrocarbon-based thin films were amorphous and displayed no evidence of nanoscale phase separation, which could potentially lead to transport resistances [211–213]. FAA-3 and a benzyltrimethylammonium-functionalized PPO ionomer have also displayed insufficient phase separation in GISAXS [209]. The importance of phase separation and morphology has been demonstrated to be key to enhancing water and ion transport through bulk membranes, therefore designing AEIs that display nano-phase separation as thin films in catalyst layers in the electrode is still a remaining challenge in this field.

## 1.8 Existing Knowledge Gap and Associated Research Challenges

The main gaps in this field can ultimately be distilled down to designing better AEMs and AEIs. At the inception of this work, there were many AEMs in development that reported high ionic conductivity and adequate chemical stability, but only a few characterized the mechanical integrity at device-relevant temperature and humidity when they tend to swell. The issue of mechanical integrity is especially apparent in liquid water applications such as electrolysis. The first target of this thesis was to develop a robust AEM with high conductivity, chemical stability in KOH, and mechanical stability in liquid water, with a facile reproducible synthesis method.

The heterogeneous microstructure and triple-phase interface between catalyst particles, ionomer, and supporting material in the CL is still not well understood. Due to the complexity of the CL, there are challenges associated with carrying out meaningful fundamental studies on an operating device, so studies of idealized model interfaces between ionomers and catalyst particles or surfaces are necessary to provide important scientific insight. Currently, there is limited work published in this area, especially in the field of AEIs and on interactions between AEIs and non-PGM catalysts. It is known from studies with Nafion<sup>®</sup> thin films and a few AEIs that restructuring can occur at catalyst interfaces and alter ionomer properties compared to their bulk characteristics, which directly affect device performance by altering ionic and water transport networks. To rationally design AEIs for the CL, this fundamental knowledge gap should be closed. The combined knowledge of potential interfacial interactions between the ionomer and catalyst and their effect on the morphology and transport properties is necessary in order to draw meaningful conclusions about the ionomer's contribution to electrochemical performance.

## 1.9 Thesis Statements

There is a critical need to synergistically improve AEMs and AEIs. AEMs need to be designed with improved mechanical integrity, while maintaining high ionic conductivity and alkaline stability. Rational design criteria for AEIs is yet to be established, for a better understanding of the nature of ionomer-catalyst interfacial interactions is still needed. The opportunity to utilize tunable block copolymer-based AEIs will allow for determining how different aspects of block copolymer architecture affect the interactions with a silver catalyst, the interaction-driven morphological shifts, and the resulting performance in an operating device. An array of block

copolymer-based anion exchange materials are utilized in this work, including the following diblock and triblock copolymer precursors: polychloromethylstyrene-*b*-polycyclooctene-*b*-polychloromethylstyrene (PCMS-*b*-PCOE-*b*-PCMS), polychloromethylstyrene-*b*-polyethylene-*b*-polychloromethylstyrene (PCMS-*b*-PE-*b*-PCMS), polyisoprene-*b*-polychloromethylstyrene (PIp-*b*-PCMS) and polychloromethylstyrene-*b*-polyisoprene-*b*-polychloromethylstyrene (PCMS-*b*-PIp-*b*-PCMS). Using this variety of precursors has allowed for the comparison of saturated (PE) and unsaturated (PCOE, PIp) backbone chemistry, and crystalline (PE, PCOE) vs. amorphous (PIp) backbone chemistry. The functionalization of the PCMS blocks with different quaternary ammonium cations is also compared using either benzyltrimethylammonium (TMA) or benzylmethylpiperidinium (MPRD). The stability and conductivity of TMA is questionable at relevant operating conditions including high pH and temperatures of 60-80 °C [85, 214], but it is still the most widely reported quaternary ammonium cation. For comparison, MPRD can offer better stability and conductivity [58, 85, 214], and the effects of their different structures can be compared. Specifically, the enclosed studies focus on AEM and AEI interactions, structure, and performance with a silver catalyst. This research will provide critical insight necessary to rationally design ionomers for AEMFCs and AEMWEs.

In this thesis, after modifying the synthesis of an AEM system to be viable in an operating device (*Chapter 2*), *we propose the following stepwise approach to elucidate the structure-property-performance relationship in the electrode:*

- (i) identify interactions between the ionomer and catalyst of interest (*Chapter 3*)
- (ii) study ionomer structure and morphology in the electrode by utilizing idealized model interfaces (*Chapter 4*), and finally
- (iii) apply these findings to the development of electrodes and integrate them into operating devices (*Chapter 5*).

The learnings from this are summarized in *Chapter 6*, with suggestions for further improvements in future work. The following hypotheses are tested and discussed in the following sections of this thesis:

*Hypothesis 1:* We can modify the block copolymer-based AEM polychloromethylstyrene-*b*-polycyclooctene-*b*-polychloromethylstyrene (PCMS-*b*-PCOE-*b*-PCMS) by saturating the C=C bonds in PCOE to make a polyethylene (PE)-based block copolymer. Because PE is semicrystalline, the resulting AEM will be more thermally robust, chemically stable, and hydrophobic, affording it better water uptake and mechanical integrity compared to its PCOE precursor.

*Hypothesis 2:* Functionalities, such as C=C bonds and quaternary ammonium cationic moieties, will interact with the surface of silver particles by varying degrees. Once these interactions are understood, they can be exploited to restructure the interfacial morphology and lead to favorable shifts in material characteristics.

*Hypothesis 3:* The morphology of neutral block copolymer precursor thin films will be determined by the interactions at the silver-polymer interface, but in AEIs thin films, quaternary ammonium cationic moieties will interact more strongly with each other (dipole-dipole interactions) than with a silver surface (van der Waals interactions) and introduce more disorder.

*Hypothesis 4:* If functionalities such as C=C bonds in PCOE and quaternary ammonium cationic moieties interact with silver, an AEI with a PE backbone and MPRD quaternary ammonium cationic moieties will demonstrate better electrochemical performance compared to a PCOE backbone and TMA quaternary ammonium cation. A PE backbone will exhibit a reduced affinity for adsorption on silver compared to PCOE, and an MPRD quaternary ammonium cationic moiety will exhibit less adsorption than TMA due to steric hinderance. Ultimately, this will free active area on the catalyst surface and mitigate transport resistances.

## CHAPTER 2

### A POLYETHYLENE-BASED TRIBLOCK COPOLYMER ANION EXCHANGE MEMBRANE WITH HIGH CONDUCTIVITY AND PRACTICAL MECHANICAL PROPERTIES

This chapter is modified from a journal article published in ACS Applied Polymer Materials.<sup>1</sup>

Nora C. Buggy,<sup>2</sup> Yifeng Du,<sup>3</sup> Mei-Chen Kuo,<sup>4</sup> Kayla A. Ahrens,<sup>5</sup> Jacob S. Wilkinson,<sup>6</sup> Soenke Seifert,<sup>7</sup> E. Bryan Coughlin,<sup>8</sup> and Andrew M. Herring<sup>9</sup>

#### 2.1 Motivation

The development of the triblock copolymer membrane polychloromethylstyrene-*b*-polyethylene-*b*-polychloromethylstyrene (PCMS-*b*-PE-*b*-PCMS) was in part motivated by the study in *Chapter 3*, which was carried out simultaneously. Our initial findings from the study in Chapter 3 suggested that the C=C double bond in the polycyclooctene (PCOE) midblock of the triblock copolymer PCMS-*b*-PCOE-*b*-PCMS was interacting with silver nanoparticles. Upon realizing this, *Hypothesis 1* was posed, and the triblock copolymer was modified by hydrogenating the midblock in an effort to compare the effects on the interactions with silver nanoparticles; however, the resulting triblock copolymer PCMS-*b*-PE-*b*-PCMS was insoluble and therefore it could not be utilized in the study in *Chapter 3*. Upon further characterization, the AEM was found to have high ionic conductivity and interesting mechanical properties suitable for aqueous applications. Hence, the following study was published on the full characterization of this material, which is now being commercialized as Tuffbrane™ by Spark Ionx.

#### 2.2 Abstract

A challenge in anion exchange membrane (AEM) development is simultaneously optimizing alkaline chemical stability, mechanical integrity during thermal and humidity cycling, and

<sup>1</sup>Reprinted with permission of ACS Applied Polymer Materials, 2020, DOI: 10.1021/acsapm.9b01182

<sup>2</sup>Primary researcher and author

<sup>3</sup>Co-author, polymer chemist

<sup>4</sup>Co-author, polymer chemist

<sup>5</sup>Co-author, research assistant

<sup>6</sup>Co-author, research assistant

<sup>7</sup>Co-author, X-ray scattering expert and beamline scientist

<sup>8</sup>Co-author, polymer expert and co-corresponding author

<sup>9</sup>Co-author, advisor and co-corresponding author

achieving high anionic conductivity. Here, we report on the hydrogenation of an ABA triblock copolymer polychloromethylstyrene-*b*-polycyclooctene-*b*-polychloromethylstyrene (PCMS-*b*-PCOE-*b*-PCMS) to yield a polyethylene-based triblock copolymer, polychloromethylstyrene-*b*-polyethylene-*b*-polychloromethylstyrene (PCMS-*b*-PE-*b*-PCMS). A polydisperse midblock was synthesized with narrowly disperse outer blocks to favor nanoscale phase separation and promote an interconnected morphology. Varying degrees of chemical crosslinking of the PCMS domains were achieved using different processing temperatures to tune the water uptake and dimensional swelling. Quaternization with either trimethylamine or methylpiperidine resulted in AEMs with improved characteristics, including excellent Cl<sup>-</sup> and OH<sup>-</sup> conductivity (119 and 179 mS cm<sup>-1</sup> at 80 °C, respectively) and moderate water uptake (33 wt%, λ, waters per charge carrier, = 12). Unexpectedly, extensional testing indicated that the mechanical strength of the film improved upon hydration. Wide-angle X-ray scattering revealed that in the presence of liquid water, the PE backbone rearranges and forms larger crystalline domains, which led to the improved stress at break. These fundamental mechanistic insights are of critical importance in designing mechanically robust AEMs for aqueous applications such as electrolysis and reverse electrodialysis. This work demonstrates the applicability of tunable block copolymer systems for developing practical AEM materials for more modest pH, liquid applications. Numerous tunable variables including chemical crosslinking and semi-crystalline variability highlight how mechanical integrity, water management, and ionic conductivity can be simultaneously achieved.

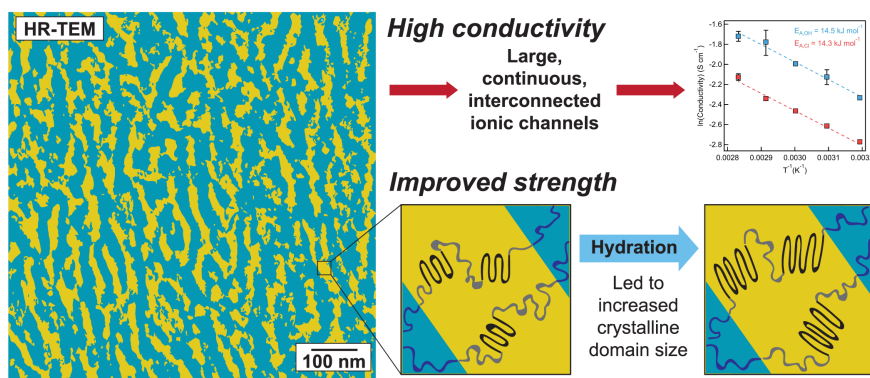


Figure 2.1 Graphical abstract.



### 2.3 Introduction

Anion exchange membranes (AEMs) have attracted increasing interest for various energy conversion applications, including fuel cells [45], electrolyzers [215], redox flow batteries [216], and reverse electrodialysis [46, 217], in addition to water purification applications [218]. One of the main advantages of alkaline systems is improved oxygen reduction reaction kinetics which can allow for the use of non-noble metal catalysts [108, 219]. Unlike proton exchange membranes (PEMs), AEM-based devices can utilize or generate more complex hydrocarbon fuels [220]. Hydrocarbon based AEMs are a potentially less expensive and more environmentally preferable alternative to perfluorinated membranes, which have been essential to mitigate the aggressive oxidizing conditions present in PEM fuel cells and electrolyzers [221]. AEMs can be constructed entirely from hydrocarbons, allowing the additional functionality of block copolymers to be accessed. For the breadth of electrochemical applications mentioned above to be implemented, several membrane properties are required: high ionic conductivity, mechanical integrity under humidified or wet conditions, and chemical stability under potentially severe alkaline conditions dependent on the application. Simultaneously achieving these properties is still a major challenge in the field of AEMs, despite significant developments in backbone chemistry and cation stability [222].

One of the main hurdles is balancing the ion exchange capacity (IEC) against water uptake and dimensional swelling. A higher IEC will contribute to having a higher ionic conductivity at the cost of increasing the hydration and swelling of the material, which can ultimately lead to mechanical failure. Many of the leading AEMs with high hydroxide ion conductivity (96–140 mS cm<sup>-1</sup> at 80 °C in liquid water) suffer from excessive water uptake > 100% [74, 223–225]. This can be especially detrimental in liquid applications.

Ongoing research has focused on identifying alkali stable polymer backbones and cation groups [226–228], since hydroxide ions can attack ionic groups along with the polymer backbone itself through multiple degradation pathways [46, 229]. Numerous cation chemistries have been explored, namely quaternary ammonium groups, of which trimethylammonium has been the most widely investigated. However, trimethylammonium functionalized polymers have been shown to have poor stability at high pH, and have low or no ionic conductivity at elevated temperatures

[214]. Marino and Kreuer studied 26 different quaternary ammonium groups at high temperature and pH and found that quaternized aliphatic-heterocycles with 5- and 6-membered rings were much more stable than the traditional trimethylammonium ions, as they were less susceptible to both nucleophilic attack and substitution [85]. Mohanty et al. came to a similar conclusion, where they found benzyl-substituted cations degraded much faster than alkyl-tethered cations [220]. Liu et al. recently reported their AEM had the highest ionic conductivity with benzylmethylpiperidinium when compared to benzylmethylpyrrolidinium and benzyltrimethylammonium groups [58]. Yao et al. also recently compared different hetero-cycloaliphatic quaternary ammonium groups, finding that benzylmethylpiperidinium had the highest hydroxide conductivity and alkaline stability when compared to trimethylammonium cations [214].

Equally important is the chemistry of the polymer backbone, where it is desirable to have a hydrophobic backbone to diminish water uptake and membrane swelling and minimize, or eliminate, the presence of polar groups that can act as sites of attack by nucleophilic hydroxide anions [230]. For these reasons, polyethylene (PE) is a great candidate for an AEM polymer backbone as it is stable under alkaline conditions, is hydrophobic, does not swell in aqueous solutions, is semi-crystalline, and has excellent mechanical properties [70, 231]. Kostalik et al. synthesized a crosslinked PE-based AEM with high hydroxide conductivity ( $140 \text{ mS cm}^{-1}$  at  $80 \text{ }^\circ\text{C}$ ), but it suffered from excessive swelling (225% at room temperature) due to having a high IEC ( $2.3 \text{ mmol g}^{-1}$ ) [71]. Wang et al. showed that low-density PE could be fabricated into an AEM with good properties and that switching from low-density to high-density PE produced materials with enhanced performance [232]. A common approach to synthesizing PE-based AEMs is via radiation grafting [233–235]. Sherazi et al. utilized radiation grafting of a vinylbenzyl chloride monomer onto a commercially available PE and obtained an  $\text{OH}^-$  conductivity of  $47.5 \text{ mS cm}^{-1}$  at  $90 \text{ }^\circ\text{C}$  with low water uptake (25%) [235]. More recently, Gupta et al. synthesized a soluble ionomer using low-density PE and vinyl benzyl chloride as the grafting monomer, which resulted in an IEC of  $1.91 \text{ mmol g}^{-1}$  and  $\text{OH}^-$  conductivity of  $180 \text{ mS cm}^{-1}$  at 100% RH and  $70 \text{ }^\circ\text{C}$  [233].

Block copolymers have been extensively investigated for use as backbones for AEMs because their structure induces a phase separated morphology, and well-interconnected hydrophilic domains have been shown to enhance water and ion transport through the membrane [60, 236]. Li

et al. previously published on a polyethylene-like block copolymer AEM, where anionic polymerization was used to synthesize polybutadiene-*b*-poly(4-methylstyrene) diblock copolymers, and subsequent hydrogenation of the polybutadiene lead to a polyethylene-like block [50]. The optimized membrane had an IEC of 1.92 mmol g<sup>-1</sup> and OH<sup>-</sup> conductivity of 73 mS cm<sup>-1</sup> at 60 °C in water, with a low water uptake of 37%. Sarode et al. have also reported on a diblock polymer of polyethylene and poly(vinylbenzyl trimethylammonium) with an IEC of 1.08 mmol g<sup>-1</sup>, fluoride ion conductivity of 34 mS cm<sup>-1</sup> at 90 °C and 95% RH, and low water uptake (~22%) [237].

We have developed an ABA triblock copolymer of polychloromethylstyrene-*b*-polycyclooctene-*b*-polychloromethylstyrene (PCMS-*b*-PCOE-*b*-PCMS) with a scalable and efficient synthesis that was optimized for high ionic conductivity [58, 238]. Based on this previous work, conductivity was shown to increase with increasing lamellar d-spacing [238]. Here we take a PCMS-*b*-PCOE-*b*-PCMS triblock precursor and modify it by hydrogenating the polycyclooctene (PCOE) midblock to PE. The ratio of PCMS:PCOE was kept similar to the previous work to ensure good mechanical integrity [58, 238]. Based on the work of Mahanthappa et al., a polydisperse midblock and narrow dispersity outer blocks were synthesized to provide a larger window for nanoscale phase separation [239, 240]. The PE-based triblock copolymer was processed by hot-pressing the polymer in a slurry of *p*-xylene into a film. Hot-pressing was performed at two different temperatures, and the elevated temperature lightly crosslinked the PCMS blocks through scission of benzyl chlorides. The films were subsequently quaternized with either trimethylamine to yield benzyltrimethylammonium (TMA) or methylpiperidine to yield benzylmethylpiperidinium (MPRD) cations. The incorporation of PE in the midblock produced anion exchange membranes with enhanced hydroxide and chloride conductivity, in addition to excellent water uptake and interesting mechanical properties. Despite vast improvements, alkaline stability was less than desirable, and the mechanism of degradation was determined to aid in future membrane designs. Overall, the new mechanistic insights combined with the remaining properties of this material make it an excellent candidate for more moderate pH applications such as electrolysis or electrodialysis.

## 2.4 Experimental Methods

### 2.4.1 Materials

The following reagents were purchased from various vendors and used as received. N-methylpiperidine ( $C_6H_{13}N$ , 99%), trimethylamine solution ( $C_6H_3N$ , 25 wt% in water), dichloromethane (DCM,  $CH_2Cl_2$ , > 99%), chloroform ( $CHCl_3$ , > 99%), methanol, ( $CH_3OH$ , ACS grade), *p*-toluenesulfonyl hydrazide (TSH,  $C_7H_{10}N_2O_2S$ , 97%), *p*-xylene ( $C_6H_4(CH_3)_2$ , 99%). The base triblock copolymer  $PCMS_{161}-b-PCOE_{648}-b-PCMS_{161}$  was synthesized as published previously [58].

### 2.4.2 Hydrogenation with *p*-Toluenesulfonyl hydrazide (TSH)

$PCMS_{161}-b-PCOE_{648}-b-PCMS_{161}$  (3.4 g, 0.0183 mol repeat units) was dissolved in *p*-xylene (450 mL) in a 500 mL, two-necked, round-bottomed flask at RT. The flask was immersed in an oil bath and the polymer solution was stirred and heated at 125 °C for 10 min. TSH (27 g, 0.146 mol, eight-fold excess) was added slowly over 20 min to the polymer solution. The reaction mixture was then stirred at 125 °C for an additional 2.5 h. The hot solution was added slowly over 20 min to excess methanol (~2,200 mL) and the hydrogenated polymer  $PCMS-b-PE-b-PCMS$  precipitated as a white powder, which was separated by filtration. The polymer powder was suspended in boiling DI water (~1,000 mL) to remove the excess hydrazide. The recovered polymer powder was collected on a fritted disc (medium), washed with methanol, and dried under vacuum at 35 °C overnight. Yield: 3.36 g (98.82%).

### 2.4.3 Membrane Fabrication and Quaternization

The hydrogenated polymer powder  $PCMS-b-PE-b-PCMS$  was suspended in a minimum amount of *p*-xylene (1 mL *p*-xylene for every 100 mg of polymer) and spread on a Teflon<sup>®</sup> sheet before being hot pressed for 5 min at 95 psi and either 130 °C or 180 °C to form films, 100 – 130 or 50 – 70 μm thick, respectively. The films were quaternized in the solid state by immersion in either trimethylamine (25 wt% in water) or N-methylpiperidine (33% in methanol) solution at 50 °C for 3 days, washed in DI water until they reached a pH of 6, and then soaked in DI water at 80 °C for 24 h. Quaternization was experimentally determined to be sufficient after soaking for 3 days in solution by using a Mohr titration, where no change in IEC was noted beyond 3 days.

Films were then hot pressed again at 90 °C to produce membranes of consistent thickness.

#### **2.4.4 NMR Characterization**

The  $^1\text{H}$  NMR spectroscopy was performed in 5 mm diameter tubes in deuterated chloroform ( $\text{CDCl}_3$ ) at 25 °C on a Bruker 500 spectrometer at 500 MHz. The  $^{13}\text{C}$  solid-state NMR spectroscopy was performed on a Bruker Avance III 600 MHz NMR spectrometer equipped with 4 mm HX, 4 mm E-free, 1.9 mm PISEMA, and diffusion probes. For the degradation studies, the AEM was soaked in 9 M KOH at RT for 1 week. The membrane was removed and the KOH solution containing degraded products was partitioned against  $\text{CDCl}_3$ . The solution was then dried with  $\text{MgSO}_4$  and filtered.

#### **2.4.5 Gel Permeation Chromatography (GPC)**

Gel permeation chromatography (GPC) was performed in THF at a flow rate of 1.0 mL  $\text{min}^{-1}$  at 40 °C, using a refractive index detector on a Polymer Laboratories PL-GPC 50 Integrated GPC system.

#### **2.4.6 Fourier-Transform Infrared Spectroscopy (FTIR)**

A Thermo Fisher Scientific Nicolet iN10 infrared microscope with a germanium attenuated total reflectance (ATR) tip was used to collect IR spectra in the range of 4000 – 650  $\text{cm}^{-1}$ . Highest resolution settings were used during all scans. For the degradation study, the membrane was soaked in 9 M KOH for 1 week at RT, then rinsed thoroughly in DI water and soaked in 1 M NaCl for 24 h to exchange it back to the Cl form before post-degradation FTIR measurements for a proper comparison to the initial membrane.

#### **2.4.7 Elemental Analysis**

Elemental analysis was performed at Huffman Hazen Laboratories in Golden, CO. Samples were dried under vacuum at ambient temperature overnight prior to analysis, and results are reported on a dried samples basis. Chlorine was determined by oxygen flask combustion followed by potentiometric titration.

#### 2.4.8 Thermal Characterization

Thermogravimetric analysis (TGA) was performed using a TA Instruments TGA Q 500. A 2 mg polymer sample was placed on a platinum pan and a ramp rate of 10 °C min<sup>-1</sup> up to 800 °C with an air flow rate of 20 mL min<sup>-1</sup> was used. Differential scanning calorimetry (DSC) was performed using a TA instruments Q20 DSC. 5 – 10 mg of polymer was loaded in Tzero aluminum pans and the change in heat flow was measured over a temperature range of 0 – 160 °C with a heating and cooling rate of 10 °C min<sup>-1</sup>. Each sample was cycled over the temperature range four times. The degree of crystallinity was calculated from the enthalpy of melting ( $\Delta H_m$ ) using 290 J g<sup>-1</sup> as the heat of fusion for a pure orthorhombic polyethylene crystallite [241].

#### 2.4.9 Ion Exchange Capacity (IEC)

The Mohr titration method was used to determine the ion exchange capacity (IEC) of each anion exchange membrane in the chloride form. This method determines the concentration of Cl<sup>-</sup> in solution by titrating with silver nitrate (AgNO<sub>3</sub>) and using a potassium chromate (K<sub>2</sub>CrO<sub>4</sub>) indicator. The formation of the brownish-red precipitate, Ag<sub>2</sub>CrO<sub>4(s)</sub>, indicates the end-point has been reached when all Cl<sup>-</sup> has precipitated from the solution. Experiments were performed in triplicate, and three replicate data points were collected for each sample. 50 – 70 mg of each membrane (chloride form) were dried overnight in a vacuum oven at RT and weighed. The samples were then soaked in 30 mL of 1 M NaNO<sub>3</sub> for 24 h to allow the Cl<sup>-</sup> to fully exchange into solution. 0.5 mL of indicator was added to 5 mL of this solution and was then titrated with AgNO<sub>3</sub> until a color change (yellow to light brown) was observed. The volume of AgNO<sub>3</sub> was then recorded and used to calculate the concentration of Cl<sup>-</sup> in solution to obtain the IEC of the AEM.

#### 2.4.10 IEC Alkaline Stability

Samples in the chloride form were tested in either 9 M KOH at RT or 1 M KOH at 80 °C. KOH solutions were made in a glove bag purged with UHP nitrogen, and samples were either placed in 9 M KOH for 7 days or in 1 M KOH at 80 °C for 1 – 3 days. The samples were then washed and placed in 1 M NaCl for 24 h so the OH<sup>-</sup> ions fully exchanged into solution. A titration was then performed using HCl and methyl orange indicator to determine the loss in IEC.

#### 2.4.11 Water Uptake Measurements

A Surface Measurement Systems DVS-Advantage instrument was used to investigate the vapor water uptake of the membranes. A dynamic vapor sorption (DVS) study was performed and gravimetric measurements of water vapor uptake, and loss, by the membrane were examined. Membrane samples were vacuum dried for 24 h at RT before placing in the DVS instrument. Samples were further dried for 120 min at 60 °C in the DVS instrument to obtain the initial dry mass. Following this, humidity was increased gradually in five steps to reach a maximum of 95% RH. At each step, the membrane was allowed to equilibrate at a particular RH for at least 120 min. The average number of water molecules absorbed to each cation/anion pair, or  $\lambda$ , was calculated using Equation 2.1,

$$\lambda = \frac{WU}{IEC * MW_{H_2O}} \quad (2.1)$$

where  $WU$  and  $MW_{H_2O}$  are the water uptake in wt% and the molar mass of water, respectively. For liquid water uptake measurements, samples were dried overnight under vacuum at RT, and initial measurements of mass, width and thickness were collected in the dry state. Samples were then soaked in DI water at RT for 24 h, and the wet measurements were collected and used to calculate the in-plane and through-plane swelling, water uptake, and  $\lambda$ .

#### 2.4.12 X-ray Scattering

Small-angle X-ray scattering (SAXS) and wide-angle X-ray scattering (WAXS) were performed at the Basic Energy Sciences Synchrotron Radiation Center (BESSRC) at the Advanced Photon Source at Argonne National Lab on beamline 12 ID-B. SAXS and WAXS were performed simultaneously using a Pilatus 2M detector to collect small angle scattering data and a Pilatus 300k detector to collect wide angle scattering data. Experiments were performed with an exposure time of 0.5 s. The X-ray beam had a wavelength of 1 Å and energy of 13.3 keV. The intensity ( $I$ ) is a radial integration of the 2D scattering pattern with respect to the scattering vector ( $q$ ). Temperature and humidity were controlled within a custom sample oven as described previously [242]. Each experiment studied three samples and one blank window to obtain a background spectrum, and three shots were averaged for each sample prior to background subtraction. Sample holders were initially inserted into the oven at ambient conditions for initial scattering

data. The samples were then heated to 60 °C with dry nitrogen and allowed to equilibrate for 40 min before the scattering experiments. Relative humidity (RH) was then ramped to 95% while the temperature was maintained at 60 °C. Once the desired conditions were reached the samples were equilibrated for 60 min. Wet samples were soaked for 5 days in DI water prior to testing and loaded at ambient conditions. Data analysis was performed in Igor using the Irena modeling suite [243]. Crystal size from WAXS spectra was determined using the Scherrer equation.

#### **2.4.13 Transmission Electron Microscopy (TEM)**

The TEM specimens were prepared using a Leica CryoUltramicrotome. The microtome chamber was cooled down to -150 °C by liquid nitrogen, where the bulk sample was microtomed with a diamond knife at a thickness of  $\sim 40$  nm. The cut sections were then transferred to 400 mesh copper support grids. Samples were stained by OsO<sub>4</sub> vapor for 30 min or RuO<sub>4</sub> vapor for 15 min at RT. TEM characterization was performed on a JEOL 2000FX TEM at an accelerating voltage of 200 kV.

#### **2.4.14 Mechanical Properties**

Mechanical testing was performed using a Sentmanat Extensional Rheometer (SER, Xpansion Instruments) attachment on an ARES G2 Rheometer (TA Instruments). Membrane samples ( $\sim 3$  mm wide) were clamped to the two counter-rotating drums on the fixture and tension was applied until the membrane broke. The Hencky strain rate used was based on the final elongation of each film: 0.0033 s<sup>-1</sup> for elongations less than 20% and 0.0167 s<sup>-1</sup> for elongations between 20 and 100%. The Hencky strain rates were calculated based on ASTM D882-12 tensile testing of thin plastic sheeting. Measurements were performed at either ambient conditions, or after the sample had been soaked in DI water.

#### **2.4.15 Chloride and Hydroxide Ion Conductivity**

The in-plane Cl<sup>-</sup> and OH<sup>-</sup> ion conductivity were measured using potentiostatic electrochemical impedance spectroscopy (PEIS) with a BioLogic Scientific Instruments VMP3 Potentiostat. Cl<sup>-</sup> conductivity measurements were performed in a TestEquity environmental chamber (model 1007H) to control temperature and RH. Experiments were performed at a constant 95% RH while varying temperature from 40 – 80 °C. A detailed procedure has been published [244].



For OH<sup>-</sup> conductivity, a custom built Bekktech conductivity cell was used in conjunction with a modified fuel cell test stand to flow humidified UHP nitrogen at a controlled temperature. A procedure detailing the measurements and methods of exchanging membranes from the Cl<sup>-</sup> form to the OH<sup>-</sup> form has been published [244, 245]. The in-plane conductivity of the membranes was calculated using Equation 2.2,

$$\sigma = \frac{d}{t * w * R} \quad (2.2)$$

Where  $d$  is the distance between two platinum electrodes,  $t$  is the thickness of the sample,  $w$  is the width of the sample, and  $R$  is the membrane resistance, obtained by fitting a Randles circuit model to the Nyquist impedance plot.

## 2.5 Results and Discussion

### 2.5.1 Polymer Synthesis and Characterization

In this work, a polycyclooctene-based triblock copolymer PCMS-*b*-PCOE-*b*-PCMS was initially synthesized and post-hydrogenated to yield an insoluble polyethylene-based triblock copolymer, PCMS-*b*-PE-*b*-PCMS. Larger PCMS blocks were synthesized based on that work to achieve high ionic conductivity. This starting PCMS:PCOE block ratio is also known to maintain adequate mechanical integrity. This strategy allowed for the synthesis of a polydisperse midblock and narrowly disperse outer blocks to achieve good phase separation.

A detailed synthesis route for PCMS-*b*-PCOE-*b*-PCMS has been published previously [58]. Briefly, a novel dual chain transfer agent (R2-CTA) was utilized to mediate the chain-transfer ring-opening metathesis polymerization (ROMP) of COE as well as the reversible addition-fragmentation chain transfer radical polymerization (RAFT) of CMS. The structures of R2-CTA, telechelic PCOE and triblock PCMS-*b*-PCOE-*b*-PCMS were confirmed by <sup>1</sup>H NMR, shown in Figure 2.2. Successful synthesis of R2-CTA was confirmed by the integrations of characteristic peaks a-f. According to the mechanism of the ROMP [246], the end-groups of PCOE come from two sources, the Grubbs 2<sup>nd</sup> generation catalyst/initiator (G2) and R2-CTA. As the feeding ratio of R2-CTA versus G2 is 50, the majority of the end-groups are from R2-CTA. Theoretical capping efficiency was calculated to be over 95%. Peaks from PCOE backbones and end-group peaks d-f were used to calculate the degree of polymerization (DP) of PCOE, which is

~648. After chain extension with CMS by RAFT polymerization, peaks from benzene rings and benzylic positions on PCMS appear. The DP of PCMS was then calculated to be ~322 (or ~161 on each side of the PCOE midblock).

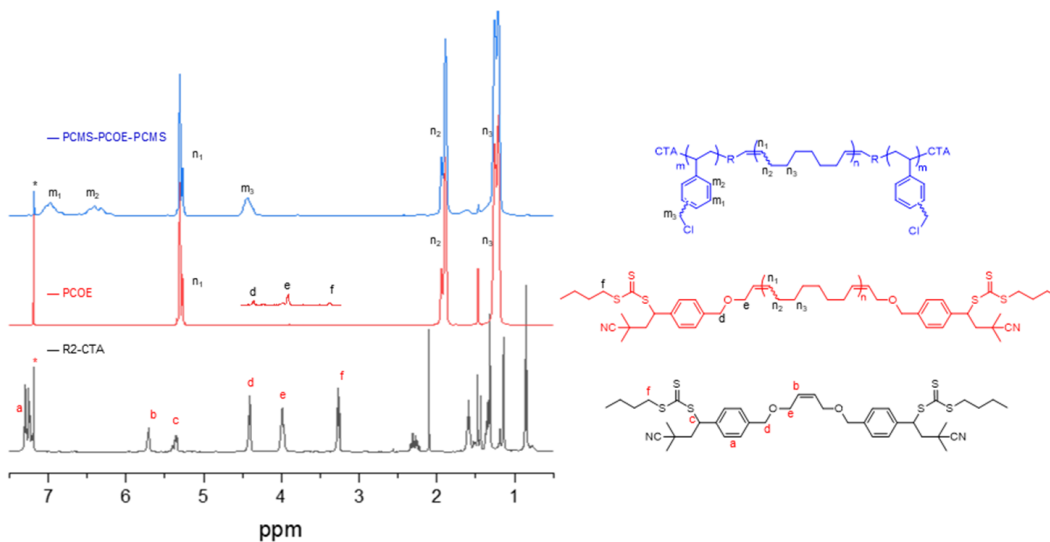


Figure 2.2  $^1\text{H}$  NMR of R2-CTA (bottom black line), telechelic PCOE with a close-up of the end-group region (middle red line) and triblock PCMS-*b*-PCOE-*b*-PCMS (top blue line).

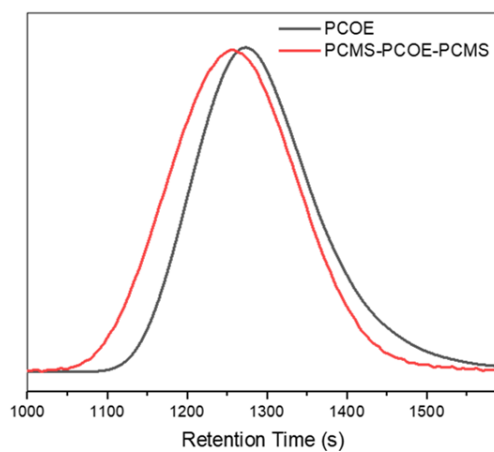


Figure 2.3 GPC traces of PCOE precursor (black line) and AEM-MP, triblock copolymer PCMS-*b*-PCOE-*b*-PCMS (red line).

The molecular weight and dispersities ( $D$ ) of telechelic PCOE and triblock PCMS-*b*-PCOE-*b*-PCMS after chain extension were determined by GPC, as shown in Figure 2.3. The resulting  $M_n$  of PCOE was  $89,000 \text{ g mol}^{-1}$  and  $D = 1.67$ , obtained using a polystyrene

standard. After chain extension by RAFT, the peak shifted to the higher-molecular weight region, indicating the formation of block copolymers, instead of polymer mixtures. The  $M_n$  of the triblock PCMS-*b*-PCOE-*b*-PCMS was  $\sim 121,500 \text{ g mol}^{-1}$  with  $D$  of 1.68, using the same standards. The high capping efficiency of R2-CTA on PCOE by metathesis ensures that all PCOE chains serve as functional macro-CTAs and can undergo chain extension by RAFT on both ends, which led to the unimodal distribution of the triblock copolymer. Serious broadening effects were not observed after chain extension, indicating the living character provided by two CTA ends on the telechelic PCOE.

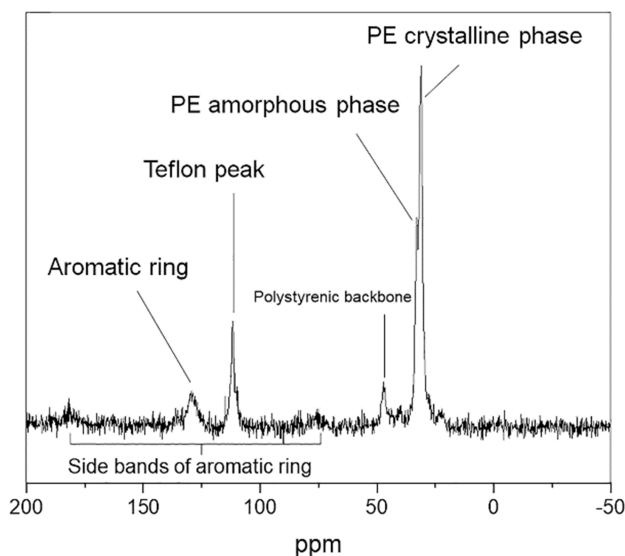


Figure 2.4 Solid-state  $^{13}\text{C}$  NMR and peak assignments of PCMS-*b*-PE-*b*-PCMS.

The hydrogenation of PCMS-*b*-PCOE-*b*-PCMS was performed using diimide derived from the thermal decomposition of *p*-toluenesulfonyl hydrazide (TSH). This produced a new triblock copolymer, PCMS-*b*-PE-*b*-PCMS, with a linear polyethylene midblock with the same molecular weight distribution. Confirmation of the hydrogenation reaction was performed with both solid-state  $^{13}\text{C}$  NMR and IR spectroscopy, shown in Figure 2.4 and Figure 2.5, respectively. The peaks from both the crystalline and amorphous phases of the PE backbone appear at 30 ppm in Figure 2.4. No residual peaks from PCOE were observed.

The IR spectrum in Figure 2.5A shows adsorption peaks for the olefinic functionalities in PCOE from  $\nu(\text{=C-H})$  at  $3050 \text{ cm}^{-1}$ ,  $\nu(\text{C=C})$  at  $1660 \text{ cm}^{-1}$ , and  $\delta(\text{=C-H})$  at  $970 \text{ cm}^{-1}$ . In

Figure 2.5B these are absent or considerably decrease in intensity, substantiating the success of the hydrogenation reaction. The PE triblock copolymer films were quaternized in the solid state with either TMA or MPRD quaternary ammonium cations by submerging films in either TMA (25 wt% in water) or MPRD (33 vol% in methanol) solution at 50 °C for 3 days. Figure 2.5C and D show the IR spectrum for the quaternized AEMs. New adsorption bands are observed near 3400 and 1650  $\text{cm}^{-1}$  from  $\nu(\text{O-H})$  and  $\delta(\text{O-H})$  of water, respectively, corresponding with the ambient water uptake of the cationic moieties. Additionally, the broad peak at 827  $\text{cm}^{-1}$  from  $\nu(\text{C-Cl})$  in benzyl chloride is replaced with three new peaks near 890, 860, and 830  $\text{cm}^{-1}$  associated with  $\nu(\text{C-N})$  from TMA (see dotted line on Figure 2.5 for clarity) [45]. Peaks that appear in the same region in Figure 2.5D are also attributed to  $\nu(\text{C-N})$  in MPRD. New peaks are also noted in the  $\nu(\text{C-N})$  range from 1300 – 1100  $\text{cm}^{-1}$  from the addition of cationic moieties.

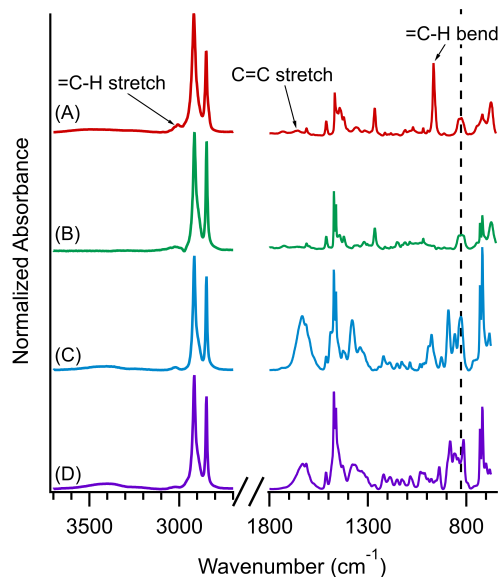


Figure 2.5 FTIR spectra of the starting PCMS-*b*-PCOE-*b*-PCMS (A), the hydrogenated PCMS-*b*-PE-*b*-PCMS (B), PCMS-*b*-PE-*b*-PCMS quaternized with TMA (C) and MPRD (D). Spectra from 1800 to 650  $\text{cm}^{-1}$  is shown at a larger scale for clarity. Dotted line indicates the  $\nu(\text{C-Cl})$  from benzyl chloride groups at 827  $\text{cm}^{-1}$ .

## 2.5.2 Membrane Fabrication and Thermal Characterization

The PE-based triblock was insoluble in organic solvents, therefore films were fabricated by hot-pressing a suspension of the polymer powder in minimum *p*-xylene (1 mL *p*-xylene for every

100 mg of polymer). The hot-pressing temperatures were selected based on thermal gravimetric analysis (TGA) and differential scanning calorimetry (DSC) of the hydrogenated triblock polymer. Results from TGA (Figure 5.16) indicate three major weight-loss steps at  $\sim 260$  °C, 445 °C and 560 °C. Weight loss occurring before 140 °C is mainly due to the evaporation of residual *p*-xylene. The first broad mass loss at 260 °C is attributed to the decomposition of the benzyl chloride groups [75], and the second degradation at 445 °C is due to polyethylene degradation via random scission of the main chain [247, 248]. Mass loss beyond 500 °C is attributed to further decomposition and oxidation of the remaining polymer backbone.

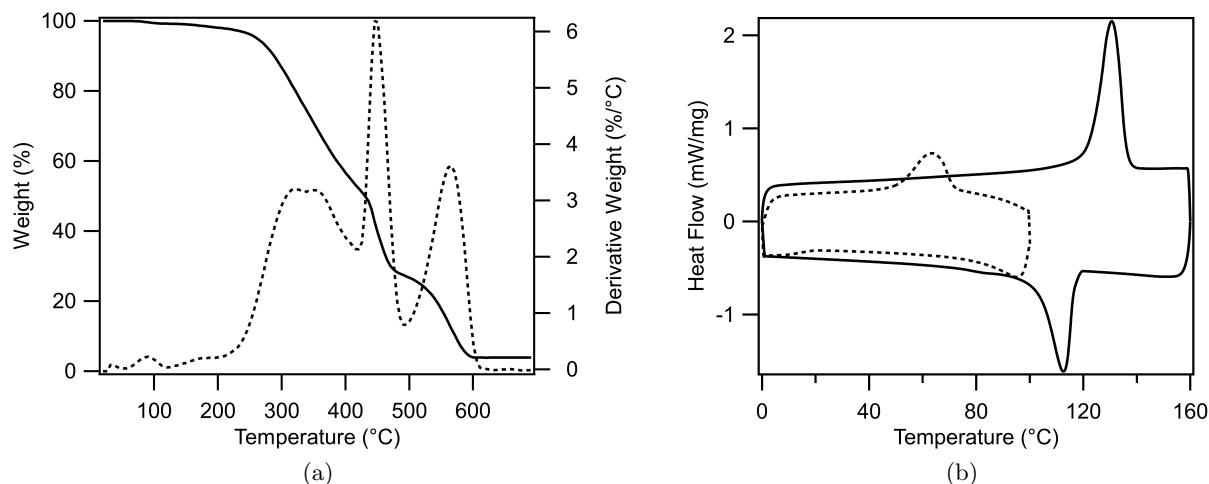


Figure 2.6 (a) TGA of PCMS-*b*-PE-*b*-PCMS, unquaternized. (Solid line is weight %, dotted line is derivative weight). (b) DSC traces of PCMS-*b*-PCOE-*b*-PCMS (dotted) and PCMS-*b*-PE-*b*-PCMS (solid) powder. Heating and cooling rates of 10 °C min<sup>-1</sup>.

There is also a 1 wt% mass loss observed in TGA between 140 °C and 260 °C. We propose that this is attributed to chloride leaving from the benzyl chloride groups [49, 244], suggesting that by hot-pressing the triblock copolymer in this temperature range a small amount of crosslinking can be introduced within the PCMS block via chloride scission and subsequent bonding of benzyl groups. To test this hypothesis, two hot-pressing temperatures were selected, one at the melting point of 130 °C, and one above at 180 °C. Elemental analysis was performed on the triblock copolymer hot-pressed at 130 °C and at 180 °C before quaternization to determine if there were any chemical differences (see Table 2.1). A small loss ( $\sim 1$  wt%) of Cl was observed in the triblock hot-pressed at 180 °C, which may substantiate this claim. Evidence given below

further suggests a small amount of crosslinking has occurred.

DSC measurements shown in Figure 5.16 highlight the melting of the PE midblock at  $\sim 130$  °C and indicate complete hydrogenation of the material as there is no residual melting point from the original PCOE midblock (occurs at  $\sim 55$  °C, dashed line Figure 5.16). The crystallization exotherm is suppressed for the PCOE-based triblock likely due to the slow cooling rate and slow crystallizing nature of the material [249].

Table 2.1 Elemental analysis of PCMS-*b*-PE-*b*-PCMS triblock backbone hot pressed at 130 °C and 180 °C, HyAEM-TM-130 and HyAEM-MP-130. Calculated values shown in parenthesis. For quaternized membranes, calculated values are based on theoretical IEC obtained from NMR.

	PE Triblock-130	PE Triblock-180	HyAEM-TM-130	HyAEM-MP-130
Carbon % (w/w)	77.40 (79.53)	77.30 (79.53)	72.80 (77.37)	74.91 (72.93)
Hydrogen % (w/w)	9.31 (10.95)	9.99 (10.95)	11.34 (10.49)	11.27 (9.81)
Nitrogen % (w/w)	0.12 (0.02)	0.52 (0.02)	2.39 (3.40)	2.33 (4.86)
Chlorine % (w/w)	7.50 (9.32)	6.80 (9.32)	4.20 (8.56)	4.80 (12.24)
Carbon (mol C/g)	6.44 (6.62)	6.44 (6.62)	6.06 (6.44)	6.24 (6.07)
Hydrogen (mol H/g)	9.24 (10.86)	9.91 (10.86)	11.25 (10.41)	11.18 (9.74)
Nitrogen (mol N/g)	0.01 (0.0016)	0.04 (0.0016)	0.17 (0.24)	0.17 (0.35)
Chlorine (mol Cl/g)	0.21 (0.26)	0.19 (0.26)	0.12 (0.24)	0.14 (0.35)

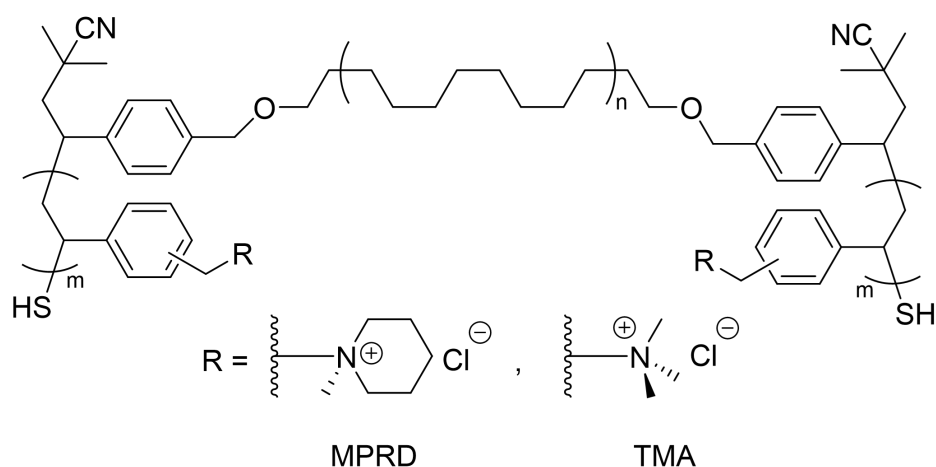


Figure 2.7 Chemical structures of triblock copolymers PCMS-*b*-PE-*b*-PCMS, shown quaternized with either MPRD or TMA.

Hot-pressed thin films of PCMS-*b*-PE-*b*-PCMS were submerged in either a solution of TMA (25 wt% in water) or MPRD (33 vol% in methanol) at 50 °C for 3 days to yield either TMA or MPRD based quaternary ammonium cations. A schematic showing the final triblock copolymer anion exchange membrane is shown in Figure 2.7. The unsaturated PCOE-based triblock copolymer was also quaternized with MPRD and the PCOE midblock was crosslinked with 1,10-decanedithiol (DT) according to the procedure published previously [58] to highlight the improvements in material characteristics after hydrogenation. The sample names and descriptions are summarized in Table 2.2.

Table 2.2 Descriptions and Ion Exchange Capacities of All Anion Exchange Membranes Studied

Sample	Midblock	Cation	Method	IEC <sub>NMR</sub> (mmol g <sup>-1</sup> )	IEC <sub>titr</sub> (mmol g <sup>-1</sup> )
AEM-MP	PCOE, no XL <sup>a</sup>	MPRD	Solution cast	2.1	1.45 ± 0.05
AEM-MP-DT	PCOE, DT XL <sup>b</sup>	MPRD	Solution cast	2.1	1.44 ± 0.02
HyAEM-TM-130	PE	TMA	Hot-pressed 130 °C	2.3	1.33 ± 0.15
HyAEM-MP-130	PE	MPRD	Hot-pressed 130 °C	2.1	1.68 ± 0.07
HyAEM-TM-180	PE	TMA	Hot-pressed 180 °C	2.3	1.83 ± 0.08
HyAEM-MP-180	PE	MPRD	Hot-pressed 180 °C	2.1	1.66 ± 0.07

<sup>a</sup>PCOE-based AEM reported previously, uncrosslinked [58].

<sup>b</sup>UV crosslinked with 1,10-decanedithiol

Thermal analysis by TGA and DSC was also performed on the quaternized membranes (see Figure 2.8 and Figure 2.9). The onset of degradation for each quaternized triblock was ~170 °C and ~190 °C for TMA and MPRD, respectively. A maximum temperature of 160 °C was used for the DSC measurements to avoid degradation of the cationic moieties. The thermal characteristics of all quaternized membranes are summarized in Table 2.3. Similar melting and crystallization temperatures for the PE midblock were observed around 130 °C and 112 °C, respectively, for all AEMs. The degree of crystallinity was calculated from the enthalpy of melting and compared to a literature value for a pure PE crystal [241].

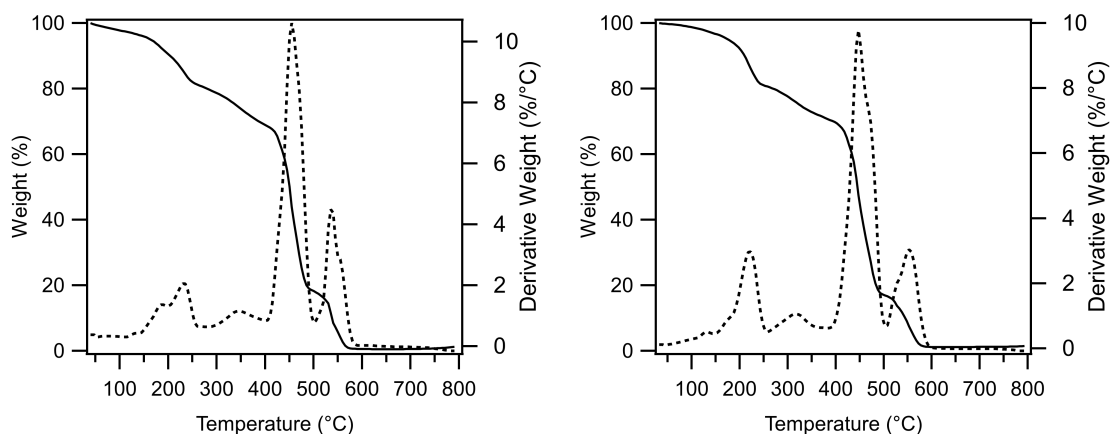


Figure 2.8 TGA of PCMS-*b*-PE-*b*-PCMS quaternized with TMA (left) and MPRD (right). Onset of degradation of each cation group was 170 °C and 190 °C, respectively. (Solid line = weight %, dotted line = derivative weight).

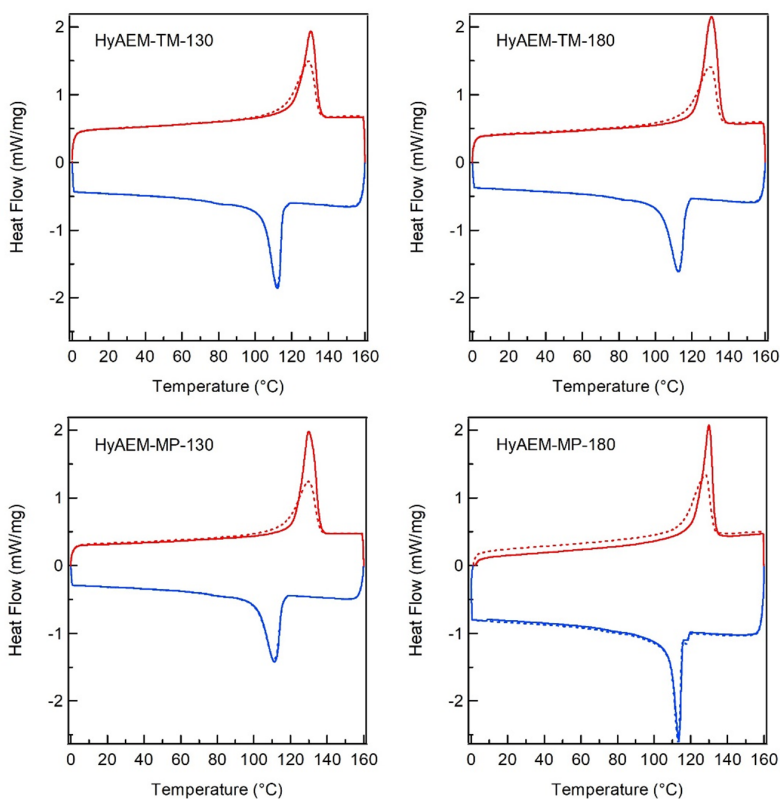


Figure 2.9 DSC of all HyAEMs. Red lines represent heating cycles and blue lines represent cooling cycles, both at 10 °C/min. Dotted lines represent second heating/cooling cycle, often the second cooling cycle nearly overlaps the first cooling cycle.



Table 2.3 Thermal Characterization from DSC

Sample	Cycle	T <sub>m</sub> (°C)	T <sub>c</sub> (°C)	ΔH <sub>m</sub> (J g <sup>-1</sup> )	ΔH <sub>c</sub> (J <sup>-1</sup> )	Crystallinity (%)
HyAEM-TM-130	1	131	113	96	60	33
	2-4	130	113	72	60	24
HyAEM-MP-130	1	130	111	80	63	27
	2-4	130	111	63	63	22
HyAEM-TM-180	1	130	112	77	59	26
	2-4	129	112	55	59	19
HyAEM-MP-180	1	130	113	79	58	27
	2-4	128	113	66	58	22

The thermal history of the material appears to affect the degree of crystallinity, where a lower crystallinity was observed across all samples after the first thermal cycle from 0 to 160 °C. The AEMs quaternized with TMA showed slight differences in crystallinity depending on their hot-pressing temperature, where HyAEM-TM-130 had an initial crystallinity of 33% that decreased to 24% after thermal cycling, and HyAEM-TM-180 had an initial crystallinity of 26% and decreased to 19% after thermal cycling (Figure 2.9). No differences in crystallinity are observed between hot-pressing temperatures in the HyAEMs quaternized with MPRD.

The theoretical ion exchange capacities (IECs) of the quaternized AEMs are compared with their titrated values in Table 2.2. The theoretical IECs were calculated from <sup>1</sup>H NMR spectra of the precursor PCMS-*b*-PCOE-*b*-PCMS and the experimental IEC was determined via a Mohr titration. The comparison highlights a discrepancy in these values. This has been previously reported for AEMs with an IEC > 2.0 mmol g<sup>-1</sup> [250, 251], and the authors speculate the titrated values are lower as a result of diffusion limitations during anion exchange.

### 2.5.3 Water Uptake

The vapor water uptake and hydration number, λ (waters per charge carrier), for the PCOE and PE-based AEMs are shown in Figure 2.10, tabulated values can be found in Table 2.4, and dynamic vapor sorption (DVS) traces of mass uptake and RH cycles can be found in Figure 2.11. Generally, the water uptake is less than 35% for all AEMs at 95% RH. When comparing the

cross-linked PCOE-based AEM to the PE-based AEMs, water uptake and  $\lambda$  appear to decrease with hydrogenation of the midblock, even more effectively than crosslinking PCOE with DT (AEM-MP-DT) to prevent excessive swelling [47].

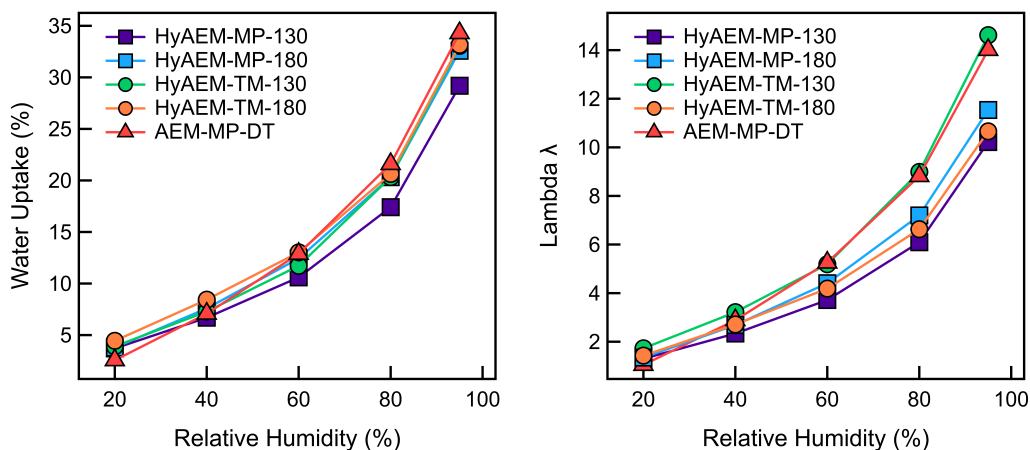


Figure 2.10 Water vapor uptake and  $\lambda$  at 60 °C from 20 – 95% RH.

Table 2.4 Water Uptake and  $\lambda$  from DVS

	AEM-MP-DT	HyAEM-TM-130	HyAEM-TM-180	HyAEM-MP-130	HyAEM-MP-180
RH (%)	Water Uptake (%)				
20	2.57 ± 0.09	3.91 ± 0.29	4.45 ± 0.24	3.71 ± 0.13	3.8 ± 0.18
40	7.08 ± 0.09	7.29 ± 0.34	8.44 ± 0.23	6.69 ± 0.16	7.59 ± 0.2
60	12.89 ± 0.16	11.73 ± 0.42	13.03 ± 0.28	10.6 ± 0.17	12.44 ± 0.16
80	21.6 ± 0.15	20.32 ± 0.55	20.64 ± 0.43	17.41 ± 0.35	20.32 ± 0.12
95	34.3 ± 0.33	33.06 ± 0.96	33.16 ± 0.61	29.19 ± 0.49	32.58 ± 0.13
RH (%)	$\lambda$ , Waters per Charge Carrier				
20	1.05 ± 0.04	1.73 ± 0.13	1.43 ± 0.08	1.3 ± 0.05	1.35 ± 0.06
40	2.89 ± 0.04	3.22 ± 0.15	2.71 ± 0.07	2.34 ± 0.05	2.69 ± 0.07
60	5.26 ± 0.06	5.19 ± 0.19	4.19 ± 0.09	3.71 ± 0.06	4.41 ± 0.06
80	8.82 ± 0.06	8.99 ± 0.24	6.63 ± 0.14	6.1 ± 0.12	7.2 ± 0.04
95	14.01 ± 0.14	14.62 ± 0.43	10.66 ± 0.2	10.22 ± 0.17	11.54 ± 0.05

The liquid water uptake and swelling properties at room temperature are summarized in Table 2.5. The water uptake and  $\lambda$  increased in all materials when submerged in liquid water when compared to the water vapor uptake. Results for HyAEM-MP-180 compared to HyAEM-TM-180 agree with reports that MPRD cations have higher hydration numbers than TMA cations [57]. Additionally, a more significant trend manifests itself, where HyAEMs show

largely reduced water uptakes and  $\lambda$  when processed at 180 °C compared to 130 °C. Both through-plane and in-plane dimensional swelling were significantly reduced as well. These observations are indicative of cross-linking the PCMS domains and were investigated further by probing the morphology and crystallinity of the HyAEMs.

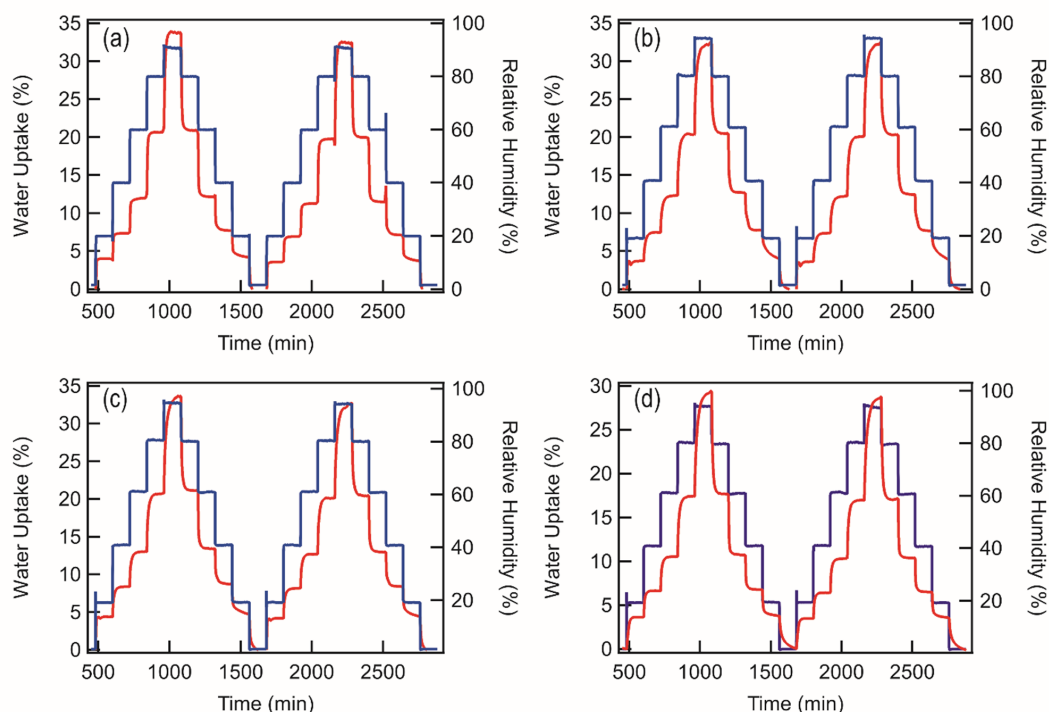


Figure 2.11 DVS traces of all PCMS-*b*-PE-*b*-PCMS samples, where red traces refer to water uptake and blue traces to the relative humidity. (a) HyAEM-TM-130, (b) HyAEM-TM-180, (c) HyAEM-MP-130, (d) HyAEM-MP-180.

Table 2.5 Liquid Water Uptake,  $\lambda$ , and Dimensional Swelling

Sample	Water uptake (%)	$\lambda$	In-plane swelling (%)	Through-plane swelling (%)
HyAEM-TM-130	185.6 $\pm$ 14.6	82.0 $\pm$ 6.5	29.0 $\pm$ 1.0	56.2 $\pm$ 6.9
HyAEM-MP-130	145.2 $\pm$ 1.9	50.0 $\pm$ 0.7	17.6 $\pm$ 0.8	31.6 $\pm$ 3.5
HyAEM-TM-180	63.7 $\pm$ 0.2	21 $\pm$ 0.1	10.0 $\pm$ 0.9	13.6 $\pm$ 1.6
HyAEM-MP-180	94.2 $\pm$ 3.2	33.0 $\pm$ 1.1	16.5 $\pm$ 0.7	6.6 $\pm$ 2.0

## 2.5.4 Morphology

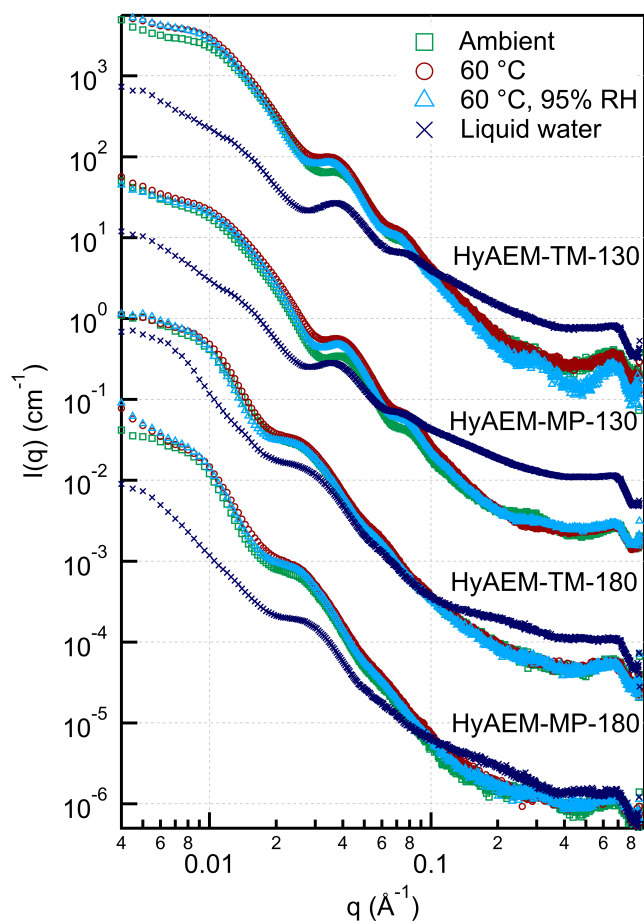


Figure 2.12 SAXS profiles for all HyAEMs in the dry state at ambient conditions (green squares), at 60 °C (red circles), at 60 °C and 95% RH (blue triangles), and after soaking in liquid water (purple x's). Shown stacked for clarity.

The morphology of each membrane was investigated by small-angle X-ray scattering (SAXS) in the dry state at ambient temperature and at 60 °C, at 95% RH and 60 °C, and after soaking in DI water for 5 days (Figure 2.12). All scattering profiles display an initial Guinier region followed by one or two scattering peaks, indicative of phase separation. Contrast arises from both the crystalline and amorphous density differences between the cation-containing blocks and PE, and from chloride ions in the hydrophilic phase [252]. The Unified Fit model was used to analyze the data and determine the radius of gyration ( $R_g$ ), Porod slope ( $P$ ), and Bragg spacing ( $d$ ) of the diffraction peaks [243]. The results are summarized in Table 2.7 for dry and soaked samples [242].

The plotted fits, standardized residuals, and all parameters can be viewed in Figure 2.15 and Figure 2.16.

In most cases  $R_g$  and  $d$  increase upon hydration in each sample, likely due to the effect of water plasticization and swelling of the hydrophilic domains. Surprisingly, despite having lower liquid water uptakes and dimensional swelling, the HyAEMs hot-pressed at 180 °C have larger  $R_g$  than their counterparts hot-pressed at 130 °C. Porod slopes correspond to different particle symmetries, where  $P = 1, 2, 3,$  and  $4$  are signature of randomly distributed rods, lamellae, cylinders, and spheres respectively [253]. From Table 2.7, it is evident  $P$  decreases upon hydration, indicating the shape of the hydrophilic domains changes when going from a dry or humidified state to a saturated wet state. For dry samples,  $P$  ranges from about 2.5 – 3.5, and decreases to about 1.5 – 2.5 when saturated with water, indicating the hydrophilic domains experience a shift from cylinders toward randomly distributed lamellae as they swell [252]. Both cylindrical and lamellar morphologies are ideal for anion conducting membranes because they form an interconnected pathway for ion transport. Two additional peaks are observed at high  $q$ , one near  $q = 0.3 \text{ \AA}^{-1}$  and one near  $q = 0.67 \text{ \AA}^{-1}$  marked by the dotted in Figure 2.13. The d-spacing for the first feature is approximately 2-3 nm and appears to broaden and then disappear once the samples are saturated in liquid water. The second peak at high  $q$  experiences a slight shift to higher  $q$  after full hydration, from approximately 8.9 to 9.7  $\text{\AA}^{-1}$ . The intensity of the feature also increases after saturation, indicating a greater content of water. The intensity of this peak is also lower in the HyAEMs hot-pressed at 180 °C compared to those at 130 °C, in agreement with their depressed water uptakes. Both of these high  $q$  features are attributed to clustering of the cationic moieties and are in the range of what has previously been reported [48, 242]. The bulk morphologies of the PCOE and PE-based AEMs were further investigated by TEM. For both PCOE-based AEMs, the TEM specimens were stained with  $\text{OsO}_4$ , which selectively stains the olefin backbones. Therefore, the dark contrast is from the hydrophobic PCOE midblock and the bright contrast is from hydrophilic polystyrene-functionalized ionic outer blocks. Cylindrical morphologies were observed for both samples in Figure 2.14A-B, with the hydrophobic PCOE block forming the continuous phase. A well-ordered morphology was maintained after crosslinking.

Table 2.6 Radius of Gyration, Porod Slope, and Bragg Spacing obtained from Unified Fit Modeling of SAXS Profiles

Sample	$R_{g,dry}$ (nm)	$R_{g,wet}$ (nm)	$P_{dry}$	$P_{wet}$	$d_{1,dry}$ (nm)	$d_{1,wet}$ (nm)	$d_{2,dry}$ (nm)	$d_{2,wet}$ (nm)
HyAEM-TM-130	15.9	15.8	3.33	2.18	15.1	18	8.8	9.7
HyAEM-MP-130	15.1	20.5	2.84	2.64	15.1	16.3	9	8.2
HyAEM-TM-180	22.2	27.4	2.54	2.19	25.6	24.1	n/a	n/a
HyAEM-MP-180	24.9	26.5	2.81	1.54	26.7	28.6	n/a	n/a

After hydrogenation, the HyAEMs were stained with RuO<sub>4</sub>, which selectively stains aromatic rings. Therefore, an inverse contrast is obtained for Figure 2.14C-F, where dark regions correspond to ionic phases and bright regions correspond to the PE midblock. The contrast indicates some degree of phase separation, however, much less ordered morphologies are observed in HyAEMs than in the PCOE-based AEMs prepared by solution casting. A much shorter membrane forming time given by the hot-pressing method is likely accountable for the loss in ordered morphology.

Nevertheless, some short-range cylinders can be seen which agree with the SAXS profile having Porod slopes around 3 and displaying some higher-order peaks. Additionally, the width of the distributed lamellae in the HyAEMs processed at 180 °C (Figure 2.11E and F) are larger than those in the HyAEMs processed at 130 °C (Figure 2.11C and D), which agrees with both the larger  $R_g$  and Bragg spacing from their SAXS profiles. Overall, the morphologies observed in both SAXS and TEM are indicative of well interconnected, large hydrophilic channels that ultimately favor the material's high ionic conductivity.

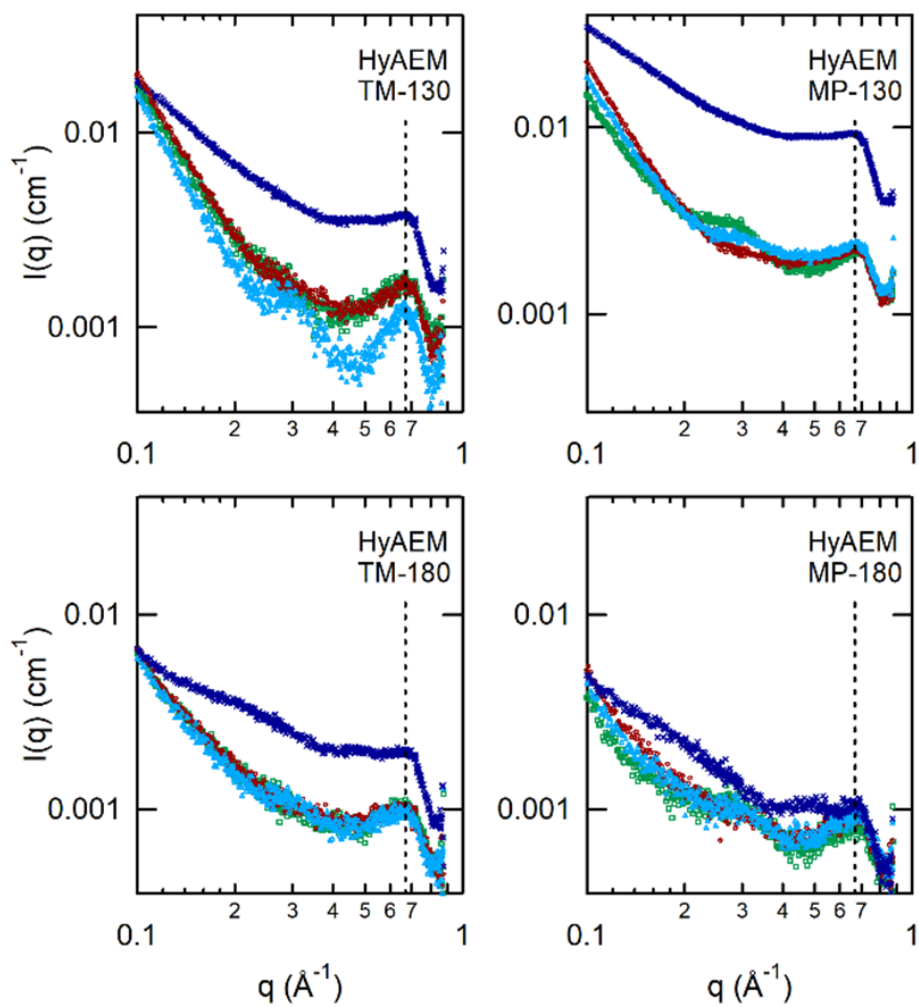


Figure 2.13 SAXS profiles for all HyAEMs highlighting high  $q$  region with peak from cationic clusters. All graphs set to same scale for comparison. Dry state at ambient conditions (green squares), at 60 °C (red circles), at 60 °C and 95% RH (blue triangles), and after soaking in liquid water (purple x's).

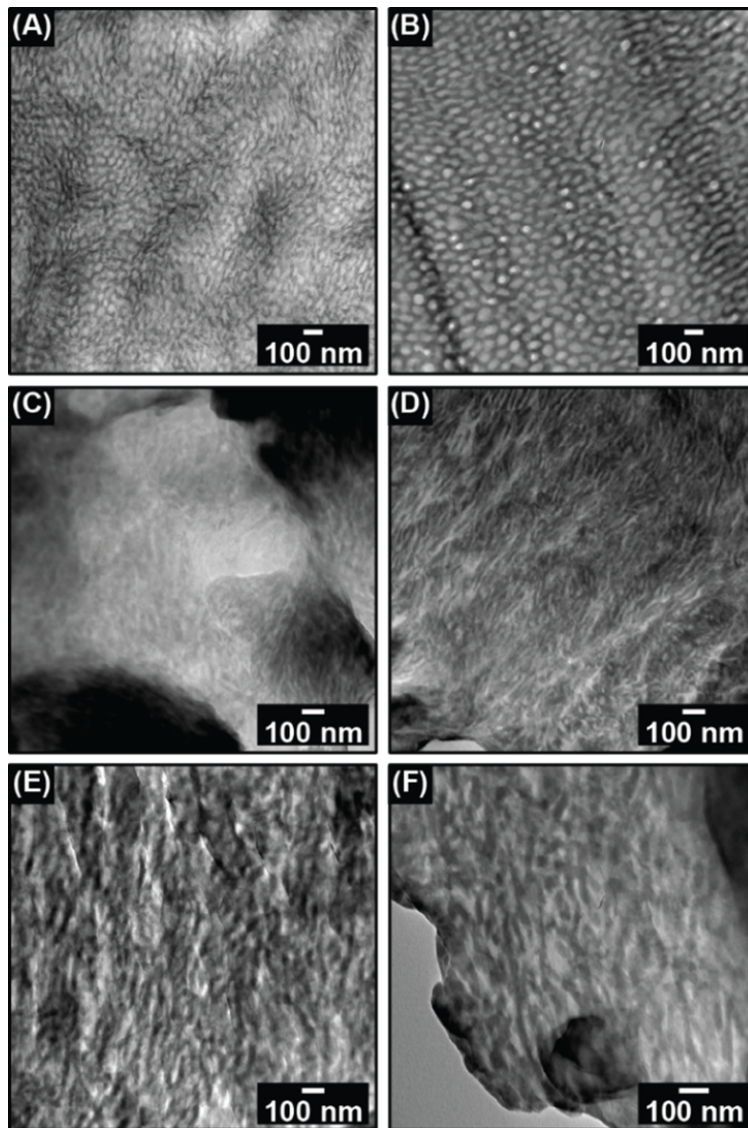


Figure 2.14 TEM for AEM-MP (A), AEM-MP-DT (B), HyAEM-TM-130 (C), HyAEM-MP-130 (D), HyAEM-TM-180 (E) and HyAEM-MP-180 (F). (A) and (B) were stained with OsO<sub>4</sub> and the dark contrast comes from the hydrophobic PCOE domains. The remaining specimens were stained with RuO<sub>4</sub> and the dark contrast comes from the hydrophilic cation-functionalized domains.



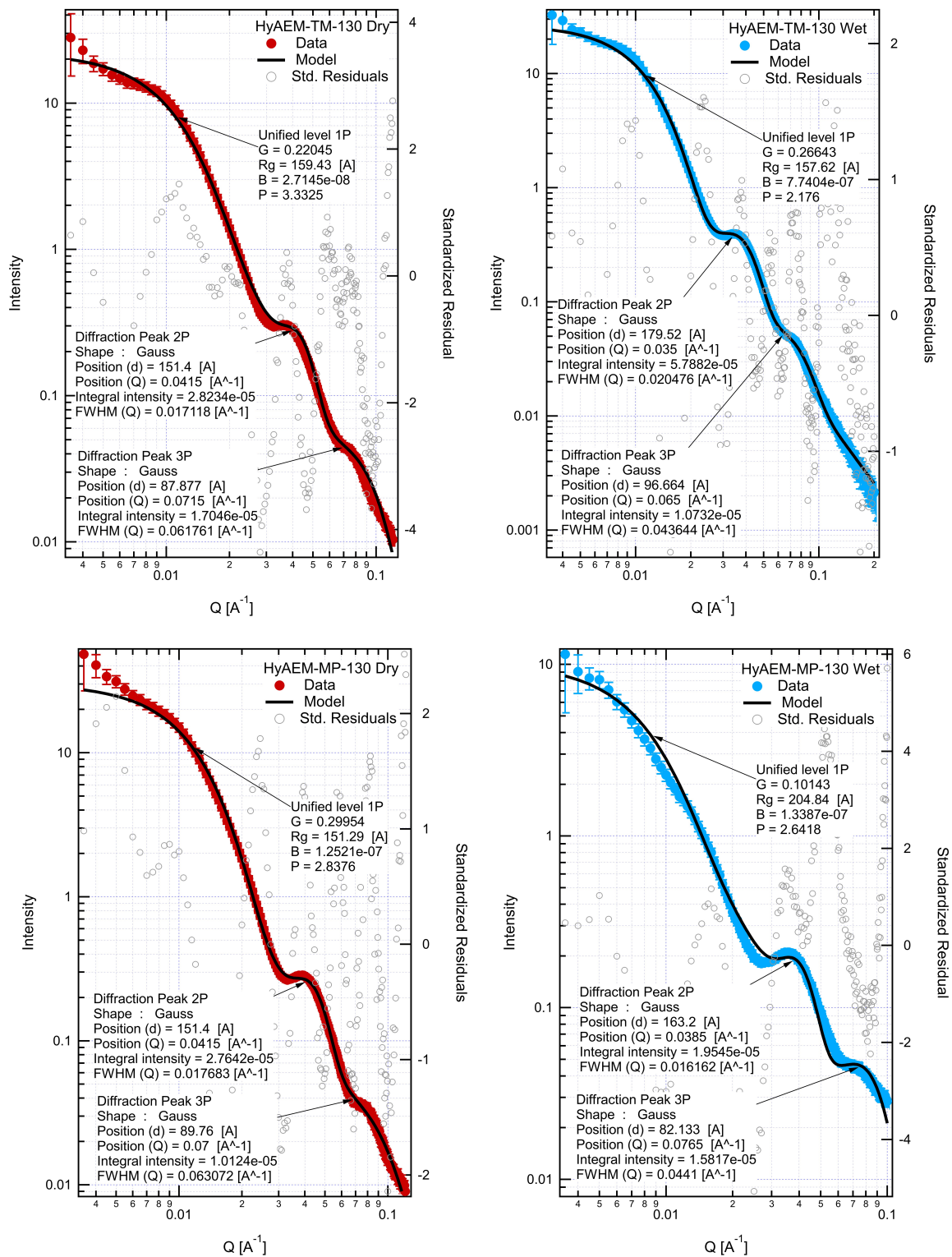


Figure 2.15 Unified Fit modeling of SAXS data of HyAEM-TM-130 dry (top left) and wet (top right) and HyAEM-MP-130 dry (bottom left) and wet (bottom right).

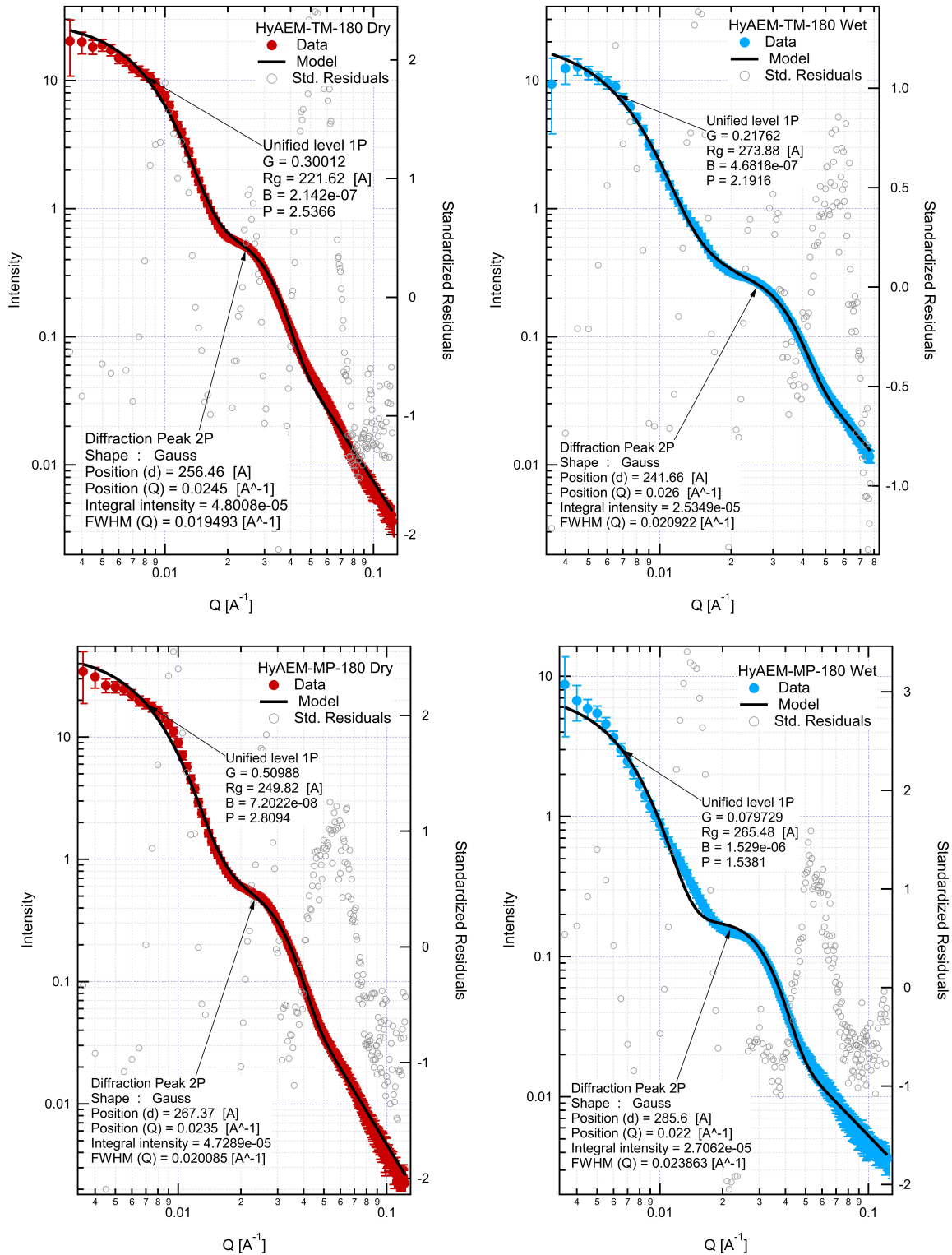


Figure 2.16 Unified Fit modeling of SAXS data of HyAEM-TM-180 dry (top left) and wet (top right) and HyAEM-MP-180 dry (bottom left) and wet (bottom right).

### 2.5.5 Crystallinity

During the SAXS experiments, WAXS spectra were simultaneously collected to investigate the size of the crystalline domains in the PE midblock. The data summarized in Figure 2.17 was determined from the (110) and (200) reflection from the orthorhombic crystal structure of polyethylene [254, 255]. All WAXS spectra are also shown in Figure 2.18.

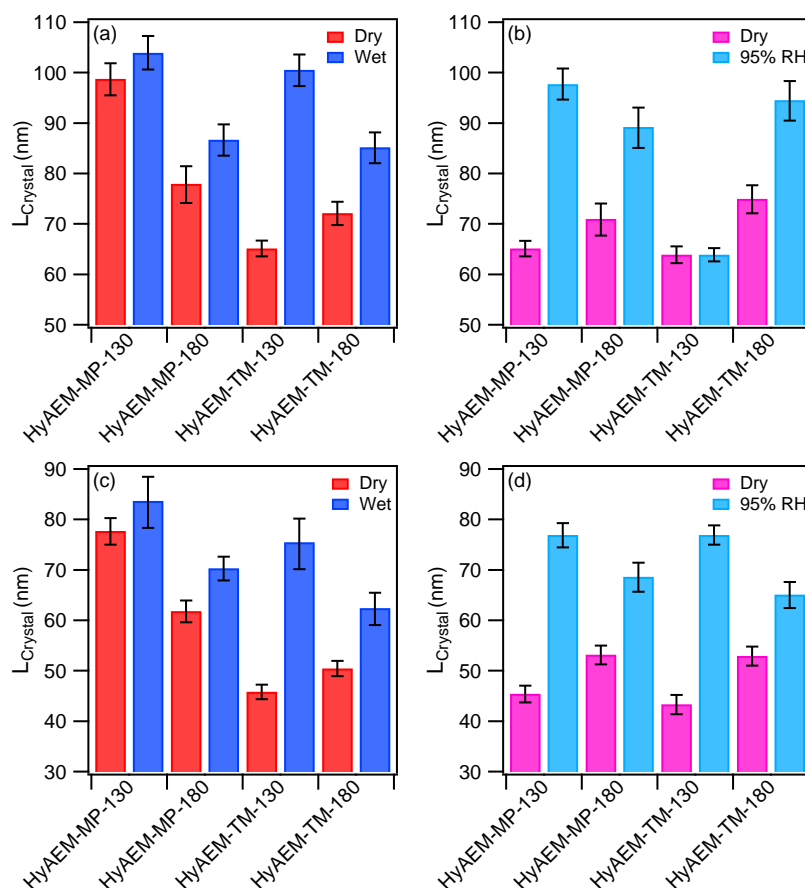


Figure 2.17 Crystal size analysis from WAXS spectra of the (110) reflection (a,b) and the (200) reflection (c,d) of the polyethylene backbone in all HyAEMs at ambient temperature (a,c) and 60 °C (b,d).

Surprisingly, the crystal size decreased from ambient conditions to 60 °C, possibly due to the strong interactions of the side chain dipoles. After equilibrating the sample at 95% RH the crystalline domains increase in size in all samples and remain statistically similar after soaking in liquid water. This indicates that as water content in the membrane increases, crystalline domains increase in size. However, the material is not gaining crystallinity, which indicates existing

crystalline domains may be agglomerating to form larger domains. This is evident in the WAXS spectra when comparing the area under the curve (see Figure 2.18) between ambient and wet samples. The decrease in area from ambient to wet indicates the degree of crystallinity, or number of crystalline domains, decreases, while their peak shift indicates an increase in size. Together, this implies there is a crystal ripening process in which some crystalline domains are aggregating to form larger domains. The increase in crystalline domain size likely stems from the plasticizing effect of water. A possible explanation is that water improves the interfacial mobility of the polymer segments and facilitates the crystallization of PE into larger domains. A similar trend is noted for samples at 60 °C upon hydration to 95% RH, and for all crystal sizes from the (200) reflection.

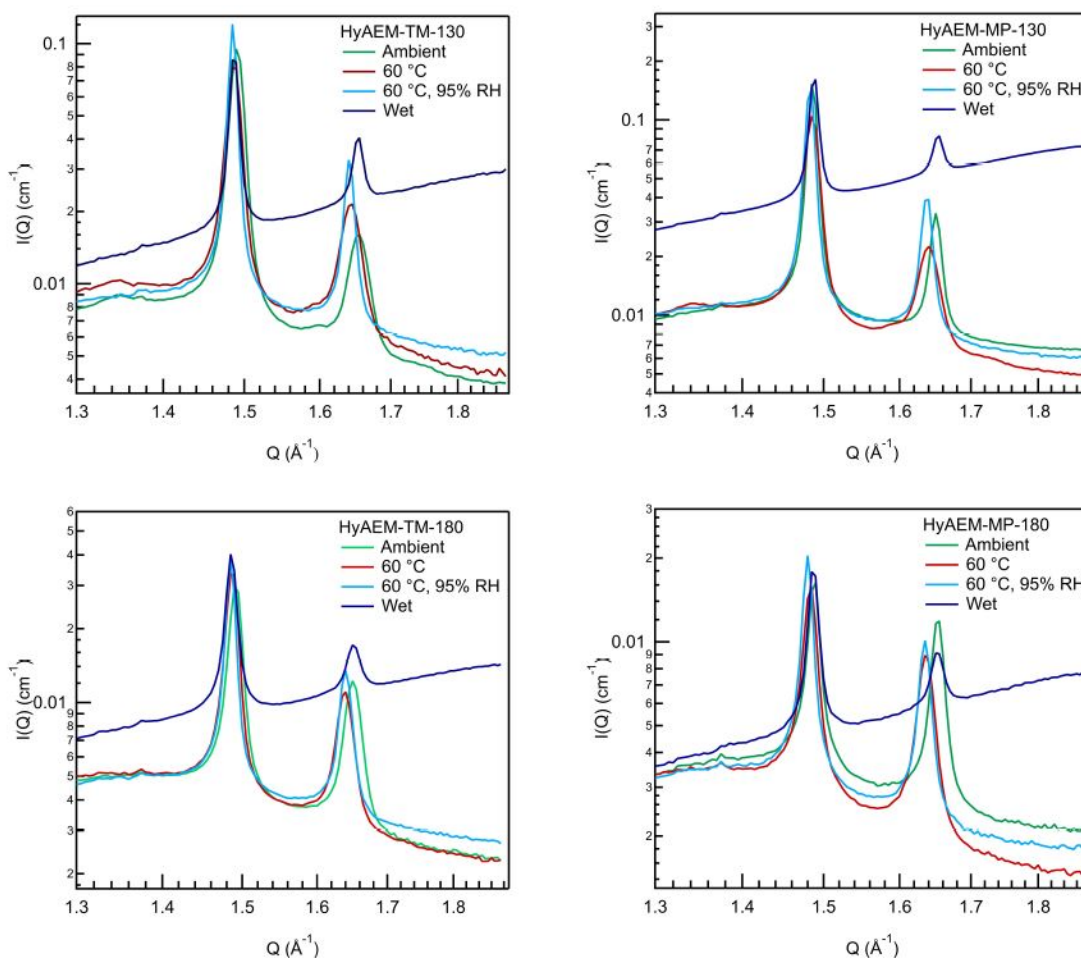


Figure 2.18 WAXS spectra for all HyAEMs investigated at ambient conditions, 60 °C, 60 °C and 95% RH, and after soaking in DI water.

### 2.5.6 Tensile Testing

HyAEM-TM-180 and HyAEM-MP-180 were selected for further mechanical characterization as their higher processing temperature allowed them to be thinner membranes than those processed at 130 °C. Extensional tests were performed on dry membrane samples at ambient conditions and on membranes soaked in DI water at RT (Table 6). Water acts as a plasticizer and typically increases elasticity and elongation of hydrophilic polymer films while simultaneously weakening the material [231]. As expected, Young’s modulus, which is a measure of stiffness, decreased by upon hydration in both membranes. Elongation increased in both membranes and, interestingly, the stress at break increased upon hydration. Though this is counterintuitive, it could be attributed to the large increase in elongation combined with maintaining a decent modulus. Higher degrees of crystallinity have also been shown to improve mechanical properties [256], and this increase in strength correlates with the WAXS data that shows an increase in crystalline domain size upon hydration. The increase in crystalline domain size then translates to an enhanced stress at break when the material is hydrated.

Table 2.7 Mechanical Properties of Dry and Wet Films

Sample	Condition	Stress at Break (MPa)	Young’s Modulus (MPa)	Elongation (%)
HyAEM-TM-180	Dry	$30.5 \pm 1.7$	$184.5 \pm 16.3$	$16.7 \pm 2.2$
	Wet	$38.9 \pm 4.6$	$34.5 \pm 3.0$	$90.5 \pm 4.0$
HyAEM-MP-180	Dry	$23.9 \pm 1.0$	$39.0 \pm 10.2$	$29.4 \pm 0.1$
	Wet	$25.9 \pm 2.1$	$21.2 \pm 1.6$	$60.9 \pm 5.9$

The improvement in strength upon hydration is a promising indication of durability during humidity cycling and in saturated conditions in electrochemical devices. The elongation at break must be greater than the degree of swelling occurring during hydration to ensure that humidity cycling will not lead to mechanical failure [257]. In the dry state, the hydrogenated AEMs have an elongation larger than their dimensional swelling in liquid water, indicating the elongation is more than sufficient. The large decrease in Young’s modulus upon hydration is potentially concerning. This much softening of the material could potentially lead to mechanical failure during testing, though the modulus when hydrated is still an improvement over previously

reported AEMs [58, 238]. The results show strengths comparable to similar materials [50, 56, 231] and overall promising mechanical properties upon hydration.

### 2.5.7 Ionic Conductivity

The chloride and hydroxide conductivity of HyAEM-MP-180 was measured at 95% RH from 40 – 80 °C (Figure 2.19). The highest  $\text{Cl}^-$  and  $\text{OH}^-$  conductivities achieved were 119 and 179  $\text{mS cm}^{-1}$ , respectively, at 80 °C. These ionic conductivities are some of the highest reported to date [222], especially given the modest water uptake and IEC of HyAEM-MP-180. Displaying ionic conductivity on an Arrhenius plot can highlight evidence of Vogel-Tamman-Fulcher (VTF) behavior [258], where a curve in the data indicates the conductivity is related to the segmental motion of the cationic moieties on the polymer backbone and that the ions are not fully dissociated. The linear behavior of the Arrhenius plot indicates that  $\text{OH}^-$  and  $\text{Cl}^-$  are both fully dissociated and that conductivity mainly occurs via the exchange of anions between cationic moieties. This is corroborated by water uptake measurements that show the  $\text{Cl}^-$  anions in the membrane are well solvated ( $\lambda = 12$ ) at 95% RH.

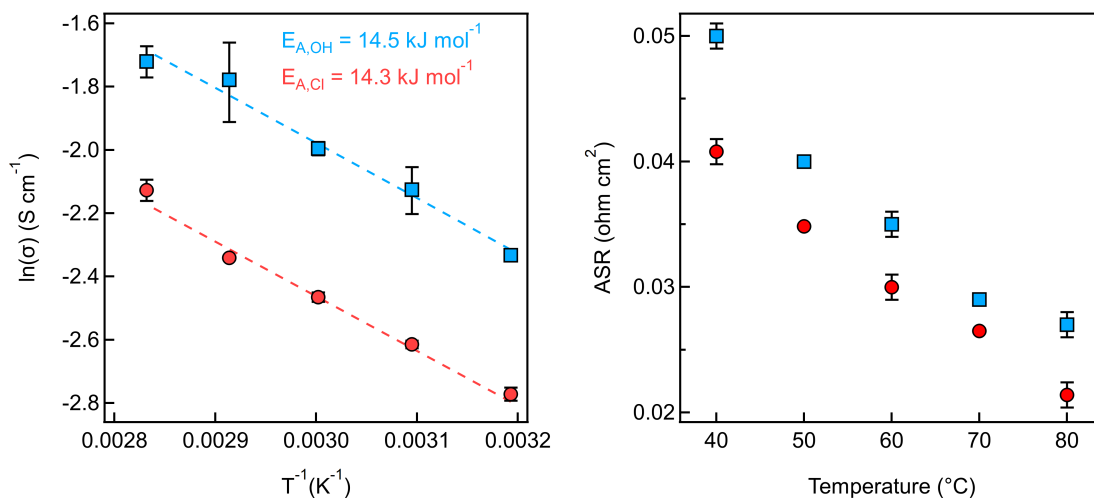


Figure 2.19 Left: Arrhenius plot of  $\text{OH}^-$  (blue squares) and  $\text{Cl}^-$  (red circles) conductivity at 95% RH for HyAEM-MP-180. Right: ASR for HyAEM-MP-180 in  $\text{OH}^-$  form (blue squares) and  $\text{Cl}^-$  form (red circles). IEC = 1.7  $\text{mmol g}^{-1}$ , thickness = 65  $\mu\text{m}$ .

It is important to note that both activation energies are unusually the same and comparatively low (14.5  $\text{kJ mol}^{-1}$  for  $\text{OH}^-$ , 14.3  $\text{kJ mol}^{-1}$  for  $\text{Cl}^-$ ) [53, 223]. Inadequate solvation of

Cl<sup>-</sup> ions would contribute to having a higher activation energy and lower conductivity for membranes in the Cl<sup>-</sup> form [259], and we expect having well solvated Cl<sup>-</sup> has led to an activation energy on par with that for OH<sup>-</sup>. The large, well-interconnected hydrophilic morphology might also favor this lower activation energy by providing pathways with low tortuosity. While a significant contribution to the transport of OH<sup>-</sup> can be from the Grotthuss hopping mechanism, the vehicular transport of chloride is unusually fast for this anion [260], but can nonetheless be attributed to being fully dissociated due to adequate solvation. The area specific resistance (ASR) plot can be found in Figure 2.19. Clearly, a modest reduction in membrane thickness would lead to practical ASR values.

### 2.5.8 Alkaline Stability

There are many studies showing the possible degradation mechanisms of TMA quaternized membranes [251, 261, 262], and studies that shown TMA cationic moieties to be generally less stable than MPRD [57, 58, 85]. For this reason, the chemical stability of the PE-based HyAEMs quaternized with MPRD were the focus of our alkaline stability tests. Membranes were submerged in 9 M KOH at RT for 1 week (Figure 2.20). The retention of cation groups was compared to the crosslinked PCOE-based triblock (AEM-MP-DT) and a commercial AEM, Fumasep FAS-50. The PE-based AEMs showed the best stability with ~50% cation retainment, compared to ~35% for the commercial membrane. Stability was vastly improved after the midblock modification.

Further testing was performed to compare HyAEM-MP-180 and FAS-50 in 1 M KOH at 80 °C to accelerate the degradation mechanisms [263]. After just one day, FAS-50 showed only 20% retainment of cation functionality, and the sample disintegrated before a 3-day measurement could be taken. The hydrogenated AEM retained 75% of cation groups after 3 days. The combination of the 6-membered ring cation and inert polyethylene backbone clearly enhanced the alkaline stability, although there are still some aspects of polymer design that could go toward further enhancements. While the stability of the hydrogenated membrane was improved compared to its PCOE-based precursor and surpasses the stability of FAS-50, a clear weakness in the material is highlighted by its rapid degradation in comparison to other high performing membranes with alkaline stability surpassing 1,000 h [264]. For this reason we further investigated the degradation using FTIR and NMR studies.

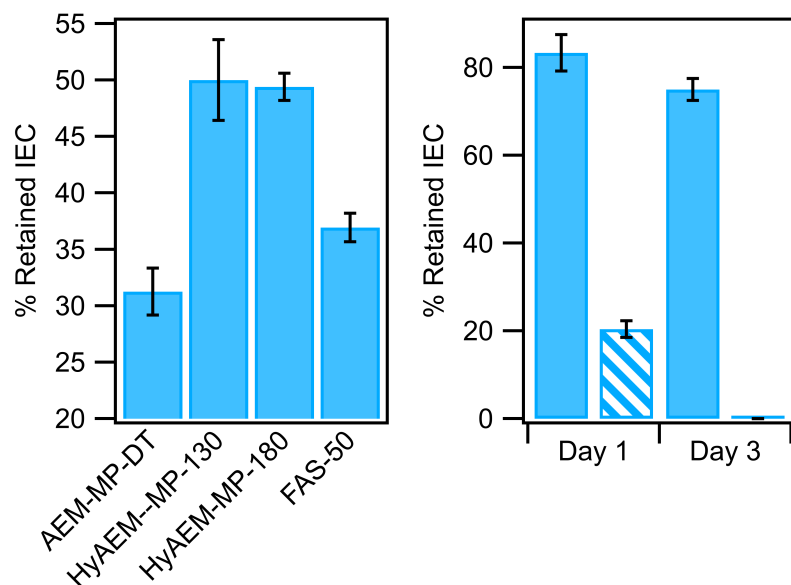


Figure 2.20 Left: IEC stability in terms of % of IEC retained after soaking in 9 M KOH at room temperature for 1 week. PCOE and PE-based AEMs compared to a commercial standard, Fumasep FAS-50. Right: IEC stability after soaking in 1 M KOH at 80°C for 1 or 3 days, comparing HyAEM-MP-180 (solid bar) to the commercial standard (cross hatch bar).

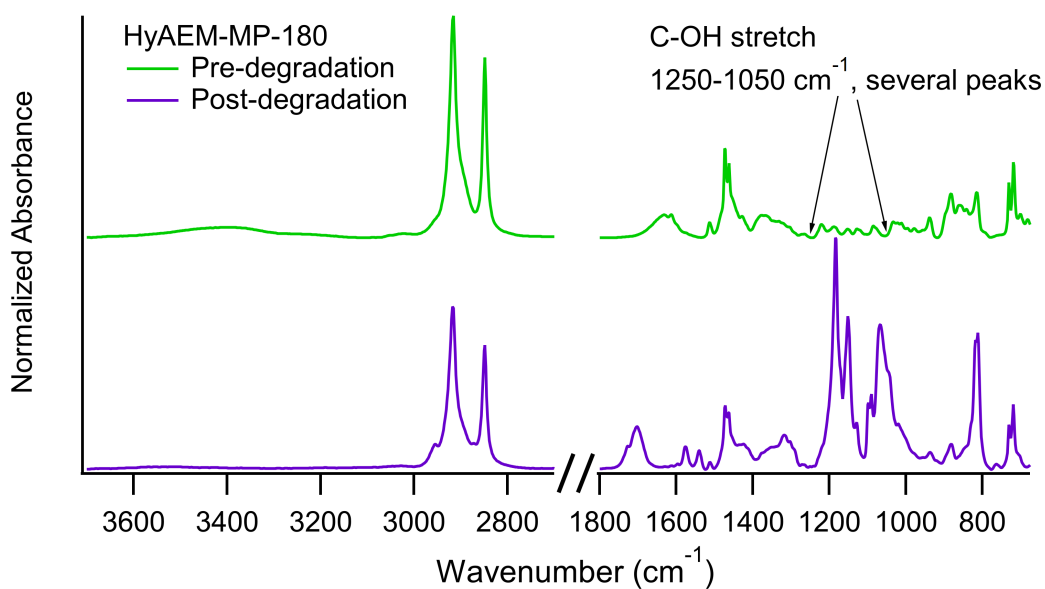


Figure 2.21 FTIR results for HyAEM-MP-180 before and after degradation in 9 M KOH.



For these studies, HyAEM-MP-180 was again soaked in 9 M KOH for 1 week at RT. The membrane was characterized by FTIR before and after degradation. For  $^1\text{H}$  NMR studies, the KOH solution was partitioned against  $\text{CDCl}_3$  to extract the small molecule degradation products. The results from FTIR and  $^1\text{H}$  NMR are given in Figure 2.21 and Figure 2.22, respectively. In the FTIR spectra, absorption bands in the C-OH stretching region appear after degradation. Additionally, the blueshift of the C=C stretching bands at  $1800 - 1600\text{ cm}^{-1}$  after degradation indicate the formation of alkenes. Additionally, from  $^1\text{H}$  NMR, MPRD was detected in the KOH solution after degradation. Therefore, four potential degradation pathways of HyAEM-MP-180 under alkaline conditions are proposed in Figure 2.23, including  $\alpha$ -nucleophilic substitution and  $\beta$ -elimination.

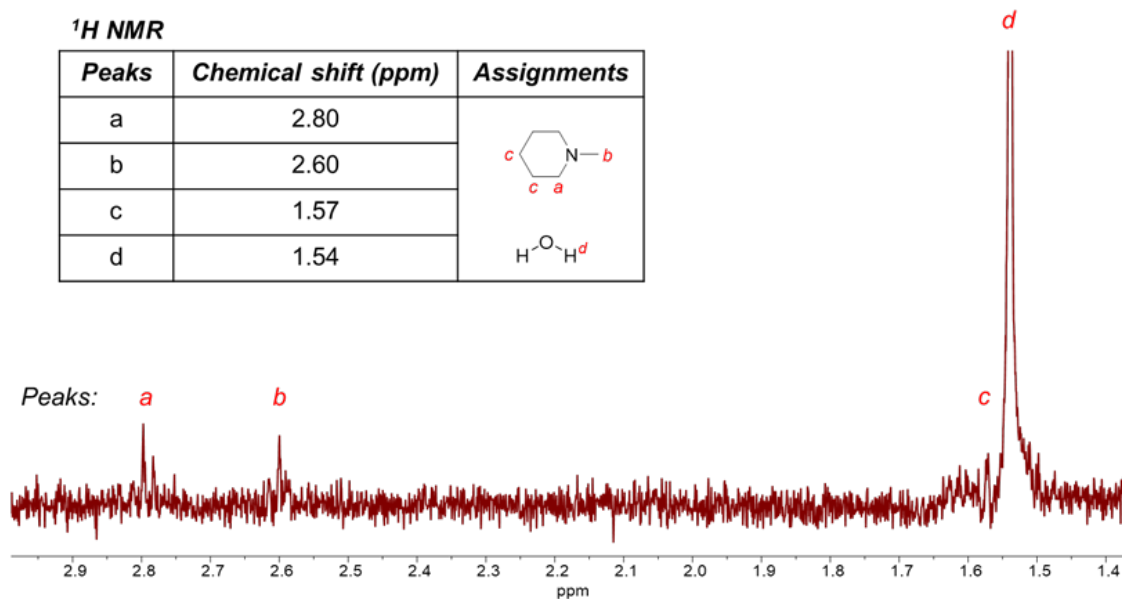


Figure 2.22  $^1\text{H}$  NMR and assignments for the small molecule degradation product of HyAEM-MP-180 in 9 M KOH.

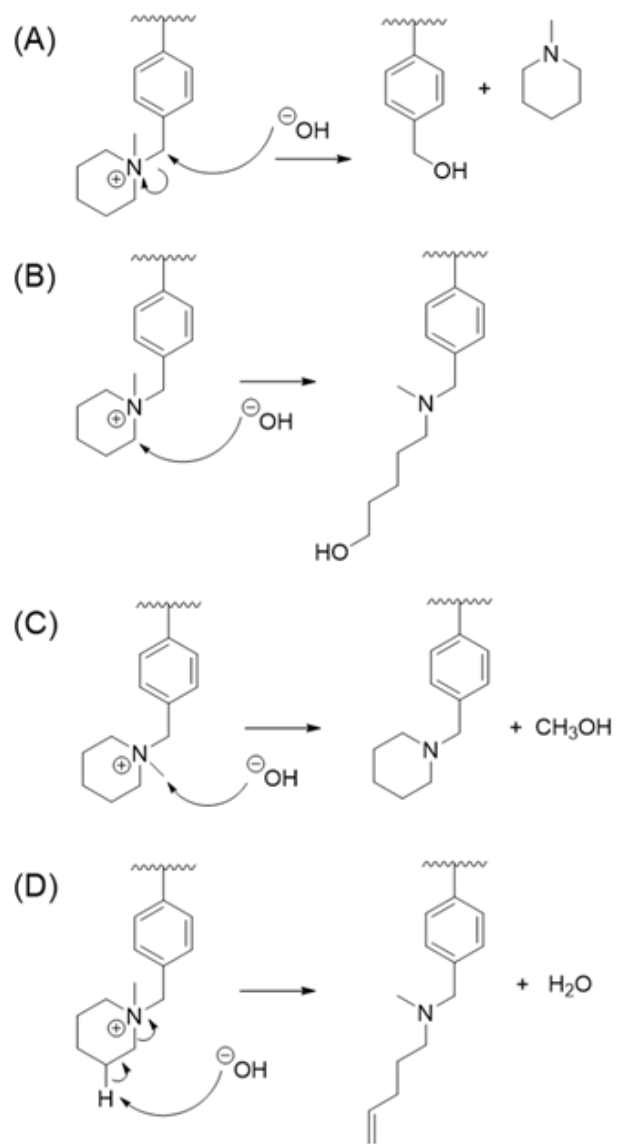


Figure 2.23 Possible degradation pathways of HyAEM-MP-180 in 9 M KOH.

## 2.6 Conclusions

A polyethylene-based triblock copolymer, PCMS-*b*-PE-*b*-PCMS, was prepared by hydrogenation of PCMS-*b*-PCOE-*b*-PCMS. Anion exchange membranes were fabricated via hot-pressing at two different temperatures and then quaternizing the films with either TMA or MPRD cations. Evidence from both TGA and elemental analysis suggests that lower water uptake and dimensional swelling achieved by processing films at 180 °C is most likely due to a small loss of Cl from crosslinking the PCMS blocks via chloride scission. Excellent Cl<sup>-</sup> and OH<sup>-</sup> conductivities ( $\sigma_{OH^-} = 179 \text{ mS cm}^{-1}$  at 80 °C and 95% RH) with low activation energies and no evidence of VTF behavior were observed, likely due to complete solvation and dissociation of the anionic species. Extensional testing performed on dry and wet films also yielded promising results, including improved strength upon hydration. This along with crystal domain size data from WAXS suggests an interesting phenomenon, where it is possible that water increased the interfacial mobility of polymer chains and facilitated the rearrangement of the PE midblock to form larger crystalline domains and improve the overall stress at break. While the chemical stability still improved with these modifications, it is still unsatisfactory for highly alkaline applications. Further modifications to the backbone will be investigated in future work.

The resulting AEMs displayed desirable characteristics that surpassed those of the original PCOE-based triblock. We have shown that using a triblock copolymer system allows for the exploration of various tunable parameters, including chemically crosslinking the hydrophilic phase and modifying the crystallinity of the hydrophobic phase, which can be optimized to simultaneously achieve a high OH<sup>-</sup> conductivity with moderate water uptake. Importantly, these results point toward methods of improving mechanical stability in fully hydrated conditions by incorporating a semi-crystalline hydrophobic backbone, design criteria which are paramount for applications such as electrolyzers, redox flow batteries, and water purification systems. In future work, we hope to improve the processing of these films by investigating melt extrusion processes, which are typically performed in a temperature range of 170 – 180 °C [265], where we hope to achieve the necessary amount of chemical crosslinking, retain a higher degree of crystallinity in the backbone, and produce thinner films.

CHAPTER 3  
INVESTIGATING SILVER NANOPARTICLE INTERACTIONS WITH QUATERNARY  
AMMONIUM FUNCTIONALIZED TRIBLOCK COPOLYMERS AND THEIR  
EFFECT ON MIDBLOCK CRYSTALLINITY

This chapter is modified from a journal article published in ACS Applied Polymer Materials.<sup>10</sup>  
Nora C. Buggy,<sup>11</sup> Yifeng Du,<sup>12</sup> Mei-Chen Kuo,<sup>13</sup> Ryan J. Gasvoda,<sup>14</sup> Soenke Seifert,<sup>15</sup> Sumit  
Agarwal,<sup>16</sup> E. Bryan Coughlin,<sup>17</sup> and Andrew M. Herring<sup>18</sup>

### 3.1 Motivation

It is known that interactions between ionomers and catalysts affect structures that form in the electrode, further affecting electrochemical device performance. The first step in elucidating the structure-property-performance relationship of ionomers in the catalyst layer was to understand the interactions occurring between ionomers and silver particles, the catalyst of interest in this thesis. This study explores *Hypothesis 2* by identifying interactions between silver nanoparticles (AgNPs) and the triblock copolymer precursor PCMS-*b*-PCOE-*b*-PCMS and polymer electrolytes PCMS-*b*-PCOE-*b*-PCMS[TMA<sup>+</sup>]Cl<sup>-</sup> and PCMS-*b*-PCOE-*b*-PCMS[MPRD<sup>+</sup>]Cl<sup>-</sup>. This set of materials was selected to decouple interactions between AgNPs and the block copolymer backbone from interactions with the quaternary ammonium cationic moieties.

### 3.2 Abstract

Interactions between silver nanoparticles and a cationic triblock copolymer significantly alter bulk material properties and can be tuned by functionalizing the polymer with different quaternary ammonium cations (QACs). In this work,

---

<sup>10</sup>Reprinted with permission of ACS Applied Polymer Materials, 2020, DOI: 10.1021/acsapm.0c00819

<sup>11</sup>Primary researcher and author

<sup>12</sup>Co-author, polymer chemist

<sup>13</sup>Co-author, polymer chemist

<sup>14</sup>Co-author, X-ray photoelectron spectroscopy

<sup>15</sup>Co-author, X-ray scattering expert and beamline scientist

<sup>16</sup>Co-author, X-ray photoelectron spectroscopy

<sup>17</sup>Co-author, polymer expert

<sup>18</sup>Co-author, advisor and corresponding author

polychloromethylstyrene-*b*-polycyclooctene-*b*-polychloromethylstyrene (PCMS-*b*-PCOE-*b*-PCMS) was quaternized with either benzylmethylpiperidinium (MPRD) or benzyltrimethylammonium (TMA). The surface interacting groups were identified using FTIR to be the phenyl rings, the QACs from the outer blocks, and vinyl groups from the PCOE midblock. Changes in thermal characteristics and crystallinity were highly dependent on the QAC, uncovering differences in the nature of the interactions between silver and TMA or MPRD. Interactions induced by TMA greatly hinder crystalline domain formation and give rise to a higher water content, while MPRD promotes certain crystalline orientations and provides a greater degree of crystallinity with a lower water content. Our findings demonstrate that bulk polymer characteristics can be tuned, a highly desirable attribute for many nanocomposite materials.

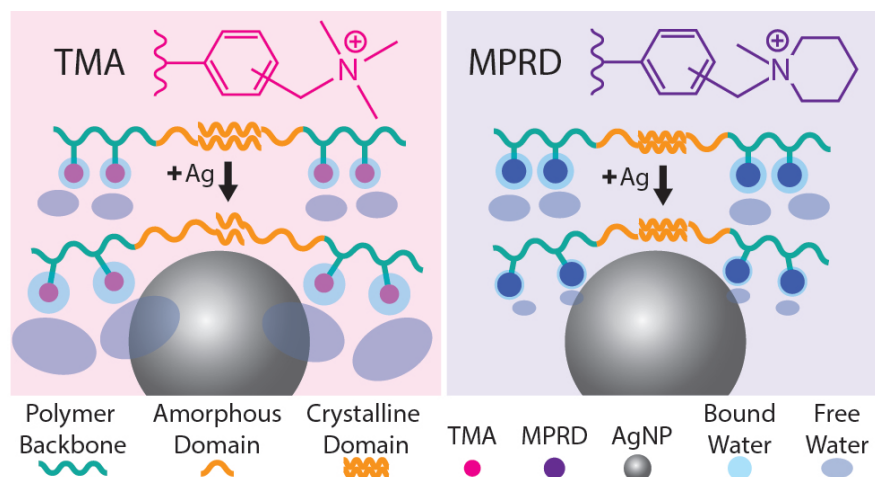


Figure 3.1 Graphical abstract.

### 3.3 Introduction

Polymer-metal nanocomposites are a growing field of materials with potential as semiconductors, high-strength materials, flexible electronics, catalysts and electrocatalysts, sensors, biocompatible materials, and in additive manufacturing applications [266–272]. Specifically, understanding the adsorption of polymers onto metal surfaces is important in adhesive bonding, corrosion protection, and colloid stabilization [273–275]. Silver nanoparticles (AgNPs) and nanocomposites, in particular, have optical and electronic properties that have led to their development for applications in catalysis, electronics, sensing, and as antimicrobial

materials [276–280]. In these systems, interactions between metal particles and the host polymer matrix ultimately dictate the structural and characteristic behaviors of the composite [281]. A fundamental understanding of interactions between polymer molecules and metal surfaces or particles and knowledge of exact interacting sites on the host polymer can provide valuable insights on design principles for polymer-metal composite materials with desired properties.

Composite materials of ion exchange polymers and electroactive metal particles are also of interest for electrochemical device applications. Interactions between metal particles and the ion exchange polymer can affect intrinsic properties such as crystallinity and morphology, which in turn influence the mechanical properties, transport of ionic species, water content, and diffusion of reactant and product gases [282–284]. Studies focused on Pt-based catalysts in both alkaline [123, 124] and acidic [196, 199, 285] systems have demonstrated the importance of identifying and minimizing polymer-catalyst interactions to mitigate polymer adsorption to the catalyst surface and improve performance. A few studies have focused on other catalyst surfaces, such as Au [187, 196, 198] and Ag [200]. Silver is of particular interest for use in alkaline systems, as silver can have oxygen reduction reaction capabilities comparable to Pt at a significantly reduced expense [151, 152]. Despite this, there has been limited investigation of electrochemical reactions on silver [286, 287] or implementing silver in operating electrochemical devices [112, 162, 288]. Literature specifically on interactions between silver and cationic polymers is also sparse.

In this study, specific interactions between AgNPs and cationic polymers are identified along with their significant effects on bulk material characteristics. This work utilizes our previously reported ABA triblock copolymer, polychloromethylstyrene-*b*-polycyclooctene-*b*-polychloromethylstyrene (PCMS-*b*-PCOE-*b*-PCMS) [58, 238]. Interactions between AgNPs and the unquaternized polymer backbone, as well as the quaternized polymers bearing two different quaternary ammonium cations (QACs), benzylmethylpiperidinium (MPRD) and benzyltrimethylammonium (TMA), are investigated. To study changes in bulk characteristics of the polymers, approximately 10 wt% Ag nanopowder (20–40 nm diameter) was added to unquaternized polymer or quaternized ionomer solutions and cast into films. Insights into the thermal behavior, crystallinity, and the potential nature of these interactions based on FTIR studies are presented.

## 3.4 Experimental Methods

### 3.4.1 Materials

The base copolymer PCMS-*b*-PCOE-*b*-PCMS was synthesized and quaternized according to the procedure published previously [238]. Silver nanopowder was purchased from Alfa Aesar (45509, average particle size 20–40 nm, 99.9% metal basis) and used as received.

### 3.4.2 Polymer and Ag-Polymer Composite Sample Fabrication

The base copolymer PCMS-*b*-PCOE-*b*-PCMS along with the quaternized ionomers were all soluble in CHCl<sub>3</sub>. The base copolymer or quaternized ionomer was dissolved in CHCl<sub>3</sub> at RT and solvent cast on a Teflon<sup>®</sup> sheet and covered with a watch glass to slow the evaporation of CHCl<sub>3</sub>. This method produced uniform 45–50 μm-thick films. Silver-polymer composite samples were produced by sonicating the polymer or ionomer chcl<sub>3</sub> solution with 10 wt% silver nanoparticles (20–40 nm average particle size) and solvent cast by an identical method.

### 3.4.3 Fourier-Transform Infrared Spectroscopy

Fourier-transform infrared spectroscopy (FTIR) measurements were collected using a Thermo Fisher Scientific Nicolet iN10 infrared microscope with a Germanium attenuated total reflectance (ATR) tip. IR spectra was collected in the range of 4000–650 cm<sup>-1</sup> using the highest resolution settings for all scans. Samples were dried under vacuum prior to measurements. Only “as-cast” samples were measured.

### 3.4.4 Thermal Characterization and Crystallization Kinetics

Thermogravimetric analysis (TGA) was performed using a TA Instruments TGA Q 500. A 2 mg sample was placed on a platinum pan. A heating rate of 10 °C min<sup>-1</sup> up to 800 °C with an air flow rate of 20 mL min<sup>-1</sup> was used. The onset of degradation was calculated using TA Universal Analysis software and is defined as the intersection of the initial tangent line with the final tangent line, where initial and final points are selected before and after the degradation peak. Differential scanning calorimetry (DSC) was performed using a TA instruments Q20 DSC. 5–10 mg of polymer was loaded in hermetically sealed Tzero aluminum pans and the change in heat flow was measured over a temperature range of 0–100 °C with a heating and cooling rate of 10 °C

min<sup>-1</sup>. Each sample was cycled over the temperature range four times. The results from the 2<sup>nd</sup>–4<sup>th</sup> cycles were identical. TA Universal Analysis software was used to determine  $X(t)$ , the relative crystallinity in terms of time, by integrating the crystallization exotherm from the 2<sup>nd</sup> cooling cycle. Crystallization kinetics can be modeled using the Avrami equation [289]:

$$X(t) = 1 - \exp(-kt^n) \quad (3.1)$$

Where  $n$  is the Avrami exponent and  $k$  is the rate parameter. For non-isothermal crystallization kinetics, a Jeziorny-modified Avrami approach [290] can be used to characterize the rate parameter, given by:

$$X(t) = 1 - \exp(-Z_t t^n) \quad (3.2)$$

$$\log Z_c = \log \frac{Z_t}{\lambda} \quad (3.3)$$

A Jeziorny plot of  $\log \{-\ln [1 - X(t)]\}$  versus  $\log(t)$  was used to determine the Avrami exponent and rate parameter from the slope and intercept, respectively, of the linear region, typically from  $X(t) = 0.2$ – $0.8$ .

### 3.4.5 X-ray Scattering

Small-angle X-ray scattering (SAXS) and wide-angle X-ray scattering (WAXS) were performed at the Basic Energy Sciences Synchrotron Radiation Center (BESSRC) at the Advanced Photon Source at Argonne National Lab on beamline 12 ID-B. 2D SAXS and WAXS were performed simultaneously using a Pilatus 2M detector and a Pilatus 300k detector to collect small angle scattering data wide angle scattering data, respectively. Experiments were performed with an exposure time of 0.5 s. The X-ray beam had a wavelength of 1 Å and energy of 13 keV. The intensity ( $I$ ) was radially integrated from the 2D scattering image with respect to the scattering vector ( $q$ ). Both SAXS and WAXS experiments were performed on as-cast polymer or polymer-silver composite samples at ambient conditions.

### 3.4.6 X-ray Photoelectron Spectroscopy

Laboratory based UHV-XPS was performed on a HiPP III Scienta Omicron photoelectron spectrometer operating in swift mode using monochromatic Al K $\alpha$  X-rays at 150 W focused to a 500  $\mu\text{m}$  spot size. The pass energy and analyzer slit width were 500 eV and 4 mm for surveys,



and 200 eV and 1.5 mm for the core level scans. The aperture on the on the analyzer entrance was fixed at 800  $\mu\text{m}$  for all scans. For the survey scans, intensity was measured every 1 eV and every 0.1 eV for the core level scans. The AgNPs were mounted on double sided carbon tape and introduced to the analysis chamber via a fast entry loadlock. All analysis was performed using CasaXPS. The Ag 3d region was fitted using a Shirley background and asymmetric line shapes.

### 3.4.7 NMR Characterization

$^1\text{H}$  NMR spectroscopy was performed in 5mm diameter tubes in deuterated chloroform ( $\text{CDCl}_3$ ) at 25  $^\circ\text{C}$  on a Bruker 500 spectrometer at 500 MHz.

### 3.4.8 Gel Permeation Chromatography

Gel permeation chromatography (GPC) was performed in THF at a flow rate of 1.0  $\text{mL min}^{-1}$  at 40  $^\circ\text{C}$ , using a refractive index detector on a Polymer Laboratories PL-GPC 50 Integrated GPC system.

## 3.5 Results and Discussion

To elucidate interactions between the silver surface and the polymer backbone and cationic moieties, the unquaternized triblock copolymer backbone (TB), in addition to the triblock functionalized with TMA (TB-TM) or MPRD (TB-MP), were studied to decouple interactions occurring with the backbone from those with the QACs. TMA is the most frequently reported QAC known for its ease of synthesis and lack of  $\beta$ -hydrogens [291], while MPRD has a bulkier cyclic structure and has shown greater stability and anionic conductivity than TMA [58, 85, 214, 292]. TB, the base copolymer PCMS-*b*-PCOE-*b*-PCMS, was synthesized [58, 238] and characterized with gel permeation chromatography (GPC) and  $^1\text{H}$  NMR spectroscopy.

Table 3.1 Chemical Composition of PCMS-*b*-PCOE-*b*-PCMS base copolymer

PCOE				PCMS- <i>b</i> -PCOE- <i>b</i> -PCMS			
$M_n^a$ (kg mol $^{-1}$ )	$M_w^a$ (kg mol $^{-1}$ )	PDI $^a$	DP $^b$	$M_n^a$ (kg mol $^{-1}$ )	$M_w^a$ (kg mol $^{-1}$ )	PDI $^a$	DP $^b$
89	150	1.67	650	120	200	1.68	320

$^a$ Measured by GPC calibrated against polystyrene standards.

$^b$ Measured by  $^1\text{H}$  NMR end-group analysis.

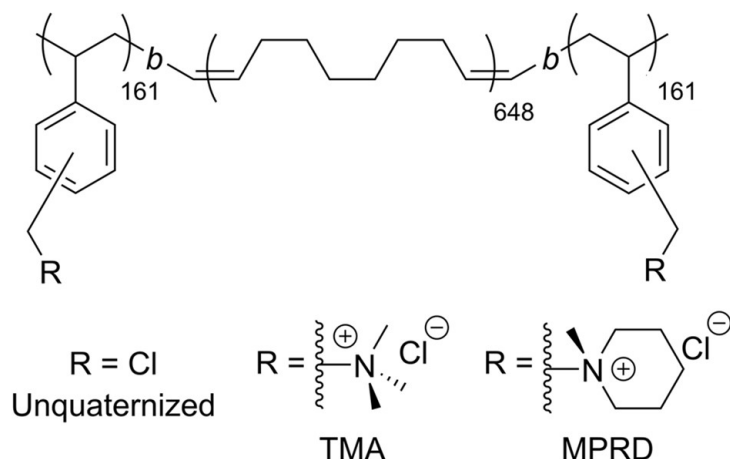


Figure 3.2 Structure of triblock copolymer PCMS-*b*-PCOE-*b*-PCMS, shown quaternized with either TMA or MPRD.

The chemical composition analysis results are summarized in Table 3.1. The degree of polymerization ratio of the PCOE midblock versus the two PCMS outer blocks is approximately 2:1. TB was then quaternized with either TMA or MPRD, giving TB-TM and TB-MP, respectively. The chemical structures of the base copolymer and quaternized ionomers are shown in Figure 3.2. The base copolymer and quaternized ionomers were dissolved in chloroform and solvent cast to produce uniform 45–50  $\mu\text{m}$ -thick films. Silver composite samples were fabricated by sonicating the polymer solution with 10 wt% silver nanoparticles (20–40 nm diameter) and solvent cast by an identical method. The pure polymer samples were characterized using small angle X-ray scattering (SAXS) (Figure 3.3) to analyze their morphology and interdomain spacing ( $d_s$ ). The unquaternized TB film displayed a distinct primary  $q^*$  scattering peak and higher-order peaks at  $2q$  and  $3q$ , indicating a well phase separated lamellar morphology with  $d_s = \sim 80$  nm. For the quaternized polymers, TB-MP and TB-TM, the broad scattering peaks indicate the morphology was maintained, but the specific well-ordered morphology and grain orientation of the original triblock backbone was lowered after quaternization. The polymer morphology change after quaternization can be attributed to synergistic effects from the shifted Flory–Huggins interaction parameters, the electrostatic interactions, and steric hindrance from the bulky QACs ultimately leading to a loss in order across the full length-scale which SAXS measures [293–295].

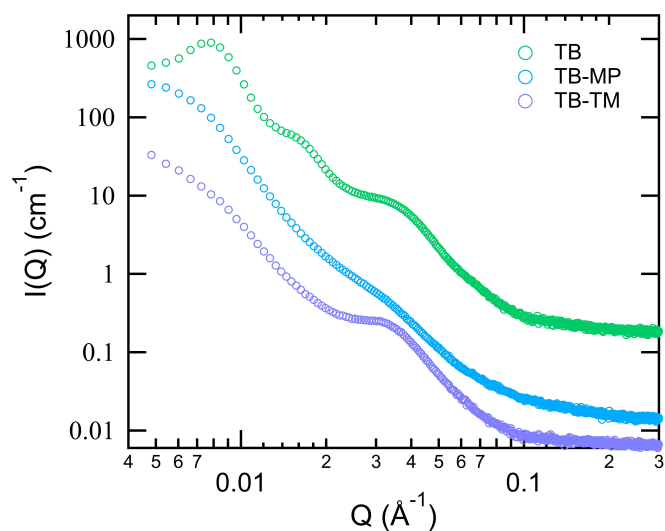


Figure 3.3 Small-angle X-ray scattering of TB, TB-MP, and TB-TM at dry, ambient conditions. Spectra are offset for clarity.

Changes in vibrational frequencies of the polymers occurring as a result of strong interactions with silver surfaces were probed using FTIR ATR spectroscopy (Figure 3.4). The spectrum of the triblock copolymer backbone was cross-referenced with spectra of the quaternized triblock copolymers and previous DFT studies to aid in peak assignments [259, 296]. The results are summarized in Table 3.2. Differences were further highlighted by subtracting the spectra of the pure polymer samples from the silver composite samples, shown in the top insets of Figure 3.4. This emphasizes changes in absorbance which relate to shifts in polymer chain segment conformations and chain segment packing, which ultimately highlights shifts in crystalline and amorphous content [297–300]. The peak assignments which increase or decrease in the presence of AgNPs cannot be correlated to specific polymer conformations, as there is no previous work related to this for either PCMS or PCOE this would require a separate study. Surprisingly, the TB-Ag composite did not show discernable changes in its IR spectrum, indicating very few or weak interactions between the triblock copolymer and AgNPs. In this case, potential interactions were initially hypothesized based on previous studies to occur between AgNPs and the C=C found in the PCOE midblock or with C=C found in benzyl chloride groups in the PCMS outer blocks [301, 302], however no evidence of this was observed in FTIR.

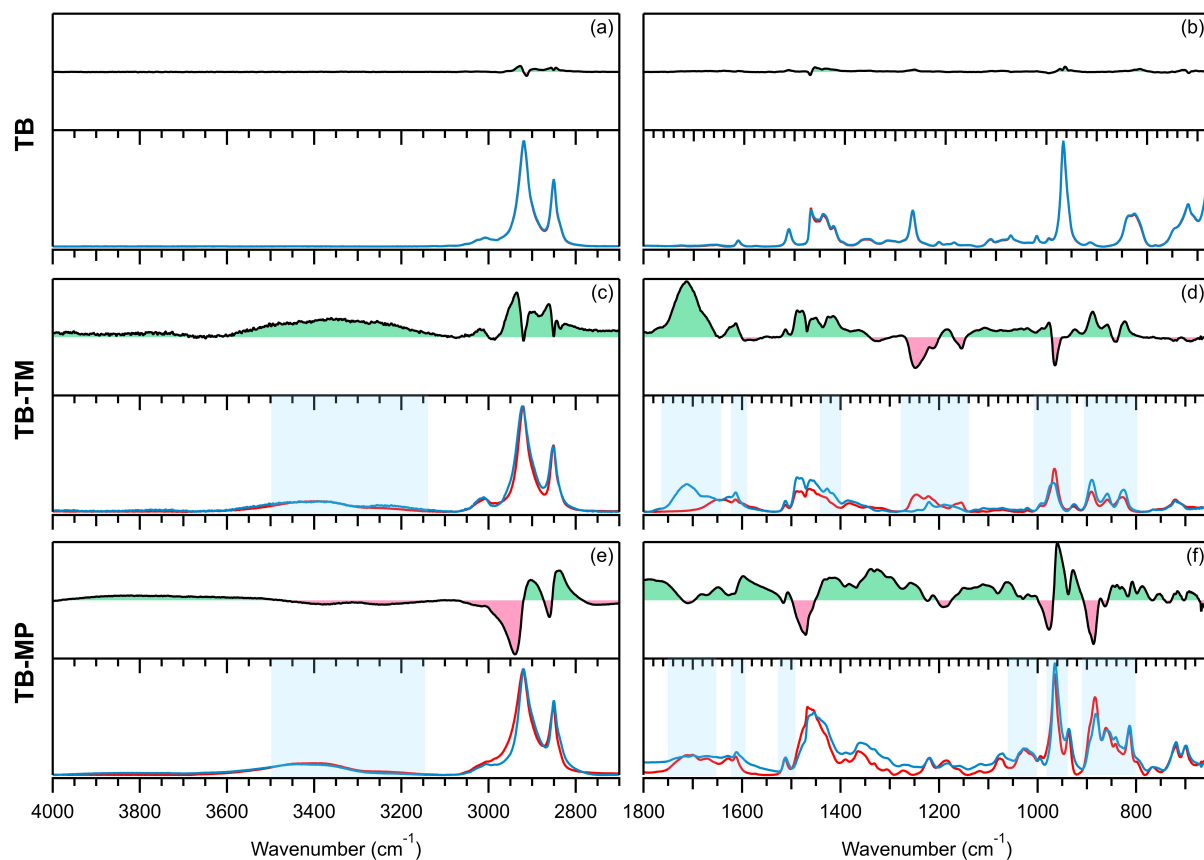


Figure 3.4 Normalized FT-IR ATR spectra are given in the bottom inset of each figure for TB (a,b), TB-TM (c,d), and TB-MP (e,f) with pure polymer samples shown by red lines and silver-polymer composites shown by blue lines. Regions of interest,  $4000\text{--}2700\text{ cm}^{-1}$  (a,c,e) and  $1800\text{--}650\text{ cm}^{-1}$  (b,d,f) are shown for clarity. In the top inset of each figure, the IR intensity differences are calculated by subtracting the spectra of the pure polymer samples from those of the silver composites. Areas where the silver composites had a higher intensity are filled in green, and lower intensity are filled in red. All axes are set to same scale for comparison.

Table 3.2 FT-IR ATR Vibrational Mode Assignments and Observations from AgNP Interactions

Sample	Wavenumber (cm <sup>-1</sup> )	Change Observed from Ag Interactions	Approximate Assignment	Reference
TB-TM	3400	Increased intensity	$\nu_b(\text{H}_2\text{O})$	[296]
	3250	Emergence	$\nu_s(\text{H}_2\text{O})$	[296]
	3005	Shifts higher and increased intensity	$\nu(\text{N}^+-\text{CH}_3)$	[259]
	1710	Emergence	$\delta_b(\text{H}_2\text{O})$	[296]
	1670	Emergence	$\delta_s(\text{H}_2\text{O})$	[296]
	1610	Increased intensity	$\nu_{ph}(\text{C}=\text{C})$	[303, 304]
	1480, 1460, 1430	Increased intensity	$\nu_{ph}(\text{C}=\text{C})$ or $\nu_{pcoe}(\text{C}=\text{C})$	[305]
	1250	Decreased intensity	$\nu(\text{H}_3\text{C}-\text{N}^+-\text{CH}_2)$	[259]
	1160	Shifts higher	$\delta_{link}(\text{C}-\text{H})$	[259]
	980	Decreased intensity	$\delta_{pcoe}(\text{C}=\text{C})$	[303]
893, 860, 829	Increased intensity	$\delta(\text{N}^+-\text{CH}_3)$	[304, 306]	
TB-MP	3410	Decreased intensity	$\nu_b(\text{H}_2\text{O})$	[296]
	3210	Decreased intensity	$\nu_s(\text{H}_2\text{O})$	[296]
	1710	Disappear entirely	$\delta_b(\text{H}_2\text{O})$	[296]
	1670	Disappear entirely	$\delta_s(\text{H}_2\text{O})$	[296]
	1610	Increased intensity	$\nu_{ph}(\text{C}=\text{C})$	[304]
	1500-1440	Decreased intensity	$\nu_{ph}(\text{C}=\text{C})$ or $\nu_{pcoe}(\text{C}=\text{C})$	[305]
	980	Increased intensity	$\delta_{pcoe}(\text{C}=\text{C})$	[303]
	883, 860	Decreased intensity	$\delta(\text{N}^+-\text{CH}_3)$ or $\delta(\text{N}^+-\text{CH}_2)$	[102]
842, 817	Increased intensity	$\delta(\text{N}^+-\text{CH}_3)$ or $\delta(\text{N}^+-\text{CH}_2)$	[102]	

*b*: bulk water, *s*: bound water in solvation shell, *ph*: phenyl ring, *pcoe*: polycyclooctene, *link*: link between phenyl group and main backbone.

For the quaternized polymers, observations indicate that once AgNPs are introduced, the stretching and bending modes associated with water domains, phenyl rings, and QACs are influenced in different ways depending on the cationic species. Changes in absorbance of many peaks are also observed and summarized in Table 3.2, indicating possible shifts in crystalline content, polymer morphology and conformation. These results demonstrate that the QACs are interacting with the silver particles, and this in turn affects both the water content and the solvation shell surrounding the QAC, in addition to the mobility of the side chain and phenyl ring. In TB-TM, Ag interactions lead to an increase in bulk water aggregates in the membrane and bound water forming the solvation shell of the TMA moiety and appear to constrain the mobility of the phenyl ring-TMA linkage as well as the phenyl ring-backbone linkage [259]. Vibrational modes associated with  $\nu(\text{C}=\text{C})$  from the phenyl rings and those from the TMA groups increase in intensity, while aliphatic  $\delta(\text{C}=\text{C})$  from PCOE decreases. Additionally, there is a blueshift of  $\nu(\text{N}^+-\text{CH}_3)$  at  $3005\text{ cm}^{-1}$  and of  $\delta(\text{C}-\text{H})$  at  $1160\text{ cm}^{-1}$  from the TMA moieties and link between the phenyl group and main backbone respectively, indicating a shortening of these bond distances.

In TB-MP, we observe an interesting contrast, where there is a decrease in bulk and bound water content. Additionally, an increase in intensity from aliphatic  $\delta(\text{C}=\text{C})$ , and a mix of increasing and decreasing intensities from MPRD  $\delta(\text{C}-\text{N}^+)$  are observed. Similarities include an increase in  $\nu(\text{C}=\text{C})$  from the phenyl rings. These findings are in agreement with previous work using surface-enhanced Raman spectroscopy and molecular modeling, which have shown aliphatic amines, alkenes, and phenyl rings can all absorb to silver surfaces [307–309]. In contrast to TB-TM, no significant shifts in peak wavenumbers are observed in TB-MP, indicating interactions between AgNPs and TB-MP were weaker in comparison.

Additional experiments further confirm that the nature of the interactions between AgNPs and TMA or MPRD differ significantly and that the PCOE C=C bonds play a role in these interactions. The different QACs led to significant changes in bulk properties, based on further evidence from thermal characteristics, crystallinity, and microstructure of the pure polymers and their silver composites. Thermal characterization was performed using thermal gravimetric analysis (TGA) (Figure 3.5) and differential scanning calorimetry (DSC) (Figure 3.6) to identify changes in the onset of thermal degradation and crystallinity as a result of interactions with AgNPs.

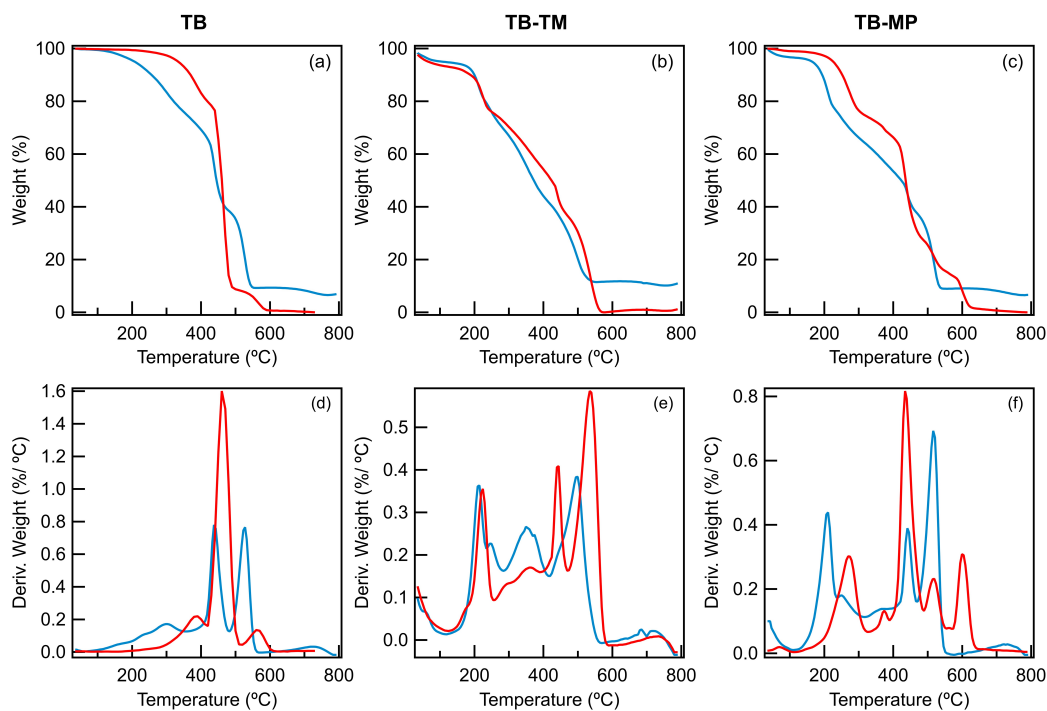


Figure 3.5 TGA curves (a-c) and derivative weight plots (d-f) for TB (a,d), TB-TM (b,e), and TB-MP (c,f). Pure polymer samples are shown by red lines and silver-polymer composites are shown by blue lines.

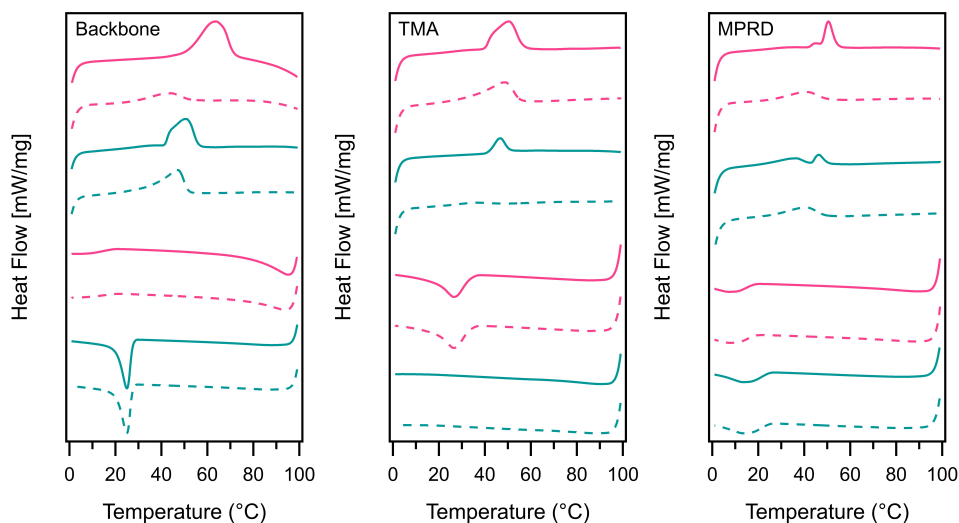


Figure 3.6 Stacked DSC heating (top) and cooling (bottom) traces for TB (left), TB-TM (middle), and TB-MP (right). 10°C/min heating and cooling rate. Red traces refer to the pure polymer sample and blue traces refer to the polymer cast with 10 wt% silver. Solid lines represent the 1st heating/cooling cycle, and dotted lines represent the 2<sup>nd</sup>–4<sup>th</sup> scans which were identical in all cases. Traces are offset for clarity.

From TGA, the weight % of silver that has been introduced was verified to be *ca.* 10 wt% (9.3, 10.2, and 9.1 wt% for TB, TB-TM and TB-MP respectively) based on residual mass measurements. In TB, the introduction of silver causes thermal decomposition at a much lower temperature, shifting from an onset of 327 to 151 °C with a more prominent decomposition at 242 °C.

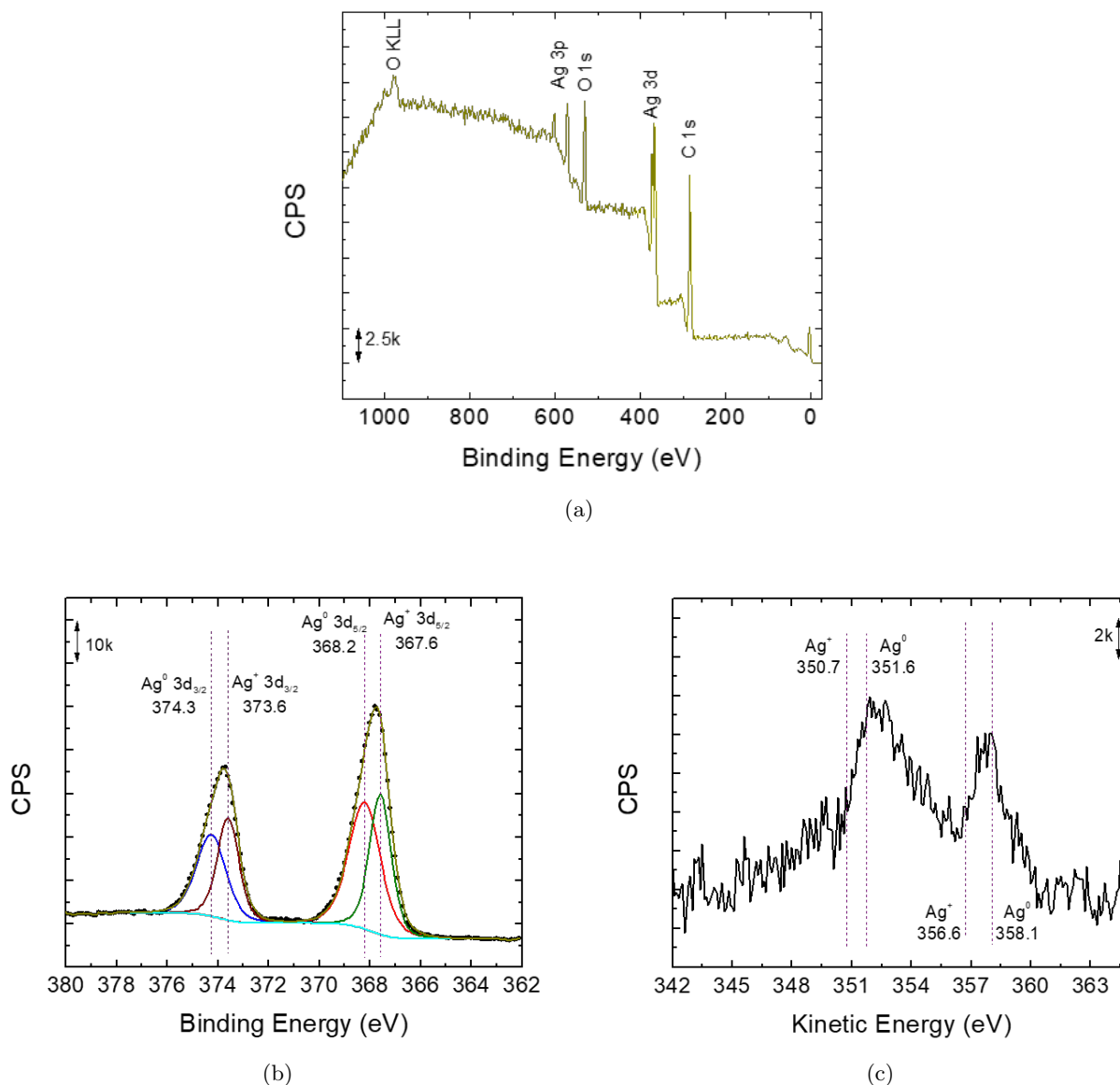


Figure 3.7 X-ray photoelectron spectroscopy of silver nanopowder, calibrated at 284.8 eV and measured at 284.7 eV, including survey spectrum (a), Ag 3d (b) and Ag MNN (c). Fitting of the Ag 3d and Ag MNN peaks indicate partial oxidation of the silver nanoparticle surface [310, 311].



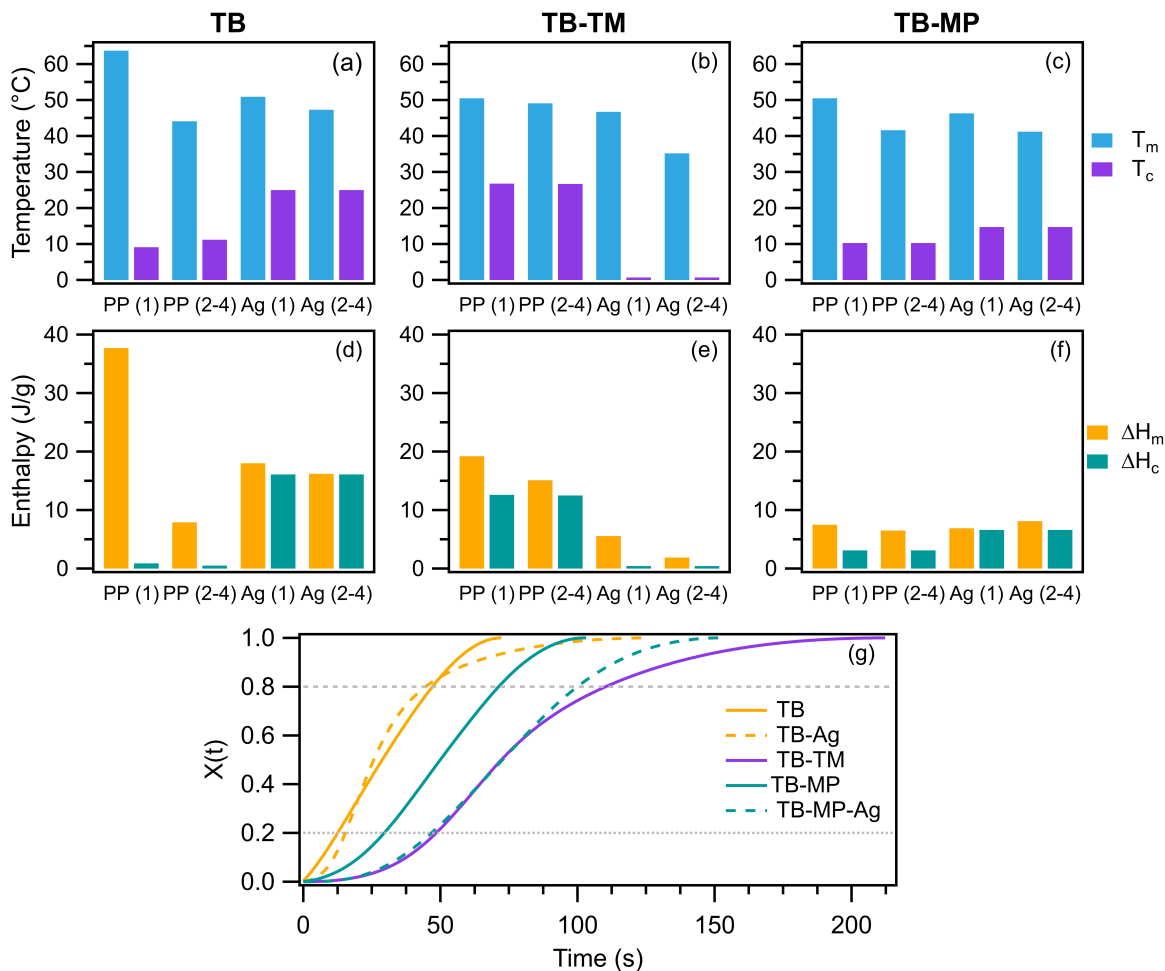


Figure 3.8 Thermal characteristics obtained from DSC scans for TB (a,d), TB-TM (b,e), and TB-MP (c,f). PP = pure polymer, Ag = silver-polymer composite. (1) refers to 1st DSC scan, (2–4) refers to 2<sup>nd</sup>–4<sup>th</sup> DSC scans, which were identical. Melting and crystallization temperatures are shown in (a-c), enthalpy of melting and crystallization shown in (d-f). The relative crystallized fraction  $X(t)$  versus time shown in (g).

The reduced decomposition temperature is most likely silver catalyzed oxidative decomposition. This first decomposition step is most likely due to the thermolysis, or scission, of benzyl chloride from the PCMS blocks [75]. The decomposition range of this first step also broadens, and two small shoulder-like features (near 167 and 230 °C) can be observed in the derivative thermal analysis on the slope to the first more prominent peak. This mass loss could in part be attributed to the decomposition of the silver oxide layer present on the AgNPs (observed using XPS, Figure 3.7), which decomposes near 200 °C [312]. The broadening of the

decomposition range and appearance of multiple features indicates mass transport may be limiting the catalytic degradation of benzyl chloride groups. Limitations in the mobility of the phenyl rings and polymer backbone, along with the polymer melt viscosity, may contribute to slower diffusion of the benzyl groups toward the silver surfaces to undergo catalytic decomposition. The next major decomposition occurs at 443 °C, coming from complete degradation of the PCOE midblock [313, 314]. This step is also shifted to a lower onset temperature of 427 °C for TB-Ag. The final mass loss between 500–600 °C is due to oxidative decomposition of the remaining polymer.

Shifts in the decomposition profile for TB-TM and TB-MP are noted as well. Previously, we have shown TMA is less thermally stable than MPRD [102], in agreement with the onset of degradation we observe for TB-TM (200 °C) and TB-MP (223 °C). With the incorporation of AgNPs, the onset of degradation shifts to lower temperatures of 192 and 177 °C for TB-TM and TB-MP, respectively. Interestingly, with the addition of silver, the MPRD cations become less thermally stable than the TMA cations, indicating the catalytic oxidative effect of silver is more detrimental to MPRD cations.

In the DSC curves, the main endothermic peak is the melting of the PCOE midblock, typically in the range of 60–70°C [315]. It is visually evident from these traces that interactions with silver surfaces induce shifts in melting point and changes in the extent of recrystallization. The melting and crystallization temperatures and enthalpies extracted from the heating and cooling curves are summarized in Figure 3.8.

It is important to decouple the analysis of the first thermal cycle from that of the second through fourth thermal cycles. The first cycle highlights differences that arise in the “as cast” state with identical thermal histories and solvent evaporation rates, while the subsequent cycles show how they compare after a melt/cool cycle. The stark differences in the thermal characteristics indicate the recrystallization of PCOE is affected not only by interactions with the silver particles, but also by the identity of the QAC. In the “as cast” state during the first thermal cycle,  $\Delta H_m$  for TB > TB-Ag, TB-TM > TB-TM-Ag, and TB-MP > TB-MP-Ag, corresponding to a degree of crystallinity decrease for samples containing AgNPs. Therefore, incorporating AgNPs significantly diminished PCOE crystallization during the solvent casting process. Regarding the effect from QAC identity,  $\Delta H_m$  for TB > TB-TM > TB-MP.

Quaternizing the triblock copolymer with TMA led to a decrease in the degree of crystallinity of 50%, and with MPRD a decrease of 80%.

Although the “as cast” crystallinity of TB is much higher than that of TB-Ag, after one thermal cycle TB is unable to recover the original crystallinity, while the TB-Ag sample maintains its initial crystallinity after thermal cycling. Additionally, TB-Ag exhibits a higher  $T_c$  than TB, indicating that AgNP surfaces are promoting crystallization at higher temperatures by initiating heterogeneous nucleation [316, 317], ultimately providing TB-Ag a higher degree of crystallinity than TB during the cooling cycle. The non-isothermal nucleation and growth kinetics were explored further using a Jeziorny-modified Avrami approach [290, 318]. In this approach, the crystallization exotherm from DSC is integrated with respect to time to determine the relative crystallized fraction,  $X(t)$ . No differences were observed between the crystallization exotherms of the first cycle compared to those of cycle 2–4 for each sample. The relative crystallized fraction  $X(t)$  versus time is shown in Figure 3.8 and Jeziorny plots are given in Figure 3.9. The Avrami exponent,  $n$ , relating to the dimension of crystal growth, and the rate parameters,  $\log Z_c$  and  $\log Z_t$ , were determined for each sample using linear regressions. The results are summarized in Table 3.3. From the Jeziorny plots for TB and TB-Ag, a two-stage crystallization mechanism is evident from the initial linear with AgNPs [319]. The crystallization half time,  $t_{\frac{1}{2}}$ , decreases with the addition of AgNPs, indicating the crystallization kinetics improve.  $Z_{t,TB-Ag}$  is also nearly 1.5 orders of magnitude larger than  $Z_{t,TB}$ , demonstrating that AgNPs can improve the rate of crystallization by serving as a surface for heterogeneous nucleation [316, 317]. Following the primary stage, both the rate and Avrami exponent decrease due to impingement effects limiting the final stages of crystal growth [317, 320].

For TB-TM, we observe nearly an opposite trend, where the pure polymer sample exhibits relatively stable melting points and crystallization enthalpies, and TB-TM-Ag has a significant melting point depression and loss of crystallinity. These results indicate the TMA groups are interacting with the AgNPs to a greater extent than the unquaternized benzyl chloride groups, and in this case completely suppressing the recrystallization of PCOE. While no crystallization exotherm was observed for TB-TM-Ag, the Jeziorny-modified Avrami analysis was still applied to the crystallization of TB-TM.

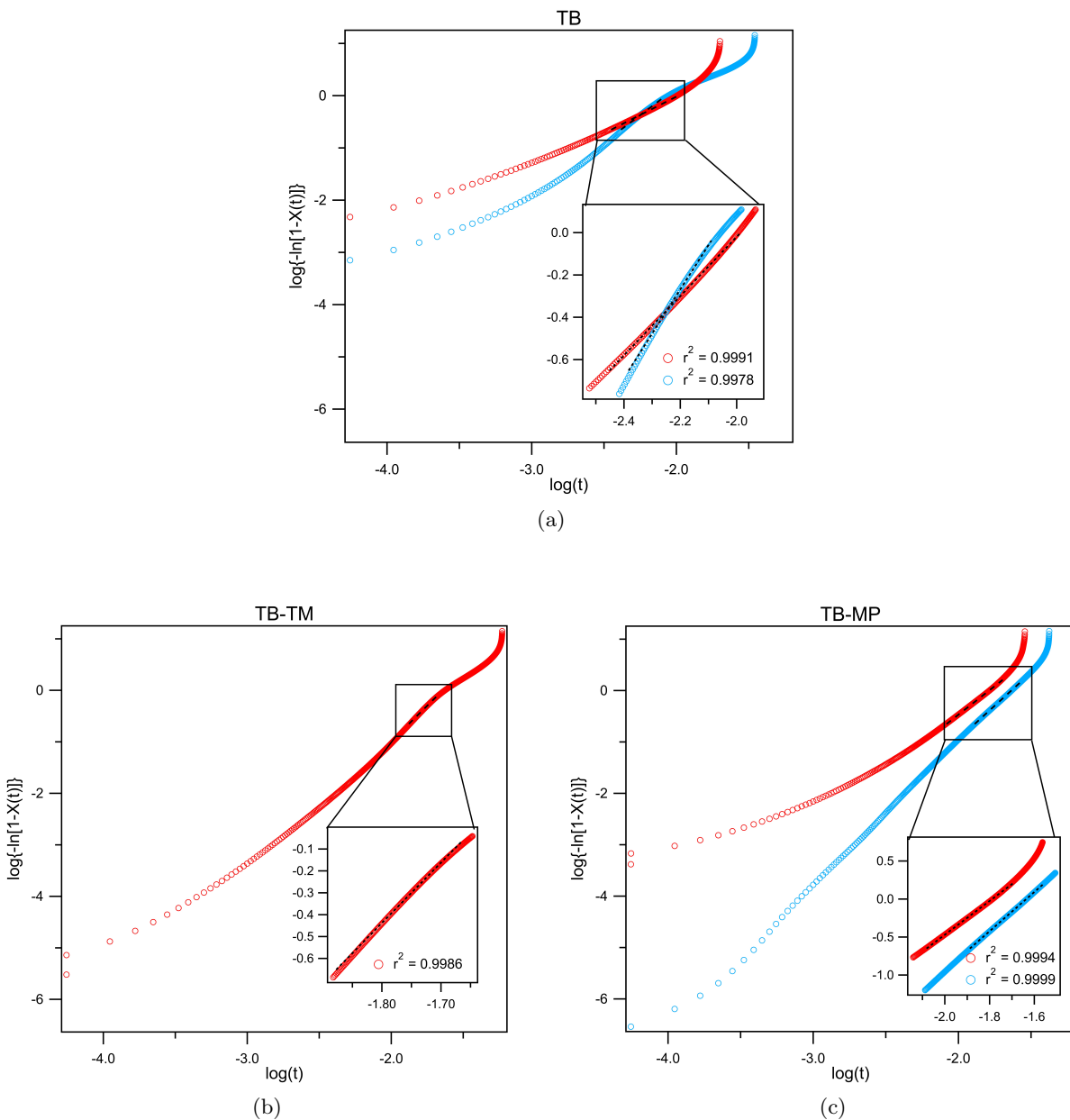


Figure 3.9 Jeziorny plots for TB (a), TB-TM (b), and TB-MP (c), where red lines show pure polymer samples and blue lines show polymer-silver composites. Note that no crystallization exotherm was noted for TB-TM-Ag, therefore it was excluded from this analysis. Inset figures highlight areas fit to determine the Avrami exponent and rate parameter from the slope and intercept, respectively, of the linear region, typically from  $X(t) = 0.2-0.8$ .  $r^2$  of linear fit is also provided in each inset.

Table 3.3 Summary of Parameters from Jeziorny-Modified Avrami Crystallization Kinetics Analysis

Parameter	TB	TB-Ag	TB-TM	TB-MP	TB-MP-Ag
$t_{\frac{1}{2}}$ (s)	29.0	25.8	72.4	50.1	72.8
$n$	1.4	2.09	2.76	2.22	2.58
$\log Z_t$	2.78	4.33	4.53	3.97	4.22
$\log Z_c$	0.28	0.43	0.45	0.4	0.42
Linear $X(t)$ Range	0.2–0.63	0.2–0.6	0.2–0.58	0.2–0.8	0.2–0.8
$r^2$ of fit	0.9991	0.9978	0.9986	0.9994	0.9999

While the primary stage of crystallization has a higher rate parameter than TB,  $t_{\frac{1}{2}}$  was longer for TB-TM which indicates the kinetics of crystal growth slowed after quaternizing TB with TMA. Additionally,  $n \sim 3$ , indicating the mechanism of PCOE crystallization shifts toward 3-dimensional crystal growth after quaternizing with TMA. Similar to TB-TM, TB-MP also has a higher  $Z_t$  and longer  $t_{\frac{1}{2}}$  compared to TB, indicating that quaternizing the triblock copolymer with MPRD had a similar effect to TMA. The disparity between observing a larger rate parameter, which would indicate faster kinetics, and a longer  $t_{\frac{1}{2}}$ , which indicates slower crystallization, highlights the complexity of the effect quaternization of the triblock backbone has on the crystallization kinetics of the PCOE midblock. Overall, it is clear from  $X(t)$  that quaternization increases the crystallization time, likely due to the cationic moieties affecting the polymer chain mobility and thus recrystallization.

In both TB-MP and TB-MP-Ag, similar, stable melting points were observed. The silver sample also showed a higher  $T_c$  and  $\Delta H_c$  due to the heterogeneous nucleating effect of AgNPs. TB-MP-Ag also showed a higher  $Z_t$ , longer  $t_{\frac{1}{2}}$ , and similar  $n$  compared to TB-MP. This further demonstrates of the complexity in analyzing the crystallization kinetics. While the rate parameter  $Z_t$  increases with AgNPs, similar to what we observe when comparing TB to TB-Ag,  $t_{\frac{1}{2}}$  is longer. Here, the larger rate parameter may be a result of AgNPs acting as nucleation sites and improving nucleation, while the cationic moiety interaction with silver prevents chain mobility and thus crystal growth.

Wide-angle X-ray scattering (WAXS) was used to investigate changes in the polymer microstructure after casting with AgNPs (Figure 3.10). WAXS experiments were conducted on

as-cast polymer and silver composite samples. The detector images can be seen in Figure 3.11. The microstructure of the polymer backbone is mainly characterized by four distinct peaks arising from the crystalline reflections of the polycyclooctene midblock. The first peak ( $q = 1.43 \text{ \AA}^{-1}$ ,  $d = 4.41 \text{ \AA}$ ) and third peak ( $q = 1.65 \text{ \AA}^{-1}$ ,  $d = 3.82 \text{ \AA}$ ) are identified as the (010) and (110) reflections of the triclinic crystalline structure, respectively [303, 321]. The second peak ( $q = 1.52 \text{ \AA}^{-1}$ ,  $d = 4.15 \text{ \AA}$ ) and much weaker fourth peak ( $q = 1.78 \text{ \AA}^{-1}$ ,  $d = 3.53 \text{ \AA}$ ) correspond to the (110) and (201) reflections of the monoclinic structure [322].

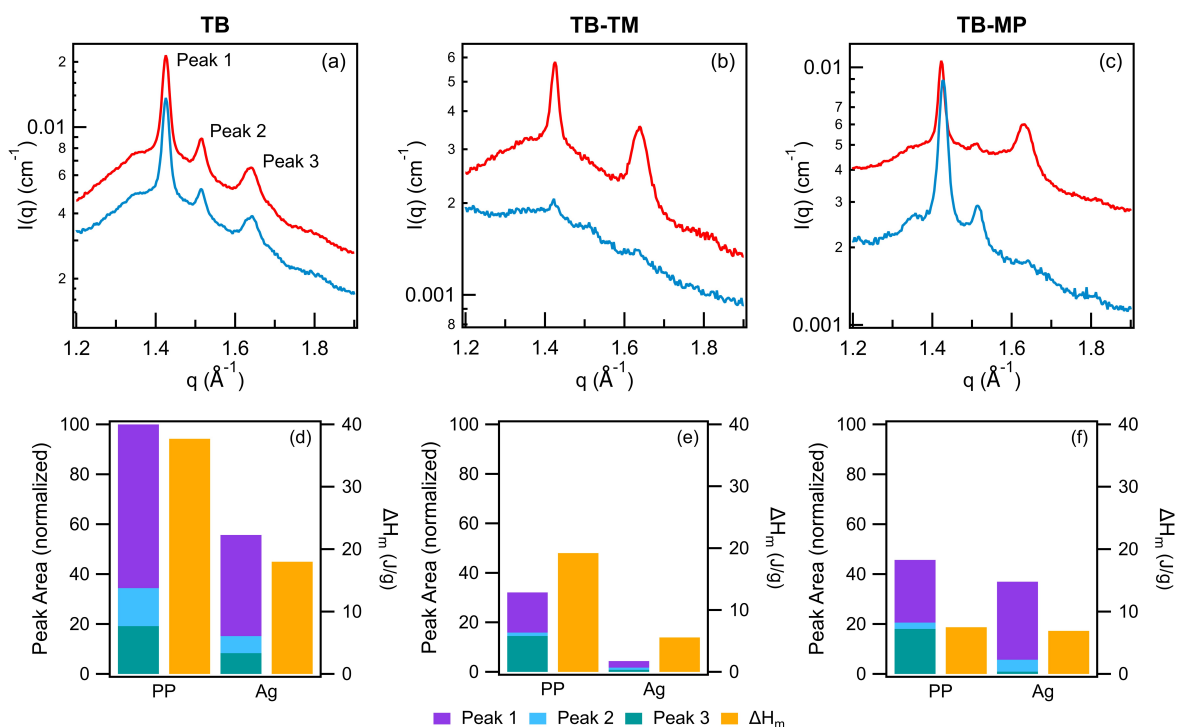


Figure 3.10 WAXS spectra (a-c) and area under the curve analysis (d-f) for TB (a,d), TB-TM (b,e), and TB-MP (c,f). For WAXS spectra, pure polymer samples are shown by red lines and silver-polymer composites are shown by blue lines. Area under the curve was normalized to the pure triblock backbone for comparison. PP: pure polymer, Ag: silver-polymer composite. The enthalpy of melting,  $\Delta H_m$ , corresponding to the degree of crystallinity from the first melt cycle from DSC, is also shown in (d-f) for comparison.

The total area under the crystalline peaks was used to assess the change in crystallinity of the PCOE backbone due to interactions with silver (see Figure 3.10). The area under the fourth peak was determined to be insignificant and was excluded from this analysis. The changes in the degree of crystallinity upon adding AgNPs for TB, TB-TM, and TB-MP were 62%, 86%, and

19% decreases, respectively. These results are in good agreement with the changes in  $\Delta H_m$  from the first thermal cycle from DSC, included in Figure 3.10 for comparison. For TB and TB-TM, silver interactions lead to a decrease in all of the crystalline reflections observed.

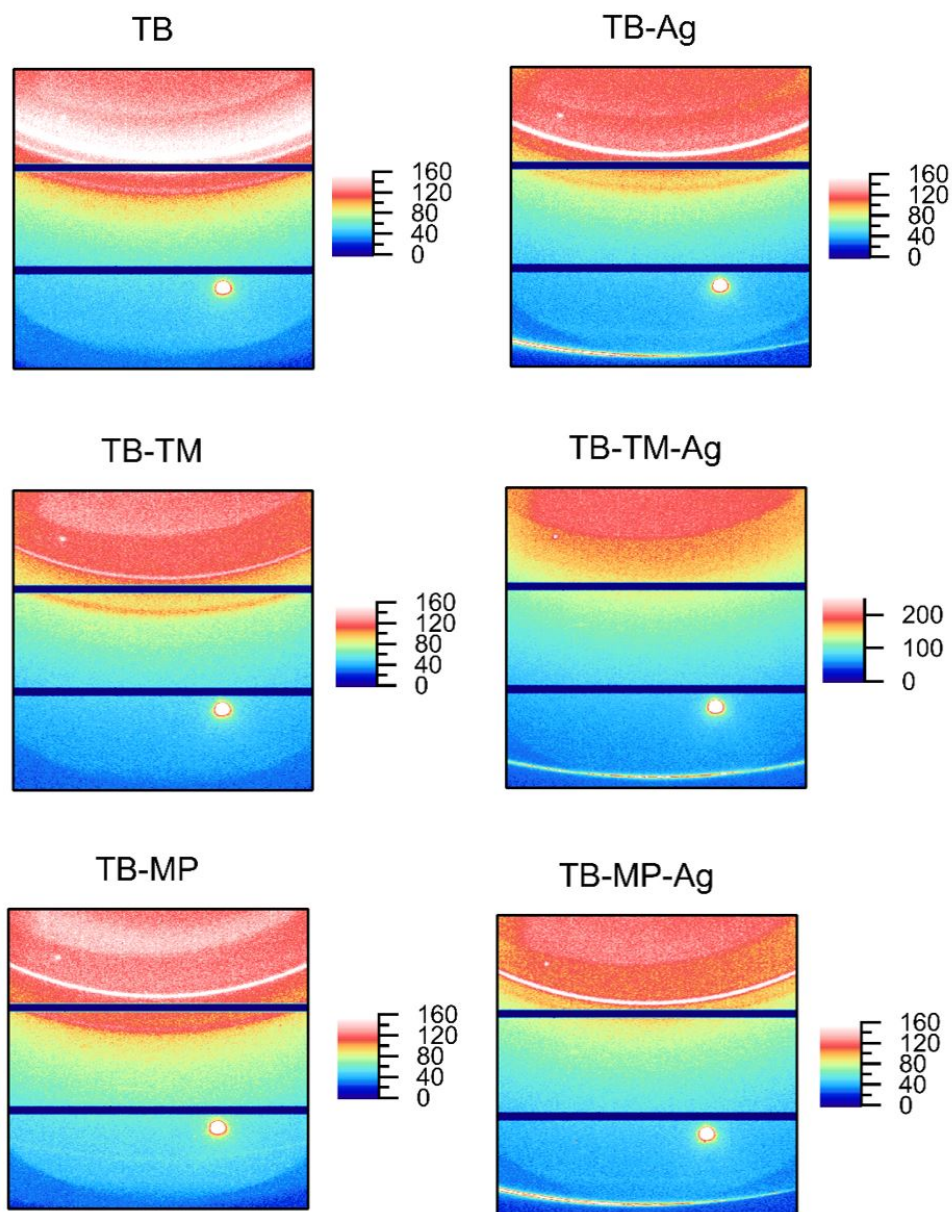


Figure 3.11 Wide angle X-ray scattering detector images, confirming no anisotropy in scattering and validating use of azimuthal averaging to obtain 2D spectra in main text. Note that the bright spot in bottom right region is from the mica window and did not affect further analysis.

However, the opposite phenomenon is observed for TM-MP, which is a substantial increase in the intensity of the (010) reflection and a slight increase in the (110) reflection after adding AgNPs. Further, AgNPs appear to shift the relative fraction of the crystal polymorphs in the quaternized samples (depicted in Figure 3.12). In both TB-TM and TB-MP, the addition of AgNPs leads to a decrease in the (110) triclinic structure reflection and an enhancement of the (110) monoclinic reflection. Overall, it is clear the crystallinity of the PCOE midblock is influenced by interactions with AgNPs and that the QACs have a strong influence on the nature of these interactions as well.

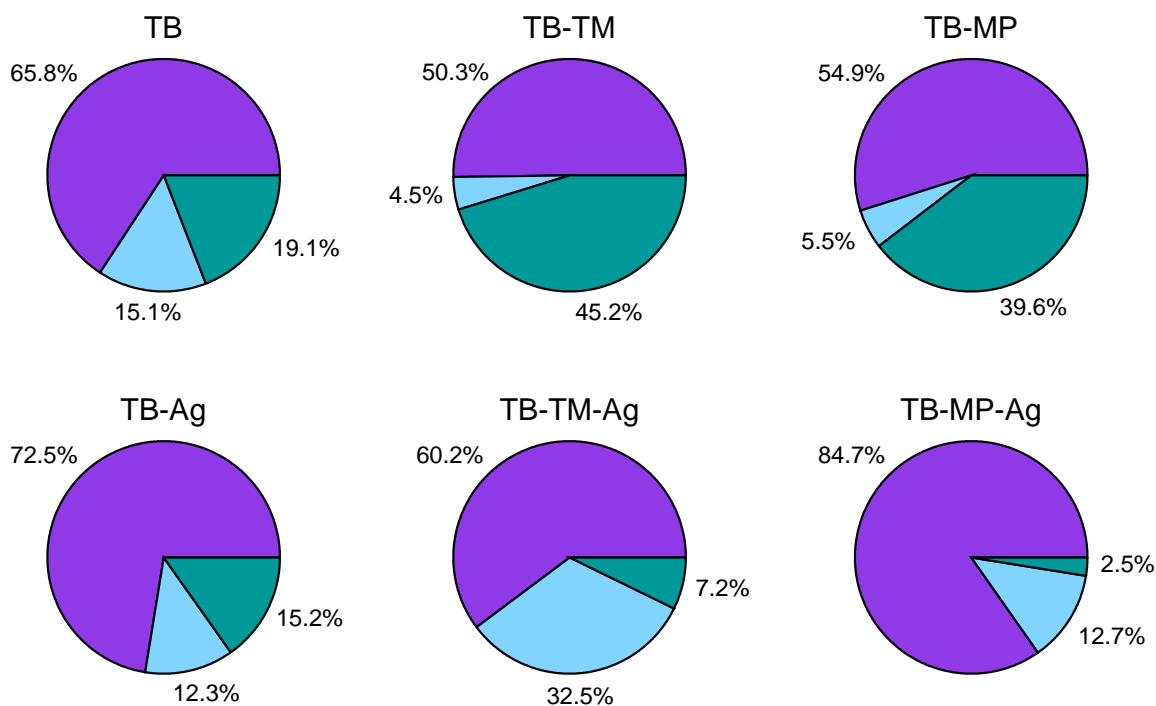


Figure 3.12 Pie charts depicting the relative fraction of the area under the curve of each crystalline reflection derived from WAXS experiments. The purple slice (peak 1 in the main text) and the green slice (peak 3 in the main text) correspond to the area under the (010) and (110) reflections of the triclinic crystalline structure, respectively. The blue slice (peak 2 in the main text) corresponds to the (110) reflection of the monoclinic structure.

### 3.6 Conclusions

Interactions between AgNPs and PCMS-*b*-PCOE-*b*-PCMS, and the ionomers derived from quaternization of the PCMS outer blocks with either TMA or MPRD cations, were investigated.



Groups with strong interactions with the AgNP surfaces include the phenyl rings, QACs, and C=C from PCOE as observed by FTIR spectroscopy. The changes in water content and crystallinity arising from these interactions were highly dependent on the QAC, where TB-TM-Ag showed a significant loss in crystallinity and an increase in both water content bound in the solvation shell surrounding the TMA moiety and in domains in the bulk, and TB-MP-Ag showed an increase in certain crystalline reflections and comparatively higher crystallinity with a lower bound solvation shell and bulk water content. Additional analysis of the non-isothermal kinetics of PCOE crystallization indicates AgNPs can either promote or suppress crystallization, depending on the QAC. In TB and TB-MP, AgNPs promoted heterogeneous nucleation at higher temperatures and resulted in higher degrees of crystallinity, whereas in TB-TM, AgNPs suppressed recrystallization of PCOE. The kinetic analysis highlights the difference in the nature of the complex interactions between the AgNPs, the TMA or MPRD moieties, and the PCOE midblock. The bulkier nature of the MPRD cationic moiety allows for enhanced crystallization likely due to a weaker interaction with AgNPs, while the smaller TMA cationic moiety has stronger interactions which ultimately prevent crystallization.

These results are of interest to the broad field of polymer nanocomposite materials. We have shown that the thermal behavior, crystallinity and mechanical properties of the nanocomposite can be tailored by the interactions between AgNPs and polymers containing different functionalities. This is relevant for many applications, including the additive manufacturing industry, where nanofiller particles play a significant role in tuning the mechanical properties of the manufactured part [312–314]. Specifically, it has been demonstrated in this study that cationic moiety selection is likely important in ionomer development for the electrodes of fuel cells and electrolyzers. With the added complexity of ionomer-catalyst interactions, a QAC that provides good performance when integrated in an anion exchange membrane may have determinantal interactions with catalyst particles when integrated in an ionomer. Beyond the possibility of ionomer adsorption reducing active catalyst surface area, we have shown that ionomer-catalyst interactions can also have a substantial impact on the microstructure and water uptake of the ionomer. It is known that intrinsic characteristics including water uptake and crystallinity can further dictate the polymer morphology, mechanical integrity, and transport of ions, water, and reactant and product species. These findings necessitate further investigation

into how implementing different QACs and electrocatalysts ultimately influence the ionomer characteristics, along with the resulting structure-property-performance relationship in electrochemical devices. The continuation of these studies will ultimately provide design principles for ionomers and QACs selection for integration with specific electrocatalyst particles.

## CHAPTER 4

### DESIGNING ANION EXCHANGE IONOMERS WITH ORIENTED NANOSCALE PHASE SEPARATION AT A SILVER INTERFACE

This chapter is modified from a paper submitted to The Journal of Physical Chemistry C. Nora C. Buggy,<sup>19</sup> Yifeng Du,<sup>20</sup> Mei-Chen Kuo,<sup>21</sup> Soenke Seifert,<sup>22</sup> Ryan J. Gasvoda,<sup>23</sup> Sumit Agarwal,<sup>24</sup> E. Bryan Coughlin,<sup>25</sup> and Andrew M. Herring<sup>26</sup>

#### 4.1 Motivation

After confirming interactions between silver nanoparticles and our tunable block copolymer-based ionomer system occur with C=C bonds in the backbone, phenyl rings on the side chains, and the quaternary ammonium cationic moieties, the next step in elucidating the structure-property-performance relationship was to investigate the thin film morphology of ionomers on silver surfaces. In this work, both block copolymer and ionomer thin films (20–60 nm) were deposited on either atomically flat silicon wafers or silicon wafers coated in a thin (ca. 5 Å) layer of silver. A new set of block copolymer-based ionomers with polyisoprene (PIp) hydrophobic blocks and high IECs were designed for this work. *Hypothesis 3* is investigated by comparing the thin film morphology of the unquaternized block copolymer precursors to that of the ionomers. Studying this nano-scale model interface provides a means of investigating the ionomer-catalyst interface at relevant scales as it exists in the catalyst layer of the electrode.

#### 4.2 Abstract

Performance of polymer electrolyte-based energy systems is significantly impacted by transport within the electrode catalyst layer, where ionomer thin films coat catalyst particles. Proton exchange ionomer thin films have been thoroughly characterized, but few studies have

---

<sup>19</sup>Primary researcher and author

<sup>20</sup>Co-author, polymer chemist

<sup>21</sup>Co-author, polymer chemist

<sup>22</sup>Co-author, X-ray scattering expert and beamline scientist

<sup>23</sup>Co-author, X-ray photoelectron spectroscopy

<sup>24</sup>Co-author, X-ray photoelectron spectroscopy

<sup>25</sup>Co-author, polymer expert

<sup>26</sup>Co-author, advisor and corresponding author

critically examined anion exchange ionomer (AEI) thin films. Further, none have reported nanoscale phase separation for hydrocarbon AEIs, which is critical to mitigate transport resistances. In this work, a set of hydrocarbon-based AEIs with nanoscale phase separation are developed from tunable block copolymer systems composed of polyisoprene (PIp) and polychloromethylstyrene (PCMS). The effect of the PIp:PCMS ratio, architecture, and thickness on the thin film morphology of the neutral block copolymer precursors on silicon and silver substrates is investigated using GISAXS and AFM. AEIs are prepared by quaternizing with trimethylamine or methylpiperidine and their cation-dependent morphology is characterized at 60 °C and 95% RH. A perpendicularly aligned morphology is observed on silver, while no phase separation is observed on silicon, indicating silver-polymer interfacial interactions drive phase separation. After quaternization, dipole-dipole interactions induce some disorder, but nanoscale phase separation is still maintained. GISAXS patterns are modeled using a Unified Fit approach to understand water uptake and swelling, and recommendations for AEI design are presented.

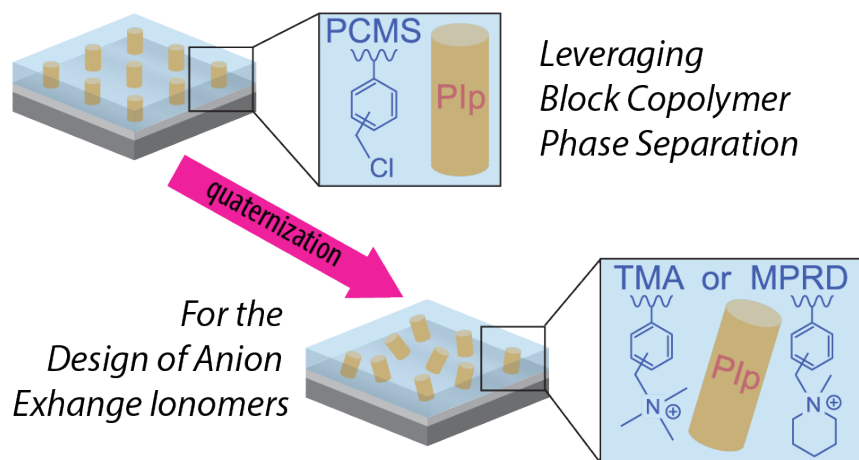


Figure 4.1 Graphical abstract.

### 4.3 Introduction

Ion exchange membranes are of interest for electrochemical energy conversion technologies including fuel cells [46], electrolyzers [34], batteries [323], and redox flow batteries [216]. Anion exchange membranes (AEMs) specifically have been targeted as a promising material for all of these devices because alkaline systems allow for more facile catalysis and utilization of

non-platinum group metal (PGM) catalysts [324, 325]. Block copolymer-based AEMs are of further interest due to their ability to self-assemble into phase-separated morphologies, which can ultimately lead to improvements in ion conduction and transport of reactant and product species across the membrane [326–329]. While phase separation in neutral block copolymers is well understood, experimental and computational studies have shown charge effects in block polyelectrolytes significantly impact the Flory-Huggins parameter [330] and phase diagram [294, 331, 332], where factors including chain length, charge fraction, charge size and the strength of Coulombic interactions all impact morphology [293, 333, 334].

An area of research which remains unexplored is understanding thin film morphology of polyelectrolytes in the catalyst layer of the electrode, where they are known as the ionomer. In proton exchange membrane (PEM) fuel cells, ionomers exist as thin films (4–10 nm) covering catalyst particles [182]. Although the microstructure and thickness of ionomers in AEM-based electrodes is still speculative, it is expected that they also exist as a thin film. Transport of species through ionomer thin films has been shown to be crucial to optimizing the catalyst layer to improve electrochemical device performance [115, 120, 183]. The ionomer is a critical component in the catalyst layer where it facilitates water, reactant and product species, and ion transport to and from the catalyst surface [335]. Studies have shown that ionomer thin film (1–100 nm) morphology differs greatly from their bulk ( $\mu\text{m}$  scale) structure, leading to changes in water uptake, transport, and ionic conductivity [189, 193, 194]. The shift in morphology is due to a combination of confinement and surface tension effects along with interfacial interactions between the ionomer and the thin film substrate [186, 187]. To date, the thin film morphology of Nafion<sup>®</sup> and other perfluorosulfonic acid (PFSA) ionomer thin films have been most commonly investigated. In their case, it has been shown that interfacial interactions contribute to a thickness-dependent morphology [188, 189] which results in changes in water uptake and proton conductivity [186, 190–192]. Substrate-dependent morphologies have also been observed [186, 195, 196], where Nafion<sup>®</sup> thin films on  $\text{SiO}_2$  display an isotropic structure, and on gold or platinum exhibit parallel backbone alignment relative to the substrate [197]. Other studies of thin films cast on hydrophilic substrates absorb more water compared to films on hydrophobic substrates [198], further explained by a parallel morphology on hydrophobic substrates slowing adsorption of water and an isotropic orientations on hydrophilic substrates favoring water

sorption [195]. Combined, these studies utilize techniques such as grazing-incidence small-angle X-ray scattering (GISAXS), ellipsometry, and thin film conductivity measurements to elucidate the thin film morphology, water uptake and ionic conductivity properties on a polished silicon wafer or model catalyst interface [184, 185, 190]. Understanding the chemistry-morphology-property relationships has provided insight into mitigating transport resistances in the catalyst layer of PEM-based devices.

Only a limited number of anion exchange ionomers (AEIs) have been studied as thin films, including Tokuyama A201 [206, 207], quaternized comb-shaped poly(2,6-dimethyl-1,4-phenylene oxide) (QA-PPO) [208], and commercial Fumasep<sup>®</sup> Fumion FAA-3 ionomer (FAA-3) [209]. Recently, a more wide-ranging study investigated a variety of AEIs with different backbones and side chain chemistries, highlighting the role of ionomer chemistry in their structure and water uptake [210]. Perfluorinated polymers showed phase separation in GISAXS, while all hydrocarbon-based thin films were amorphous and displayed no evidence of nanoscale phase separation, which could potentially lead to transport resistances [211–213]. FAA-3 and a benzyltrimethylammonium-functionalized PPO ionomer have also displayed insufficient phase separation in GISAXS [209].

The importance of phase separation and morphology has been demonstrated to be key to enhancing water and ion transport through bulk membranes. One way to achieve a better phase-separated morphology and ultimately enhance species transport is to utilize amphiphilic block copolymers as the backbone for synthesizing AEIs. Almost all AEIs are prepared from quaternizing the halogenated component with an amine such as trimethylamine, methylpyrrolidine or methylpiperidine [57, 58, 214]. Trimethylamine derived cations are the most commonly implemented, however their chemical stability has been called into question at higher temperature and elevated pH, and more sterically hindered methylpiperidine derived cations are more favorable for stability [85]. The thin film morphology of neutral block copolymers has been extensively studied [336, 337], but there are no studies that extensively characterize the morphology of block copolymer-based AEIs or their neutral precursors. The implementation of block copolymer-based AEIs has been demonstrated in device studies using styrene-ethylene/butylene-styrene (SEBS)-based block copolymers quaternized with trimethylammonium in both AEM-fuel cells [51, 233] or water electrolyzers [165]. Tunable

tetrablock poly(norbornene) copolymer-based ionomers have also been used in AEM-fuel cells [115]. Chen et al. compared the nanostructured morphology of their block copolymer SEBS-based ionomer with three different levels of quaternization [111]. They observed hydrophobic nano-domains and a continuous hydrophilic matrix on mica substrates using AFM. While they discuss the observed surface morphology and how it relates to ionomer swelling and the AEM-fuel cell performance they obtained, the catalyst they used in the device was platinum and it is now well established that the ionomer morphology of thin films,  $< 100$  nm, is dependent on the chemistry of the surface.

One of the main benefits of AEM-fuel cells is their ability to utilize non-PGM catalysts for the oxygen reduction reaction (ORR). While acidic conditions require the use of Pt or Pt-alloys for long term stability [338], increasing the pH allows for lower overpotentials and faster reaction kinetics by decreasing the binding energy of spectator ions [143, 339]. Historically, the National Aeronautics and Space Administration (NASA) developed alkaline fuel cells and found that Au-Pt alloys showed superior activity and durability compared to the original PGM catalyst used in the Apollo program [149], and more recent work has shown that Ag-Pt alloys are an equally active and durable alternative to Au, available at a lower cost [150]. Ag has been shown to have promising ORR performance in alkaline conditions [152, 340, 341], and compared to other high activity Pt-group metals including Pt, Pd, Ir and Ru, it is also a more abundant element. Therefore, this work focuses on Ag surfaces to investigate the interface-dependent morphology from a fundamental perspective. Pure Ag-coated substrates were utilized, however it should be noted that catalysts are typically alloyed with other non-noble metals to both improve their performance and further decrease catalyst costs [342, 343].

A remaining challenge is to design AEMs that display nano-phase separation as thin films at catalyst interfaces. Obtaining an understanding of interfacial interaction-driven morphologies on metal surfaces that model catalysts of interest is recommended in order to establish rational design principles for AEMs. In this work, two tunable block copolymer chemistries are developed, the diblock copolymer PIP-*b*-PCMS (PIP, polyisoprene and PCMS, polychloromethylstyrene) and the triblock copolymer PCMS-*b*-PIP-*b*-PCMS. The synthesis of these materials is described, and their bulk morphology is characterized. The neutral block copolymers are then studied as thin films of 30, 45, or 60 nm on silicon or Ag-coated silicon substrates using GISAXS and atomic force

microscopy (AFM). The block copolymer thin films are then quaternized with trimethylamine or methylpiperidine to functionalize the backbone with pendant trimethylammonium (TMA) or methylpiperidinium (MPRD) quaternary ammonium cationic moieties. Their humidity dependent morphology is discussed in the context of block copolymer architecture, film thickness, and quaternary ammonium cation selection. Definitive correlations between morphology and water swelling are established, and recommendations are presented to aid in future design of AElS.

## 4.4 Experimental Methods

### 4.4.1 Materials

Isoprene (Ip) (99%, Arcos Organics) was distilled and stored under -20 °C before use. Chloromethylstyrene (CMS) (mixture of para- and meta- isomers, 97%, Sigma-Aldrich) was passed through basic alumina to remove the inhibitor and stored at -20 °C before use. 2,2'-Azobis(2-methylpropionitrile) (AIBN) was recrystallized from methanol. *N-tert-Butyl-N*-[1-diethylphosphono-(2,2-dimethylpropyl)] nitroxide (SG1) was kindly provided by Arkema. *n*-Hexane (97%, Sigma-Aldrich), anisole (99%, Sigma-Aldrich), ethyl acetate (99%, VWR), diethyl ether (99%, VWR), tetrahydro furan (THF) (99%, VWR), magnesium sulfate (anhydrous, 99%, Sigma-Aldrich), carbon disulfide (99%, Sigma-Aldrich), dibromo-*p*-xylene (97%, Sigma-Aldrich), potassium hydroxide (85%, Sigma-Aldrich), *N*-methylpiperidine (99%, Acros Organics), trimethylamine (pure, 7.3M, 50 wt% aqueous solution, Acros Organics), chloroform (>99.5%, Sigma-Aldrich), and methanol (ACS grade, Pharmco) were purchased and used as received. Silicon wafers (standard prime grade <100>, single side polished) were purchased from MSE Supply Company. Silver pellets (99.99% purity, 1/4" diameter x 1/4" long) and a tungsten boat source used for thermal evaporation were purchased from Kurt J. Lesker Company.

### 4.4.2 Synthesis of PIP-SG1

*N-tert-Butyl-N*-[1-diethylphosphono-(2,2-dimethylpropyl)]nitroxide (SG1, 38.14 mg, 0.1 mmol), isoprene (Ip, 4 g, 58.7 mmol) and pyridine (6.0 mL) were added to a thick-walled Schlenk tube. Three cycles of freeze-pump-thaw were applied to degas the mixture. Then, the flask was backfilled with N<sub>2(g)</sub> and placed in an oil bath at 115 °C. After 72 h, the chain extension reaction was quenched by immersing the flask into an ice bath. The solution was transferred to a



pre-weighed vial. Solvent and unreacted isoprene were removed by purging with dry  $N_{2(g)}$  overnight and then kept in a vacuum oven at room temperature for 24 h. A viscous light-yellow liquid was obtained (PIp-SG1,  $M_n = 8,200 \text{ g mol}^{-1}$ , PDI = 1.15). The synthesis of PIp-SG1 with a lower molecular weight ( $M_n = 8,000 \text{ g mol}^{-1}$ , PDI = 1.11) was performed using the same method but with a polymerization time of 48 h.

#### 4.4.3 Synthesis of diblock copolymer PIp-*b*-PCMS, Di-1 and Di-2

PIp-SG1 (1g,  $M_n = 8,200 \text{ g mol}^{-1}$ , PDI = 1.15), CMS (3.22 g, 21.1 mmol), and anisole (6 mL) were added to a thick-walled Schlenk flask. Three cycles of freeze-pump-thaw were applied to degas the mixture. Then, the flask was backfilled with  $N_{2(g)}$  and placed in an oil bath at 105 °C for 12 h. The chain extension reaction was quenched by immersing the flask into an ice bath. The solution was precipitated into n-hexane three times to remove the excess monomer CMS and dormant PIp homopolymer without chain extension. A light-yellow powder was obtained (PIp-*b*-PCMS, Di-1,  $M_n = 21,000 \text{ g mol}^{-1}$ , PDI = 1.36). The synthesis of Di-2 was performed using the same method but with a different PIp-SG1 precursor (1 g,  $M_n = 8,000 \text{ g mol}^{-1}$ , PDI = 1.11) and three times the amount of CMS (9.66 g, 62.2 mmol) to obtain a larger PCMS block.

#### 4.4.4 Synthesis of difunctional chain transfer agent (CTA)

The difunctional CTA, butyl 4-(((butylthio)carbonothioyl]thio) methyl)benzyl trithiocarbonate, was synthesized based on the reaction of a carbodithioate salt with alkyl dibromide (see Figure 4.2). 1-butanethiol (2.7 g, 30 mmol), potassium hydroxide (10% aqueous solution, 20 ml), carbon disulfide (2.28 g, 30 mmol) were added to a flask with an ice bath. Dibromo-*p*-xylene (3.7 g, 14 mmol) in THF (20 ml) was then added dropwise into the reaction mixture under stirring over 1 h. The reaction mixture was then slowly brought to room temperature and then heated to 60 °C. The temperature was maintained for 3 h until the bottom yellow layer was clear. The reaction flask was allowed to cool to room temperature. The reaction mixture was then partitioned between  $H_2O$  and diethyl ether. The organic layer was collected and washed with  $H_2O$  three times. The organic layer was then dried with magnesium sulfate. The magnesium sulfate was filtered off and the solvent was removed under reduced pressure. The yellow crude oil product was further purified using column chromatography (hexanes: ethyl

acetate = 10:1 as the eluent) to yield a yellow crystalline solid (yield = 77%).

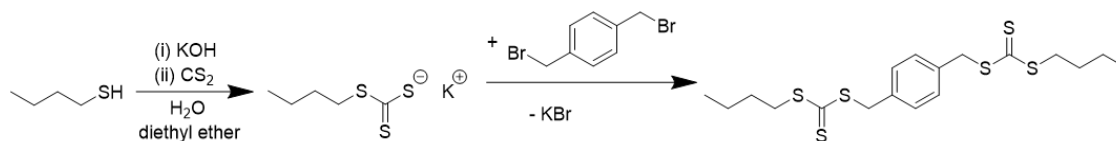


Figure 4.2 Synthesis of difunctional RAFT CTA

#### 4.4.5 Synthesis of telechelic PIP macro-CTA

*Di-tert*-butyl peroxide (dtBP, 2 mg, 0.012 mmol), difunctional CTA (54 mg, 0.12 mmol), isoprene (Ip, 3.4 g, 50 mmol) and anisole (6.0 mL) were added to a thick-walled Schlenk tube. Three cycles of freeze-pump-thaw were applied to degas the mixture. Then, the flask was backfilled with  $N_{2(g)}$  and placed in an oil bath at 120 °C. After 48 h, the chain extension reaction was quenched by immersing the flask into an ice bath. The solution was transferred to a pre-weighed vial. Solvent and unreacted isoprene were removed by purging with dry nitrogen overnight and then kept in a vacuum oven at room temperature for 24 h. The product was obtained as a viscous light-yellow liquid (telechelic PIP macro-CTA,  $M_n = 12,600 \text{ g mol}^{-1}$ , PDI = 1.18).

#### 4.4.6 Synthesis of triblock copolymer PCMS-*b*-PIp-*b*-PCMS, Tri-1 and Tri-2

Telechelic PIP macro-CTA (250 mg,  $M_n = 12,600 \text{ g mol}^{-1}$ , PDI = 1.18), CMS (8.6 g, 56 mmol), AIBN (0.54 mg, 0.003 mmol) and anisole (8 mL) were added to a thick-walled Schlenk flask. Three cycles of freeze-pump-thaw were applied to degas the mixture. Then, the flask was backfilled with  $N_{2(g)}$  and placed in an oil bath at 70 °C for 12 h. The chain extension reaction was quenched by immersing the flask into an ice bath. The solution was precipitated into *n*-hexane three times to remove the excess monomer CMS and dormant PIP homopolymer without chain extension. A light-yellow powder was obtained (PCMS-*b*-PIp-*b*-PCMS, Tri-1,  $M_n = 30,400 \text{ g mol}^{-1}$ , PDI = 1.44). The synthesis of Tri-2 was performed using the same method but with three times the amount of CMS (25.8 g, 158 mmol) to obtain a larger PCMS block.

#### 4.4.7 Gel Permeation Chromatography (GPC)

GPC was performed in THF at a flow rate of 1.0 mL min<sup>-1</sup> using a refractive index detector on a Polymer Laboratories PL-GPC 50 integrated GPC system.

#### 4.4.8 Nuclear Magnetic Resonance (NMR) Spectroscopy

NMR spectroscopy was performed in 5 mm diameter tubes in deuterated chloroform (CDCl<sub>3</sub>) at 25 °C. <sup>1</sup>H and <sup>31</sup>P NMR spectroscopies were performed on a Bruker 500 spectrometer at 500 MHz (<sup>1</sup>H) and 202 MHz (<sup>31</sup>P).

#### 4.4.9 Transmission Electron Microscopy (TEM)

The TEM specimens were prepared using a Leica (Reichert & Jung) CryoUltramicrotome. The microtome chamber was cooled to -160 °C using N<sub>2(l)</sub>, where the bulk sample was microtomed with a diamond knife to a thickness of ~40 nm. The cut sections were then mounted on a 400-mesh copper grid support and stained by OsO<sub>4</sub> vapor for 30 min at room temperature. TEM imaging was performed on a JEOL 2000FX TEM operated at an accelerating voltage of 200 kV.

#### 4.4.10 Small Angle X-ray Scattering (SAXS)

Small-angle X-ray scattering (SAXS) measurements were performed using a GANESHA 300 XL instrument with a Cu K $\alpha$  0.154 nm line in SAXS mode. Scattering profiles were collected for 15 min. For polymer membrane preparation, the polymer was dissolved in chloroform at a concentration of 50 mg mL<sup>-1</sup> and cast onto a Teflon<sup>®</sup> substrate. The solution area was covered by a Petri dish to allow slow evaporation of the solvent at room temperature overnight. The polymer membrane (~50  $\mu$ m) was then peeled off and dried under vacuum prior to SAXS characterization.

#### 4.4.11 Preparation of Thin Film Samples

1 mm thick polished silicon wafers with a ~1.5 nm native oxide layer were cut into ~2 cm<sup>2</sup> squares using a diamond knife. Substrates were cleaned of organics in acetone and methanol and blown dry with N<sub>2</sub>. Ag-coated substrates were fabricated using an Angstrom Thermal Evaporator to deposit an atomically flat ~3 Å layer of Ag at a rate of 0.3 Å s<sup>-1</sup> on the silicon substrates. The composition of the silver surface was verified using XPS (see Figure 4.3) and the uniformity was verified using AFM (see Figure 4.4).

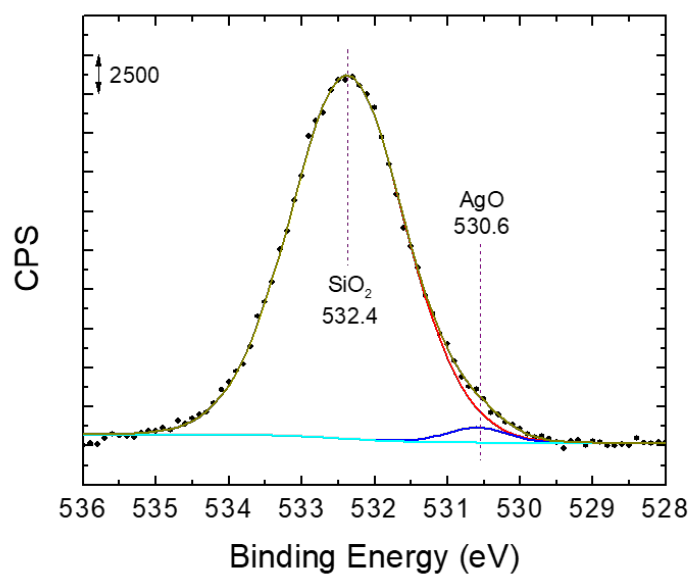
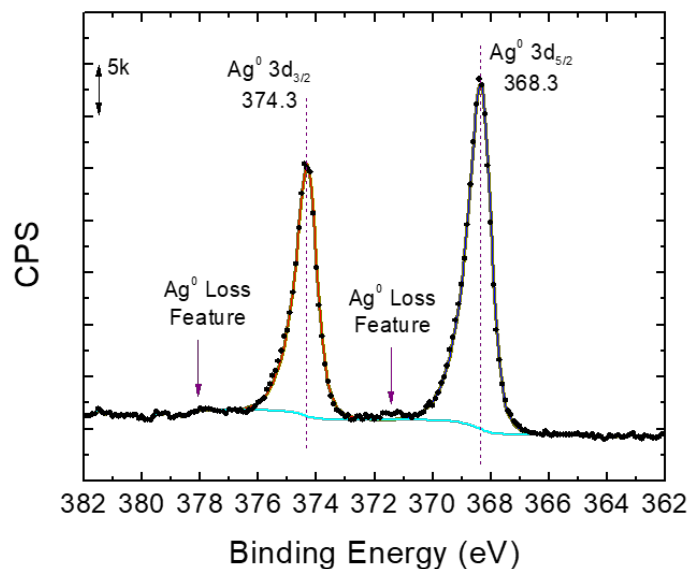


Figure 4.3 High resolution core-level spectra of the Ag (top) and O (bottom) regions of the silver-coated silicon substrates. The peak position the Ag  $3d_{3/2}$  and  $3d_{5/2}$  peaks as well as the Ag<sup>0</sup> loss features indicates the silver surface and film is not heavily oxidized and most of the Ag is metallic [310]. Further, the O 1s deconvolution shows a minuscule amount of oxygen that could be attributed to AgO which we speculate is at the interface between the native SiO<sub>2</sub> layer and the metallic Ag film.

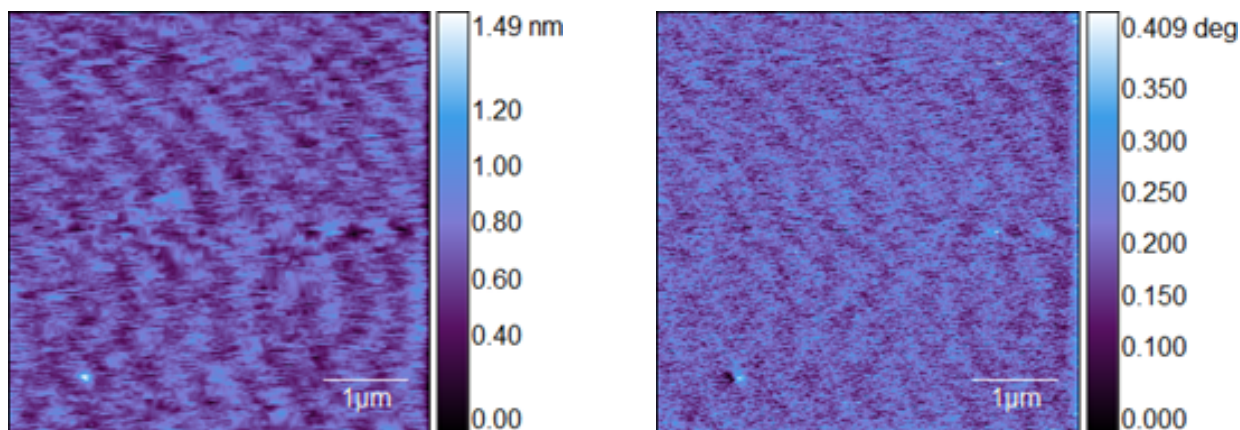


Figure 4.4 5x5  $\mu\text{m}$  AFM height (left) and phase (right) image of a Ag-coated silicon substrate, confirming a thin uniform layer of Ag was deposited on the silicon wafer by thermal evaporation

1–10  $\text{mg mL}^{-1}$  solutions of block copolymers PIP-*b*-PCMS and PCMS-*b*-PIP-*b*-PCMS were prepared in  $\text{CHCl}_3$ . The solutions were spin-cast at 2000 rpm for 1 min onto the silicon substrates and the Ag-coated silicon substrates. Varying the solution concentration allowed for the sample thickness to be controlled to obtain samples of 30, 45, or 60 nm thick for each block copolymer investigated. Thin films were quaternized with either trimethylamine or *N*-methylpiperidine vapor to fabricate films functionalized with either TMA or MPRD cationic moieties. For the vapor reactions, the substrates were kept on a glass stage above the liquid level and the glass reaction vessel was sealed (see Figure 4.5).

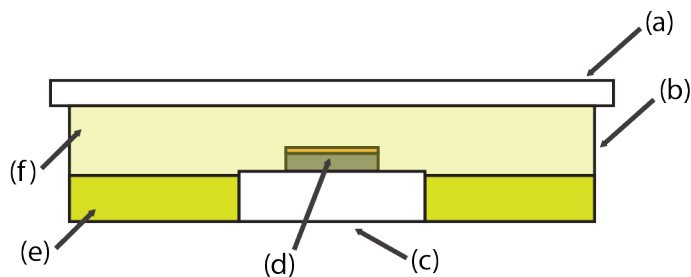


Figure 4.5 Setup for vapor quaternization reaction of thin films. (a) glass lid, (b) tall glass bottom, (c) glass stage, (d) polymer thin film on substrate, (e) reactant liquid, (f) reactant vapor.

For TMA functionalized thin films, 50/50 trimethylamine/water was used at room temperature. For MPRD functionalized thin films, 50/50 *N*-methylpiperidine/MeOH was used, and the reaction vessel was heated to 80 °C to vaporize the reactant liquid. Reactions took place for 1 h to ensure full quaternization of the thin film [344]. The samples were then dried under vacuum at 80 °C for 12 h to ensure removal of all residual reactant vapor and solvent.

#### 4.4.12 Ellipsometry

A VASE<sup>®</sup> (variable angle spectroscopic ellipsometer) (J.A.Woolam Co.) was used to measure the thickness of the spin-cast polymer thin films deposited on silicon substrates at two angles of incidence, 50° and 70°. A multilayer optical model was used comprised of the silicon substrate and a Cauchy layer to describe the transparent polymer thin film using a two parameter Cauchy equation:

$$n(\lambda) = A + \frac{B}{\lambda^2} \quad (4.1)$$

Where  $n$  is the refractive index,  $\lambda$  is the wavelength, and  $A$  and  $B$  are the two Cauchy constants used for fitting.

#### 4.4.13 Grazing-Incidence Small-Angle X-ray Scattering (GISAXS)

GISAXS data was collected at beamline 12-ID-B/C-D at the Advanced Photon Source at Argonne National Laboratory. The X-ray energy was set to 18 keV. Exposure time for each measurement was 0.07 s. The samples were placed on a data collection stage and held in place via vacuum. An incident angle of  $\theta = 0.09^\circ$  was used for all measurements, above the critical angle of the polymer film and just below the critical angle of the substrate ( $\text{SiO}_2$   $\theta_c \sim 0.1^\circ$  at 18 keV). For environmental GISAXS, a humidity and temperature controlled environmental chamber with X-ray transparent Kapton<sup>®</sup> windows was custom-built and designed to hold eight GISAXS samples. The chamber was connected to a previously implemented temperature and humidity control system [345]. Samples were kept at 60 °C and 95% RH for 1 h to ensure adequate equilibration with the environment. The 2D images were analyzed using the GISAXSshop software package in Igor Pro 8 (Dr. Byeongdu Lee, Argonne National Lab.). Horizontal, vertical, and azimuthal line cuts were taken using the software package to characterize the orientation-dependent features of the polymer morphology. Line cuts were fit using the Unified

Fit model in the Irena software package in Igor Pro 8 [243].

#### 4.4.14 X-ray photoelectron spectroscopy (XPS)

Laboratory based UHV-XPS was performed on a HiPP III Scienta Omicron photoelectron spectrometer operating in swift mode using monochromatic Al K $\alpha$  X-rays at 150 W focused to a 500  $\mu\text{m}$  spot size. The pass energy and analyzer slit width were 200 eV and 1.5 mm for the core level scans. The aperture on the on the analyzer entrance was fixed at 800  $\mu\text{m}$  for all scans. The Ag-coated silicon substrate was mounted on double sided carbon tape and introduced to the analysis chamber via a fast entry loadlock. All analyses were performed using CasaXPS with adventitious carbon calibrated to 284.8 eV. The Ag 3d region was fitted using a Shirley background and asymmetric line shapes [310].

#### 4.4.15 Atomic Force Microscopy (AFM)

Height and phase images were collected in AC tapping mode using an Asylum Research MF3PD Atomic Force Microscope. Silicon AFM probes (Ted Pella, Prod. No. TAP150AL-G) with a resonant frequency of  $\sim 150$  kHz and a force constant of  $5 \text{ N m}^{-1}$  were used. All images were collected in repulsive mode. Domain sizes and surface coverage were analyzed using ImageJ software by applying a threshold to the image and using the built-in particle size analysis tool.

### 4.5 Results and Discussion

#### 4.5.1 Polymer Synthesis

##### 4.5.1.1 Diblock Copolymer Synthesis

Diblock and triblock copolymers of isoprene (Ip) and chloromethylstyrene (CMS) were synthesized by two living polymerization methods. As shown in Figure 4.6, the diblock copolymer PIp-*b*-PCMS was synthesized via nitroxide-mediated radical polymerization (NMP) due to its fast propagation rate at high temperature (115 °C).

*N*-*tert*-butyl-*N*-[1-diethylphosphono-(2,2-dimethylpropyl)] nitroxide (SG1) was used to initiate the polymerization and provide living character required to prepare block copolymers. By changing the feeding ratio of Ip and SG1, various molecular weights of PIp were achieved with a narrow dispersity ( $PDI_{PIp} < 1.2$ ), as shown in Table 4.1.

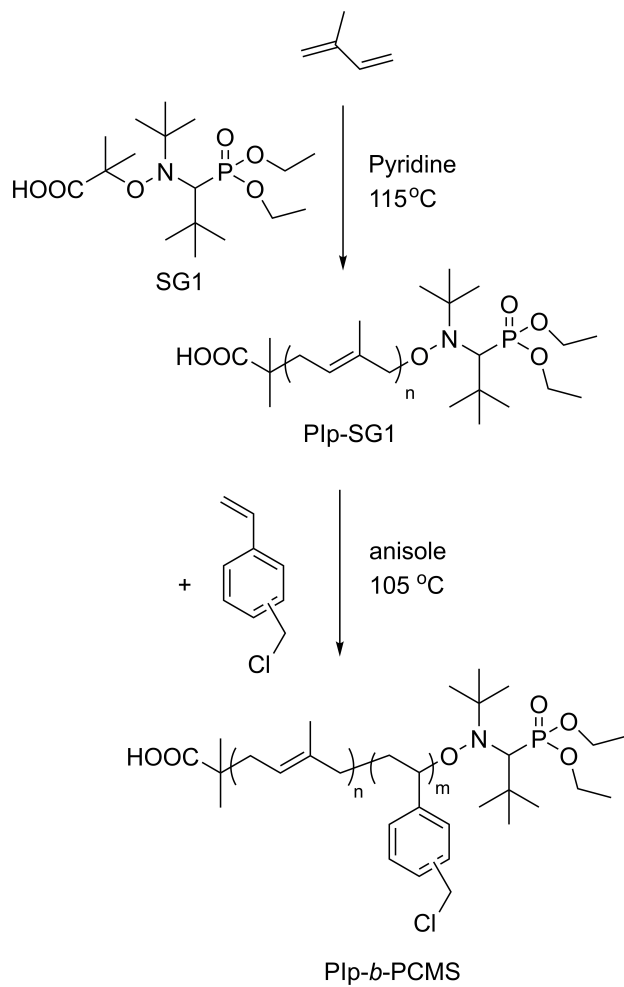


Figure 4.6 Synthesis of diblock copolymer PIp-*b*-PCMS, Di-1 and Di-2.



Table 4.1 Chemical composition and bulk morphology of diblock copolymer PIp-*b*-PCMS and triblock copolymer PCMS-*b*-PIp-*b*-PCMS

PIp Block			
Sample	$M_n^a$ (g mol <sup>-1</sup> )	$M_w^a$ (g mol <sup>-1</sup> )	$PDI^a$
Di-1	8120	9370	1.15
Di-2	8000	8850	1.11
Tri-1	12600	14900	1.18
Tri-2	12600	14900	1.18

PIp and PCMS Block Copolymer			
Sample	$M_n^a$ (g mol <sup>-1</sup> )	$M_w^a$ (g mol <sup>-1</sup> )	$PDI^a$
Di-1	21000	28500	1.36
Di-2	45200	64000	1.42
Tri-1	30400	43800	1.44
Tri-2	66300	100400	1.51

Sample	Composition	PCMS:PIp <sup>b</sup>	f <sub>PCMS</sub> <sup>c</sup> (%)	Morphology <sup>d</sup>	$d_s^e$ (nm)
Di-1	PIp <sub>119</sub> - <i>b</i> -PCMS <sub>511</sub>	4:1	57	C	20
Di-2	PIp <sub>117</sub> - <i>b</i> -PCMS <sub>2407</sub>	20:1	79	C	24
Tri-1	PCMS <sub>77</sub> - <i>b</i> -PIp <sub>110</sub> - <i>b</i> -PCMS <sub>77</sub>	1.4:1	54	C and L <sup>f</sup>	30
Tri-2	PCMS <sub>231</sub> - <i>b</i> -PIp <sub>110</sub> - <i>b</i> -PCMS <sub>231</sub>	4.2:1	78	C	30

<sup>a</sup>Determined from GPC

<sup>b</sup>Degree of polymerization (DP) ratios between PCMS and PIp blocks, calculated from <sup>1</sup>H NMR

<sup>c</sup>Volume fraction of PCMS block, calculated from PCMS:PIp ratio and the densities of homopolymers, PIp and PCMS

<sup>d</sup>Morphology from SAXS and TEM, where L denotes lamellar and C denotes a worm-like cylindrical morphology

<sup>e</sup>d-spacing determined from SAXS primary peak

<sup>f</sup>A disordered combination of C and L morphologies

Previously, the chain extension of the macro-initiator PIp-SG1 with CMS was performed in *o*-xylene [295]. In this work, anisole was selected as the solvent due to it having a lower chain transfer to solvent ratio. The ratio of PIp-SG1 to CMS was adjusted to tune the molecular weight of the PCMS block. Two diblock copolymers were synthesized and characterized by gel permeation chromatography (GPC) (Figure 4.7). The narrow dispersity observed in these polymerizations confirmed the living character provided by the PIp-SG1 macro initiator. The ratio of the degree of polymerization (DP) for both blocks can be calculated from <sup>1</sup>H NMR (Figure 4.8). The volume fractions of the PCMS block were calculated from the molar masses and densities of the respective homopolymers ( $\rho_{PIp} = 0.906 \text{ g cm}^{-3}$ ,  $\rho_{PCMS} = 1.088 \text{ g cm}^{-3}$ ).

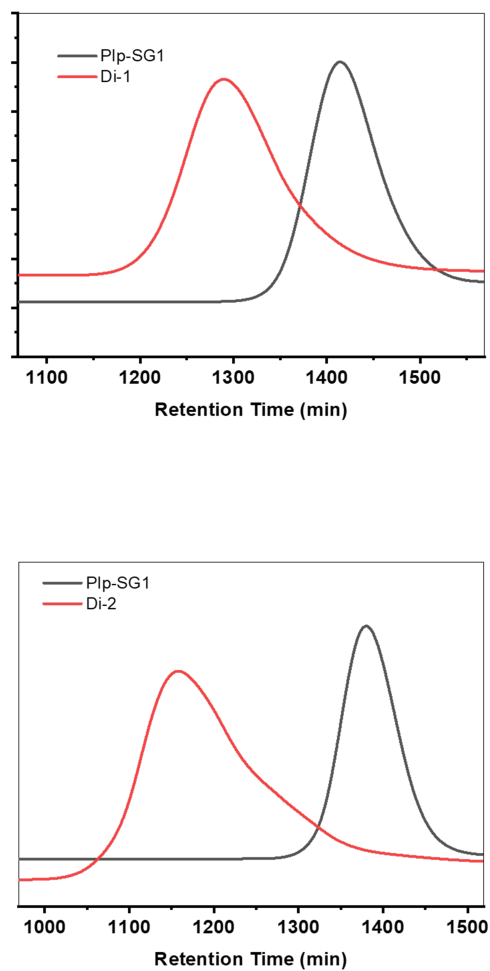


Figure 4.7 GPC of PIp-SG1 and Di-1 (top) and PIp-SG1 and Di-2 (bottom).

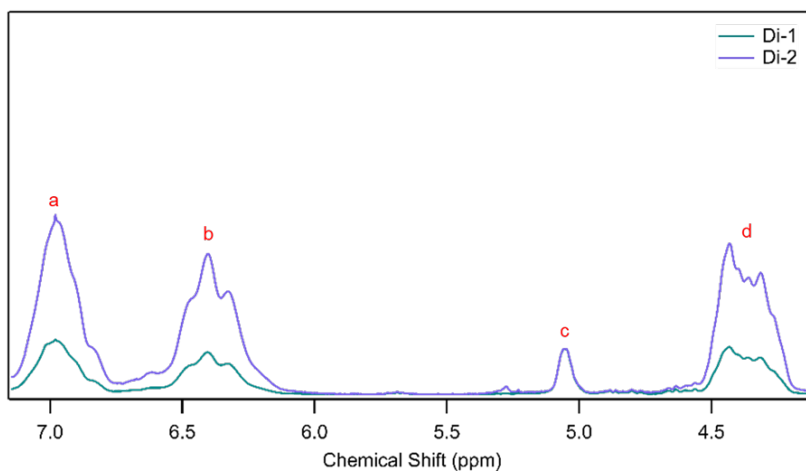
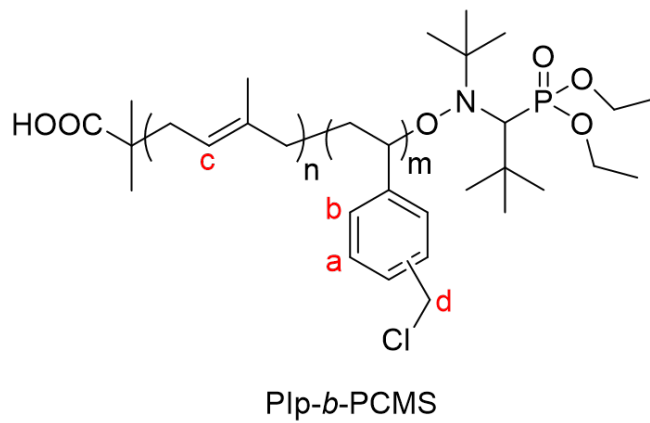


Figure 4.8 <sup>1</sup>H NMR and corresponding labeled chemical structure of Di-1 and Di-2.

#### 4.5.1.2 Triblock Copolymer Synthesis

Atom transfer radical polymerization (ATRP) for triblock copolymer syntheses requires the polymerization of the first block to be stopped at relatively low conversion, because the extent of bimolecular termination increases as the monomer concentration decreases [346]. Different from NMP and ATRP, the living character of RAFT is able to be maintained even at full conversion, due to the unique fragmentation transfer mechanism [347]. Thus, the RAFT method was chosen for the triblock copolymer syntheses in this study. The difunctional CTA was synthesized based on a previously reported method [348]. The two triblock copolymers were synthesized and characterized by GPC (Figure 4.9). The chemical structures were confirmed by electron spray ionization mass spectroscopy (Figure 4.10) and  $^1\text{H}$  NMR (Figure 4.11). The synthesis method of the triblock copolymers using the difunctional CTA is shown in Scheme 2. The telechelic PIP macro-CTA was then chain extended with CMS at 75 °C (see Figure 4.12). The molar ratio between telechelic PIP macro-CTA and initiator, AIBN, was kept at 10:1, whereas the feed ratio of CMS was adjusted to obtain different molecular weights of the PCMS block.

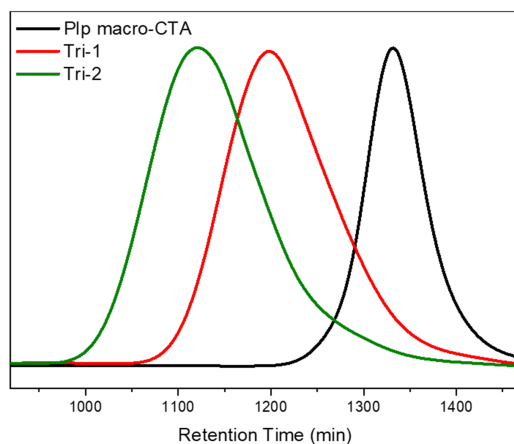


Figure 4.9 GPC of Tri-1 and Tri-2.

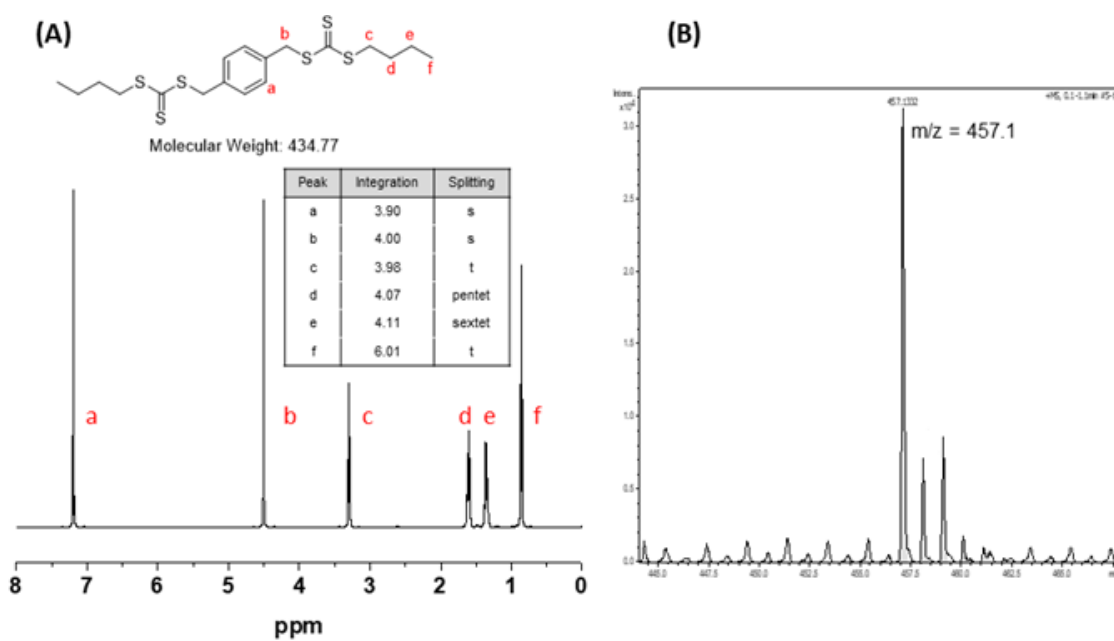


Figure 4.10 (A)  $^1\text{H}$  NMR and (B) ESI mass spectra of difunctional CTA. The sodium ion adduct of the molecule was detected in positive ionization mode, with  $m/z$  of  $\sim 457$  u/e ( $M_w = M_{w,CTA} + M_{w,Na}$ )

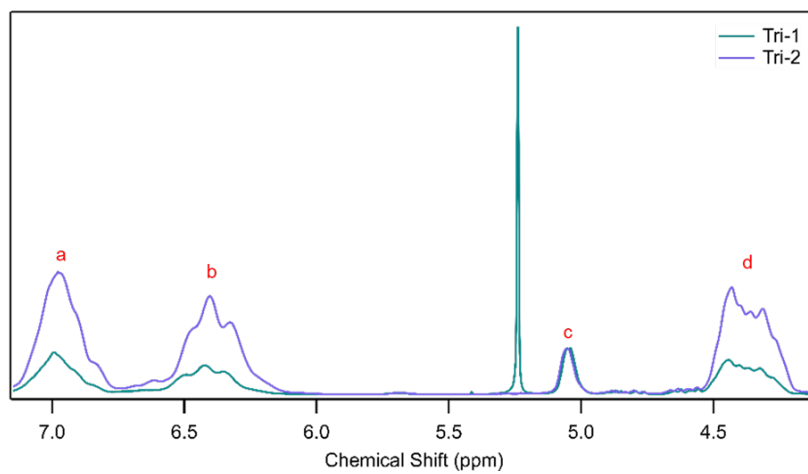
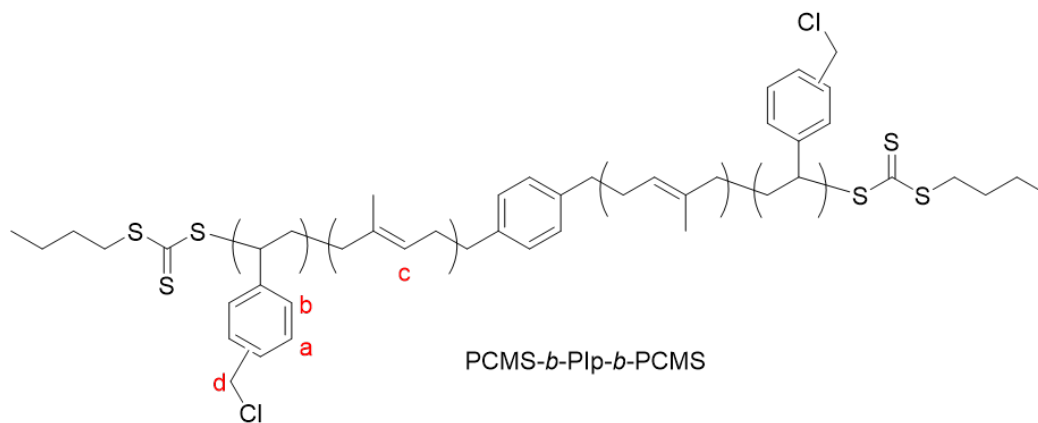


Figure 4.11  $^1\text{H}$  NMR and corresponding labeled chemical structure of Tri-1 and Tri-2.

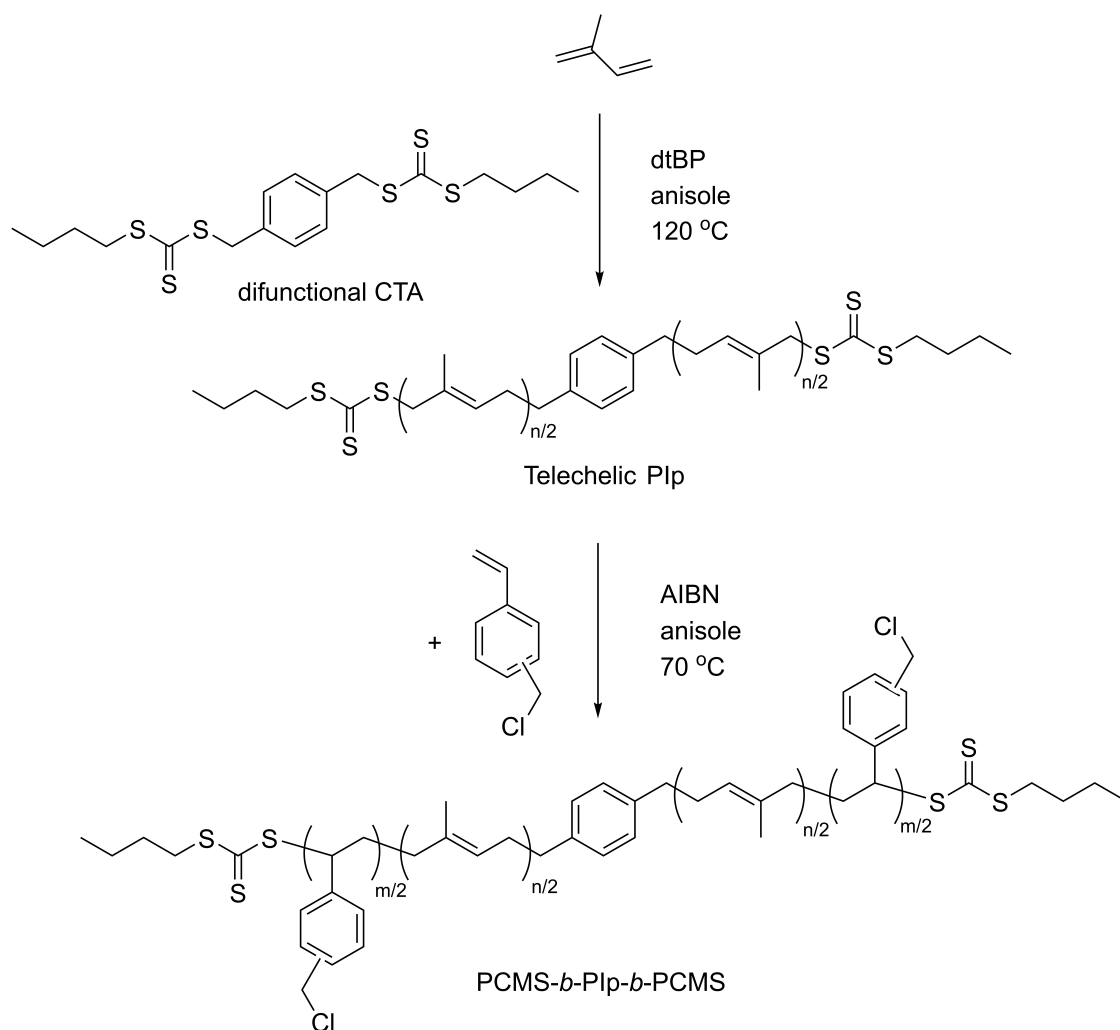


Figure 4.12 Synthesis of triblock copolymer PCMS-*b*-Pip-*b*-PCMS, Tri-1 and Tri-2.

### 4.5.2 Bulk Film Morphology

The morphology of both diblock and triblock copolymers was first investigated by SAXS on drop-cast films (Figure 4.13). The domain spacing (d-spacing),  $d_s = \frac{2\pi}{q^*}$ , was determined for each specimen, where  $q^*$  is the primary peak. Morphology was inferred from the higher order peak positions in SAXS in conjunction with the observed morphology from TEM (Figure 4.14). The d-spacing and morphology results are summarized in Table 4.1. SAXS patterns of all of the block copolymers investigated show some evidence of higher order peaks, but they are generally not very distinct. This indicates a lack of long-range ordering of the morphology. In TEM, the PIp domains are selectively stained with  $\text{OsO}_4$ . For the Di-1 and Di-2 membranes, a worm-like cylindrical morphology is observed (Figure 4.14a and b), in agreement with some of the broad higher order peaks observed in the SAXS pattern. A disordered combination of lamellar and cylindrical morphologies was observed in the TEM of Tri-1 (Figure 4.14c), which is consistent with the SAXS where the assignment of higher order peaks for a lamellar ( $q^* : 2q : 3q\dots$ ) or cylindrical ( $q^* : \sqrt{3}q : \sqrt{4}q\dots$ ) morphologies [349] are comparable. A larger PCMS block led to a shift toward a purely cylindrical morphology in Tri-2 (Figure 4.14d). The lack of definitive higher-order peaks in SAXS make the assignment of a morphology less clear. While TEM confirms the lack of long range ordering, it also assists in assigning a worm-like cylindrical morphology (Di-1, Di-2 and Tri-2) or a mixture of disordered cylinder and lamellar domains (Tri-1). The d-spacings observed in TEM are in agreement with what is calculated from the SAXS patterns.

### 4.5.3 Neutral Block Copolymer Thin Film Morphology

In our previous work, various triblock copolymer systems have been optimized as high-performance AEMs [58, 102]. However, in the electrode layer the mechanical integrity restraint is relaxed, therefore diblock copolymers and materials with more quaternizable content of PCMS can be used. Accordingly, the neutral block copolymers were used to study the effect of diblock versus triblock configuration and extending the PCMS block length on thin film morphology. Thin film samples were spin-cast on both plain silicon wafers and silicon wafers coated with a thin layer of Ag. The thickness of the samples was varied by adjusting the dilution of the spin-casting solution (1–10 wt% polymer in  $\text{CHCl}_3$ ). All samples in this study cast on plain silicon wafers did not show distinct scattering profiles, even after probing multiple incident angles.



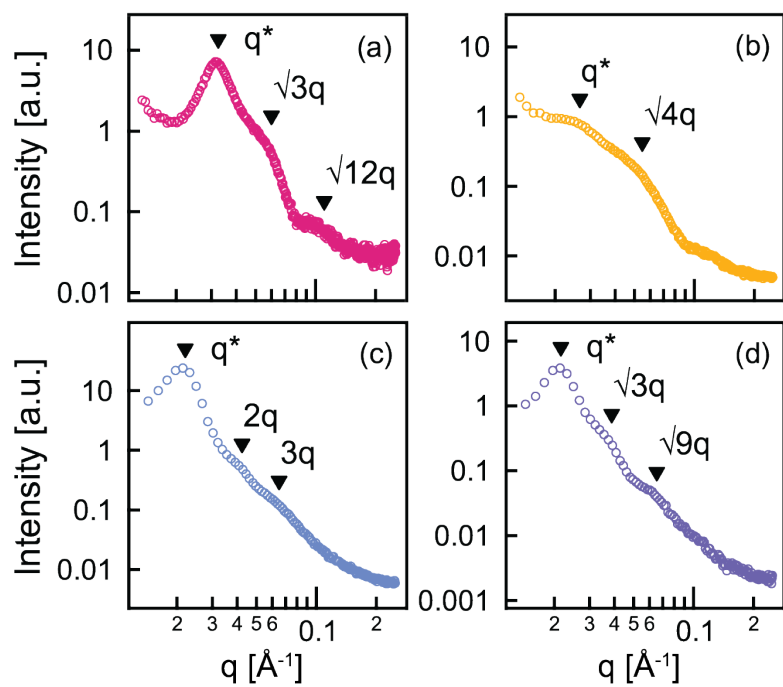


Figure 4.13 SAXS of  $\sim 50 \mu\text{m}$  films of Di-1 (a), Di-2 (b), Tri-1 (c) and Tri-2 (d).

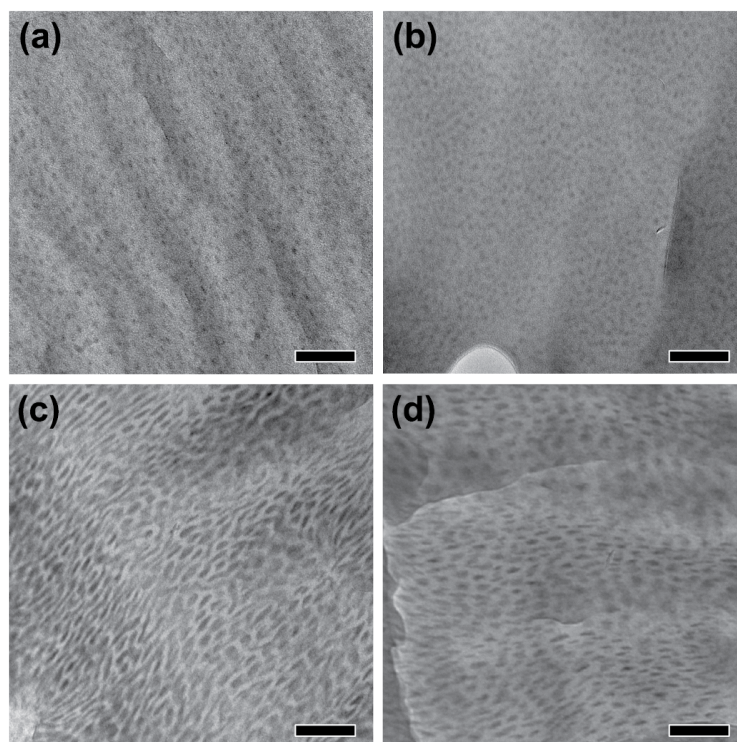


Figure 4.14 TEM of Di-1 (a), Di-2 (b), Tri-1 (c), and Tri-2 (d). Dark domains are PIP selectively stained with  $\text{OsO}_4$ . Scale bars are all 100 nm.

A representative GISAXS image can be seen in Figure 4.15. Samples fabricated on Ag-coated silicon substrates displayed more discrete scattering profiles that varied with sample thickness. The GISAXS scattering patterns for samples of 30, 45, and 60 nm thicknesses are shown in Figure 4.16. The measured sample thickness will be attached to the sample name, e.g. Di-1-30 will refer to the 30 nm thick sample of Di-1.

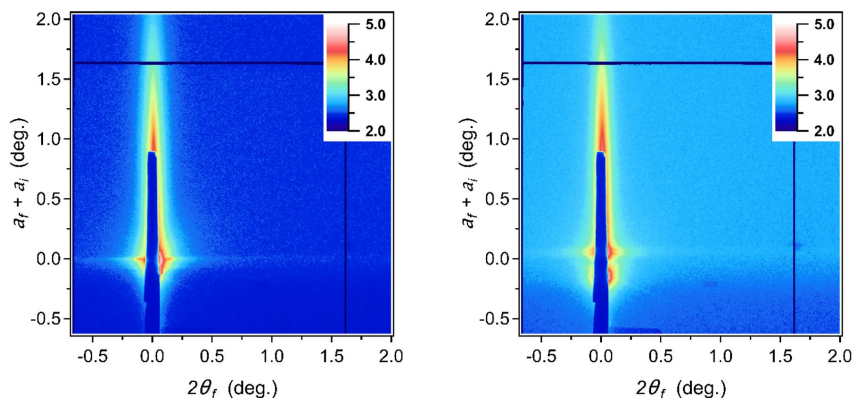


Figure 4.15 Scattering of Di-1-30 (left) and Tri-1-30 (right) on plain silicon substrates. No distinct scattering features are noted.

The PIP-*b*-PCMS diblock copolymer exhibits vertically oriented features on the Ag substrates. This indicates the ordering of the morphology is driven by interfacial interactions between the diblock copolymer and the Ag surface. The observed scattering corresponds to vertically oriented PIP domains surrounded by a continuous PCMS matrix, based on the molecular weight and  $f_{PCMS}$ . Although the lack of higher-order peaks makes the exact assignment of the morphology challenging, the domains are most likely vertically aligned cylinders or vertically aligned spherical micelles. The d-spacing of the PIP domains (Table 4.2) in all of the investigated samples are substantially smaller compared to their bulk d-spacing, likely induced by a combination of interactions with the Ag interface and confinement effects. Additionally, the sample thickness, along with the PCMS:PIP ratio and molecular weight all appear to have some influence on the relative order of the morphology – highlighted by the broadness of the scattering profile. At 30 nm, Di-1 and Di-2 show discrete, vertically oriented domains with similar d-spacing. Once the sample thickness is increased to 45 nm or 60 nm, the d-spacing increases slightly and the scattering profile broadens.

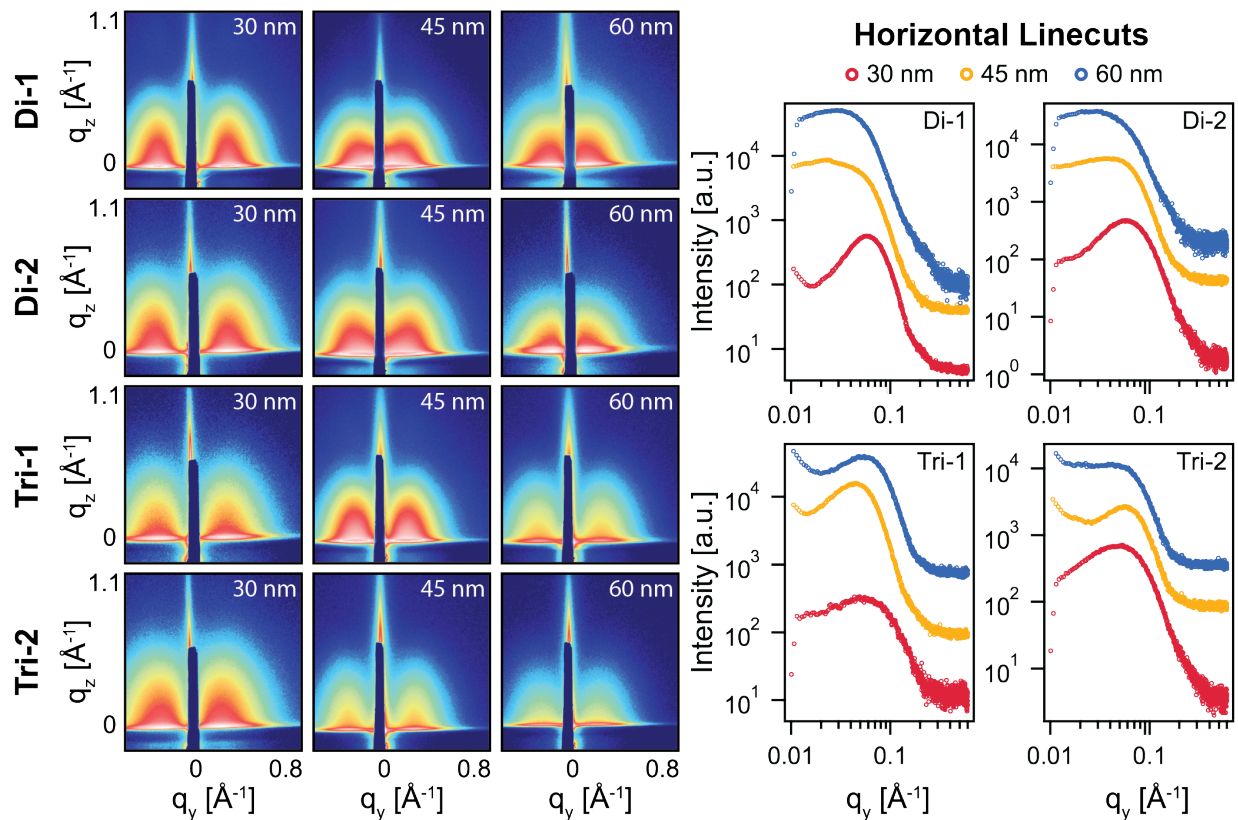


Figure 4.16 2D GISAXS images for Di-1, Di-2, Tri-1 and Tri-2 of the 30, 45 and 60 nm samples. Horizontal linecuts are compared for the 30 nm (red), 45 nm (yellow) and 60 nm (blue) thin films. Linecut traces are offset for clarity.

Table 4.2 Domain Spacing of Neutral Block Copolymers Determined from GISAXS  $q^*$

Sample	Domain Spacing (nm)		
	$t = 30$ nm	$t = 45$ nm	$t = 60$ nm
Di-1	9.4	11.4	12.4
Di-2	10.0	10.2	12.1
Tri-1	7.8	10.4	9.4
Tri-2	9.4	9.0	10.3

Broadening of this feature indicates that both the relative order of the spacing of the PIP vertically oriented domains becomes less ordered, and their orientation becomes more random, as the film thickness increases. Increasing the PCMS:PIp ratio and Mw does not have a significant effect on the d-spacing or morphology, in contrast with the difference in d-spacing and relative

order observed in the bulk SAXS of Di-1 and Di-2. Thin films of the PCMS-*b*-PIp-*b*-PCMS triblock copolymers were also studied at thicknesses of 30, 45, and 60 nm. Unlike Di-1 and Di-2 where there is broadening of the scattering profile as film thickness increases, Tri-1 and Tri-2 show a discrete vertically aligned feature at all of the thicknesses investigated. Spacing of the PIp domains also tends to increase slightly with film thickness.

While GISAXS probes the entirety of the thin film, AFM can provide a complimentary morphology at the air-polymer interface. Figure 4.17 shows AFM height and phase images of Di-1, Di-2, Tri-1 and Tri-2, all 30 nm thick on Ag substrates. Di-1-30 on plain silicon was also imaged for comparison (Figure 4.18). Based on the volume fraction of PIp, the discrete circular regions are assigned to PIp and the continuous phase to PCMS. Bright domains in the height image and dark domains in the phase image correspond to PIp. On the plain silicon substrate (Figure 4.18), the morphology appears more disordered, with some randomly distributed larger regions of PCMS but a predominant PIp-rich surface coverage. PIp can tend to cover the surface regardless of bulk film morphology, possibly due to its lower surface tension [350, 351]. However, on Ag substrates, more discrete separation and order of the two phases is observed. In the height (and phase) images, the bright (and dark) circular PIp regions correspond to the vertically oriented features observed in GISAXS, indicating that the domains aligning perpendicular to the Ag substrate propagate through to the polymer-air interface. The diameter of the PIp domains observed in AFM and the surface coverage of PCMS is summarized in Table 4.3. The domain sizes determined from the thresholding procedure all have a relatively broad size distribution, which can be seen in Figure 4.19. Di-2 shows larger domains than Di-1, and visually they appear to have larger spacing, in agreement with what is observed in GISAXS. Tri-1 and Tri-2 have a similar domain size as well. The surface coverage of PCMS also trends with the  $f_{PCMS}$  for each block copolymer, also shown in Table 4.3 for ease of comparison.

Table 4.3 Domain Size and Surface Coverage of Neutral Block Copolymers Determined from AFM

Sample	PIp Domain Diameter (nm)	Surface Coverage PCMS (%)	$f_{PCMS}$ (%)
Di-1	11.1 ± 5.3	85.6	57
Di-2	13.6 ± 5.2	86.3	79
Tri-1	14.9 ± 7.9	75.0	54
Tri-2	12.6 ± 5.9	83.6	78

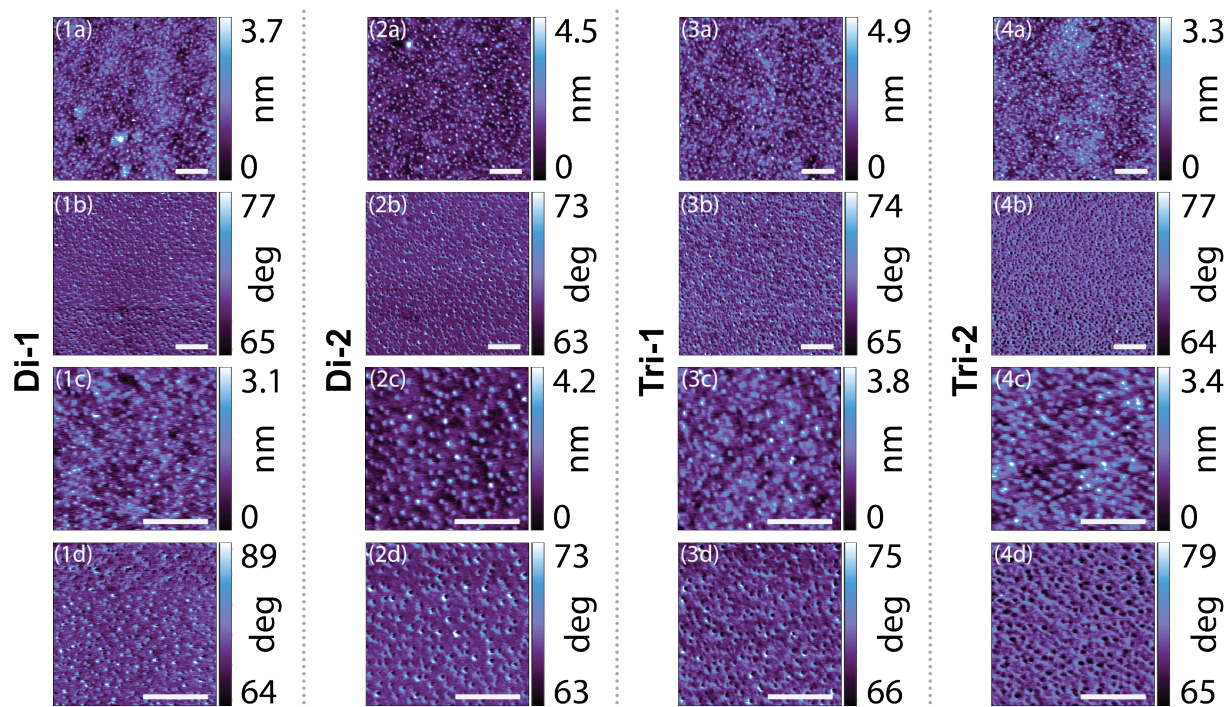


Figure 4.17 AFM height (a,c) and phase (b,d) images of Di-1 (1), Di-2 (2), Tri-1 (3), and Tri-2 (4) 30 nm samples on Ag substrates. 1x1  $\mu\text{m}$  (a,b) and 500x500 nm (c,d) images are shown. Scale bars all represent 200 nm. In height images, bright contrast represents PIP domains. In phase images, dark regions correspond to PIP domains.

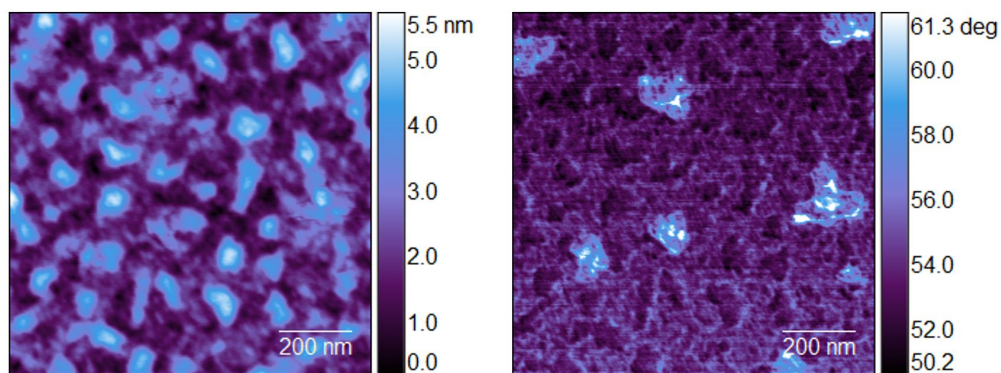


Figure 4.18 1x1  $\mu\text{m}$  AFM height (left) and phase (right) image of Di-1-30 on plain silicon. Both height and phase image show less distinct ordering and separation of the surface morphology. Bright domains in the height image and darker regions in the phase image correspond to PIP

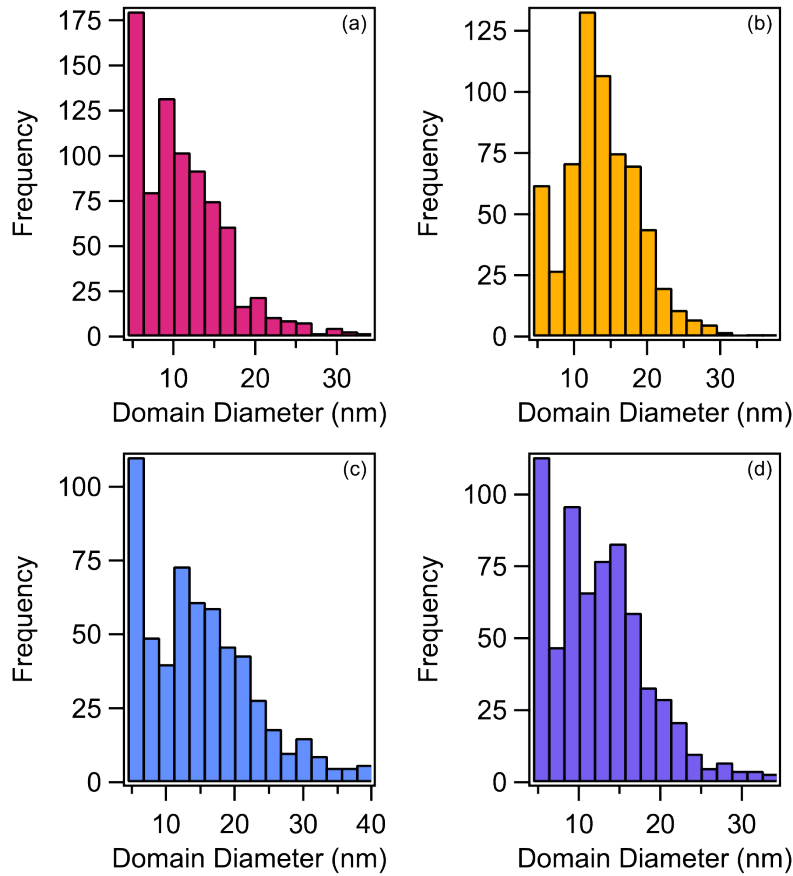


Figure 4.19 Domain size distributions determined from AFM images for Di-1 (a), Di-2 (b), Tri-1 (c) and Tri-2 (d).

To confirm that the observed morphologies were also reproducible, additional samples of the same thicknesses along with thinner, 20 nm samples of Di-1, Di-2, Tri-1 and Tri-2 were also prepared (Figure 4.20). While confirming the reproducibility of the morphology observed for samples of 30-60 nm thick, the scattering of the thinner samples appeared to be more isotropically oriented while still displaying nanoscale phase separation. To further analyze domain orientation, azimuthal linecuts were taken from  $\chi = 0^\circ$  (vertical linecut) to  $\chi = 90^\circ$  (horizontal linecut). Based on this analysis, for Di-2, Tri-1 and Tri-2 it is clear the feature most distinctly emerges at  $\chi = 90^\circ$ , indicating that while the thinner samples are less ordered, they still tend toward a vertical orientation. For Di-1, the scattering profile does not vary as significantly with  $\chi$ , indicating there is no favored orientation. In this case, the domains are oriented randomly within the thinner film.

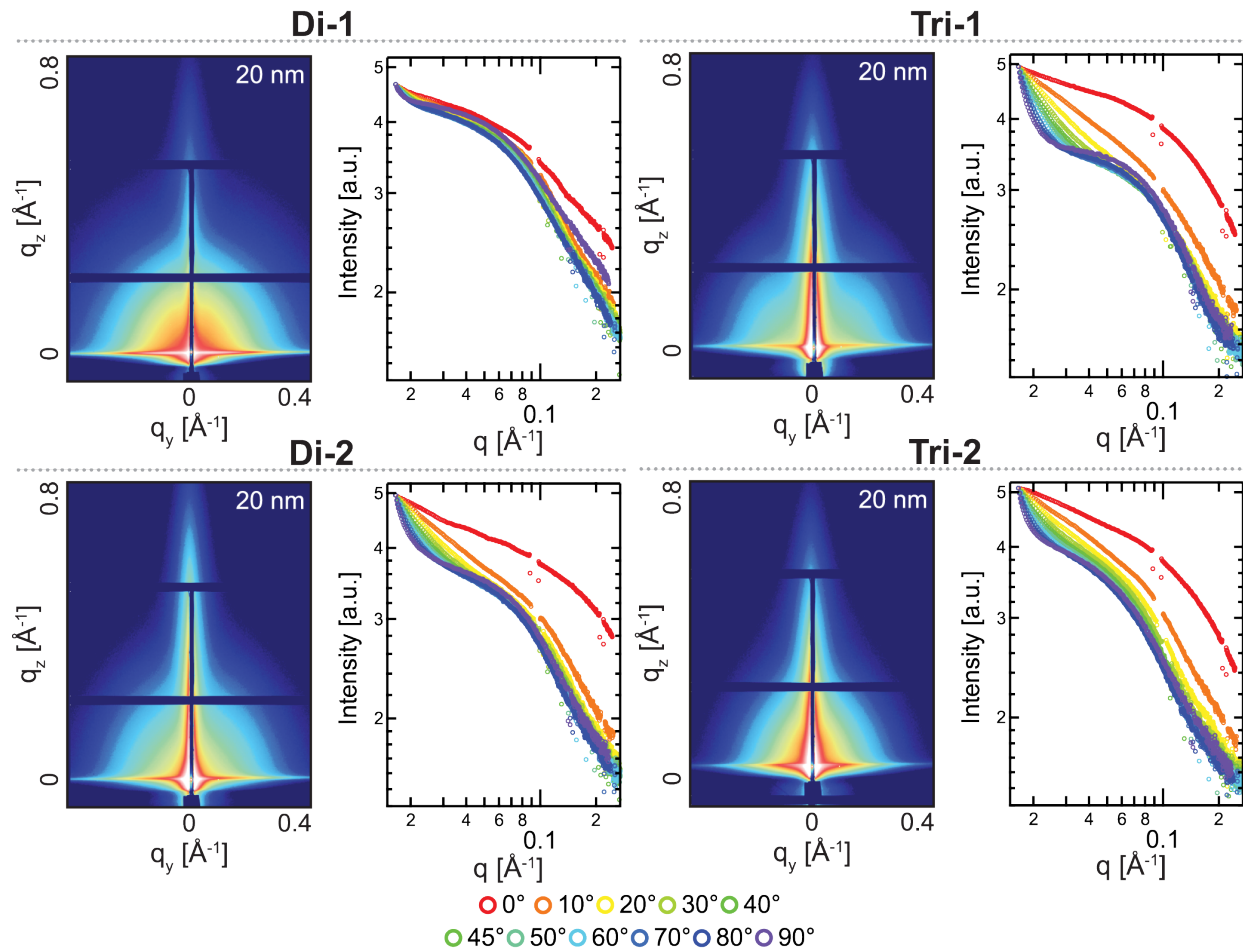


Figure 4.20 20 nm samples of Di-1, Di-2, Tri-1 and Tri-2 (from top to bottom). Left column shows 2D GISAXS images, right column shows azimuthal linecuts taken at angles varying from 0-90°.

To determine whether the morphology was due to a non-equilibrium kinetically trapped state produced from spin coating, Tri-1-30 was thermally annealed above the glass transition temperature ( $T_g$ ) of PCMS ( $\sim 130$  °C) [352] to observe any changes in the morphology (see Figure 4.21). The sample was heated from room temperature to 130 °C, during which only a slight decrease in the intensity of the scattering was observed. The sample was then further heated in increments of 5 °C up to 145 °C, where the intensity of the scattering steadily decreased. The decrease in the scattering intensity is likely from a loss in long range order as the sample becomes more rubbery above the  $T_g$ .

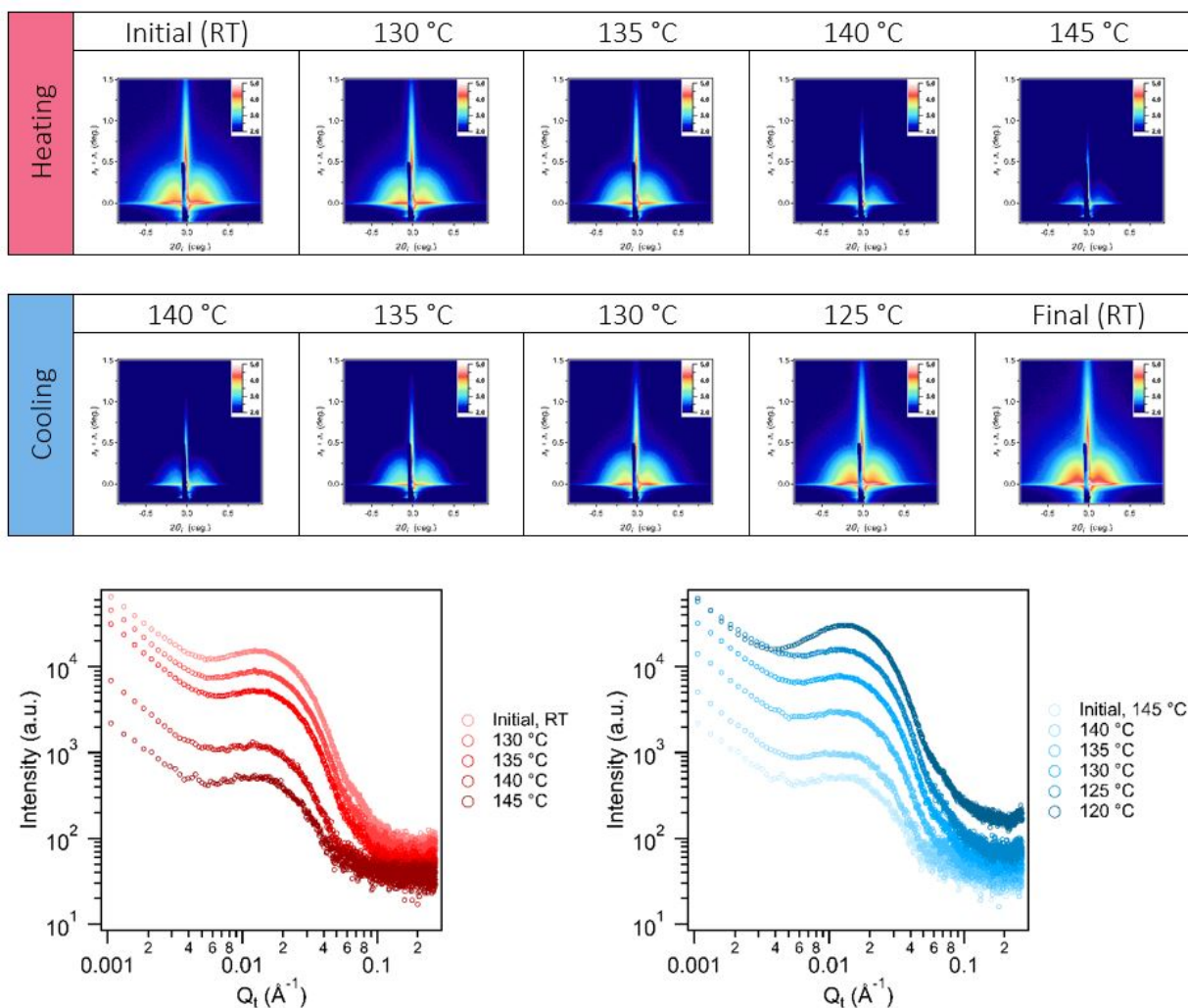


Figure 4.21 Annealing experiment for Tri-1-30. Top shows GISAXS images during heating and cooling. Bottom left shows horizontal line cuts from heating images, bottom right shows horizontal line cuts from cooling images.



No further changes were observed by holding the sample at 145 °C. As the sample was cooled, the intensity of the scattering began to increase. Once the sample was stabilized at room temperature, the scattering intensity had recovered completely and was slightly more intense than the original sample. The increase in intensity after cooling is most likely due to improved long-range order of the PIP segments. While the intensity changes over the course of the annealing experiment, no changes in the d-spacing of the vertically oriented domains were observed, indicating the morphology and spacing of the PIP domains remained constant during thermal annealing above the  $T_g$  of PCMS. This further indicates there are few non-equilibrium effects on the morphology in the as-cast film, as these would likely be relaxed by annealing above the  $T_g$  of PCMS. Additionally, this highlights the significance of the interfacial interactions with the Ag substrate – the fact that the scattering intensity is lost as the polymer softens, but is then fully recovered and does not change, indicates the interfacial interactions with Ag that drive this morphological ordering are strong and not affected by annealing the sample.

#### 4.5.4 Ionomer Thin Film Morphology

To contrast the two polymer architectures, Di-1 and Tri-1 were selected for further characterization as quaternized AEIs. As the quaternized diblock and triblock copolymers are insoluble, they had to be fabricated from pre-cast neutral block copolymer thin films. Therefore, 30, 45 and 60 nm films on Ag-substrates were quaternized with trimethylamine or *N*-methylpiperidine vapor. The theoretical ion exchange capacities (IECs) for Di-1-TMA ( $4.4 \pm 0.4$  mmol g<sup>-1</sup>), Di-1-MPRD ( $3.7 \pm 0.4$  mmol g<sup>-1</sup>), Tri-1-TMA ( $3.8 \pm 0.4$  mmol g<sup>-1</sup>), and Tri-1-MPRD ( $3.3 \pm 0.4$  mmol g<sup>-1</sup>) were calculated from the PCMS:PIP ratio and the molar mass of TMA and MPRD. For the AEI samples, GISAXS was performed in a temperature and humidity-controlled chamber at ambient conditions (room temperature, ~20% RH) or at 60 °C and 95% RH to simulate relevant operating conditions of fuel cells. Films were equilibrated for 1 h before taking measurements.

Figure 4.22 shows horizontal linecuts of Di-1 at 30, 45, and 60 nm thicknesses, functionalized with either TMA or MPRD cationic moieties (see Figure 4.23, Figure 4.24, Figure 4.25, and Figure 4.26 for all 2D GISAXS images). Overall, the AEI thin films exhibit more weakly correlated phase separation compared to their neutral block copolymer backbone thin films.

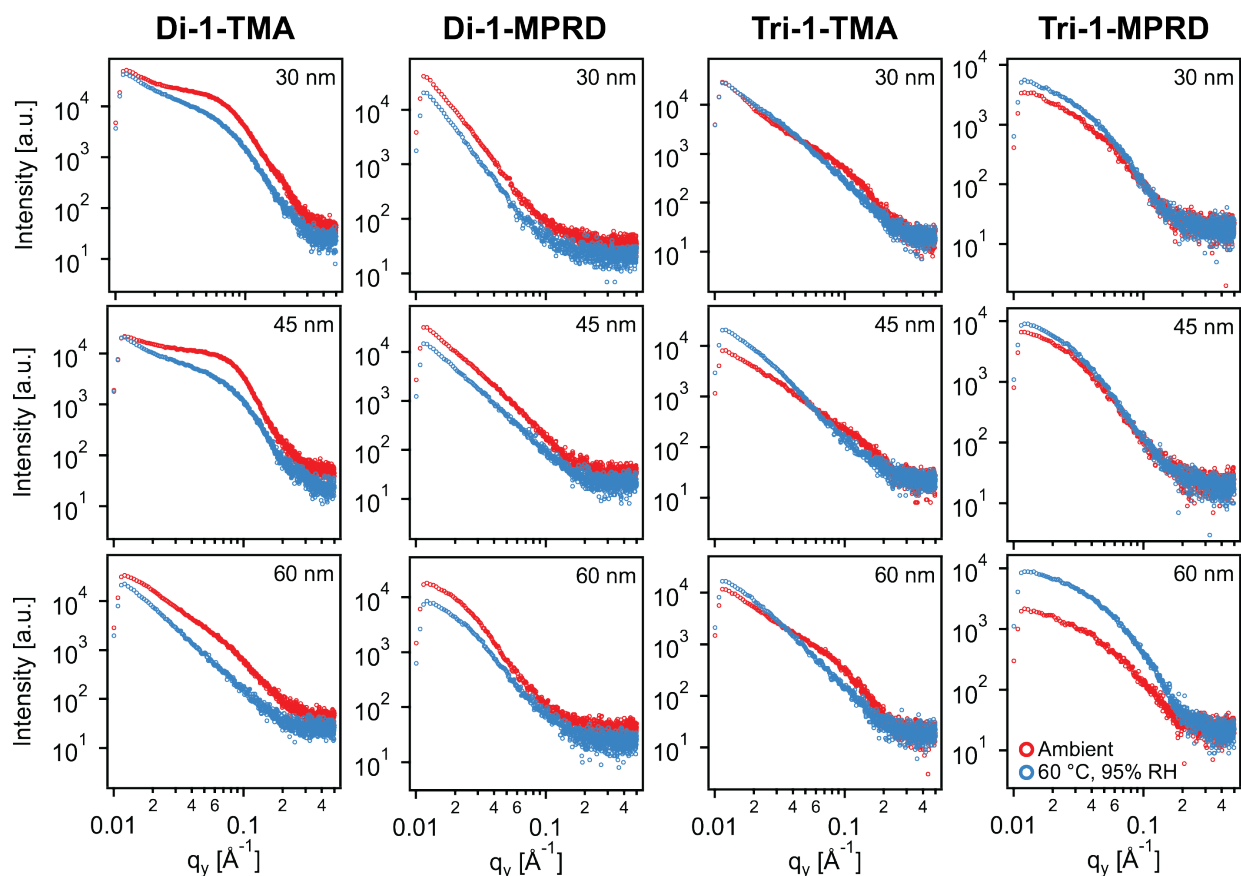


Figure 4.22 Horizontal linecuts from 2D GISAXS images. Red traces are from ambient conditions, blue traces were taken at 60 °C and 95% RH.

The initial ordered morphology of the block copolymer precursors is likely disrupted by quaternary ammonium cations introducing dipole-dipole interactions ( $\sim 1 \text{ kJ mol}^{-1}$ ) with each other that are stronger than the van der Waals (VDW) interactions ( $\sim 0.1\text{--}1 \text{ kJ mol}^{-1}$ ) between the polymer and the Ag surface [353]. While VDW interactions between the neutral precursor and the silver surface initially drove ordering of the thin film morphology, the strong attraction between pendant quaternary ammonium cationic groups leads to an overall decrease in order.

Rigorous analysis of GISAXS requires complex models utilizing the distorted wave born approximation (DWBA) [354–356]. However, it has been shown that  $q_y$  scattering can be described using the Unified Fit approach with reasonable accuracy, despite being a born approximation (BA)-based model [357]. The Unified Fit approach is commonly used to analyze transmission geometry SAXS at multiple structural levels.

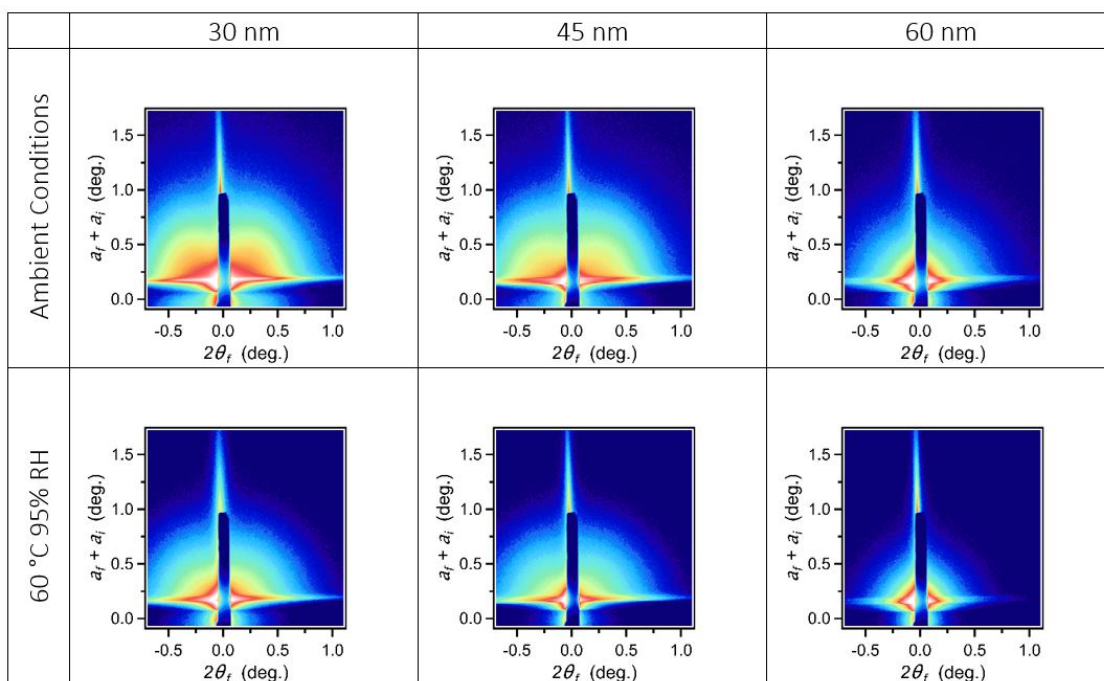


Figure 4.23 Di-1-TMA GISAXS 2D images at ambient conditions (top row) and 60 °C 95% RH (bottom row). From left to right: 30 nm, 45 nm and 60 nm samples.

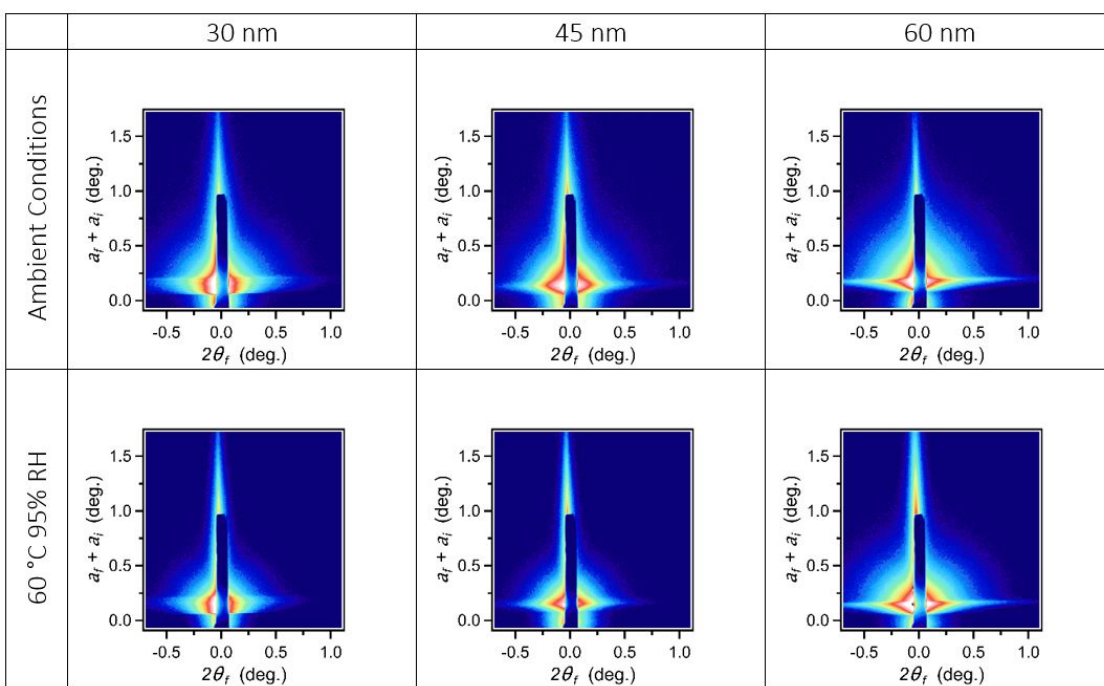


Figure 4.24 Di-1-MPRD GISAXS 2D images at ambient conditions (top row) and 60 °C 95% RH (bottom row). From left to right: 30 nm, 45 nm and 60 nm samples.

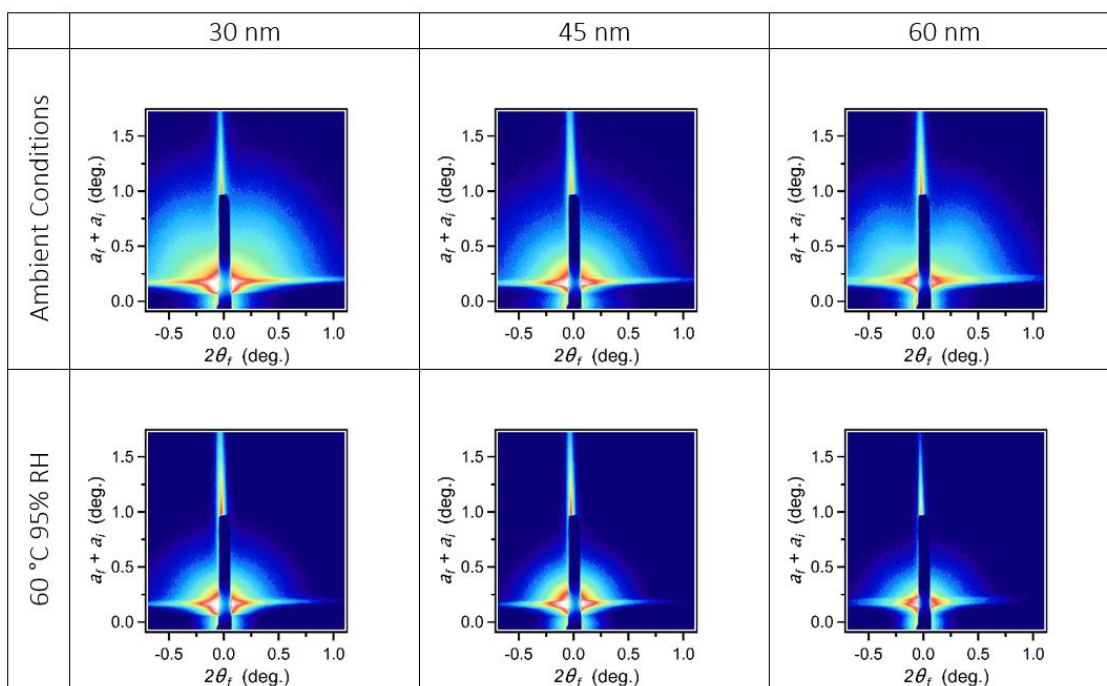


Figure 4.25 Tri-1-TMA GISAXS 2D images at ambient conditions (top row) and 60 °C 95% RH (bottom row). From left to right: 30 nm, 45 nm and 60 nm samples.

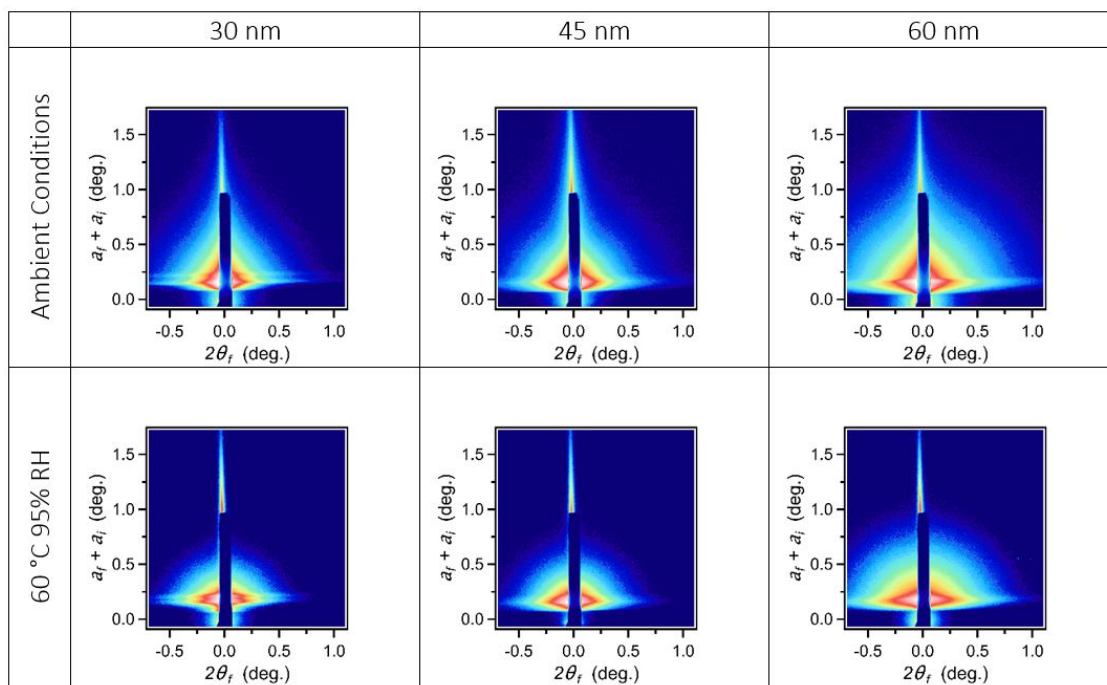


Figure 4.26 Tri-1-MPRD GISAXS 2D images at ambient conditions (top row) and 60 °C 95% RH (bottom row). From left to right: 30 nm, 45 nm and 60 nm samples.

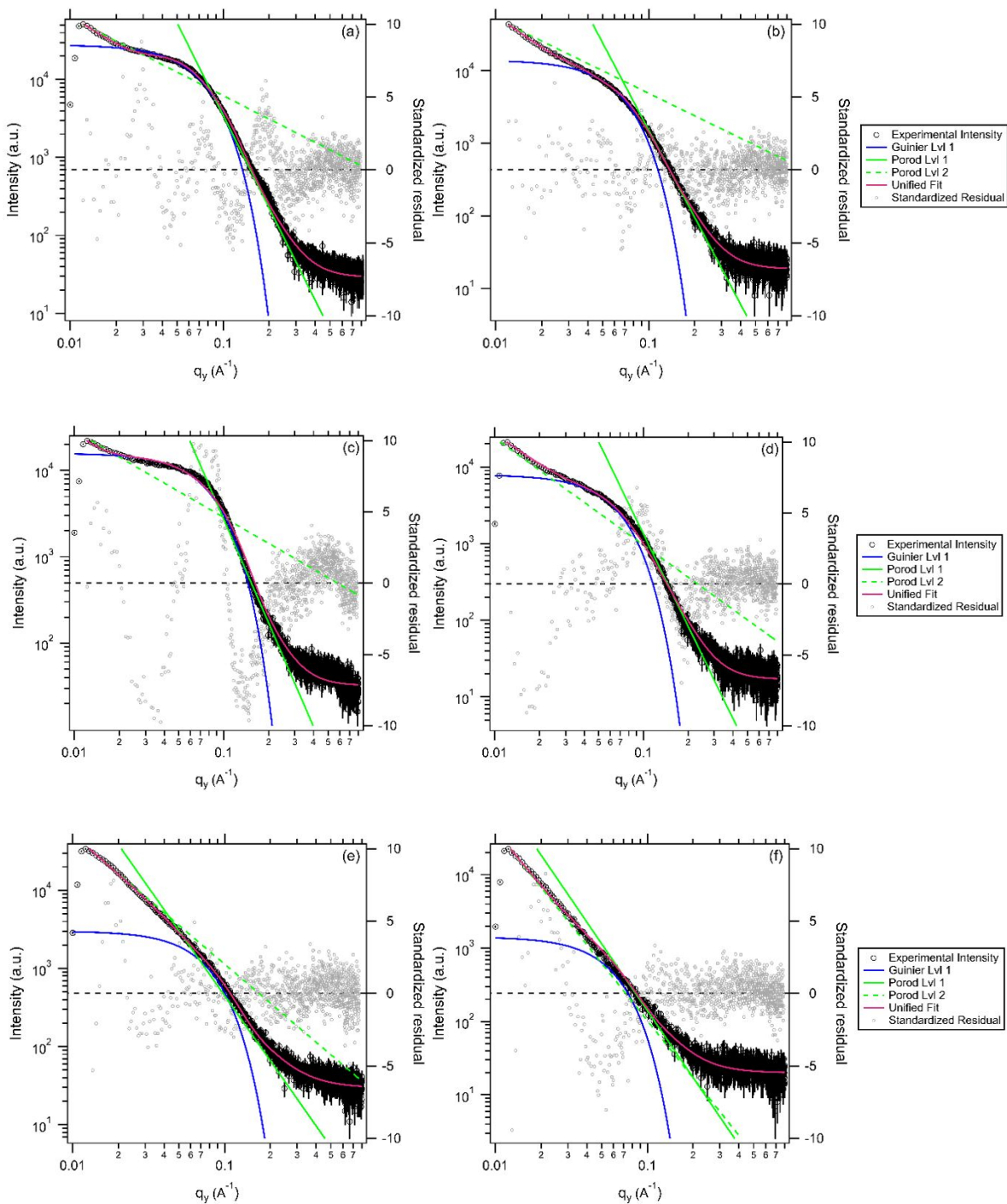


Figure 4.27 Unified Fit Modeling for Di-1-TMA. (a) Di-1-30-TMA, dry. (b) Di-1-30-TMA, 60 °C and 95% RH. (c) Di-1-45-TMA, dry. (d) Di-1-45-TMA, 60 °C and 95% RH. (e) Di-1-60-TMA, dry. (f) Di-1-60-TMA, 60 °C and 95% RH.

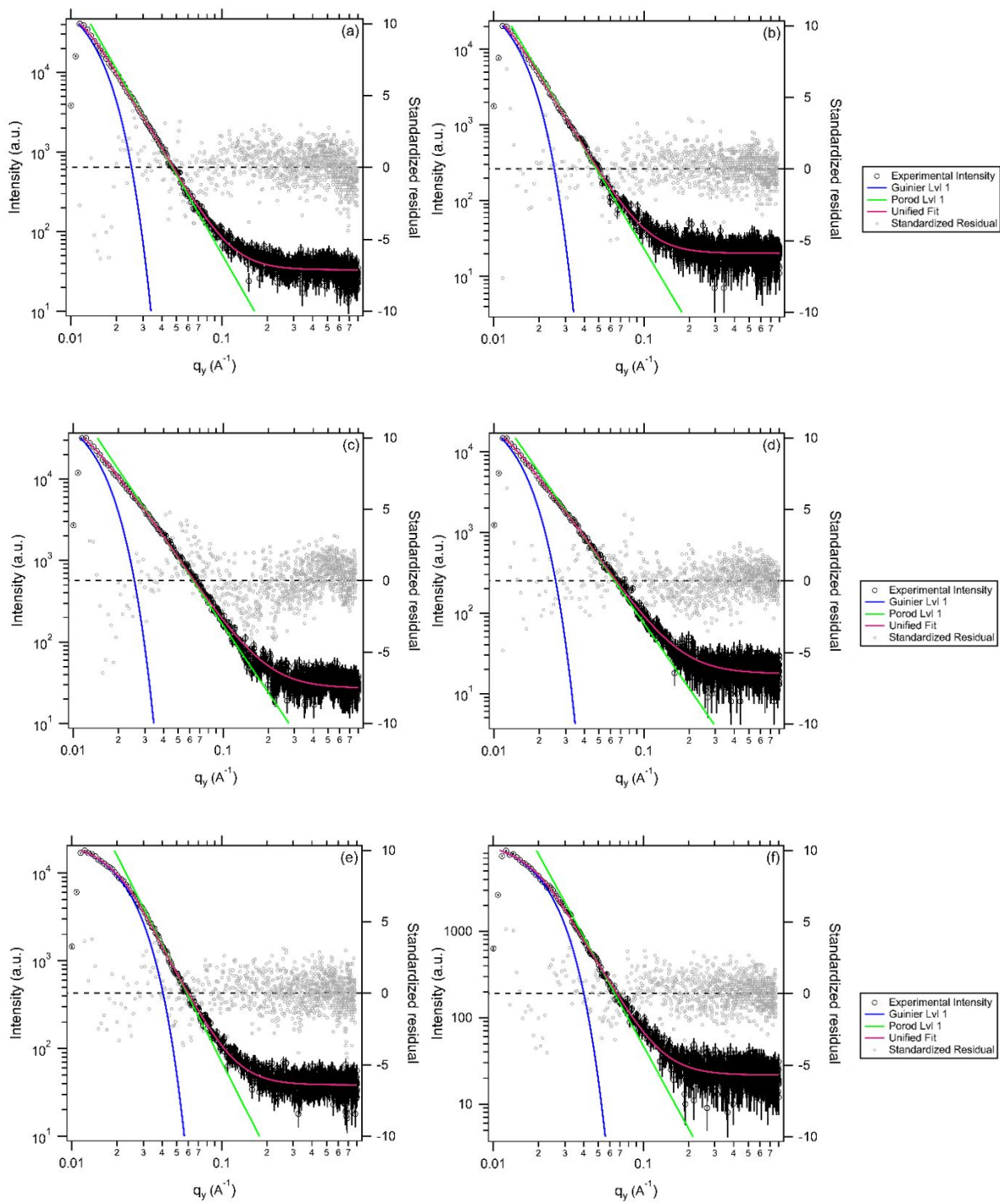


Figure 4.28 Unified Fit Modeling for Di-1-MPRD. (a) Di-1-30-MPRD, dry. (b) Di-1-30-MPRD, 60 °C and 95% RH. (c) Di-1-45-MPRD, dry. (d) Di-1-45-MPRD, 60 °C and 95% RH. (e) Di-1-60-MPRD, dry. (f) Di-1-60-MPRD, 60 °C and 95% RH.

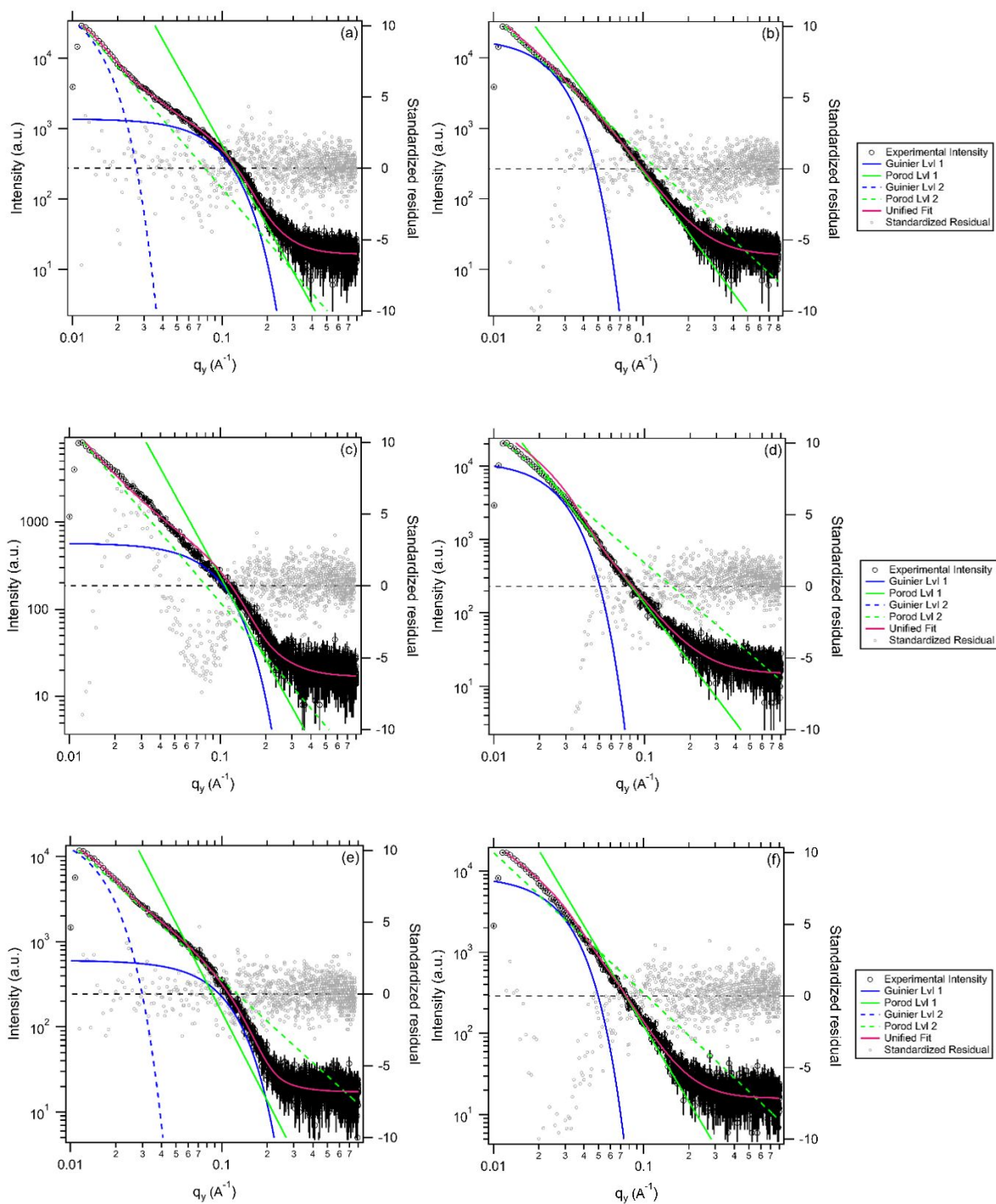


Figure 4.29 Unified Fit Modeling for Tri-1-TMA. (a) Tri-1-30-TMA, dry. (b) Tri-1-30-TMA, 60 °C and 95% RH. (c) Tri-1-45-TMA, dry. (d) Tri-1-45-TMA, 60 °C and 95% RH. (e) Tri-1-60-TMA, dry. (f) Tri-1-60-TMA, 60 °C and 95% RH.

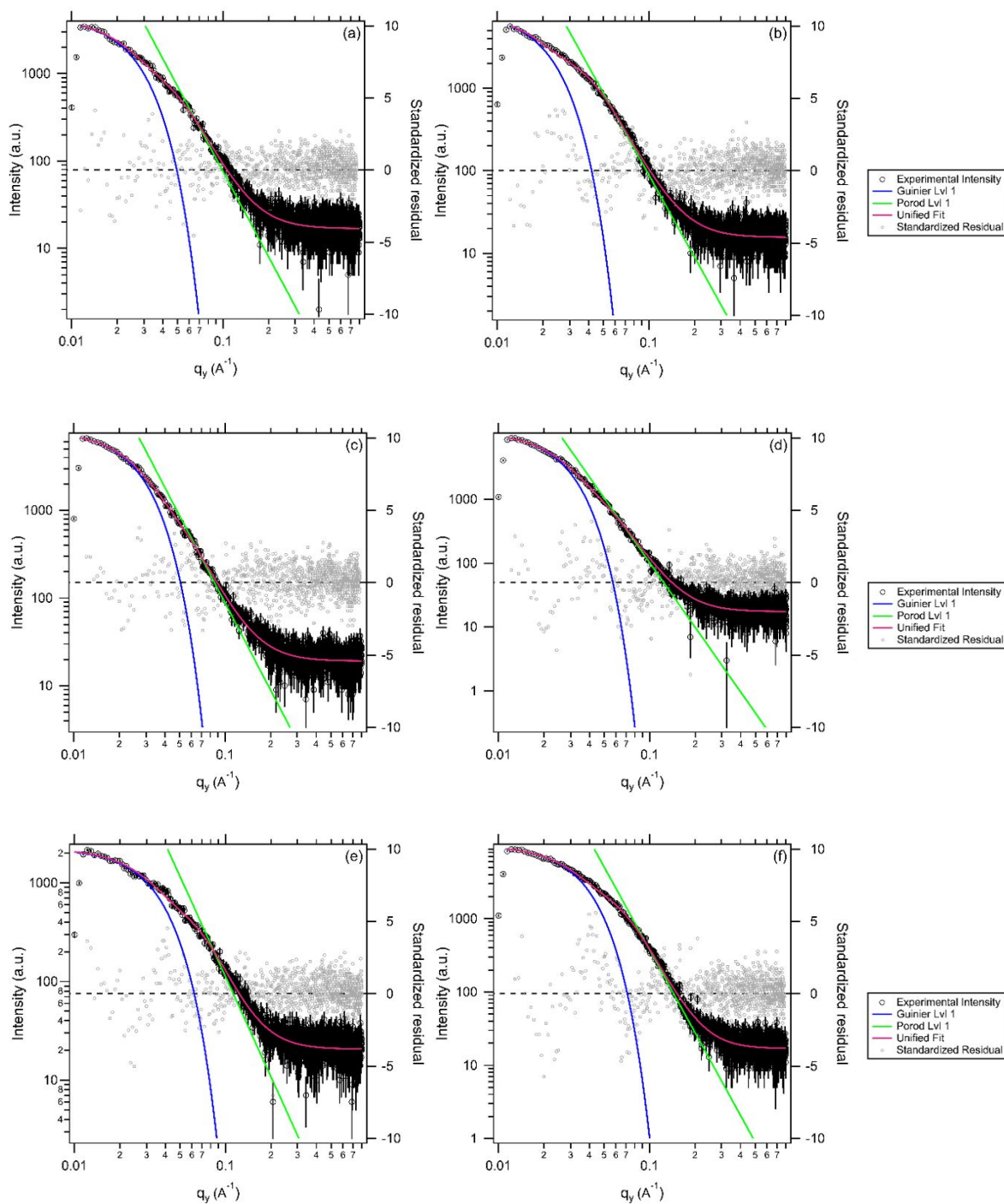


Figure 4.30 Unified Fit Modeling for Tri-1-MPRD. (a) Tri-1-30-MPRD, dry. (b) Tri-1-30-MPRD, 60 °C and 95% RH. (c) Tri-1-45-MPRD, dry. (d) Tri-1-45-MPRD, 60 °C and 95% RH. (e) Tri-1-60-MPRD, dry. (f) Tri-1-60-MPRD, 60 °C and 95% RH.



Table 4.4 Unified Fit Model Parameters for Di-1-TMA Samples.

Dry	$G_1$	error	$R_{g1}$	error	$B_1$	error	$P_1$	error	$B_2$	error	$P_2$	error
30nm	27,882	31	24.86	0.03	0.389	0.019	4.00	-	624.6	78.9	1.00	0.03
45nm	15,801	20	22.10	0.02	0.275	0.003	4.00	-	286.5	47.3	1.00	0.11
60nm	3,007	42	23.31	0.15	0.766	0.012	2.77	0.05	24.9	1.0	1.66	0.01
Wet	$G_1$	error	$R_{g1}$	error	$B_1$	error	$P_1$	error	$B_2$	error	$P_2$	error
30nm	13,963	24	28.11	0.12	0.152	0.001	4.00	-	446.8	32.8	1.07	0.02
45nm	7,879	13	27.20	0.06	0.134	0.001	4.00	-	38.6	3.0	1.40	0.02
60nm	1,421	110	30.91	1.08	0.130	0.028	3.03	0.11	0.3	0.1	2.60	0.01

Table 4.5 Unified Fit Model Parameters for Di-1-MPRD Samples.

Dry	$G_1$	error	$R_{g1}$	error	$B_1$	error	$P_1$	error
30nm	113,730	282	156.17	2.26	0.025	0.001	3.32	0.01
45nm	82,891	2,417	151.04	2.42	0.294	0.007	2.74	0.01
60nm	25,187	143	86.06	0.31	0.030	0.002	3.37	0.02
Wet	$G_1$	error	$R_{g1}$	error	$B_1$	error	$P_1$	error
30nm	62,177	1,297	159.73	1.45	0.011	0.001	3.33	0.02
45nm	38,480	1,081	150.61	2.28	0.156	0.005	2.68	0.01
60nm	11,785	111	87.54	0.56	0.031	0.003	3.18	0.03

Table 4.6 Unified Fit Model Parameters for Tri-1-TMA Samples.

Dry	$G_1$	error	$R_{g1}$	error	$B_1$	error	$P_1$	error
30nm	1,380	38	18.74	0.06	0.096	0.037	3.78	0.26
45nm	571	17	17.54	0.31	0.172	0.080	3.14	0.31
60nm	601	45	17.08	0.38	0.052	0.006	3.46	0.12
Dry	$G_2$	error	$R_{g2}$	error	$B_2$	error	$P_2$	error
30nm	75,138	1208	152.97	1.17	0.47	0.04	2.48	0.02
45nm	-	-	-	-	1.14	0.03	2.02	0.01
60nm	20,276	317	122.15	1.27	8.70	2.19	1.61	0.07
Wet	$G_1$	error	$R_{g1}$	error	$B_1$	error	$P_1$	error
30nm	19,100	276	74.69	1.98	0.337	0.015	2.86	0.01
45nm	11,660	139	68.02	2.37	0.273	0.004	2.69	0.01
60nm	8555	499	64.07	2.17	0.099	0.010	3.10	0.04
Wet	$G_2$	error	$R_{g2}$	error	$B_2$	error	$P_2$	error
30nm	-	-	-	-	4.30	1.12	1.98	0.05
45nm	-	-	-	-	8.08	1.89	1.77	0.04
60nm	-	-	-	-	5.84	2.02	1.73	0.06

Table 4.7 Unified Fit Model Parameters for Tri-1-MPRD Samples.

Dry	$G_1$	error	$R_{g1}$	error	$B_1$	error	$P_1$	error
30nm	4,367	53.72	70.04	0.91	0.044	0.004	3.24	0.03
45nm	8,090	62.89	68.10	0.45	0.044	0.003	3.31	0.03
60nm	2,238	25.05	51.40	0.69	0.047	0.006	3.38	0.05
Wet	$G_1$	error	$R_{g1}$	error	$B_1$	error	$P_1$	error
30nm	8,233	83.36	86.65	0.93	0.044	0.003	3.31	0.03
45nm	11,438	78.85	70.72	0.40	0.044	0.003	3.37	0.02
60nm	10,047	22.08	52.40	0.29	0.066	0.003	3.76	0.02

The Unified Fit model can describe the fractal scattering of weakly correlated systems by their fractal dimensions from the Porod exponent ( $P$ ) and radius of gyration ( $R_g$ ) from fitting of the Porod and Guinier regions, respectively.  $R_g$  characterizes the size of the domains, while  $P$  can provide insight into the particle shape, where  $P = 1, 2, 3,$  or  $4$  refers to rigid rods, lamellae, cylinders, or spheres. Porod exponents can also indicate particle arrangement in a 2D ( $1 < P < 2$ ) or 3D ( $2 < P < 3$ ) mass fractal [358].

The scattering profiles of the quaternized films still show distinct Guinier areas and Porod slopes, therefore the Unified Fit model was selected to further interpret the changes with samples thickness, quaternary ammonium cation, and humidification. Each individual Unified Fit can be seen in Figure 4.27, Figure 4.28, Figure 4.29, and Figure 4.30. The fitted parameters for Di-1 and Tri-1 quaternized with TMA and MPRD are summarized in Table 4.4, Table 4.5, Table 4.6, and Table 4.7. Within this experimental  $q$  range, a portion of level 2 Porod scattering was also observed in some samples. In most cases this region only consists of few data points, so these fits are not of substantial quality and will therefore not be discussed, but are included in Table 4.4, Table 4.5, Table 4.6, and Table 4.7.

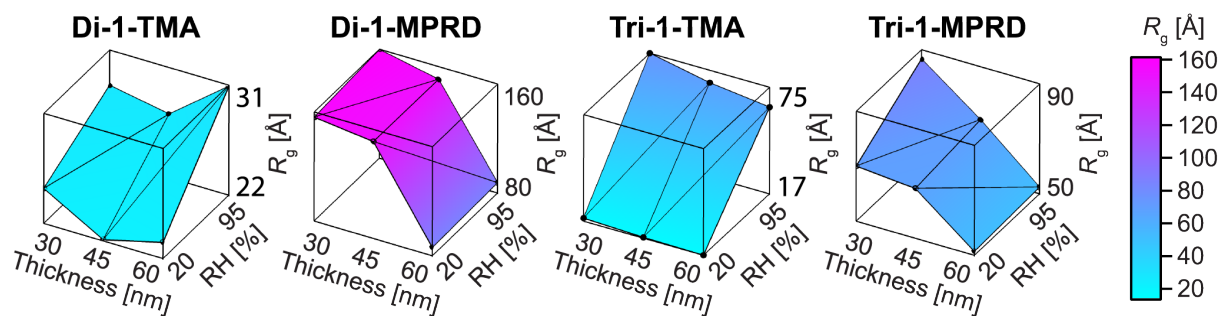


Figure 4.31 Surface plots illustrating the correlation between film thickness and relative humidity on the radius of gyration for Di-1-TMA, Di-1-MPRD, Tri-1-TMA, and Tri-1-MPRD (from left to right). A global color scale to the right is provided for comparison of the radius of gyration across all samples investigated.

Surface plots illustrating the correlation between film thickness and relative humidity on the radius of gyration for all ionomer thin films investigated is shown in Figure 4.31. The ionomers quaternized with TMA have a smaller ambient  $R_g$  than those quaternized with MPRD, indicating the films quaternized with MPRD have a higher ambient water uptake. Further, the ambient  $R_g$  of Tri-1-TMA  $<$  Di-1-TMA and Tri-1-MPRD  $<$  Di-1-MPRD, which also trends with their

theoretical IECs.

Generally, across all of the samples investigated,  $R_g$  increases when the film is hydrated, indicating the spacing of the polymer coils increases as the film swells and takes up water. Increasing the sample thickness appears to mainly decrease  $R_g$  in both ambient and hydrated conditions, with the only exception being the Di-1-TMA samples where  $R_{g,30nm} > R_{g,60nm} > R_{g,45nm}$ . This trend is in contrast to what has been reported for PFSA ionomers, where water uptake decreases with film thickness from  $\sim 20$ – $100$  nm due to confinement effects, and then a transition from ordered to disordered morphology causes water uptake to increase in thinner films  $< 20$  nm [186, 206, 359]. This contrast can be attributed to a major differences between the Nafion<sup>®</sup> fluorocarbon backbone and these block copolymer-based ionomers – while Nafion<sup>®</sup> typically aligns parallel to the substrate interface, these diblock and triblock-based ionomers align mainly perpendicular to the substrate, and perpendicular alignment is driven by interactions at the Ag interface. As thickness of the ionomer decreases, the interfacial interactions with the surface become more significant and drive perpendicular alignment and order of the domains, thus increasing water uptake. This can also be observed by comparing the intensity difference between horizontal and vertical linecuts (Figure 4.32 and Figure 4.33). When the horizontal and vertical linecuts from a 2D GISAXS image are of similar intensity, it indicates the phase separation does not favor a particular orientation and is more or less composed of isotropic, randomly oriented domains and features a mixture of domain orientations with no preference. In Figure 4.32 and Figure 4.33, the horizontal linecuts are more intense than the vertical linecuts, indicating a perpendicular orientation is more prominent throughout the sample. It can be noted in Figure 4.32 and Figure 4.33 that in 30 nm samples, the intensity difference between the horizontal and vertical linecut is greater than their difference at 60 nm. This further emphasizes that in thinner films, the interfacial Ag-ionomer interactions are more prominent and drive perpendicular alignment and ordering, which ultimately leads to a higher water uptake in thinner samples.

After equilibration at 60 °C and 95% RH, the Di-1-TMA samples have the smallest humidified  $R_g$ , and the Tri-1-TMA samples have the largest. The GISAXS horizontal linecuts for the Di-1-TMA samples provide evidence that these thin films exhibit the most ordered phase separation. Di-1-30-TMA and Di-1-45-TMA are also the only two samples which exhibit a Porod exponent,  $P \sim 4$ , indicating the scattering of vertically arranged spherical domains.

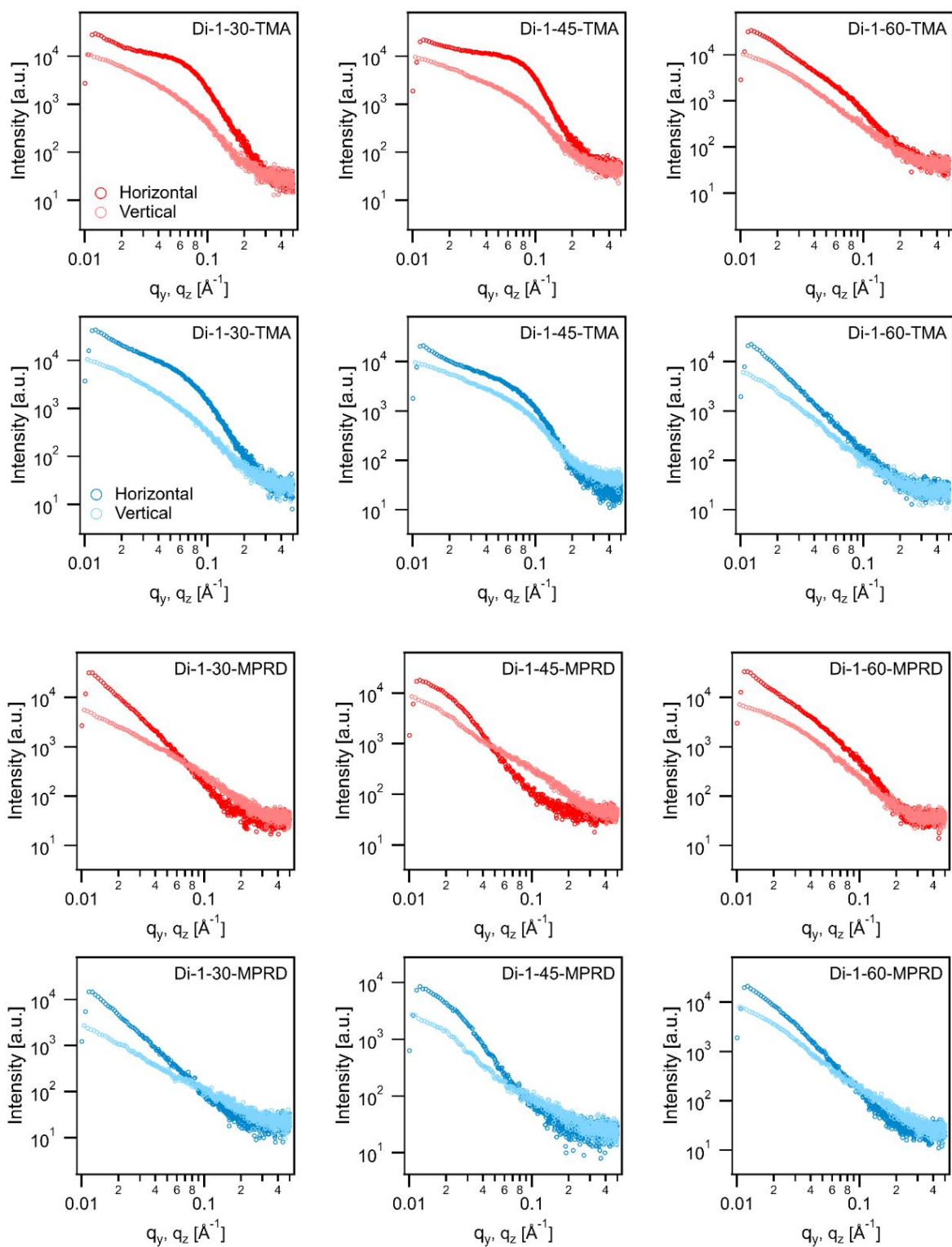


Figure 4.32 Comparison of horizontal and vertical linecuts for Di-1-TMA and Di-1-MPRD, at dry (red traces) and 60 °C and 95% RH (blue traces).

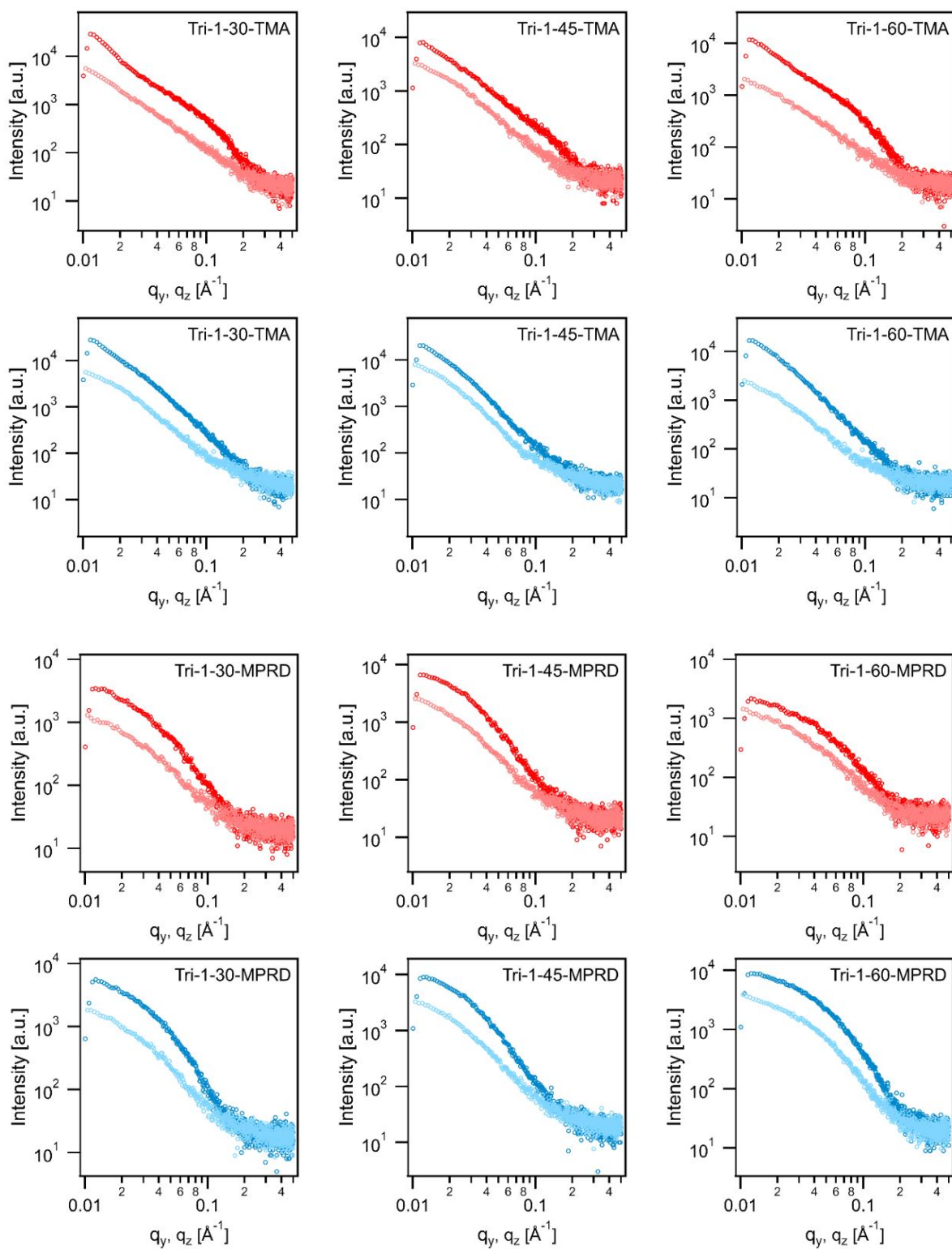


Figure 4.33 Comparison of horizontal and vertical linecuts for Tri-1-TMA and Tri-1-MPRD, at dry (red traces) and 60 °C and 95% RH (blue traces).

The Di-1-TMA samples likely show the lowest water uptake due to the formation of spherical domains. Di-1-TMA also has the highest IEC of the ionomers under investigation, meaning it also contains more cationic moieties that can act as dipoles. The cationic moiety dipoles can interact with each other and cause clustering, which can lower conductivity and water uptake in bulk AEMs [360].

For all other samples, which also generally show less correlation in their phase separation,  $2.7 < P < 3.8$ , indicating the scattering of mainly cylindrical domains in a 3D mass fractal. Comparatively, Tri-1-TMA shows less phase separation, and ultimately exhibits the largest humidified  $R_g$ . In the case of films quaternized with MPRD, the humidified  $R_g$  of Tri-1-MPRD  $>$  Di-1-MPRD, owing to the more obvious ordered phase separation in Tri-1-MPRD than in Di-1-MPRD. This also indicates the polymer architecture, i.e. diblock versus triblock, or their respective molecular weights ( $M_w$ , Di-1 = 28,500 g mol<sup>-1</sup>,  $M_w$ , Tri-1 = 43,800 g mol<sup>-1</sup>) influence the morphological ordering and water uptake, along with the chemistry of the cationic moiety.

Additionally, the change in  $R_g$  between ambient and humidified conditions can provide some insight into the water uptake and swelling in the sample. The percent change in  $R_g$ , or  $\frac{\Delta R_g}{R_{g0}}$ , varies depending on the quaternary ammonium cation (see Figure 4.34). Di-1-TMA (13-33%) and Tri-1-TMA (275-298%) both have a larger percent change in  $R_g$  than Di-1-MPRD (1-2%) and Tri-1-MPRD (2-24%) at all thicknesses (with the one exception where the percent change in  $R_g$  for Tri-1-30-MPRD  $>$  Di-1-30-TMA). This indicates that generally, MPRD quaternized ionomers experienced less of a change when going from ambient conditions to 60 °C and 95% RH.

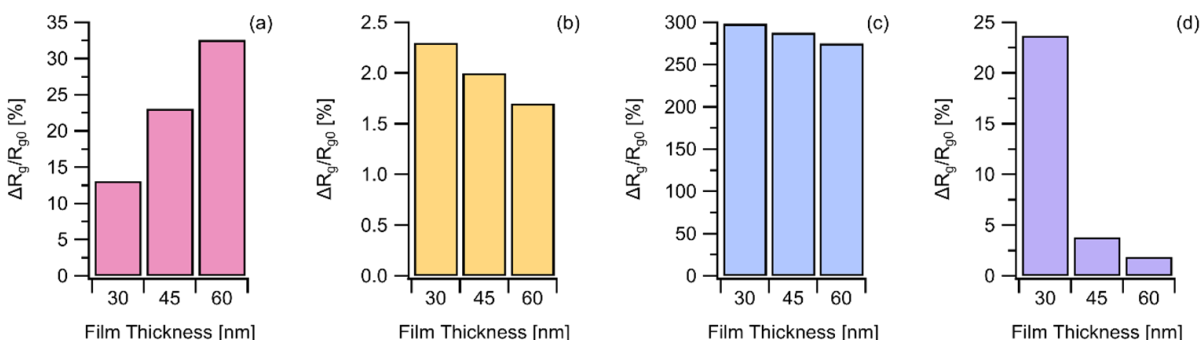


Figure 4.34 Percent change in  $R_g$  with hydration for Di-1-TMA samples (a), Di-1-MPRD samples (b), Tri-1-TMA samples (c) and Tri-1-MPRD samples (d).

## 4.6 Conclusions

In this work, AEIs were rationally designed from a tunable block copolymer system composed of PIP and PCMS. The thin film morphology of the neutral block copolymer precursors was investigated on plain silicon or on Ag, a relevant component of non-Pt catalysts for AEI-devices. A perpendicularly oriented morphology was observed on Ag, while no phase separation was observed on silicon, indicating Ag-polymer interfacial interactions drove the phase separation and assembly. AFM imaging confirmed the phase-separated morphology propagated to the polymer-air interface. Annealing above the T<sub>g</sub> of the neutral block copolymer did not alter the thin film morphology, emphasizing the strength of the interactions at the Ag-polymer interface. The d-spacing of the PIP cylinders in the thin film samples ( $d_s = 8\text{--}12$  nm) differed from the bulk film samples ( $d_s = 20\text{--}30$  nm) due to confinement effects.

AEIs were then fabricated by quaternizing with trimethylamine or *N*-methylpiperidine vapor to functionalize the block copolymer backbone with TMA or MPRD quaternary ammonium cations. The effect of polymer architecture, quaternary ammonium cation, IEC, and film thickness on thin film morphology at an Ag interface were characterized at ambient conditions and at 60 °C and 95% RH. In this system, there is a complex interplay between the Ag-interfacial interactions, confinement effects, and dipole-dipole interactions between the cationic moieties that all influence the thin film morphology and water swelling. Namely, water uptake increases as film thickness decreases – Ag-ionomer interfacial interactions drive the PIP domains to align vertically, and the improved order leads to an increase in water uptake for thinner films, observed by their radius of gyration. Additionally, AEIs with MPRD cationic moieties have a higher ambient water uptake than films with TMA cationic moieties. AEIs with MPRD cationic moieties also exhibit a smaller change in  $R_g$  between ambient and humidified conditions, indicating they may swell less than films with TMA cationic moieties. Based on these observations, design rules for block copolymer-based AEI systems at an Ag interface can be recommended:

- (i) Quaternizing with MPRD may be desirable to achieve improved water uptake in lower RH applications, as indicated by having a larger  $R_g$  at ambient conditions
- (ii) Quaternizing with MPRD may also lead to less swelling for thinner films, as indicated by the percent change in  $R_g$ , which could promote a better ionomer-Ag interface. When the



ionomer does not swell as dramatically, there is less risk for it to delaminate from the catalyst surface and create interfacial resistances in the electrode

- (iii) Utilizing a triblock over a diblock architecture further suppressed the swelling of the ionomer quaternized with MPRD by enhancing the nanoscale phase separation. Choosing a triblock architecture in conjunction with MPRD will likely lead to the most favorable ionomer-catalyst interface.

This work exhibits the benefit of utilizing block copolymer-based AEIs to achieve thin film nanoscale phase separation. Although the discrete perpendicular alignment observed for the neutral block copolymer precursors becomes more disordered after functionalization with quaternary ammonium cations, nanoscale phase separation is still maintained with a preferential vertical orientation. In contrast, most PFSA ionomer thin films show a morphology aligned parallel to the substrate [186, 194, 195, 197], which could potentially lead to transport resistances [211–213]. Achieving sufficient phase separation in an AEI thin film should lead to improved anion conduction in the catalyst layer, as it has been shown in bulk polymer electrolyte membranes [326] and in thin films [192, 213]. Further, domain alignment perpendicular to the catalyst surface should be ideal for water, reactant and product species, and ion transport, mitigating resistances associated with the parallel alignment of domains that has been observed for PFSA ionomer thin films. These findings demonstrate how block copolymer precursors with tunable characteristics can be leveraged and optimized to provide a rational framework for designing next-generation anion exchange ionomers.

## CHAPTER 5

### EVALUATING THE EFFECT OF IONOMER CHEMICAL COMPOSITION IN SILVER- IONOMER CATALYST INKS TOWARD THE OXYGEN EVOLUTION REACTION BY HALF-CELL MEASUREMENTS AND WATER ELECTROLYSIS

This chapter is modified from a journal article submitted to *Electrochimica Acta*.

Nora C. Buggy,<sup>27</sup> Ivy Wu,<sup>28</sup> Yifeng Du,<sup>29</sup> Ria Ghosh,<sup>30</sup> Mei-Chen Kuo,<sup>31</sup> Morgan S. Ezell,<sup>32</sup>  
James M. Crawford,<sup>33</sup> Soenke Seifert,<sup>34</sup> Moises A. Carreon,<sup>35</sup> E. Bryan Coughlin,<sup>36</sup> and Andrew  
M. Herring<sup>37</sup>

#### 5.1 Motivation

After understanding the morphology and water uptake of ionomer thin films on silver, the final step toward elucidating the structure-property-performance relationship was to evaluate the electrochemical performance of different ionomer-silver catalyst inks. In this work, the learnings from previous fundamental studies are demonstrated in a more complex system. *Hypothesis 4* is probed by studying the oxygen evolution reaction (OER) kinetics and performance of a set of ionomer-silver catalyst inks in a separated-anode half-cell study. *Hypothesis 4* is anticipated by all of our previous results, namely that interactions are dictated by the chemistry of the backbone and quaternary ammonium cation, and that the thin film morphology is also dependent on the ionomer architecture. Therefore, it is justified that the quaternary ammonium cationic moiety, along with the block copolymer backbone, will affect the OER kinetics and performance. Finally, the optimized ionomer-silver catalyst ink is tested in an AEM electrolyzer, utilizing the PE-based AEM developed in *Chapter 2*.

---

<sup>27</sup>Primary researcher and author

<sup>28</sup>AEM SAXS

<sup>29</sup>Co-author, polymer chemist

<sup>30</sup>Co-author, polymer chemist

<sup>31</sup>Co-author, polymer chemist

<sup>32</sup>Co-author, research assistant

<sup>33</sup>Co-author, surface area characterization

<sup>34</sup>Co-author, X-ray scattering expert and beamline scientist

<sup>35</sup>Co-author, surface area characterization

<sup>36</sup>Co-author, polymer expert

<sup>37</sup>Co-author, advisor and corresponding author

## 5.2 Abstract

The effect of anion exchange ionomer (AEI) chemistry on the kinetics of the oxygen evolution reaction (OER) was systematically studied in both half-cell and single-cell electrolysis experiments. OER was studied in 1 M  $\text{K}_2\text{CO}_3$  at 50 °C using an array of ionomer-silver catalyst inks deposited on Ni foam. Different ionomer modifications were investigated to optimize the OER performance. The AEI used in this work features a block copolymer backbone of polychloromethylstyrene-*b*-polycyclooctene-*b*-polychloromethylstyrene which was functionalized with either benzyltrimethylammonium (TMA) or benzylmethylpiperidinium (MPRD) quaternary ammonium cations. Using an MPRD quaternary ammonium cation shifted the rate determining step at high overpotentials, ultimately providing enhanced performance. Increasing the catalyst ink dilution was also found to substantially improve mass activity and catalyst utilization (increase from 35 to 88  $\text{A g}^{-1} \text{Ag}$ ), likely by reducing the ionomer thickness and decreasing transport resistances. In the final ionomer modification, the Ni foam substrate was leveraged to partially hydrogenate the polycyclooctene midblock to be polyethylene-like at the Ni interface. A significant increase in the electrochemical surface area ( $C_{dl}$  increased from 8.8 to 20.8  $\text{mF cm}^{-2}$ ) and performance (by 47  $\text{mA cm}^{-2}$  or 29  $\text{A g}^{-1} \text{Ag}$ ) was observed with the incorporation of polyethylene. Kinetic results from half-cell experiments were validated via single-cell anion exchange membrane electrolysis experiments, where the optimized electrode displayed enhanced performance in both 1 M  $\text{K}_2\text{CO}_3$  and in DI  $\text{H}_2\text{O}$ .

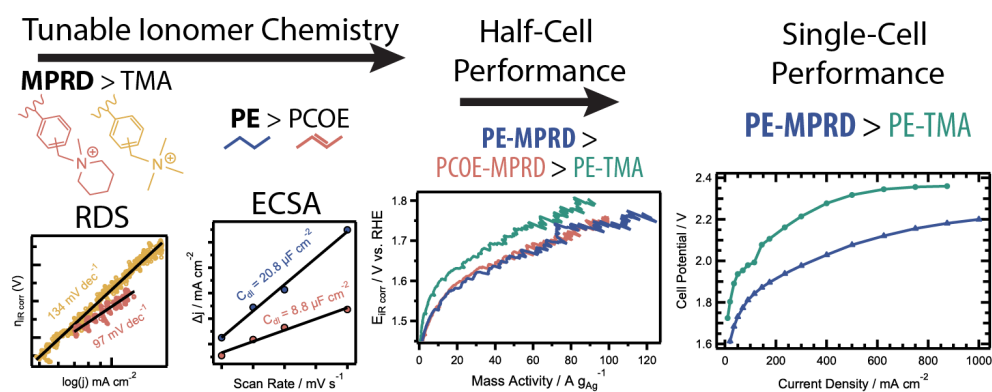


Figure 5.1 Graphical abstract.

### 5.3 Introduction

Electrochemical production of hydrogen via water electrolysis is a key technology necessary for the development of a sustainable hydrogen-based energy infrastructure [8, 361]. Alkaline electrolyzers, which utilize 30–40 wt% aqueous KOH solutions, are a commercially mature technology, but various drawbacks inherent to their architecture, such as limited lifetime, poor efficiency, large footprint, and low power density have left substantial room for improvement even for large scale hydrogen production. Proton exchange membrane (PEM) and anion exchange membrane (AEM) water electrolyzers provide enhanced conversion efficiencies with a smaller footprint. Despite the promising performance of PEM water electrolyzers (PEMWEs), the high cost of the required platinum group metal (PGM) catalysts (iridium oxide and platinum) in addition to their corrosion-resistant cell components position PEMWEs to be prohibitively expensive for large scale commercialization [42].

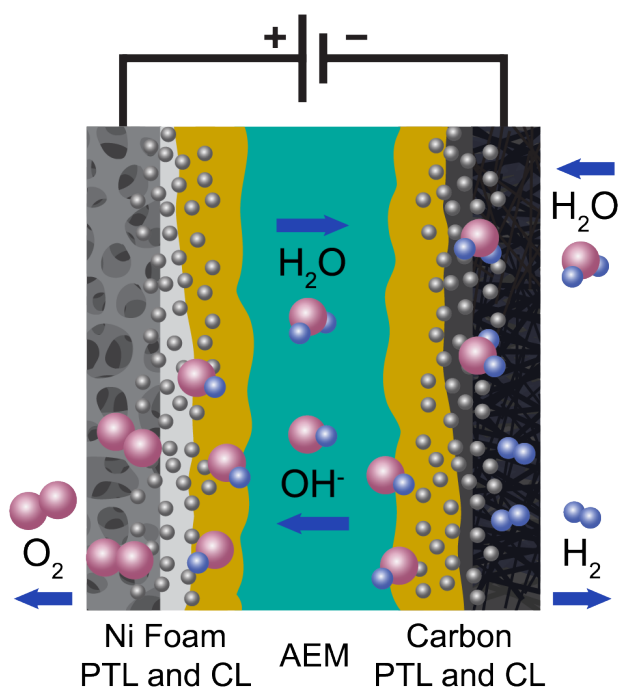
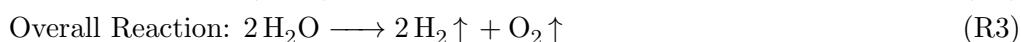
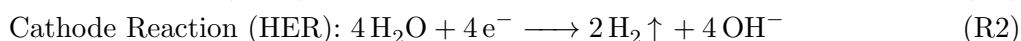
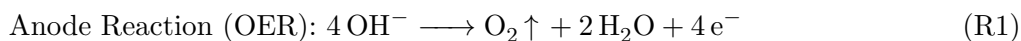


Figure 5.2 Diagram of an anion exchange membrane (AEM) water electrolysis cell, including detailed interfaces of the Ni foam and carbon paper porous transport layers (PTLs) and catalyst layers (CLs).

Anion exchange membrane water electrolyzers (AEMWEs) operate in alkaline media which allows for the utilization of less expensive, more abundant non-PGM catalysts, thus combining

the advantages of alkaline electrolyzers and PEMWEs. Anion exchange membranes (AEMs) are polymer electrolytes with covalently bound cationic functional groups that facilitate the transport of anions (typically  $\text{OH}^-$  or  $\text{CO}_3^{2-}$  across the device from cathode to anode. The electrochemical reactions in an AEMWE are the oxygen evolution reaction (OER) at the anode and the hydrogen evolution reaction (HER) at the cathode. A schematic of an AEMWE is given in Figure 5.2.

The half-cell reactions and overall reaction for water electrolysis in alkaline media are,



At the cathode, water is reduced to hydrogen and hydroxide ions which move across the AEM to the anode where they are oxidized and yield oxygen, water, and electrons. Since water is both a product and reactant, water produced at the anode would ideally diffuse through the AEM to the cathode; however, electro-osmotic drag tends to carry water in the opposite direction, i.e. the direction of hydroxide ion transport, depending on the membrane thickness. Ideally, an AEMWE would utilize pure water, but in practice, the current densities achieved in pure water are poor. For this reason, AEMWEs commonly report utilizing a supporting electrolyte such as aqueous KOH or  $\text{K}_2\text{CO}_3$ , typically 0.01 M–1.0 M [34, 362, 363], which improves the performance compared to using water alone [364]. Previous studies have shown how the kinetics for OER improve (e.g. Tafel slope decreases from ca. 160-274 mV dec<sup>-1</sup> to 53-72 mV dec<sup>-1</sup> [365]) as the pH increases from 7 (neutral water) to 14 (1 M KOH) [366, 367]. Additionally, while KOH-fed electrolyzers outperform  $\text{K}_2\text{CO}_3$ -fed electrolyzers at the same molar concentration, the performance of  $\text{K}_2\text{CO}_3$  outperforms KOH at the same pH [368]. A recent modeling study suggested that the addition of  $\text{OH}^-$  reduces ohmic resistances of the AEM and catalyst layer and improves reaction kinetics by increasing the electrochemically active surface area [369].

In the case of using a supporting electrolyte such as  $\text{K}_2\text{CO}_3$ , after hydroxide ions are produced at the cathode, a mixture of hydroxide, along with the present carbonate (and possibly bicarbonate) ions diffuse toward the anode. At the anode, carbonate and bicarbonate anions are purged from the system via the following reactions [370, 371]:



Hydroxide ions are then oxidized to water and  $\text{O}_2$  according to reaction (R1). The self-purging reactions are well documented for anion exchange membrane fuel cells (AEMFCs) [372]. In the case of the oxygen reduction reaction (ORR) in AEMFCs, and likely in OER in AEMWEs, it is assumed that  $\text{HCO}_3^-$  and  $\text{CO}_3^{2-}$  are not directly participating in the electrochemical reactions [373, 374]. The reactions for electrolysis with carbonate-based electrolytes where  $\text{CO}_3^{2-}$  ions participate directly to realize the production of both  $\text{H}_2$ ,  $\text{O}_2$  and  $\text{CO}_2$  are extremely sluggish and require a cell voltage upwards of 3 V [367, 375]. Operating beneath this voltage further ensures that during electrolysis with supporting carbonate-based electrolytes, only  $\text{OH}^-$  participates via the conversion of  $\text{CO}_3^{2-}$  and  $\text{HCO}_3^-$  in reactions (R4) and (R5).

Much recent work has focused on the development of AEMs with high ionic conductivity, water management, mechanical integrity, and resiliency to hydroxide-induced degradation mechanisms. Fewer reports exist on the optimization of the electrode and catalyst layer. Fundamental studies have been conducted using density functional theory (DFT) [376] and/or using experimental techniques such as rotating disk electrodes (RDEs) [126, 377], where it has been shown ionomer adsorption to the catalyst surface can play a significant role in performance and available catalyst active area. Recently, a study using quaternary ammonium cations (QACs) with long tethered groups (triethylammonium) demonstrated that they were worse than shorter groups (trimethylammonium) because when adsorbed to the catalyst the longer ethyl group blocked more active sites [376]. The authors suggested utilizing other bulkier QACs that may be more sterically hindered from adsorption would be beneficial. In contrast, a recent microelectrode and AEMFC study showed triethylammonium outperformed trimethylammonium by reducing cation adsorption [129]. While insight from different approaches is useful and can correlate to real device performance under the right conditions [378], it is also known that the catalyst and ionomer kinetics and performance in an RDE study can diverge significantly from the activity in an operating device [379]. Therefore, many optimization studies are done in an operating cell

[122]. Recently, Huang et al. optimized the water uptake of the ionomer incorporated in both the anode [100] and cathode [99] in an AEMWE by balancing a high ion exchange capacity (IEC) with crosslinking to reduce swelling. Faid et al. used an in-situ half-cell approach by adding a reference electrode to an AEMWE experiment to separately optimize ionomer loading for OER and HER [116].

There are many disadvantages to optimizing a single electrode using full cell tests. It can be challenging to separate the performance of the anode from the cathode. It is a more time intensive process to optimize one electrode at a time. Furthermore, MEA preparation and cell assembly introduce additional variables to the system. A more efficient solution is to perform ex-situ half-cell studies, where the electrochemical performance of each electrode can be isolated. These experiments also reduce the number of interfaces and therefore contributions to the electrochemical performance. Studies of this nature have been performed more frequently for ORR in acidic media [380–382] and more recently for ORR [383] and OER [384] in alkaline media and HER in acidic media [385].

This study reports for the first time the optimization of ionomer structures using a separated anode half-cell approach. We utilize a tunable triblock copolymer system of polychloromethylstyrene-*b*-polycyclooctene-*b*-polychloromethylstyrene (PCMS-*b*-PCOE-*b*-PCMS) [58] that we previously modified via hydrogenation [102] to fabricate a polyethylene (PE) triblock copolymer-based anion exchange membrane which excellent mechanical properties in water for AEMWE applications. It is advantageous to utilize an ionomer with similar chemical composition in the catalyst layer (CL) to reduce interfacial resistances in a membrane electrode assembly. Therefore, this work utilizes the same PCOE-based triblock copolymer precursor, which is post functionalized with quaternary ammonium cations (QACs) and incorporated as the anion exchange ionomer.

Electrodes for AEMWEs are made by coating a porous support in a catalyst-ionomer ink. Commonly implemented porous substrates include carbon paper or cloth for the cathode, or metal felts, foams, or meshes of stainless steel, titanium, or nickel for the anode [34]. Using an electrically conductive porous support is essential because the widely porous interconnected framework allows for gas and fluid transport while simultaneously providing electrical conductivity [386]. In addition to possessing high surface area and electrical conductivity, porous

Ni foams are an attractive substrate because of their resistance to corrosion at high pH [387–390] and excellent OER performance [391–394]. Therefore, this work utilizes a Ni foam electrode coated in a catalyst-ionomer ink.

Our previous work has highlighted interactions that can occur between ionomers and Ag nanoparticles [395] and the implications of those interactions on the thin film morphology on Ag surfaces [396]. In this work, the electrochemical performance toward OER of various Ag-ionomer catalyst inks on Ni foam are evaluated in half-cell experiments. The ionomer is optimized through a series of modifications including different backbone chemistries and QAC functionalities. The two QACs compared in this work are benzyltrimethylammonium (TMA) and benzylmethylpiperidinium (MPRD). The effect of ink dilution, which relates to the thickness of the ionomer thin film coating the Ag catalyst particles, was also investigated. Improvements in kinetics and performance are discussed, and the final optimized electrode was incorporated into an AEMWE. The results are summarized, and recommendations are provided for tuning ionomer-Ag interactions to develop a favorable interface and enhanced electrochemical performance.

## 5.4 Experimental Methods

### 5.4.1 Materials

Ni foam substrates (thickness = 0.3mm) were purchased from MSE Supply Company. The substrates were pre-cleaned by sonicating for 30 min in acetone followed by sonicating for 30 min in 2 M HCl and then rinsing in DI water. Ag nanopowder (average particle size 20–40 nm) was purchased from Alfa Aesar and used as received. The following reagents were purchased from various vendors and used as received. *N*-methylpiperidine ( $C_6H_{13}N$ , 99%), trimethylamine solution ( $C_6H_3N$ , 50wt% in water), chloroform ( $CHCl_3$ , >99%), methanol, (MeOH,  $CH_3OH$ , ACS grade), and 1,1,2,2-tetrachloroethane (reagent grade  $\geq 98.0\%$ ). The block copolymers used in this work, including polychloromethylstyrene-*b*-polycyclooctene-*b*-polychloromethylstyrene (PCMS-*b*-PCOE-*b*-PCMS) and polyisoprene-*ran*-polychloromethylstyrene (PIp-*ran*-PCMS), were synthesized via methods published previously [49, 238]. The base triblock copolymer used for the AEM fabrication, Tuffbrane™, was supplied by Spark Ionx Inc.



#### 5.4.2 Gel Permeation Chromatography (GPC)

GPC was performed in THF at a flow rate of 1.0 mL min<sup>-1</sup> using a refractive index detector on a Polymer Laboratories PL-GPC 50 integrated GPC system.

#### 5.4.3 Nuclear Magnetic Resonance (NMR) Spectroscopy

NMR spectroscopy was performed in 5 mm diameter tubes in deuterated chloroform (CDCl<sub>3</sub>) at 25 °C. <sup>1</sup>H NMR was performed on a Bruker 500 spectrometer at 500 MHz.

#### 5.4.4 Environmental scanning electron microscopy (ESEM) and energy dispersive spectroscopy (EDS)

Scanning electron microscopy images were collected using an FEI Quanta 600 operating under low vacuum at 25 kV. EDS was performed with an element EDAX energy dispersive spectroscope. Standard parameters were used to quantify elements using EDAX Genesis software.

#### 5.4.5 BrunauerEmmetTeller (BET) Surface Area

The BET surface area of Ni foam was extracted from N<sub>2</sub> isotherms. An ASAP 2020 porosimeter (Micromeritics, Norcross, GA, USA) was used to collect N<sub>2</sub> isotherms at 77 K. Prior to analysis, the sample was degassed for 8 h at 150 °C under high vacuum. Surface areas were calculated using the BET method following criterion described previously [397].

#### 5.4.6 Half-Cell Electrode Fabrication

Ni foam substrates were cut to a size of 3.0 cm x 4.5 cm (13.5 cm<sup>2</sup>). This is the size necessary to contact the working electrodes in the FlexCell<sup>®</sup> apparatus. For Ag-ionomer catalyst ink coated electrodes, Ag nanopowder was added to a 10 mg mL<sup>-1</sup> solution of PCMS-*b*-PCOE-*b*-PCMS in CHCl<sub>3</sub> and sonicated for 1 h prior to dip coating. The ionomer:catalyst (I:C) ratio of 15:85 was kept constant in all experiments, and the target loading of Ag was either 2.6 or 1.6 mg cm<sup>-2</sup>. In all dip-coating processes, between each dip the electrodes were placed on a hot plate at 60 °C to evaporate the CHCl<sub>3</sub> solvent. After the total amount of polymer-Ag ink was deposited on each electrode, they were dried under vacuum for 12 h to remove any residual solvent.

To partially hydrogenate the PCOE midblock to PE, electrodes with PCMS-*b*-PCOE-*b*-PCMS-Ag ink were hydrogenated by utilizing the Ni foam substrate as the

hydrogenation catalyst. Electrodes were placed in a vessel purged for 30 min with N<sub>2</sub>(g), followed by purging with H<sub>2</sub>(g) for 30 min. The vessel was then sealed with a balloon which was inflated with H<sub>2</sub>(g), and the samples reacted under H<sub>2</sub>(g) for 24 h.

The Ag-polymer coated electrodes were quaternized in 50 wt% trimethylamine/water to yield benzyltrimethylammonium (TMA) cationic moieties, or in 50 vol% *N*-methylpiperidine/MeOH to yield benzylmethylpiperidinium (MPRD) cationic moieties. Electrodes were submerged in solution for 48 h at room temperature, then thoroughly rinsed in DI water and dried under vacuum for 12 h.

#### 5.4.7 Half-Cell Experiments

Half-cell tests were performed using a PTFE FlexCell<sup>®</sup> (Gaskatel, gmbH). 3.0 x 4.5 cm electrodes were placed in the cell. A 3 cm<sup>2</sup> active area was isolated by the silicone gaskets. The current densities in this study are normalized to this planar surface area. The working electrode (WE), counter electrode (CE), and reference electrode (RE) were the Ni foam electrodes, a Pt wire, and a Pt-H<sub>2</sub> HydroFlex<sup>®</sup> reference electrode (Gaskatel, gmbH) respectively. Prior to experiments, the working electrodes were soaked in 1 M K<sub>2</sub>CO<sub>3</sub> for 1 h to exchange from the Cl<sup>-</sup> form to the CO<sub>3</sub><sup>2-</sup> form. Once the cell was assembled with the WE, 1 M K<sub>2</sub>CO<sub>3</sub> electrolyte was added to the cell and heated to 50 °C and allowed to equilibrate at that temperature for 1 h prior to beginning experiments. A stir bar was added to the electrolyte compartment to reduce noise from gas bubble formation during OER. A VMP-300 potentiostat (Biologic) was used for electrochemical measurements. Linear sweep voltammetry (LSV) was collected at 5 mV s<sup>-1</sup>. The reaction kinetics can be described by the Butler-Volmer equation [398]:

$$j = j_{fwd} - j_{rev} = j_0 \exp\left(\frac{\alpha\eta F}{RT}\right) - j_0 \exp\left(\frac{-(1-\alpha)\eta F}{RT}\right) \quad (5.1)$$

Where  $j_0$  is the exchange current density,  $\alpha$  is the charge transfer coefficient,  $\eta$  is the overpotential,  $R$  is the ideal gas constant, and  $T$  is the temperature. At large overpotentials ( $\eta > 15$  mV) where the reactions become irreversible, the Butler-Volmer equation simplifies to the Tafel equation, expressed in common logarithmic terms as:

$$\eta = \left(\frac{2.303RT}{\alpha F}\right) \log j - \left(\frac{2.303RT}{\alpha F}\right) \log j_0 \quad (5.2)$$

Tafel equation fits were calculated for both 100% iR compensated LSVs and iR-uncompensated LSVs. Electrochemical impedance spectroscopy (EIS) was performed at open circuit voltage (OCV) to determine the solution resistance used for performing iR correction. Cyclic voltammetry (CV) collected at 10, 20, 30, and 50 mV s<sup>-1</sup> in the potential range of 1.12–1.22 V was used to calculate the double layer capacitance ( $C_{dl}$ ) as an estimate of electrochemical surface area.  $C_{dl}$  was calculated by plotting  $j_A - j_C$ , or  $\Delta j$ , at 1.17 V versus the scan rate, where the linear slope =  $2C_{dl}$ .

#### 5.4.8 Anion Exchange Membrane (AEM) Fabrication

The AEMs used in this work were fabricated from a block copolymer precursor, Tuffbrane™, supplied by Spark Ionx. Membranes were produced by suspending the polymer in 1,1,2,2-tetrachloroethane (TeCA). Films were solution cast onto Teflon® coated polyetheretherketone (PEEK) sheets with a dropper pipette and were partially covered by a glass plate and allowed to dry at ambient conditions. Once dry, another Teflon® sheet was placed on top of the polymer film on the Teflon® coated PEEK sheet and was then hot pressed at 160 °C and 90 psi for 5 minutes, four times. Films were then easily peeled from the sheet with an approximate thickness of  $38 \pm 5$  μm. The films were post-quaternized in 50% *N*-methylpiperidine in MeOH for 3 days at 50 °C to yield AEMs. The AEMs were washed with DI H<sub>2</sub>O until the H<sub>2</sub>O had a neutral pH. The membranes were then annealed in DI H<sub>2</sub>O at 80 °C in the oven for 24 h. AEMs were stored in DI H<sub>2</sub>O at room temperature before use.

#### 5.4.9 Differential Scanning Calorimetry (DSC)

Differential scanning calorimetry (DSC) was performed using a TA instruments Q20 DSC. 1.3 mg of PCMS-*b*-PCOE-*b*-PCMS was deposited by dip coating a small (ca. 1 cm<sup>2</sup>) piece of Ni foam. The polymer-coated Ni foam was loaded in a Tzero aluminum pan and the change in heat flow was measured over a temperature range of 0 – 160 °C with a heating and cooling rate of 10 °C min<sup>-1</sup>.

#### 5.4.10 Ionic Conductivity Measurements

The in-plane Cl<sup>-</sup> and CO<sub>3</sub><sup>2-</sup> ionic conductivity of the AEM were measured using electrochemical impedance spectroscopy (EIS) with a BioLogic VMP3 Potentiostat. Conductivity measurements were performed in 4-electrode BektTech conductivity cells immersed in water

(W6-4 Optima<sup>®</sup> LS/MS grade, Fisher Chemical) on a hot plate with a magnetic stirrer. Experiments were performed at room temperature ( $\sim 25$  °C) and at 50 °C. The in-plane conductivity of the membranes was calculated using,

$$\sigma = \frac{d}{twR} \quad (5.3)$$

where  $d$  is the distance between two platinum electrodes,  $t$  is the thickness of the sample,  $w$  is the width of the sample, and  $R$  is the membrane resistance.  $R$  is obtained by fitting a Randles circuit model to the Nyquist impedance plot.

#### 5.4.11 Small-angle X-ray Scattering (SAXS)

Small angle X-ray scattering (SAXS) was performed at the Basic Energy Sciences Synchrotron Radiation Center (BESSRC) at the Advanced Photon Source at Argonne National Lab on beamline 12 ID-B. SAXS was performed using a Pilatus 2M detector. Experiments were performed with an exposure time of 0.5 s. The X-ray beam had a wavelength of 1 Å and energy of 13.3 keV. The intensity ( $I$ ) is a radial integration of the 2D scattering pattern with respect to the scattering vector ( $q$ ). AEM samples were placed in capillary tubes dry or in DI water. SAXS was collected for the dry, ambient samples and for samples immersed in DI water for 1 week. For dry samples, scattering of an empty capillary tube was used for background subtraction. For DI water immersed samples, scattering of a DI water filled capillary tube was used for background subtraction. 3 shots were averaged for each sample prior to background subtraction.

#### 5.4.12 Membrane Electrode Assembly (MEA) Fabrication

Anodes and cathodes were fabricated using the catalyst-coated substrate method. Ni foam or Toray carbon paper (TGP-H-60) was cut to a size of 5 cm<sup>2</sup> for use as the porous transport layer (PTL) for the anode or cathode, respectively. For the anode, Ag-ionomer catalyst inks were prepared and deposited via the same dip-coat method described above. The same I:C ratio of 15:85 was used with a target Ag loading of 4 mg cm<sup>-2</sup>.

For the cathode catalyst ink, platinum supported carbon (Pt/C, Tanaka TEC10E50E, 46.3% Pt) and DI H<sub>2</sub>O was added to a 5 mg mL<sup>-1</sup> solution of polyisoprene-*ran*-polychloromethylstyrene functionalized with methylpiperidinium cations (PIp-*ran*-PCMS[MPRD]) ionomer [47, 49] in MeOH and sonicated for 1 h prior to deposition. An I:C ratio of 15:85 was used, and the target

loading of Pt/C was  $1.5 \text{ mg cm}^{-1}$ . Carbon paper PTLs were placed on a hot plate at  $60 \text{ }^\circ\text{C}$  and the catalyst ink was applied by a manual painting method. After the total amount of catalyst ink was deposited on each electrode, they were dried under vacuum for 12 h to remove any residual solvent.

The membrane electrode assemblies (MEAs) were made using a  $5 \text{ cm}^2$  anode and cathode and an  $8\text{--}9 \text{ cm}^2$  AEM. Before cell assembly, the Ni foam anodes were pressed at 90 psi for 1 min. The anode, cathode and membrane were then individually ion-exchanged to the  $\text{CO}_3^{2-}$  form by soaking in 1 M  $\text{K}_2\text{CO}_3$  for 60 min. The AEM was placed between the anode and cathode in  $5 \text{ cm}^2$  Fuel Cell Technologies hardware between two graphite serpentine flow-fields with PTFE-coated fiberglass fabric gaskets (McMaster-Carr) with thicknesses of 152 and  $380 \text{ }\mu\text{m}$  for the cathode and anode side, respectively. The cell was assembled with a torque of 2.5 ft-lbs.

#### 5.4.13 Single-Cell Electrolyzer Testing

MEAs were tested using a custom-built electrolysis test station. Aqueous 1 M  $\text{K}_2\text{CO}_3$  (or MilliQ DI  $\text{H}_2\text{O}$ ) was fed to both the anode and cathode at  $15 \text{ mL min}^{-1}$ . The cell and liquid feed line were heated to  $50 \text{ }^\circ\text{C}$  and the cell was allowed to equilibrate for 1 h prior to testing. To collect polarization curves, chronopotentiometry was performed at each current step for 1 min to allow for equilibration. EIS was also performed from 10 kHz to 50 mHz at OCV to determine the high frequency resistance (HFR) to calculate the area specific resistance (ASR) of the cell.

### 5.5 Results and Discussion

#### 5.5.1 PCMS-*b*-PCOE-*b*-PCMS Triblock Copolymer Characterization

The ionomer used in this work is derived from the neutral triblock copolymer precursor polychloromethylstyrene-*b*-polycyclooctene-*b*-polychloromethylstyrene (PCMS-*b*-PCOE-*b*-PCMS). The PCMS-*b*-PCOE-*b*-PCMS triblock copolymer was characterized using GPC and  $^1\text{H}$  NMR, shown in Figure 5.3 and Figure 5.4. The molecular weight and chemical composition, along with the theoretical IEC, are summarized in Table 5.1.

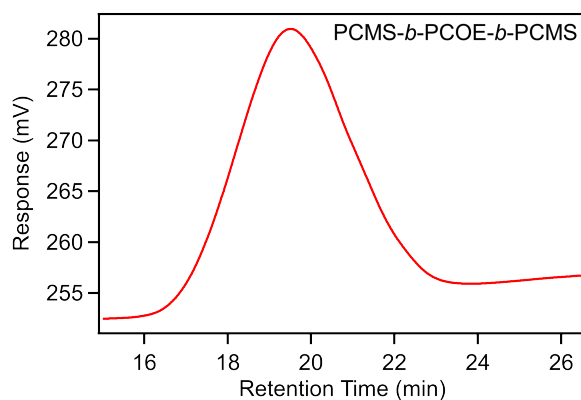


Figure 5.3 GPC of PCMS-*b*-PCOE-*b*-PCMS used to calculate  $M_n$ ,  $M_w$  and PDI.

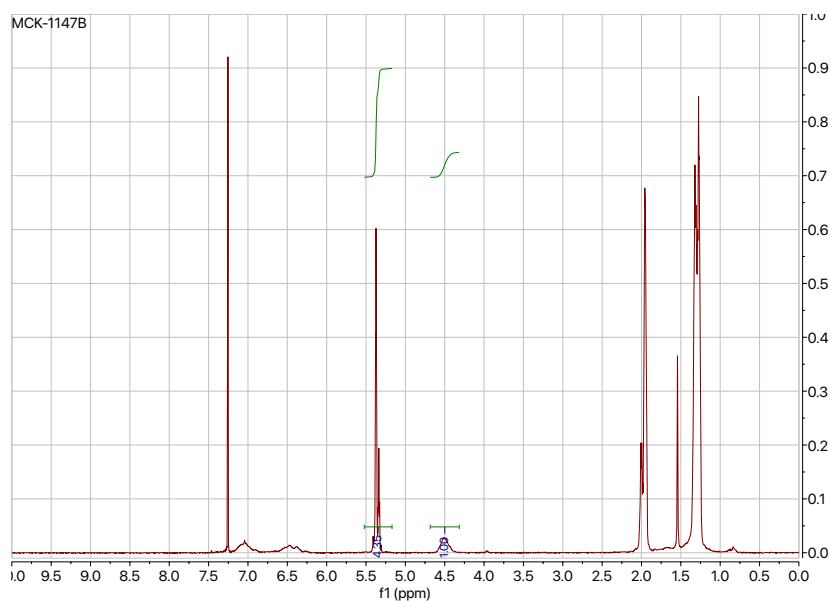


Figure 5.4  $^1\text{H}$  NMR of PCMS-*b*-PCOE-*b*-PCMS used to calculate the degree of polymerization (DP) and ion exchange capacity (IEC).

Table 5.1 Chemical Composition and Ion Exchange Capacity of PCMS-*b*-PCOE-*b*-PCMS from GPC and NMR.

$M_n^a$	$M_w^a$				$\text{IEC}_{\text{TMA}}^b$	$\text{IEC}_{\text{MPRD}}^b$
( $\text{g mol}^{-1}$ )	( $\text{g mol}^{-1}$ )	PDI <sup>a</sup>	$\text{DP}_{\text{PCMS}}^b$	$\text{DP}_{\text{PCOE}}^b$	$\text{mmol g}^{-1}$	$\text{mmol g}^{-1}$
82,200	147,000	1.79	64	561	1.44	1.36

<sup>a</sup>Measured by GPC calibrated against polystyrene standards.

<sup>b</sup>Measured by  $^1\text{H}$  NMR end-group analysis

### 5.5.2 Electrode Fabrication and Characterization

Most reports on AEMWEs that use porous supports normalized the current density by the planar surface area of the support [399]. While this is relevant, the electrochemically active surface area of porous catalyst materials, including Ni foams, is always much larger than its geometric surface area. To characterize this, an N<sub>2</sub> isotherm (Figure 5.5) was used to calculate the BET surface area of the pristine Ni foam substrates. The BET surface area of the pristine Ni foam was  $0.104 \pm 0.004 \text{ m}^2 \text{ g}^{-1}$ , making the real Ni surface area ca. 32 times larger than the planar surface area of the substrate.

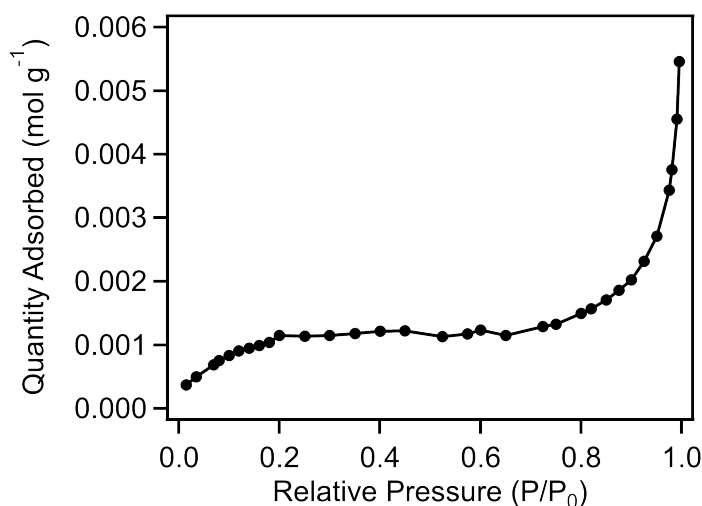


Figure 5.5 N<sub>2</sub> isotherm of pristine nickel foam substrate, used to calculate the BET surface area.

Figure 5.6 shows the Ni foam electrode before and after depositing Ag-ionomer catalyst ink. The SEM images highlight the large porous framework of the Ni foam substrate. After Ag-ionomer catalyst ink deposition, the Ni framework is coated in both ionomer and Ag nanoparticles. Some of the holes in the Ni foam framework are covered by a layer of Ag-ionomer, evident in Figure 5.6d.

EDS was used to characterize the electrode before and after depositing an ionomer-Ag ink. The results are summarized in Table 5.2. The pre-cleaned Ni foam electrodes show a small percentage of oxygen, indicating partial oxidation of the Ni foam surface. After depositing Ag-ionomer ink, Ag C and N are detected as well.

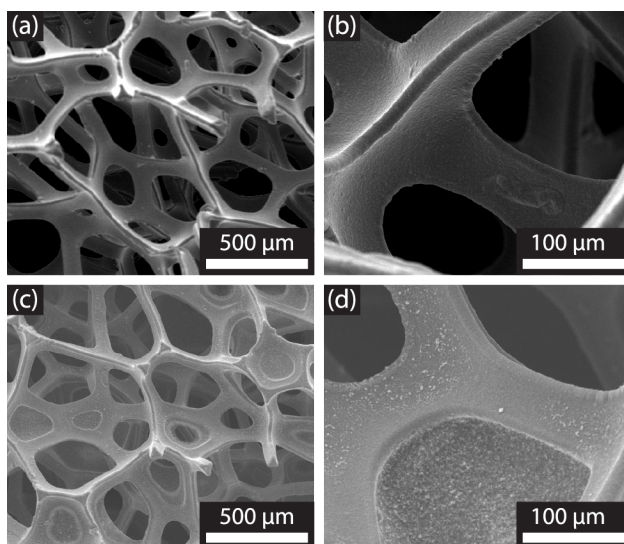


Figure 5.6 SEM images of pristine nickel foam (a,b) and representative as-deposited Ag-ionomer catalyst ink on Ni foam (c,d).

Table 5.2 Surface elemental composition for Ni foam and Ag-ionomer coated Ni foam, from EDS.

Element (%)	Ni Foam	Ag-Ionomer Coated Ni Foam
Ni	97.3	54.3
O	2.7	2.6
C/N	0	17.0
Ag	0	26.1

### 5.5.3 Electrochemical Characterization: Half-Cell Experiments

The electrochemical performance of the Ni foam-coated electrodes was studied in a FlexCell<sup>®</sup> three electrode half-cell apparatus (see Figure 5.7). Ni foam catalyst ink-coated electrodes were used as the working electrode and a Pt wire and HydroFlex<sup>®</sup> electrode were used as the counter and reference electrodes, respectively. Aqueous 1 M  $K_2CO_3$  was used as the electrolyte. The catalyst inks used in this work are summarized in Table 5.3. The I:C ratio was kept constant at 15:85 for all the electrodes in this study. The current densities in the following experiments are normalized by the planar active surface area of the electrode,  $3 \text{ cm}^2$ , for comparison to other studies.



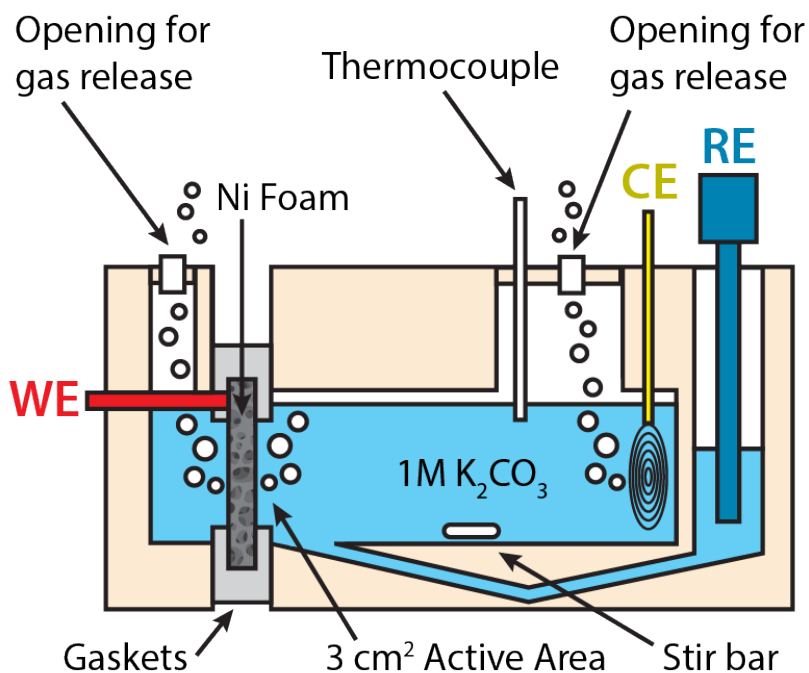


Figure 5.7 Cross-sectional diagram of the FlexCell<sup>®</sup> half-cell electrochemical measurement apparatus.

Table 5.3 Summary of Ag-ionomer inks used in this work.

Catalyst Ink <sup>a</sup>	Ink Dilution <sup>b</sup>	Ionomer midblock	Quaternary Ammonium Cation	Ag loading (mg cm <sup>-2</sup> )
PC-TM-25	1:25	PCOE	TMA	2.6 ± 0.1
PC-MP-25	1:25	PCOE	MPRD	2.6 ± 0.1
PC-TM-100	1:100	PCOE	TMA	1.6 ± 0.2
PC-MP-100	1:100	PCOE	MPRD	1.6 ± 0.2
PE-TM-100	1:100	PE <sup>c</sup>	TMA	1.6 ± 0.2
PE-MP-100	1:100	PE <sup>c</sup>	MPRD	1.6 ± 0.2

<sup>a</sup>PC: polycyclooctene midblock, PE: partially polyethylene midblock, TMA: trimethylammonium quaternary ammonium cation, MPRD: methylpiperidinium quaternary ammonium cation

<sup>b</sup>Mass solid:liquid ratio

<sup>c</sup>Partially hydrogenated PCOE, PE at the interface

### 5.5.3.1 Comparison of Quaternary Ammonium Cation

The first step toward optimizing the ionomer chemistry was comparing the performance of two QACs, trimethylammonium (TMA) and methylpiperidinium (MPRD). An Ag catalyst ink was made with the block copolymer precursor PCMS-*b*-PCOE-*b*-PCMS and coated onto the Ni foam substrate. The coated substrate was functionalized by quaternizing in either trimethylamine or methylpiperidine to obtain TMA or MPRD moieties. Figure 5.8 shows the OER linear sweep voltammograms (LSVs) of PC-TM-25 and PC-MP-25.

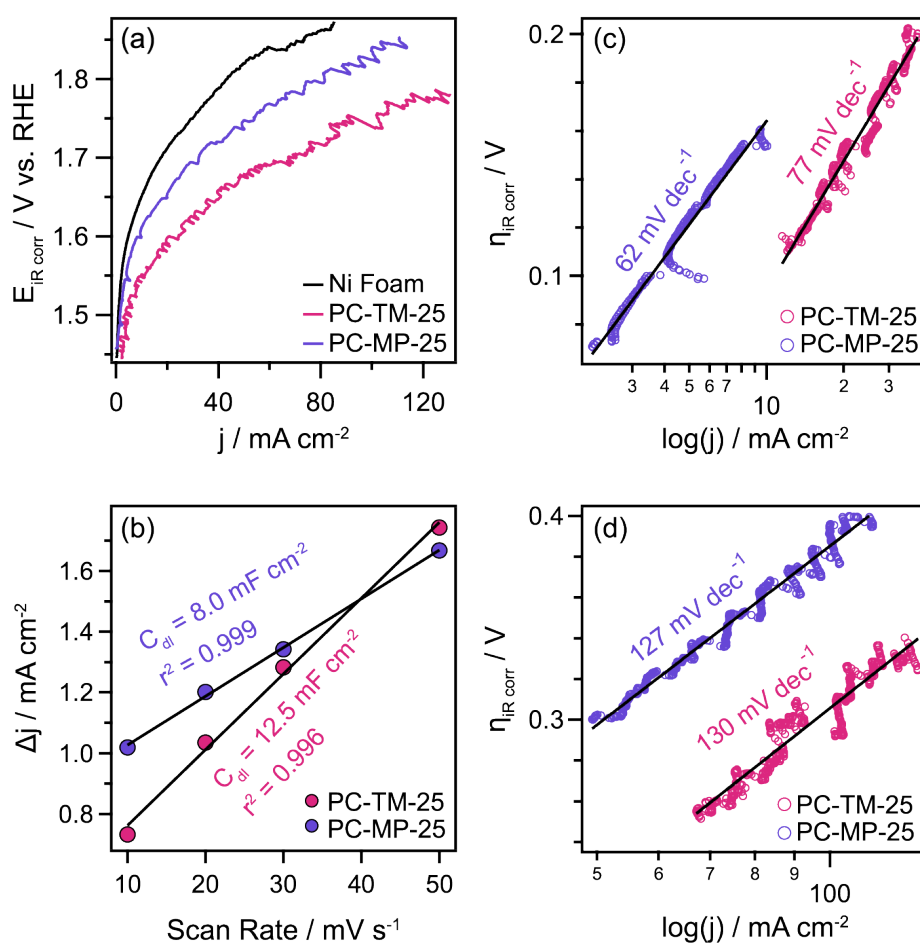


Figure 5.8 iR corrected LSVs (a), double layer capacitance (b), and Tafel Plots at low (c) and high (d) overpotential comparing PC-TM-25 and PC-MP-25.

EIS used to determine the solution resistance for iR correction (Figure 5.9),  $C_{dl}$  and Tafel plots for Ni foam (Figure 5.10 and Figure 5.11), CV scans used to calculate  $C_{dl}$  (Figure 5.12), LSVs and Tafel plots without iR correction (Figure 5.13 and Figure 5.14) for all catalyst inks

investigated are shown below. Relevant electrokinetic parameters extracted from modeling the iR-corrected LSVs with the Butler-Volmer equation are summarized in Table 5.4. LSVs without iR correction were modeled as well for comparison (Table 5.5). The Tafel slope, charge transfer coefficient ( $\alpha$ ), and exchange current density ( $j_0$ ) are dependent on both the potential and surface coverage of species [400]. Our results indicate the presence of two distinct kinetic regimes at lower (ca. 0.1 – 0.2 V) and higher (ca. 0.25 – 0.4 V) overpotentials. Therefore, the kinetics in both regions are reported and discussed.

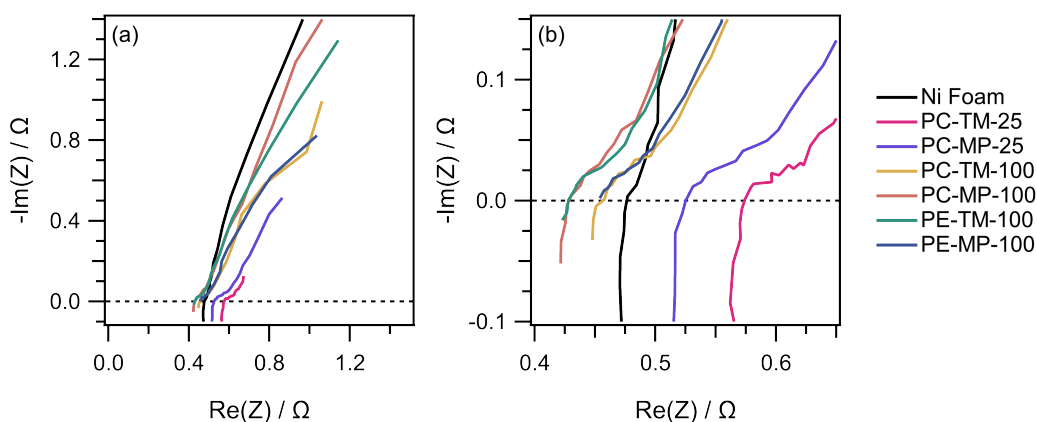


Figure 5.9 Nyquist impedance plots of EIS performed at OCV to determine the high frequency intercept, i.e. the solution resistance, used for iR correction. (a) shows full impedance spectra, (b) shows the high frequency intercepts for clarity.

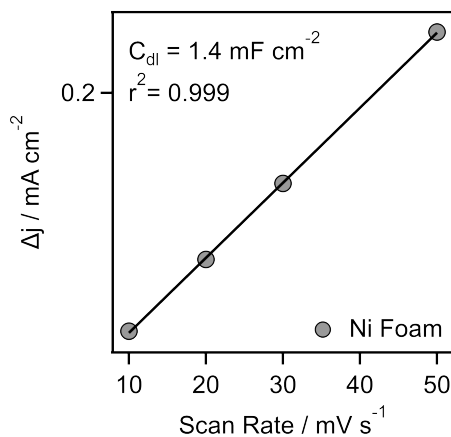


Figure 5.10 Ni Foam Double Layer Capacitance.

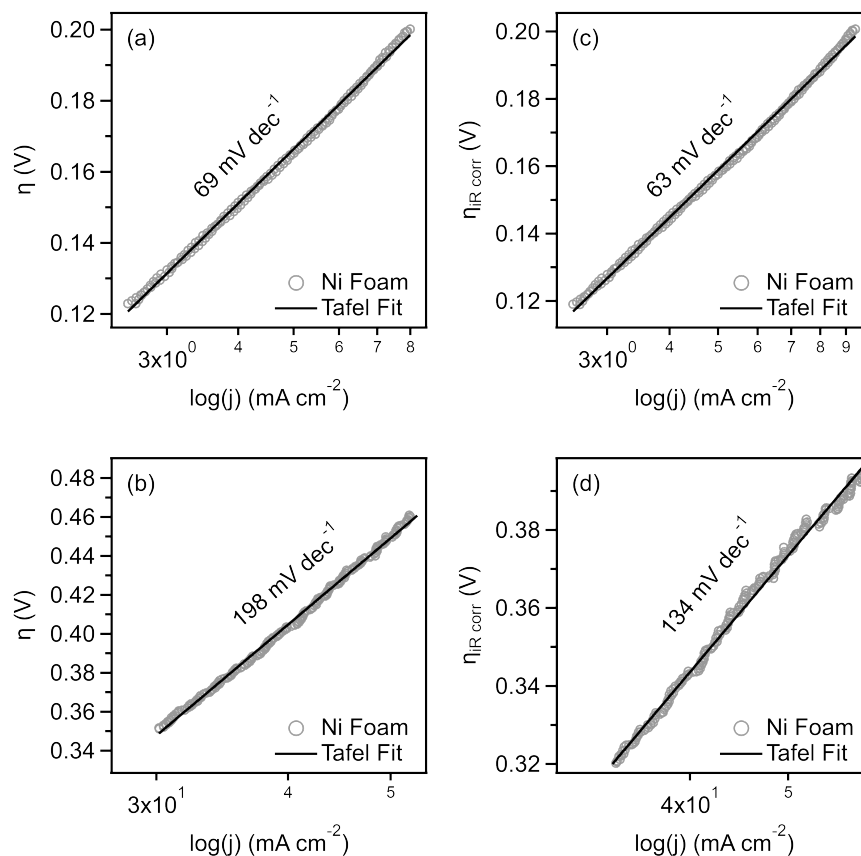


Figure 5.11 Tafel plots of Ni foam at low (a,c) and high (b,d) overpotentials, showing results with no iR correction (a,b) and 100% iR correction (c,d).

Table 5.4 Summary of Electrokinetic Parameters from iR Corrected LSVs fit to Tafel Equation.

Sample	Low $\eta$ Region			High $\eta$ Region		
	Tafel Slope (mV dec <sup>-1</sup> )	$\alpha$	$j_0$ (mA cm <sup>-2</sup> )	Tafel Slope (mV dec <sup>-1</sup> )	$\alpha$	$j_0$ (mA cm <sup>-2</sup> )
Ni Foam	63	0.44	2.5	134	0.21	0.33
PC-TM-25	77	0.36	0.34	130	0.21	0.11
PC-MP-25	62	0.45	1.44	127	0.22	0.21
PC-TM-100	78	0.36	0.17	134	0.21	0.07
PC-MP-100	74	0.38	0.23	97	0.29	0.12
PE-TM-100	58	0.48	0.77	126	0.22	0.11
PE-MP-100	73	0.38	0.22	117	0.24	0.08

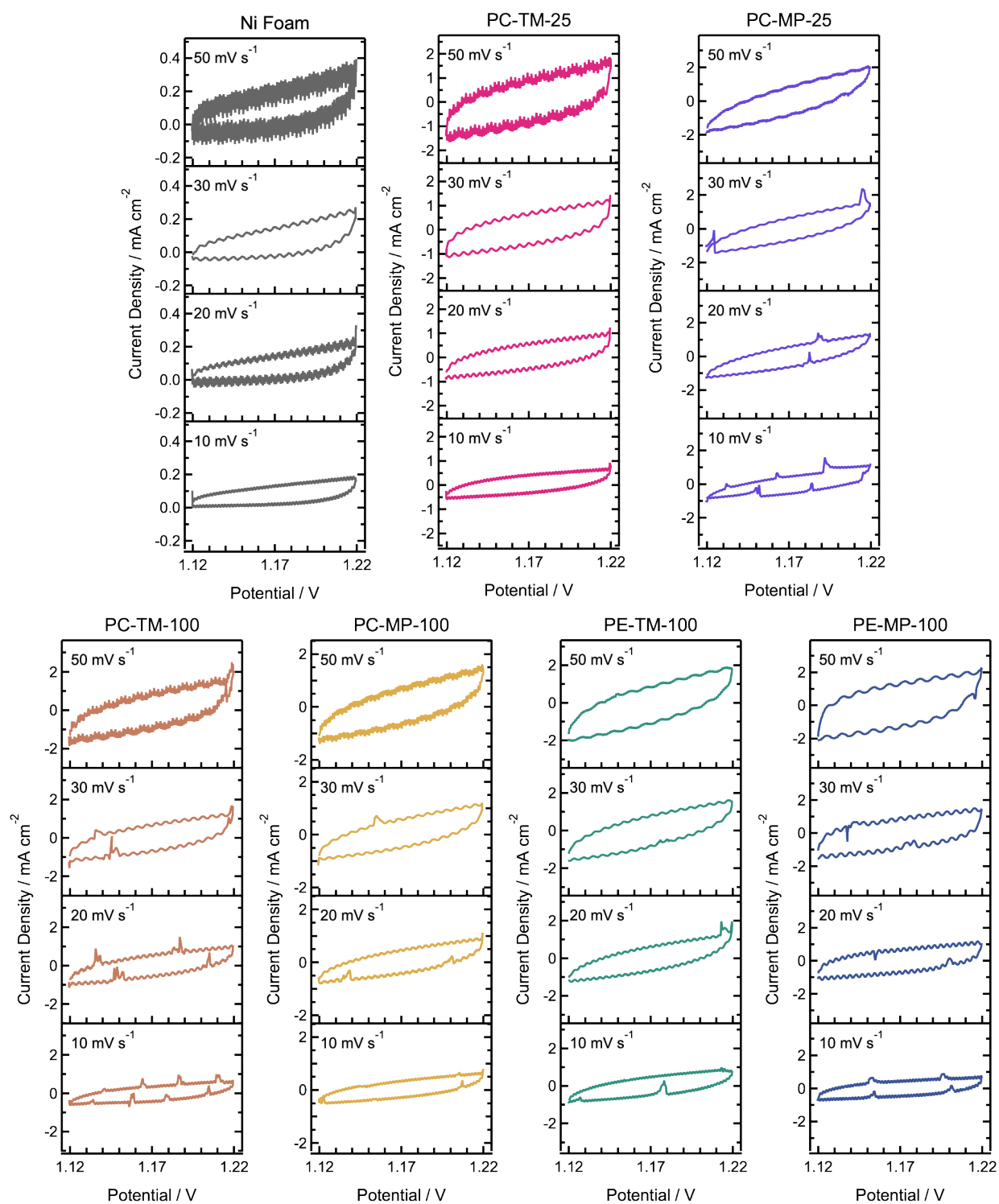


Figure 5.12 CV scans performed at 10, 20, 30 and 50 mV dec<sup>-1</sup> between 1.12 and 1.22 V, used to calculate  $C_{dl}$ .

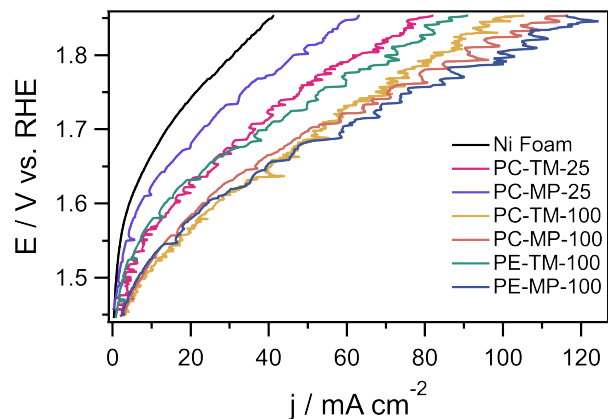


Figure 5.13 LSV comparing all samples investigated, no iR correction.

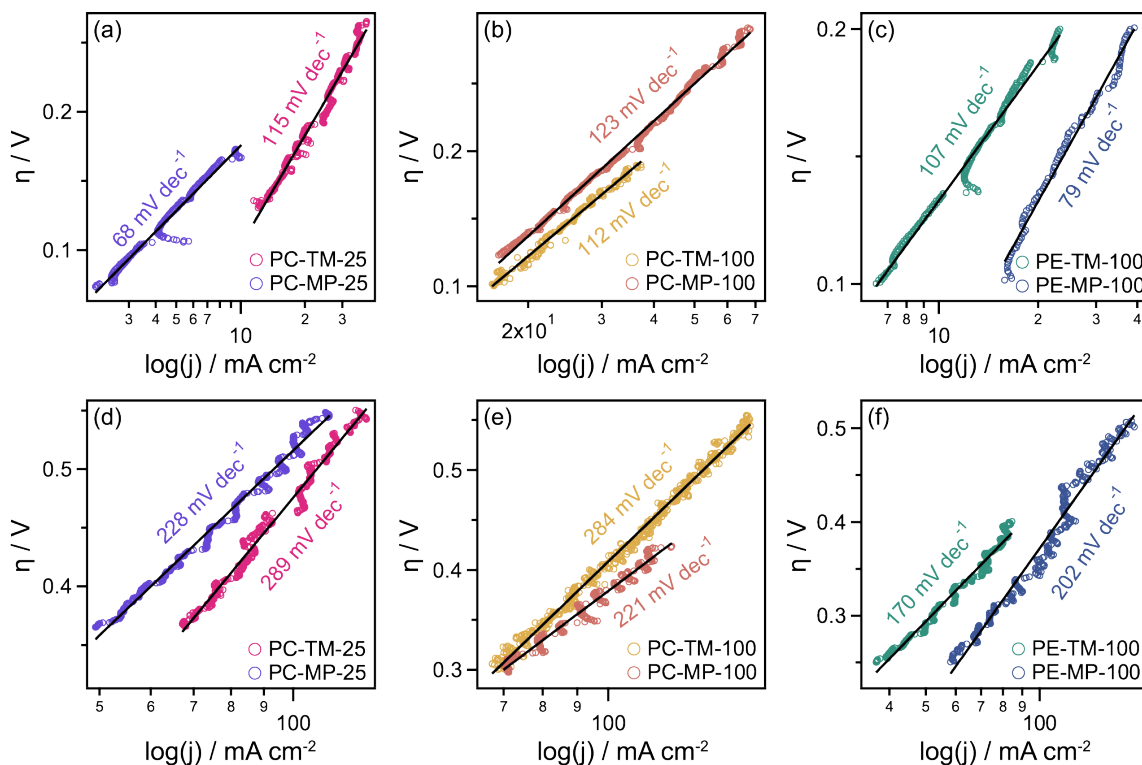
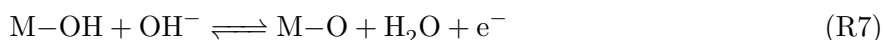


Figure 5.14 Tafel slopes from LSVs with no iR correction for PC-TM-25 and PC-MP-25 at low (a) and high (d) current densities, for PC-TM-100 and PC-MP-100 at low (b) and high (e) current densities, and PE-TM-100 and PE-MP-100 at low (c) and high (f) current densities.

Table 5.5 Summary of Electrokinetic Parameters from LSVs with no iR correction fit to the Tafel Equation.

Sample	Low $\eta$ Region			High $\eta$ Region		
	Tafel Slope (mV dec <sup>-1</sup> )	$\alpha$	$j_0$ (mA cm <sup>-2</sup> )	Tafel Slope (mV dec <sup>-1</sup> )	$\alpha$	$j_0$ (mA cm <sup>-2</sup> )
Ni Foam	69	0.41	2.27	198	0.14	0.19
PC-TM-25	115	0.24	0.25	289	0.1	0.05
PC-MP-25	68	0.41	1.32	228	0.12	0.1
PC-TM-100	112	0.25	0.15	284	0.1	0.04
PC-MP-100	123	0.23	0.15	221	0.13	0.06
PE-TM-100	77	0.36	0.56	180	0.15	0.1
PE-MP-100	101	0.28	0.19	246	0.11	0.05

PC-MP-25 shows an improvement in kinetics compared to PC-TM-25 in regard to Tafel slope at low  $\eta$  (62 vs. 77 mV dec<sup>-1</sup>) and slightly at high  $\eta$  (127 vs. 130 mV dec<sup>-1</sup>). The change in Tafel slope from low to high overpotential can be due to changes in the rate determining step (rds) and/or changes in the surface composition of adsorbed species [400, 401]. It has been reported that observing a second Tafel slope at higher overpotential of  $\sim 120$  mV dec<sup>-1</sup> is typically due to a build-up of surface species formed in the step just prior to the rds [400], where the reaction rate becomes exponentially dependent on the applied potential [402]. The Tafel slope can be used to predict the rds in the OER mechanism. Although the OER mechanism is complex and debated, assuming a single-site mechanism, it may proceed via the following steps [400]:



Each rds possesses a unique Tafel slope that can be calculated from the Tafel equation (Eq. 5.2) based on the number of electron transfers ( $n$ ) that occur prior to the rds [403]. Assuming a perfectly reversible reaction ( $\alpha = 0.5$ ) at  $T = 50$  °C, the Tafel slope if the rds were (R6), the first electron transfer step where  $n = 0$ , would be  $\sim 128$  mV dec<sup>-1</sup>. If the rds were (R7) or (R8), Tafel

slopes of  $\sim 43$  or  $\sim 26$  mV dec $^{-1}$  would be predicted, respectively. Alternatively, if the rds is the initial adsorption of OH $^{-}$  while the subsequent electron transfer is more facile, a Tafel slope of 64 mV dec $^{-1}$  (or 60 mV dec $^{-1}$  at 30 °C [402, 403]) is calculated. Considering the Tafel slopes for PC-TM-25 and PC-MP-25 are 77 and 62 mV dec $^{-1}$  respectively, the rds is most likely the initial adsorption of OH $^{-}$ , which is comparatively faster for PC-MP-25 than PC-TM-25. Similar Tafel slopes have been reported for other Ni-based catalysts in alkaline media [173, 367, 404, 405].

The charge transfer coefficient ( $\alpha$ ) for PC-MP-25 is also comparatively higher (0.45 vs. 0.35) and close to 0.5, indicating the OER reaction shows nearly reversible behavior. Marcus theory describes a model for an outer-sphere single electron charge transfer where both the reactant and product do not interact directly with the electrode surface [406]. In Marcus theory,  $\alpha$ , the charge transfer coefficient, is described by Eq. 5.4 as a function of  $\eta$ , the overpotential, and  $\lambda$ , the reorganization energy required to transform the nuclear configuration of the reactant to the product:

$$\alpha = \frac{1}{2} \left( 1 + \frac{\eta F}{\lambda} \right) \quad (5.4)$$

From Eq. 5.4, when  $\lambda \gg \eta F$ ,  $\alpha \rightarrow 0.5$ , indicating a perfectly reversible reaction.  $\alpha$  will deviate from 0.5 when either  $\lambda$  is lowered or at higher  $\eta$  in the Tafel region.  $\lambda$  can decrease when reactions occur with a reactant adsorbed to a surface, which decreases solvent effects by eliminating part of the solvation shell, or by shortening the distance between the reactant and electrode [407]. Therefore, PC-TM-25 may exhibit a lower  $\alpha$ , which deviates more significantly from 0.5, because of detrimental effects between the catalyst interface and TMA moieties.

Table 5.6 Summary of OER Performance Parameters from iR Corrected LSVs.

Sample	Onset Potential (V)	$\eta_{10}$ (mV)	$\eta_{100}$ (mV)	$j$ @ 1.75 V (mA cm $^{-2}$ )	Mass Activity @ 1.75 V (A g $^{-1}$ )	$C_{dl}$ (mF cm $^{-2}$ )
Ni Foam	1.59	210	n/a	30	n/a	1.4
PC-TM-25	1.51	100	290	90	35	12.5
PC-MP-25	1.57	170	380	54	21	8
PC-TM-100	1.46	60	260	128	80	12.4
PC-MP-100	1.48	60	250	140	88	8.8
PE-TM-100	1.54	119	288	103	64	12.1
PE-MP-100	1.54	69	226	187	117	20.8



Table 5.7 Summary of OER Performance Parameters from LSVs with no iR correction.

Sample	Onset Potential (V)	$\eta_{10}$ (mV)	$\eta_{100}$ (mV)	$j$ @ 1.75 V (mA cm <sup>-2</sup> )	Mass Activity @ 1.75 V (A g <sup>-1</sup> )
Ni Foam	1.59	220	n/a	31	n/a
PC-TM-25	1.51	120	460	63	24.2
PC-MP-25	1.56	180	510	46	17.7
PC-TM-100	1.46	70	400	85	53.1
PC-MP-100	1.47	80	380	91	56.9
PE-TM-100	1.54	133	430	71	47.3
PE-MP-100	1.52	82	353	101	124.7

Additional performance parameters for all electrodes investigated in this work are provided in Table 5.6 (and for results from LSVs without iR correction, Table 5.9). PC-MP-25 displays a much larger exchange current density than PC-TM-25 and approaches that of the pristine Ni foam. As exchange current density is a measure of the intrinsic electron transfer rate, this result further demonstrates the superior kinetics afforded by the MPRD cationic moiety. Despite this, PC-TM-25 ultimately displayed better performance, having a slightly lower onset potential, a lower overpotential at both 10 and 100 mA cm<sup>-2</sup> ( $\eta_{10}$  and  $\eta_{100}$ ), and a higher  $j$  and mass activity @ 1.75 V. To investigate this further, the double layer capacitance ( $C_{dl}$ ) was also determined from cyclic voltammetry (CV) at scan rates of 10, 20, 30 and 50 mV s<sup>-1</sup> between 1.12 and 1.22 V (see Figure 5.12 for all CV scans).  $C_{dl}$  is directly proportional to the electrochemical surface area (ECSA) and can be used as a representation of that when comparing similar samples. Notably, upon adding any Ag-ionomer ink to the Ni foam,  $C_{dl}$  increases substantially due to the addition of Ag nanoparticles. The effect of the QAC is also substantial on  $C_{dl}$ , where PC-TM-25 shows a larger  $C_{dl}$  than PC-MP-25 (12.5 vs 8.0 mF cm<sup>-2</sup>) and therefore possesses a larger ECSA. PC-TM-25 possessing a higher ECSA is counterintuitive, considering charge transfer is typically promoted with a higher availability of active sites [408]. Nonetheless, PC-TM-25 shows better performance despite PC-MP-25 having faster kinetics.

### 5.5.3.2 Comparison of Ink Dilution

Next, the effect of ink dilution was investigated. The mass ratio of solid:liquid was increased from 1:25 to 1:100 to make PC-TM-100 and PC-MP-100. The catalyst loading was also reduced

from 2.6 to 1.6 mg cm<sup>-2</sup>, keeping the same I:C ratio. The LSVs for PC-TMA-100 and PC-MPRD-100 can be seen in Figure 5.15.

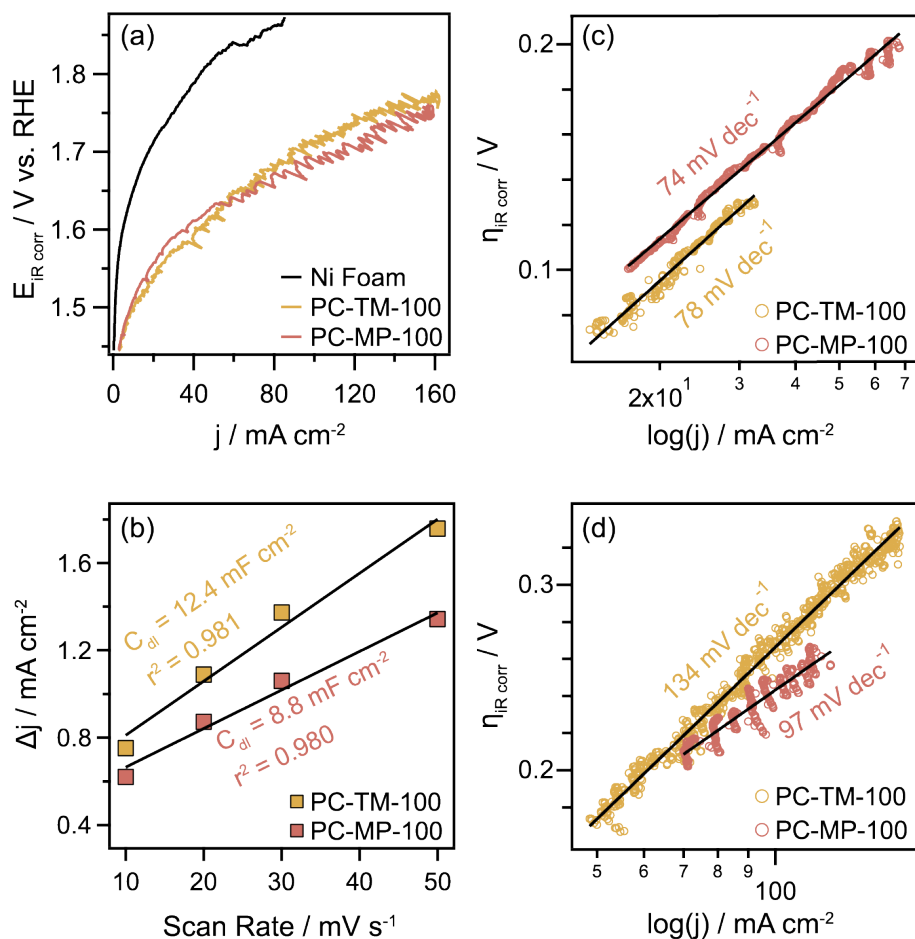


Figure 5.15 iR corrected LSVs (a), double layer capacitance (b), and Tafel Plots at low (c) and high (d) overpotential comparing PC-TM-100 and PC-MP-100.

Ink dilution did not have a substantial effect on the OER kinetics of the PC-TM electrodes. Dilution led to a slight increase in the Tafel slope in both the low and high current density regions. A slight decrease in  $j_0$  (0.34 vs. 0.17 mA cm<sup>-2</sup>) is also noted. Despite minor effects on the kinetics, a more significant decrease in  $\eta_{10}$  and  $\eta_{100}$ , and a higher  $j$  and mass activity @ 1.75 V are seen with dilution. Additionally, only small variations in  $C_{dl}$  were observed with ink dilution for both PC-TM-100 and PC-MPRD-100.

Ink dilution had a more substantial effect on the OER kinetics of the PC-MP electrodes. At low current densities, the Tafel slope at low  $\eta$  increased with ink dilution from 62 for PC-MP-25

to  $74 \text{ mV dec}^{-1}$  for PC-MP-100. However, at higher overpotentials, the Tafel slope decreased considerably to  $97 \text{ mV dec}^{-1}$ , giving PC-MP-100 a lower Tafel slope than PC-MP-25, PC-TM-25 and PC-TM-100. A Tafel slope of  $97 \text{ mV dec}^{-1}$  also indicates the reaction kinetics are not yet limited by the surface coverage of adsorbed OH (ceM-OH), which would result in a Tafel slope closer to  $128 \text{ mV dec}^{-1}$  at  $50 \text{ }^\circ\text{C}$ . Instead, the initial adsorption of  $\text{OH}^-$  is still the rds at higher overpotentials, just with comparatively slower kinetics. Ultimately, this manifests in lower overpotentials at higher current densities for PC-MP-100. Additionally, the exchange current density decreases with ink dilution, with the MPRD-functionalized ionomer ink still possessing higher intrinsic charge transfer. Kinetics aside, the overall performance of PC-TM-100 and PC-MP-100 is similar. The most significant enhancements with ink dilution can be observed in mass activity (normalized per g Ag), which greatly improved with ink dilution as shown in ??, or in ?? with no iR correction. This indicates catalyst utilization was greatly improved by diluting the catalyst ink, which effectively decreases the ionomer thickness on the Ag catalyst particles and Ni foam support.

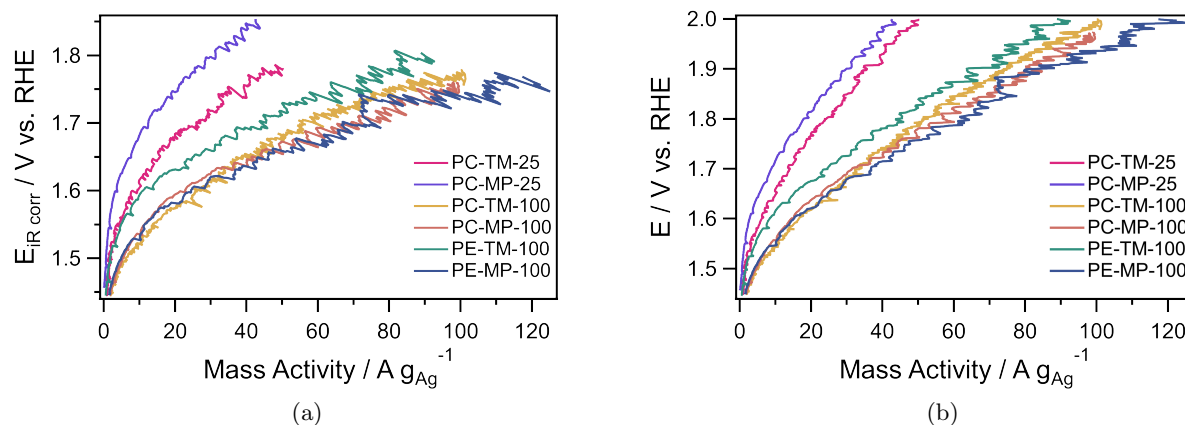


Figure 5.16 Mass activity (per gram Ag catalyst) comparing all samples investigated, with iR correction (a) and without iR correction (b).

### 5.5.3.3 Comparison of Partial Hydrogenation at Ni Foam Interface

For nearly a century the efficacy of Ni and Ni-based catalysts for facilitating hydrogenation reactions has been demonstrated in a variety of applications including the hydrogenation of nitriles [409], *n*-butyraldehyde and acetone [410], internal alkyne-containing nitroarene [411], and

polybutadiene to polyethylene [412]. Therefore, in this work, the authors leveraged the catalytic properties of the Ni foam substrate to partially hydrogenate the triblock block copolymer PCMS-*b*-PCOE-*b*-PCMS coating to PCMS-*b*-PE-*b*-PCMS (see Experimental Methods for detailed procedure).

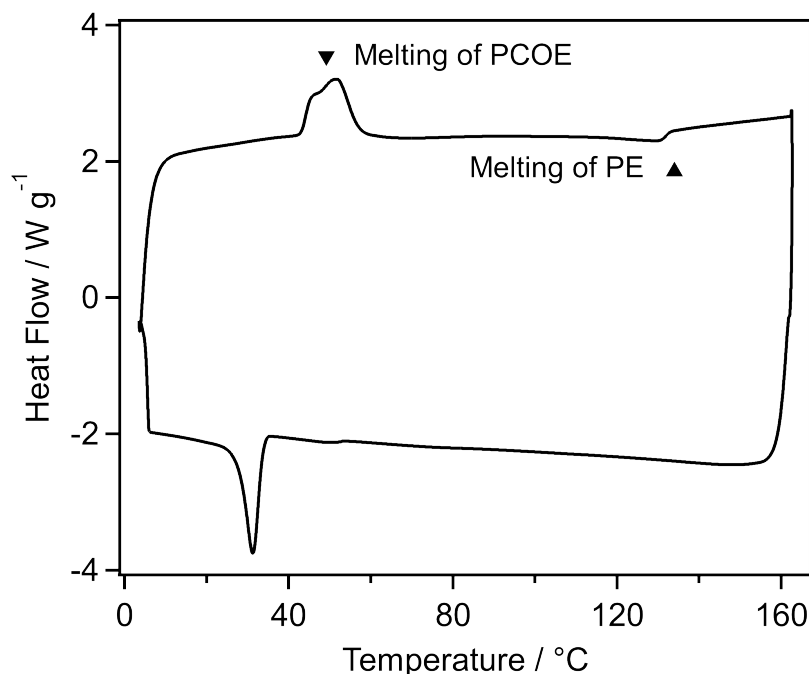


Figure 5.17 DSC of PCMS-*b*-PCOE-*b*-PCMS coated Ni foam sample after partial hydrogenation to PE under H<sub>2</sub>(g). Heating and cooling rates at 10 °C min<sup>-1</sup>.

The characterization of the hydrogenated block copolymer on Ni foam proved challenging with spectroscopic techniques including FTIR, where adequate intensity of the thin film was difficult to obtain using ATR-FTIR, and Raman, where only broad amorphous carbon peaks were observed, likely due to laser-induced Ag nanoparticle-catalyzed degradation [413]. Therefore, differential scanning calorimetry (DSC) was used to identify changes in the melting point, where PCOE melts near ~55 °C and PE near ~130 °C. For DSC, a small (~1 cm<sup>2</sup>) piece of Ni foam was coated in 1.3 mg of the PCMS-*b*-PCOE-*b*-PCMS triblock copolymer precursor and hydrogenated in H<sub>2</sub>(g). While this was nearly ~4 times the polymer loading used in experiments, the DSC experiment was limited by the volume of Ni foam that could fit in the pan and mass of polymer required to obtain an adequate heat flow signal. The DSC curves can be viewed in Figure 5.17. It is clear

PCOE is still present in the sample, but there is partial hydrogenation noted by the small deviation near the melting point of PE. It is likely the Ni foam was only able to hydrogenate the block copolymer at the Ni foam interface, while the rest of the polymer remained unsaturated. A larger ratio of the block copolymer would be hydrogenated with the polymer loadings utilized on the electrodes in this work. Therefore, the effect of partially hydrogenating the ionomer was still investigated, as PE can offer enhanced properties compared to PCOE [70, 231], most notably reduced water uptake and swelling [102], which is critical for water management in AEMWEs [43, 99, 100, 210, 414].

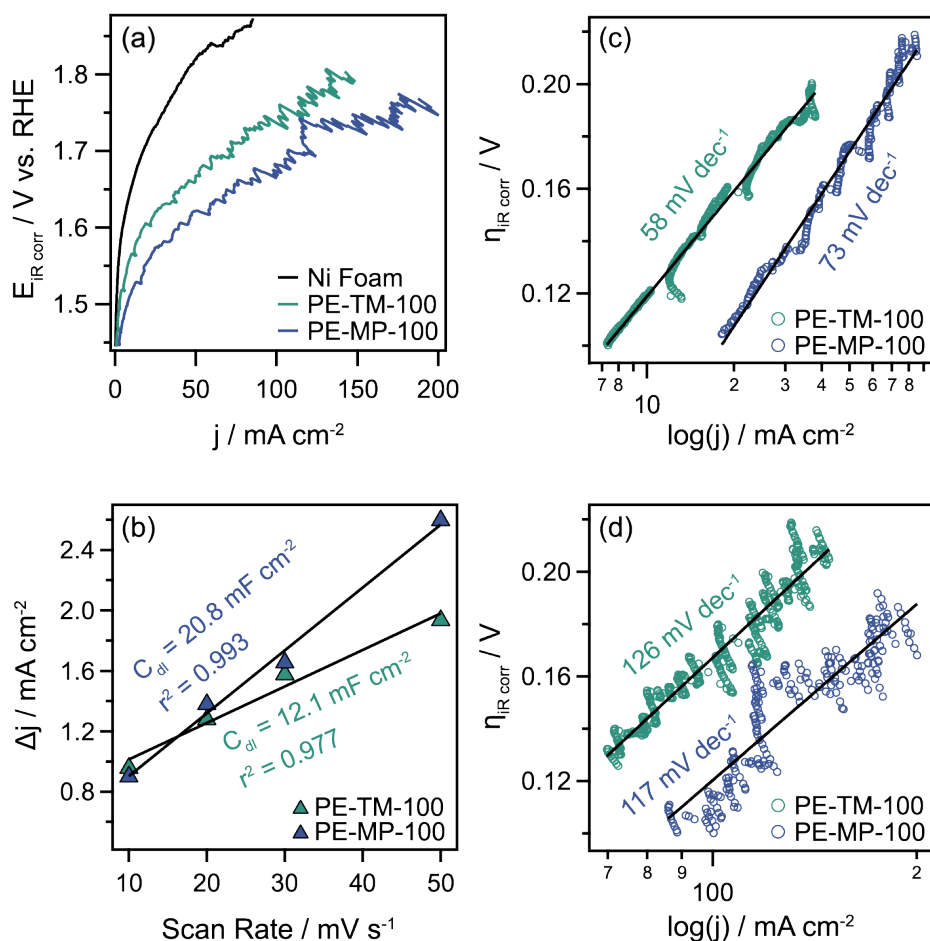


Figure 5.18 iR corrected LSVs (a), double layer capacitance (b), and Tafel Plots at low (c) and high (d) overpotential comparing PE-TM-100 and PE-MP-100.

Further evidence of the partial hydrogenation of the ionomer at the Ni-foam interface is shown in the substantial effect on the OER kinetics and performance of both PE-TM-100 and

PE-MP-100 electrodes (Figure 5.18). For PE-TM-100, partial hydrogenation led to a decrease in the Tafel slope in both the low and high current density regions, an increase in  $\alpha$ , and an increase in  $j_0$  (from 0.17 to 0.77 mA cm<sup>-2</sup>). The decrease in the Tafel slope from 78 to 58 mV dec<sup>-1</sup> indicates the kinetics of OER are much faster after hydrogenating the ionomer at the Ni foam interface. Further, charge transfer is clearly improved, as noted by the increase in  $j_0$  and  $\alpha = 0.48$ . This behavior indicates nearly reversible, facile kinetic behavior. For PC-MP-100, the kinetics are essentially unchanged except for a higher Tafel slope at high  $\eta$  near 117 mV dec<sup>-1</sup>. The Tafel slope being this far below the predicted slope for the rds being the first electron transfer (128 mV dec<sup>-1</sup>) indicates the mechanism may be the same as on PC-MP-100, where the reaction kinetics are not yet limited by the surface coverage of adsorbed OH (M–OH) and the initial adsorption of OH<sup>-</sup> is still the rds at higher overpotentials. This phenomenon, which enhanced the performance of PC-MP-100 beyond PC-TM-100, also improves the performance of PE-MP-100 beyond that of PC-TM-100. It also affords PE-MP-100 a lower  $\eta_{10}$  than PE-TM-100, in addition to the lowest  $\eta_{100}$  and the higher  $j$  and mass activity @ 1.75 V of any catalyst ink investigated in this work. The mass activity of PE-TM-100 and PE-MP-100 can also be viewed in ??.

In addition to the rds at high overpotentials, the ECSA had a substantial effect on enhancing the performance of the PE-MP-100 electrode. While the  $C_{dl}$  of PE-TM-100 remained relatively consistent after partial hydrogenation, the  $C_{dl}$  of PE-MP-100 was significantly enhanced after partial hydrogenation, increasing from 8.8 mF cm<sup>-2</sup> for PC-MP-100 to 20.8 mF cm<sup>-2</sup> for PE-MP-100. This >2-fold increase in  $C_{dl}$ , and therefore ECSA, resulted in large OER performance enhancement. The highest performing electrode is therefore PE-MP-100.

## 5.5.4 Performance Demonstration in AEM electrolyzer

### 5.5.4.1 PIp-*ran*-PCMS Characterization

The ionomer used in the cathode catalyst ink is derived from the neutral random copolymer precursor polyisoprene-*ran*-polychloromethylstyrene (PIp-*ran*-PCMS). The PIp-*ran*-PCMS random copolymer was characterized using GPC and <sup>1</sup>H NMR, shown in Figure 5.19 and Figure 5.20. The molecular weight and chemical composition, along with the theoretical IEC, are summarized in Table 5.8.

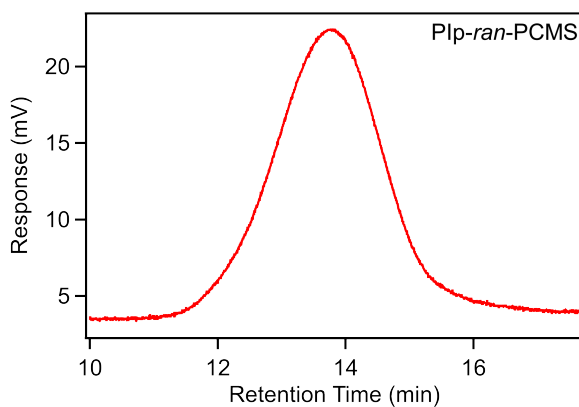


Figure 5.19 GPC of PIp-ran-PCMS used to calculate  $M_n$ ,  $M_w$  and PDI.

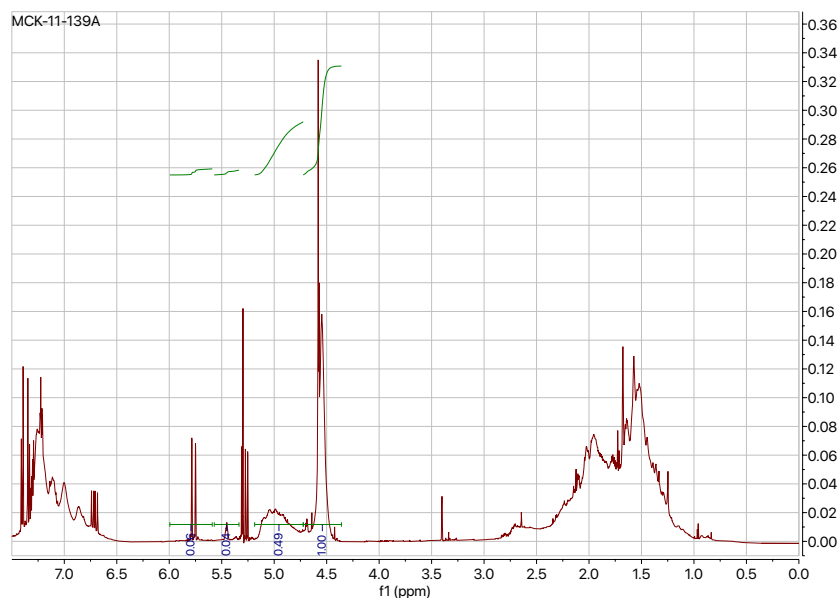


Figure 5.20  $^1\text{H}$  NMR of PIp-ran-PCMS used to calculate the degree of polymerization (DP) and ion exchange capacity (IEC).

Table 5.8 Chemical Composition and Ion Exchange Capacity of PCMS-*b*-PCOE-*b*-PCMS from GPC and NMR.

$M_n^a$ (g mol $^{-1}$ )	$M_w^a$ (g mol $^{-1}$ )	PDI $^a$	DP <sub>PIP</sub> $^b$	DP <sub>PCMS</sub> $^b$	IEC <sub>MPRD</sub> $^b$ (mmol g $^{-1}$ )
53,200	307,000	5.71	270	229	3.01

$^a$ Measured by GPC calibrated against polystyrene standards.

$^b$ Measured by  $^1\text{H}$  NMR end-group analysis

### 5.5.4.2 AEM Characterization

The Tuffbrane™ polymer is one commercial iteration of a triblock copolymer published previously [102] of the same chemistry with a different composition. The AEMs were fabricated in-house with a thickness of  $38 \pm 5 \mu\text{m}$  with an IEC of  $0.64 \pm 0.04 \text{ mmol g}^{-1}$ . The ionic conductivity and morphology of the AEM were characterized in aqueous conditions relevant to the electrolysis tests. Conductivity in the  $\text{Cl}^-$  and  $\text{CO}_3^{2-}$  form was determined using EIS at both 25 and 50 °C and is summarized in Table 5.9.

Table 5.9 Ionic Conductivity of the AEM fabricated from Tuffbrane™ in Liquid Water.

Anion	Temperature (°C)	Conductivity ( $\text{mS cm}^{-1}$ )
$\text{Cl}^-$	25	$13.1 \pm 1.3$
	50	$36.8 \pm 1.2$
$\text{CO}_3^{2-}$	25	$3.8 \pm 0.5$
	50	$11.5 \pm 0.4$

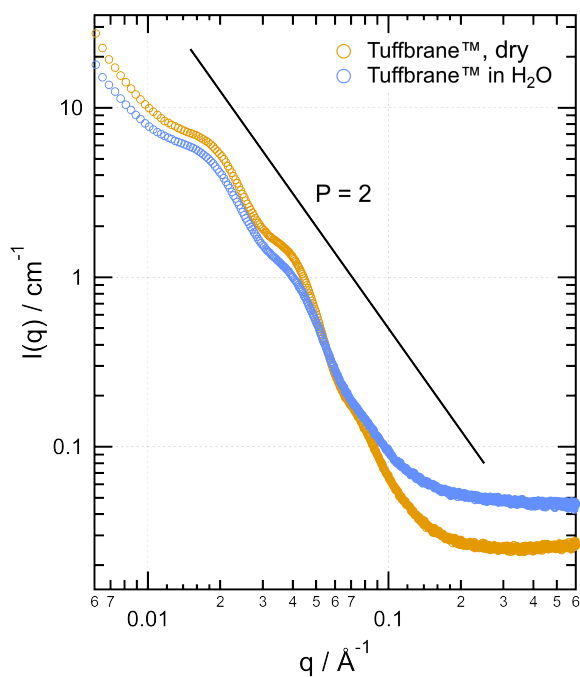


Figure 5.21 SAXS of the AEM fabricated from Tuffbrane™ at ambient, dry conditions and immersed in liquid water. Porod slope of 2 indicates a particle symmetry of randomly distributed lamellae.



SAXS was performed on dry and H<sub>2</sub>O immersed membranes (Figure 5.21). The domain spacing (d-spacing) was calculated from the primary  $q^*$  peak. D-spacing of the membrane increased from 33.7 to 36.1 nm with hydration in liquid water due to swelling of the hydrophilic domains. The secondary peak is located at  $\sim 2q$ , indicating a lamellar morphology [415]. Additionally, the Porod slope is close to 2 (highlighted in Figure 5.21), indicating a particle symmetry of lamellar domains in agreement with the ratio of  $q$  values at each peak [253].

### 5.5.4.3 AEM Electrolyzer Performance

The optimized OER anode, PE-MP-100, along with PE-TM-100, were demonstrated in an AEM electrolyzer to correlate the results from the half-cell study to an operating device [416]. Membrane electrode assemblies (MEAs) were prepared using PE-TM-100 or PE-MP-100 anodes as described in the Experimental Methods. The electrolyzer with the PE-TM-100 or PE-MP-100 anode will be referred to as EL-PE-TM and EL-PE-MP, respectively. Polarization curves were collected at 50 °C in both 1 M K<sub>2</sub>CO<sub>3</sub> and DI water (see Figure 5.22 for iR corrected polarization curves, Figure 5.23 for raw polarization curves). iR correction was performed by evaluating the high-frequency resistance (HFR) from EIS measurements (see Figure 5.24). The area specific resistances (ASRs) of the EL-PE-TM and EL-PE-MP electrolyzers are summarized in Table 5.10.

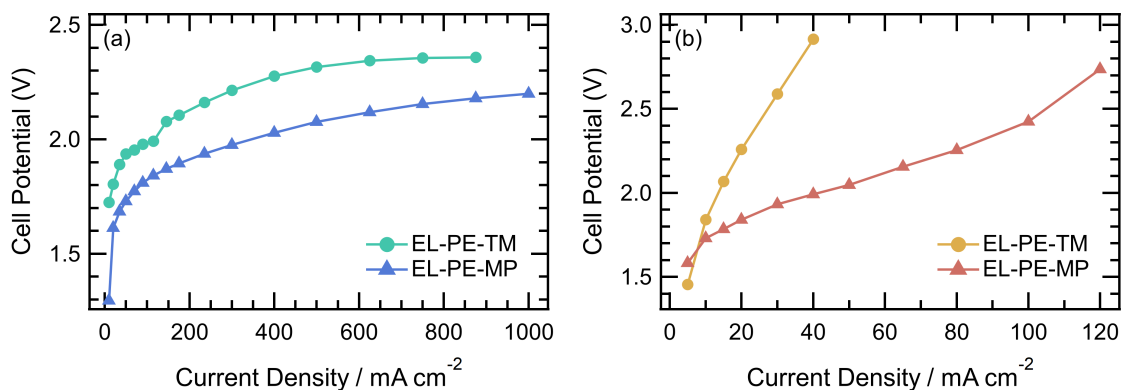


Figure 5.22 Polarization curves for AEM electrolyzers EL-PE-TM and EL-PE-MP in 1 M K<sub>2</sub>CO<sub>3</sub> (a) or DI H<sub>2</sub>O (b) at 50 °C with iR correction. 60% iR correction was used for polarization curves in 1 M K<sub>2</sub>CO<sub>3</sub> and 100% iR correction was used for polarization curves in DI H<sub>2</sub>O.

Figure 5.22 shows that EL-PE-MP maintains superior performance over EL-PE-TM. In 1 M K<sub>2</sub>CO<sub>3</sub>, the EL-PE-MP cell achieved a performance of 1 A cm<sup>-2</sup> at 2.20 V.

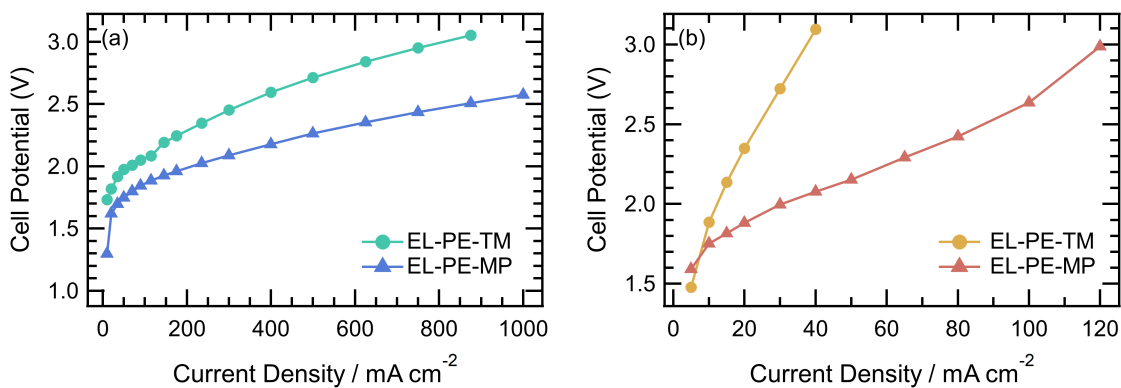


Figure 5.23 Polarization curves for AEM electrolyzers EL-PE-TM and EL-PE-MP in 1 M  $\text{K}_2\text{CO}_3$  (a) or DI  $\text{H}_2\text{O}$  (b) at 50 °C with no  $iR$  correction.

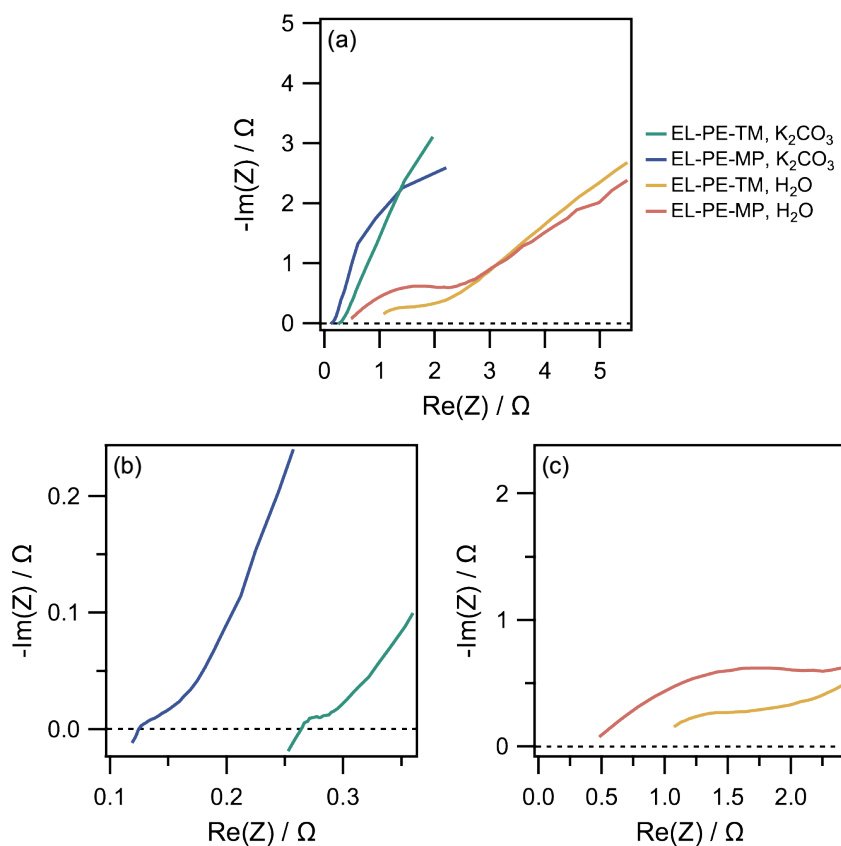


Figure 5.24 Nyquist impedance plots of EIS performed at OCV to determine the HFR for  $iR$  correction and calculation of the ASR. (a) shows all electrolyzer cells, (b) shows EL-PE-TM and EL-PE-MP in 1M  $\text{K}_2\text{CO}_3$ , and (c) shows EL-PE-TM and EL-PE-MP in DI  $\text{H}_2\text{O}$ .

Table 5.10 Area Specific Resistances (ASR) of AEM Electrolyzers in 1 M  $\text{K}_2\text{CO}_3$  and DI  $\text{H}_2\text{O}$ .

Electrolyzer	Feed Liquid	ASR (ohm $\text{cm}^2$ )
EL-PE-MP	1 M $\text{K}_2\text{CO}_3$	0.62
	DI $\text{H}_2\text{O}$	2.10
EL-PE-TM	1 M $\text{K}_2\text{CO}_3$	0.74
	DI $\text{H}_2\text{O}$	4.50

This is further corroborated by the ASR, which is slightly higher for EL-PE-TM due to TMA cationic functionality. The performance gap between the two anodes is emphasized in DI  $\text{H}_2\text{O}$ . Performance was significantly reduced in both cells, with EL-PE-TM only reaching a current density of  $40 \text{ mA cm}^{-2}$  at 2.92 V and EL-PE-MP reaching a current density of  $120 \text{ mA cm}^{-2}$  at 2.74 V. The ASR also substantially increases in DI  $\text{H}_2\text{O}$  due to the removal of circulating electrolyte, and EL-PE-TM has an ASR more than double that of EL-PE-MP. Poorer performance in AEM water electrolyzers is attributed to a lowering of the pH and degradation in catalyst activity as a result. Developing effective catalysts for OER in neutral pH still remains a challenge in the field [417].

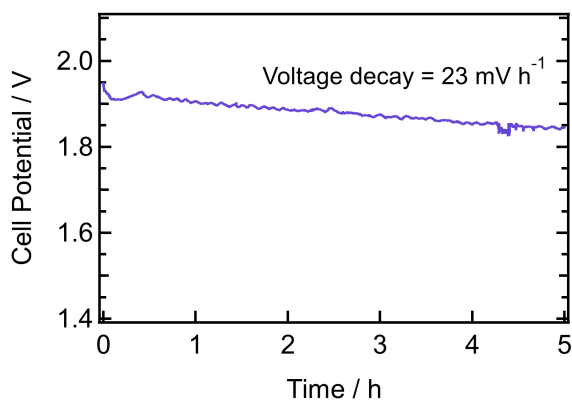


Figure 5.25 Voltage degradation of EL-PE-MP electrolyzer. The current density of the cell was held constant at  $500 \text{ mA cm}^{-2}$  for a duration of 5 h.

Diagnosing device durability to achieve a practical device is a complex and time consuming task [43]. However, the durability of this first iteration of the EL-PE-MP electrolyzer was

assessed by applying a constant current of  $500 \text{ mA cm}^{-2}$  for 5 h (see Figure 5.25), as a baseline. Over the course of the experiment, the cell voltage decreased, indicative of either a soft short,  $\text{H}_2$  cross-over, or membrane thinning, though this type of degradation mechanism is challenging to diagnose [43]. Further optimization of the MEA components and assembly of the cell, including the hardware, gaskets, sealing pressure and flow rates is expected to result in dramatic improvements in performance and durability.

## 5.6 Conclusions

The OER performance of a series of Ag-ionomer catalyst inks on Ni foam are evaluated in half-cell experiments. Different ionomer modifications are investigated to optimize the OER performance. First, the block copolymer precursor PCMS-*b*-PCOE-*b*-PCMS is functionalized with either benzyltrimethylammonium (TMA) or benzylmethylpiperidinium (MPRD) quaternary ammonium cations. While the MPRD-functionalized ionomer facilitates enhanced OER kinetics, the TMA-functionalized ionomer ultimately has better performance likely due to exhibiting a larger ECSA. Both catalyst inks were subsequently diluted and their catalyst loading was reduced while keeping the same I:C ratio. Ink dilution had a negligible effect on the kinetics of the TMA-functionalized ionomer. In contrast, diluting the MPRD-functionalized ionomer catalyst ink enabled the rds at higher overpotentials to be the initial adsorption of OH (indicated by a Tafel slope of  $97 \text{ mV dec}^{-1}$ ). Comparatively, all TMA-functionalized ionomer catalyst inks were limited by the surface coverage of adsorbed OH (M-OH) and the first electron transfer at high overpotentials (indicated by a Tafel slopes  $>128 \text{ mV dec}^{-1}$ ). Overall, ink dilution also enhanced the performance and catalyst utilization in both samples likely by reducing transport resistances via decreasing the ionomer thickness on the Ag catalyst particles and Ni foam support.

The catalytic activity of the Ni foam support was leveraged to partially hydrogenate the deposited PCMS-*b*-PCOE-*b*-PCMS block copolymer midblock to polyethylene (PE). After functionalization with MPRD, this variation of the electrode displayed further enhancements in performance, likely due to the enhanced properties of PE compared to PCOE. The same enhanced kinetics at higher overpotentials were also observed. Interestingly, a large enhancement in the ECSA was observed only in the MPRD-functionalized ink, which likely played a role in the observed performance enhancement. Overall, MPRD cationic moieties consistently provided lower

Tafel slopes and higher charge transfer coefficients at high overpotentials, which ultimately had a larger impact on the overall performance than the Tafel slope and kinetics observed at lower overpotentials. This was mainly due to a shift in the rds at high overpotentials, which was only observed in MPRD-functionalized catalyst ink samples. Finally, the performance of the optimized electrode PE-MP-100 was compared to PE-TM-100 in an AEM electrolyzer operating at 50 °C in both 1 M  $\text{K}_2\text{CO}_3$  and DI  $\text{H}_2\text{O}$ . The performance observations from the half-cell experiments correlated well to single-cell performance, with PE-MP-100 significantly outperforming PE-TM-100 in both achievable current density and operating at lower cell voltages. The degradation behavior of the AEM electrolyzer indicates that further optimization of the cell assembly or membrane are required to realize further performance improvements.

## CHAPTER 6

### CONCLUSIONS AND RECOMMENDATIONS

#### 6.1 Summary and Conclusions

Considering the dangers that climate change entails, the justification for transitioning to renewable sources of energy is irrefutable. A hydrogen-based energy infrastructure is a promising solution to the many, multi-faceted issues surrounding both climate change, environmental preservation, energy resiliency, and infrastructure. Hydrogen-based energy systems could reliably deliver energy at an affordable cost. The opportunities for utilizing hydrogen as an energy carrier are potentially vast – including as both a stationary and mobile power source, or as an energy storage medium for electricity produced from intermittent renewable sources such as solar or wind.

Polymer electrolyte-based fuel cells and electrolyzers are well-positioned to realize the flexible, scalable conversion and production of hydrogen fuel. Current state-of-the-art systems are designed with proton exchange membranes (PEMs), which have several drawbacks. The magnitude of the environmental impacts caused by PEM perfluorinated chemistry has recently become apparent. Additionally, the acidic operating conditions of PEM-based fuel cells and electrolyzers require expensive platinum group metal catalysts. As the demands for hydrogen production and conversion applications increase, the rarity and cost of platinum, iridium, and ruthenium-based catalysts will limit the use of PEM-based devices for large scale power generation. Anion exchange membranes (AEMs) offer an encouraging alternative to PEMs. Namely, there are more viable polymer architectures for AEMs compared to PEMs, including purely hydrocarbon backbone chemistries. Additionally, the alkaline operating environment allows for the use of more widely available non-precious metal catalysts, along with cheaper cell hardware components that are not required to be resistant to highly corrosive acidic conditions. Despite recent advanced in AEM development, the best AEMs still report lower conductivity and insufficient durability compared to state-of-the-art PEMs [418].

To improve the performance of AEM-based devices beyond that of PEM-based devices, the two main objectives are developing better AEMs and optimizing the components and fabrication of the catalyst layer (CL). AEMs with high ionic conductivity, decent water management,

exceptional durability, and that can be mass-produced via a scalable syntheses are required. While challenges remain in commercializing high-performance membranes, many have already come to market in the time since the conception of this thesis work [419], highlighting the advances that can be made in only a few years' time. In addition to the AEM, electrochemical device performance is also strongly dictated by structures that form in the CL of the electrode. The CL is comprised of a heterogeneous mixture of conductive supporting material, catalyst particles, and anion exchange ionomer (AEI). The CL in PEM-based devices was optimized empirically, but with the advent of more sophisticated diagnostic techniques, AEM-device CLs can be developed using a more thorough, scientific approach. In this thesis work, a commercially viable AEM is developed. Further, the rational design of the catalyst layer is carried out by synergistically developing ionomer chemistry with fundamental knowledge of ionomer-catalyst interactions. Tunable block copolymer-based AEIs are developed and their interactions, structure and performance with a silver catalyst are investigated.

In *Chapter 2*, a novel block-copolymer AEM is developed with a polyethylene midblock, affording the membrane high  $\text{OH}^-$  conductivity excellent mechanical properties in liquid water for aqueous applications like water electrolysis [102]. In this work, the PCMS-*b*-PCOE-*b*-PCMS triblock copolymer was successfully hydrogenated to PCMS-*b*-PE-*b*-PCMS using diimide derived from the thermal decomposition of *p*-toluenesulfonyl hydrazide. The triblock copolymer was then post functionalized with either benzyltrimethylammonium (TMA) or benzylmethylpiperidinium (MPRD). The new PE midblock, along with an MPRD cation, ultimately afforded the AEM a variety of enhanced properties. The PE-midblock was more thermally robust, melting at 125 °C ( $T_m$  of PE), as opposed to PCOE which melts at ~55 °C. The alkaline stability improved greatly, retaining more quaternary ammonium cationic groups after soaking in 1 M KOH at 80 °C and in 9 M KOH at room temperature than either the previous PCOE-midblock AEM [58] and a commercial membrane, Fumasep<sup>®</sup> FAS-50. The water uptake and dimensional swelling significantly improved with the incorporation of PE. Unexpectedly, the inclusion of PE improved the mechanical properties of this AEM in liquid water, where the stress at break improved when hydrated compared to the dry membrane. This had not been observed previously, where typically the plasticization effect of water weakens the mechanical integrity of the AEM. This made the material well-positioned for applications in liquid water.

In *Chapter 3*, the nature of interactions occurring between silver nanoparticles (AgNPs) and the block copolymer-based ionomer PCMS-*b*-PCOE-*b*-PCMS functionalized with either TMA or MPRD is investigated. In this study, groups from the ionomer which strongly interacted with AgNPs were the phenyl rings, quaternary ammonium cations, and C=C from the PCOE midblock. Shifts in material characteristics were observed due to interactions which were dependent on the quaternary ammonium cation, including in ambient water content and crystallinity. With TMA, the ionomer showed a loss in crystallinity and an increase in both water content bound in the solvation shell surrounding the TMA moiety and in domains in the bulk. With MPRD, the ionomer showed an increase in certain crystalline reflections and comparatively higher crystallinity with a lower bound and bulk water content. The bulkier nature of the MPRD cationic moiety likely led to weaker interactions with AgNPs, which allowed for enhanced crystallization compared to TMA.

In *Chapter 4*, the thin film morphology of a series of diblock and triblock copolymers derived from polyisoprene (PIp) and PCMS, along with ionomers derived from their functionalization with TMA or MPRD were investigated. The thin film morphology of the neutral block copolymer precursors was found to align perpendicular to a silver-coated substrate, while no order was observed on plain silicon. This indicates the ordered morphology was driven by polymer-silver interactions. Additionally, the PIp domain-spacing was found to differ substantially in the thin films (8–12 nm) compared to the bulk films (20–30 nm) due to confinement effects. Block copolymer thin films were functionalized with TMA or MPRD and their morphology was investigated at ambient conditions and at relevant fuel cell operating conditions of 60 °C and 95% RH. A complex interplay between silver-polymer interfacial interactions, confinement effects, and dipole-dipole interactions between the pendant cationic moieties is revealed to affect the thin film morphology and water uptake. A greater tendency toward perpendicular alignment is found in thinner films where Ag-interfacial interactions are more dominant, leading to an increase in water uptake. As film thickness increases, Ag-interfacial interactions are less pronounced, and dipole-dipole interactions between pendant quaternary ammonium cations induce more disorder in the film, leading to a decrease in water uptake. While ionomers functionalized with MPRD have higher ambient water uptake than ionomers functionalized with TMA, ionomers with MPRD exhibit less of a change between ambient and humidified conditions, indicating they may swell less



than ionomers with TMA. This work concludes with a series of recommendations: first, that MPRD cations may be desirable to achieve improved water uptake in low RH applications; second, that MPRD cations lead to less swelling and therefore may reduce the chances of ionomer delamination from catalyst surfaces; and third, that utilizing a triblock architecture compared to a diblock architecture further suppresses water uptake and swelling.

In *Chapter 5*, the findings from the previous studies were demonstrated in a more complex, electrochemically relevant system. The oxygen evolution reaction (OER) kinetics and performance of a set of ionomer-AgNP catalyst inks coated on Ni foam substrates were studied in a separated-anode half-cell study and validated in a single-cell water electrolyzer. Using the PCMS-*b*-PCOE-*b*-PCMS block copolymer precursor from *Chapter 3*, different ionomer modifications were investigated to optimize the OER performance. The effect of functionalizing with TMA or MPRD, ink dilution, and partial hydrogenation of the PCOE midblock to PE was investigated. The cation functionality affected the rate determining step (rds) of the OER reaction at high overpotentials. The MPRD-functionalized ionomer catalyst ink enabled the rds at higher overpotentials to be the initial adsorption of OH (indicated by a Tafel slope of 97 mV dec<sup>-1</sup>). Comparatively, all TMA-functionalized ionomer catalyst inks were limited by the surface coverage of adsorbed OH and the first electron transfer at high overpotentials (indicated by a Tafel slopes >128 mV dec<sup>-1</sup>). Diluting the catalyst ink from 1:25 to 1:100 solid:liquid mass enhanced the performance and catalyst utilization, likely by reducing transport resistances via decreasing the ionomer thickness on the Ag catalyst particles and Ni foam support. The catalytic activity of the Ni foam support was leveraged to partially hydrogenate the deposited PCMS-*b*-PCOE-*b*-PCMS block copolymer midblock to PE. After functionalization with MPRD, this electrode displayed the best performance, likely due to the enhanced properties of PE compared to PCOE. Finally, the two partially hydrogenated ionomers with either TMA or MPRD were compared in a single-cell electrolyzer, where the MPRD-functionalized electrode significantly outperformed the TMA-functionalized electrode in both 1 M K<sub>2</sub>CO<sub>3</sub> and DI water.

With the results of this thesis summarized, the hypotheses proposed in *Chapter 1* can be addressed in the context of the results.

*Hypothesis 1:* We can modify the block copolymer-based AEM polychloromethylstyrene-*b*-polycyclooctene-*b*-polychloromethylstyrene (PCMS-*b*-PCOE-*b*-PCMS)

by saturating the C=C bonds in PCOE to make a polyethylene (PE)-based block copolymer. Because PE is semicrystalline, the resulting AEM will be more thermally robust, chemically stable, and hydrophobic, affording it better water uptake and mechanical integrity compared to its PCOE precursor.

As mentioned above, in *Chapter 2* the PCMS-*b*-PCOE-*b*-PCMS triblock copolymer was successfully hydrogenated to PCMS-*b*-PE-*b*-PCMS. The incorporation of PE provided the AEM with enhanced thermal and alkaline stability. Additionally, the water uptake and dimensional swelling greatly improved, and further afforded the material practical mechanical properties for aqueous applications. The findings in *Chapter 2* confirm *Hypothesis 1*.

*Hypothesis 2*: Functionalities, such as C=C bonds and quaternary ammonium cationic moieties, will interact with the surface of silver particles by varying degrees. Once these interactions are understood, they can be exploited to restructure the interfacial morphology and lead to favorable shifts in material characteristics.

The hypothesis is partially proven; in *Chapter 3*, interactions were identified between the C=C bonds and quaternary ammonium cations, in addition to the phenyl rings; however, the exact strength of these interactions could not be directly elucidated from the methods used in this work. Future work addressing this is proposed in the next section of the chapter. Additionally, in *Chapter 3*, ionomer characteristics including ambient water content and crystallinity were found to be dependent on the cation. In *Chapter 4*, interactions between the ionomer thin films and a silver surface are shown to influence the morphology and water uptake, which were also determined to be dependent on the cationic moiety; accordingly, it is reasonable to confirm ionomer properties can be understood, tuned, and leveraged, as stated in this hypothesis.

*Hypothesis 3*: The morphology of neutral block copolymer precursor thin films will be determined by the interactions at the silver-polymer interface, but in AEIs thin films, quaternary ammonium cationic moieties will interact more strongly with each other (dipole-dipole interactions) than with a silver surface (van der Waals interactions) and introduce more disorder.

In *Chapter 4*, the thin film morphology of the neutral block copolymer precursors was found to align perpendicular to a silver-coated substrate, while no order was observed on plain silicon. This indicates the ordered morphology was driven by polymer-silver interactions. For ionomer thin films, a complex interplay between silver-polymer interfacial interactions, confinement effects,

and dipole-dipole interactions between the pendant cationic moieties is revealed to affect the thin film morphology and water uptake. A greater tendency toward perpendicular alignment is found in thinner films where Ag-interfacial interactions are more dominant. As film thickness increases, Ag-interfacial interactions are less pronounced, and dipole-dipole interactions between pendant quaternary ammonium cations induce more disorder in the film; hence, *Hypothesis 3* is confirmed, with the caveat that interactions between the ionomer and the silver surface still influence the morphology, especially in thinner films.

*Hypothesis 4*: If functionalities such as C=C bonds in PCOE and quaternary ammonium cationic moieties interact with silver, an AEI with a PE backbone and MPRD quaternary ammonium cationic moieties will demonstrate better electrochemical performance compared to a PCOE backbone and TMA quaternary ammonium cation. A PE backbone will exhibit a reduced affinity for adsorption on silver compared to PCOE, and an MPRD quaternary ammonium cationic moiety will exhibit less adsorption than TMA due to steric hinderance. Ultimately, this will free active area on the catalyst surface and mitigate transport resistances.

In *Chapter 5*, the OER performance is optimized using an ionomer with an MPRD cation and a partially hydrogenated PE backbone. The PCOE-midblock TMA-cation ionomer maintained a higher ECSA than the PCOE-midblock MPRD-cation ionomer, which would indicate the TMA-cation yielded a larger available surface area for electrochemical reactions to take place. However, the MPRD cationic moiety improved the kinetics of the OER reaction by shifting the rate determining step at higher overpotentials to the initial adsorption of OH. With the partial hydrogenation of PCOE to PE, the PE-midblock MPRD-cation ionomer displayed a higher ECSA than the PE-midblock TMA-cation ionomer. This indicates there is a synergistic benefit to utilizing the PE-midblock along with the MPRD cation. Ultimately, the combination of enhanced ECSA and kinetics led to the PE-midblock MPRD-cation ionomer having the best OER performance; therefore, *Hypothesis 4* is partially confirmed in that the PE-MPRD combination was superior, however the reason is more complex than just a matter of surface coverage.

This thesis work has demonstrated the value in taking a stepwise, fundamental approach to elucidate the structure-property-performance relationship for optimization of the catalyst layer, in addition to the advantages of utilizing a tunable block copolymer electrolyte system. We conclude that interactions between this set of block copolymer electrolytes and silver catalyst particles

occur with the phenyl rings, quaternary ammonium cationic moieties, and C=C bonds in the polymer backbone. Resulting ionomer properties, including crystallinity and water uptake, are influenced by the nature of the interactions between silver and the two different quaternary ammonium cations investigated, TMA and MPRD. With TMA, the ionomer showed a loss in crystallinity and an increase in water content, while with MPRD, the ionomer showed an increase in certain crystalline reflections and comparatively higher crystallinity with a lower water content. Further, the ionomer thin film morphology on a silver surface is dependent on a complex interplay of quaternary ammonium cation dipole-dipole interactions, silver-polymer interfacial interactions, the block copolymer architecture (diblock vs triblock), and film thickness and confinement effects. It is concluded that MPRD cations along with a triblock copolymer architecture will provide enhanced water content at lower RH with reduced swelling at higher RH. Enhancing the water content at low RH can provide better ionic conductivity in drier operating conditions, while reduced swelling can mitigate the risk of ionomer delamination from the catalyst surface.

Ultimately, the fundamental findings concerning the interactions and thin film morphology are connected to a more complex, electrochemically realistic system by studying the OER kinetics and performance of a set of ionomer-catalyst inks. An MPRD cation is found to enhance the OER kinetics by reducing the Tafel slope and shifting the rds at high overpotentials. In combination with the MPRD cation, partial hydrogenation of the PCOE-midblock to PE led to an increase in the ECSA and yielded the highest performing ionomer-catalyst ink. The findings were validated in a single-cell AEM electrolyzer, utilizing the PE-based AEM developed at the beginning of this thesis work. This novel block copolymer AEM was enhanced by the incorporation of a PE-midblock, which ultimately provided the AEM with enhanced thermal and alkaline stability, improved water uptake and dimensional swelling, and further afforded the material practical mechanical properties for aqueous applications. In addition to demonstrating the application of this AEM in a water electrolyzer in the final study in this thesis, the scalable synthesis and highly desirable material properties have made this AEM commercially viable, and it is now available as Tuffbrane<sup>®</sup> from Spark Ionx Inc.

## 6.2 Recommendations for Future Work

This work has demonstrated that by starting with a fundamental understanding of interactions between ionomers and catalyst particles, an intentional, scientific approach can be taken to optimize the catalyst layer. Furthermore, the benefits of utilizing tunable block copolymers, which can be easily modified based on the application and desired properties, are shown. At the start of this work, silver was not yet considered an “endangered element”, with a serious threat of limited supply in the next 100 years [101]. Ultimately, this will negate silver as a catalyst for large scale applications. While the results on how to optimize a silver-based electrode are now less applicable, the scientific approach to catalyst layer optimization remains an important step of progress of this field.

The scope of this work targets both AEM fuel cells and electrolyzers, with each containing an anode and cathode that will need to be separately optimized. With such a variety of catalysts and supported catalysts reported each year, the most common base metals incorporated in each should be investigated so that ionomer-catalyst investigations can be carried out from a fundamental starting point. If we focus on the AEMWE anode where OER takes place, there are two cases to consider; alkaline and neutral pH catalysis. Currently, one of the biggest challenges in enhancing the performance of AEMWEs is developing an OER catalyst that is active in neutral pH. Figure 6.1 shows that cobalt, manganese, iron, and nickel, among a variety of others, are all promising candidates for neutral or near-neutral OER catalysis [417].

With the most plausible options for promising catalysts determined, the use of simulations to predict interactions between ionomers and catalysts should be thoroughly carried out to screen which catalysts might be more viable with certain ionomer chemistries. Simulating adsorption energies can speed up the initial process of honing in on a particular set of catalysts and ionomer frameworks before diving into experimental validation. Similar to the work of Bae and Kim regarding the adsorption of TMA on Pt, Pd and Ru based catalysts [123, 125, 126], density functional theory (DFT) calculations can be used to model the adsorption of specific chemical groups from the ionomer on different catalyst surfaces. Investigating a variety of quaternary ammonium cationic moieties, in addition to different backbone chemistries, will allow for the selection of a framework of tunable ionomer chemistries with which to move forward in

experimental validation. Using a simulation-based approach will also help answer the gap in *Hypothesis 2* concerning the exact strength of different interacting groups in future experiments.

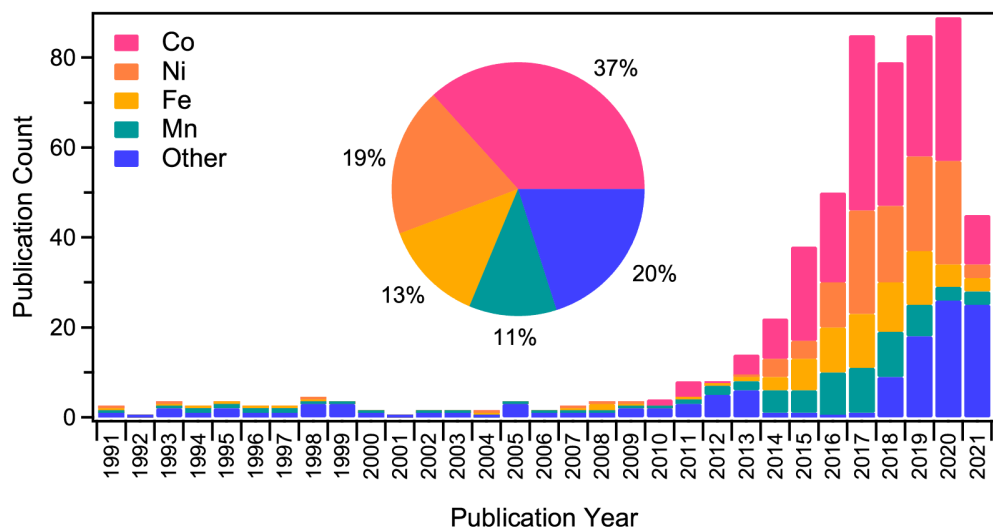


Figure 6.1 Bibliometric analysis the publications for OER catalysts at neutral pH. “Oxygen evolution reaction” and “neutral pH”, along with each catalyst were used as search terms. This citation report was generated using Web of Science.

For experiments, the two main focuses should be on model ionomer thin films on atomically flat substrates, like the study conducted in *Chapter 4*, or on more complex systems like the separated anode study conducted in *Chapter 5*. GISAXS was shown to be a very useful technique for probing the thin film morphology for both ambient and humidified conditions. In future work, the temperature and humidity-controlled chamber used for GISAXS could be re-designed to accommodate the measurement of film thickness and swelling during GISAXS experiments. In similar work, a white-light interferometer has been used to simultaneously measure film thickness during GISAXS experiments studying the effects of solvent vapor annealing or water uptake [420]. This type of in-situ thickness measurement would be highly beneficial for correlating the dimensional swelling to the changes in radius of gyration observed during humidification of ionomer thin films. Additionally, the use of quartz-crystal microbalance (QCM) measurements of thin film water uptake has also been shown to be a useful strategy [192, 206, 208]. Although QCM crystals can only be purchased with single-metal coatings, making them limited in their application to water uptake of ionomers on alloyed-catalyst systems, QCM could provide a useful

comparison to correlate with other water uptake and swelling data.

The PTFE FlexCell<sup>®</sup> (Gaskatel, gmbH) half-cell apparatus used in *Chapter 5* can be used for a variety of ionomer-catalyst optimization studies. This study focused on the PCMS-*b*-PCOE-*b*-PCMS triblock copolymer system functionalized with TMA or MPRD. Future work could incorporate the PCMS-*b*-PIp-*b*-PCMS triblock copolymer system utilized in *Chapter 4*. Preliminary results showed this polymer system could be hydrogenated via the method used in *Chapter 2* [102], where the PIp midblock can be hydrogenated to polymethylbutylene (PMb) using diimide derived from the thermal decomposition of *p*-toluenesulfonylhydrazide (TSH).

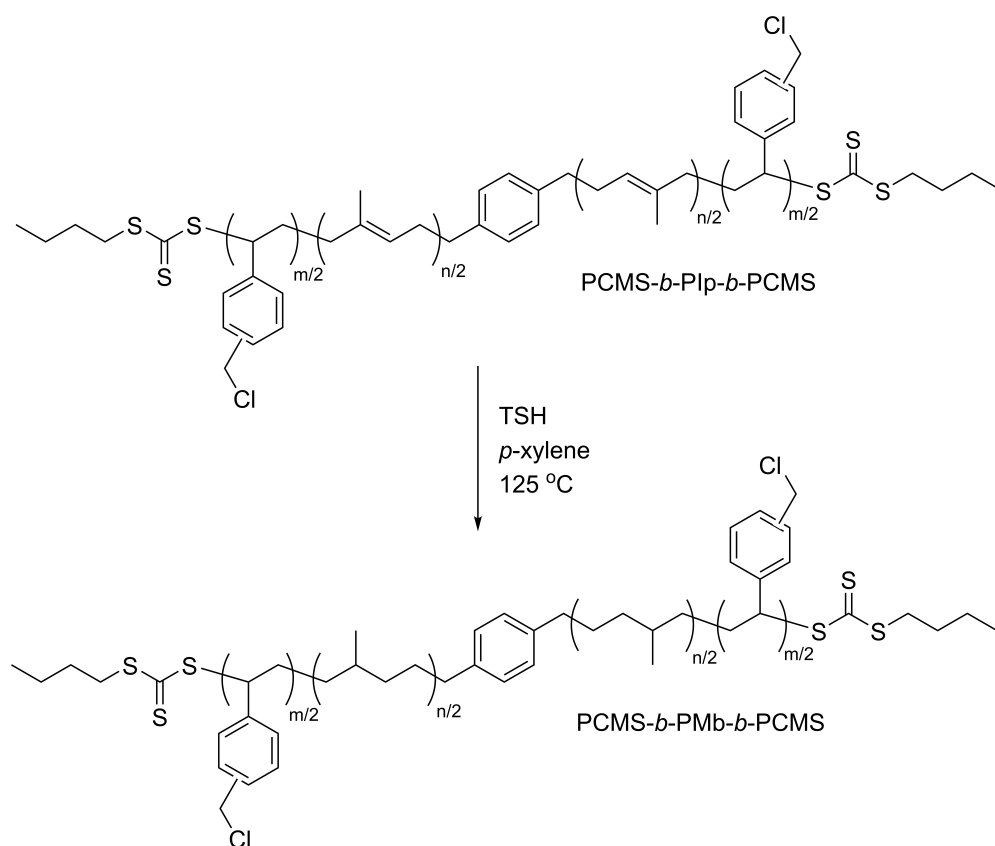


Figure 6.2 Reaction scheme showing the hydrogenation of PCMS-*b*-PIp-*b*-PCMS to PCMS-*b*-PMb-*b*-PCMS.

This system could be more interesting as an ionomer, as the hydrogenated version of the triblock was still soluble in  $\text{CHCl}_3$ . Future studies optimizing this set of triblock copolymers by varying the midblock (PIp vs PMb), cation chemistry (TMA vs MPRD), and ion exchange capacity (length of PCMS block) would be a viable next step. In order to further characterize this

system, the water uptake of the ionomer-catalyst ink coated substrates can be characterized using a dynamic vapor sorption (DVS) instrument. DVS is a gravimetric technique that subjects a sample to a relative humidity and measures the change in mass. By knowing the exact amount of ionomer loaded onto the substrate, the change in mass can be correlated to water uptake of the ionomer specifically incorporated into catalyst inks. The water uptake will be affected by interactions with different catalyst particles or by different ionomer chemistries. By measuring the water uptake of a catalyst-ink coated substrate, a comparison can be made to thin film water uptake to aid in understanding how a more heterogenous system affects these results. The only limitation on experiments carried out in the FlexCell<sup>®</sup> is the required concentrated electrolyte; hence, neutral pH studies cannot be conducted in this system, and must be completed using different experiments entirely.



## REFERENCES

- [1] Ulrich Cubasch, Donald Wuebbles, Deliang Chen, Maria Cristina Facchini, David Frame, Natalie Mahowald, and Jan-Gunnar Winther. Introduction in climate change 2013. *Intergovernmental Panel on Climate Change 2013: The Physical Science Basis. Contribution of Working Group I to the Fifth Assessment Report of the Intergovernmental Panel on Climate Change*, pages 119–158, 2013. ISSN ISBN 978-1-107-66182-0. doi: 10.1017/CBO9781107415324.007.
- [2] Lin Wang, Gordon Huang, Xiuquan Wang, and Hua Zhu. Risk-based electric power system planning for climate change mitigation through multi-stage joint-probabilistic left-hand-side chance-constrained fractional programming: A canadian case study. *Renewable and Sustainable Energy Reviews*, 82:1056–1067, 2018. ISSN 1364-0321. doi: <https://doi.org/10.1016/j.rser.2017.09.098>. URL <http://www.sciencedirect.com/science/article/pii/S1364032117313497>.
- [3] Fan Zhang, Pencheng Zhao, Meng Niu, and Jon Maddy. The survey of key technologies in hydrogen energy storage. *International Journal of Hydrogen Energy*, 41:14535–14552, 2016. doi: 10.1016/j.ijhydene.2016.05.293.
- [4] Ibrahim Dincer and Canan Acar. A review on potential use of hydrogen in aviation applications. *International Journal of Sustainable Aviation*, 2(1):74–100, 2016.
- [5] Giovanni Cipriani, Vincenzo Di Dio, Fabio Genduso, Diego La Cascia, Rosario Liga, Rosario Miceli, and Giuseppe Ricco Galluzzo. Perspective on hydrogen energy carrier and its automotive applications. *International Journal of Hydrogen Energy*, 39(16):8482–8494, 2014. ISSN 0360-3199. doi: <https://doi.org/10.1016/j.ijhydene.2014.03.174>. URL <https://www.sciencedirect.com/science/article/pii/S0360319914008660>.
- [6] Canan Acar and Ibrahim Dincer. *Energy and Exergy Analyses of a Zero Emission Power Plant for Coproduction of Electricity and Methanol*. Springer, Cham, 2014. ISBN 978-3-319-04680-8. doi: [https://doi.org/10.1007/978-3-319-04681-5\\_13](https://doi.org/10.1007/978-3-319-04681-5_13).
- [7] Elizabeth Connelly, Michael Penev, Anelia Milbrandt, Billy Roberts, Nicholas Gilroy, and Marc Melaina. Resource assessment for hydrogen production. Report, National Renewable Energy Laboratory, 2020.
- [8] Mark F. Ruth, Paige Jadun, Nicholas Gilroy, Elizabeth Connelly, Richard Boardman, A.J. Simon, Amgad Elgowainy, and Jarett Zuboy. The technical and economic potential of the h2@scale concept within the united states. Report, National Renewable Energy Laboratory, 2020.

- [9] Canan Acar and Ibrahim Dincer. Review and evaluation of hydrogen production options for better environment. *Journal of Cleaner Production*, 218:835–849, 2019. ISSN 0959-6526. doi: <https://doi.org/10.1016/j.jclepro.2019.02.046>. URL <https://www.sciencedirect.com/science/article/pii/S0959652619304251>.
- [10] Benedetto Nastasi and Gianluigi Lo Basso. Hydrogen to link heat and electricity in the transition towards future smart energy systems. *Energy*, 110:5–22, 2016. ISSN 0360-5442. doi: <https://doi.org/10.1016/j.energy.2016.03.097>. URL <https://www.sciencedirect.com/science/article/pii/S0360544216303413>.
- [11] U.S. DRIVE. Hydrogen production tech team roadmap. URL <https://www.energy.gov/eere/vehicles/vehicle-technologies-office>.
- [12] Hydrogen production processes, hydrogen and fuel cell technologies office, 2018. URL <https://www.energy.gov/eere/fuelcells/hydrogen-production-processes>.
- [13] H. Hassanzadeh and S. H. Mansouri. Efficiency of ideal fuel cell and carnot cycle from a fundamental perspective. *Proceedings of the Institution of Mechanical Engineers, Part A: Journal of Power and Energy*, 219(4):245–254, 2005. ISSN 0957-6509. doi: 10.1243/095765005X28571. URL <https://doi.org/10.1243/095765005X28571>.
- [14] W. R. Grove. Xxiv. on voltaic series and the combination of gases by platinum. *The London, Edinburgh, and Dublin Philosophical Magazine and Journal of Science*, 14(86-87): 127–130, 1839. ISSN 1941-5966. doi: 10.1080/14786443908649684. URL <https://doi.org/10.1080/14786443908649684>.
- [15] W.W. Jacques. Electricity direct from coal. *Harper’s Mag*, 94:144–150, 1896.
- [16] F. T. Bacon. The properties of the hydrogen–oxygen fuel cell. *BEAMA J*, 61:6–12, 1954.
- [17] George E. Evans and Karl V. Kordesch. Hydrazine-air fuel cells. *Science*, 158(3805):1148, 1967. doi: 10.1126/science.158.3805.1148. URL <http://science.sciencemag.org/content/158/3805/1148.abstract>.
- [18] Thousands of industrial facilities likely discharging toxic ‘forever chemicals’ into air and water, 2020. URL <https://www.ewg.org/news-insights/news/update-thousands-industrial-facilities-likely-discharging-toxic-forever>.
- [19] Sen. cohen leads senate in passing bill to ban dangerous pfas chemicals in firefighting foam food packaging, 13 May 2021. URL <http://www.senatedems.ct.gov/cohen-news/3785-cohen-210513#sthash.xaeH5Kdj.aNvfRxu1.dpbs>.
- [20] Rapidah Othman, Andrew L. Dicks, and Zhonghua Zhu. Non precious metal catalysts for the pem fuel cell cathode. *International Journal of Hydrogen Energy*, 37(1):357–372, 2012. ISSN 0360-3199. doi: <https://doi.org/10.1016/j.ijhydene.2011.08.095>. URL <http://www.sciencedirect.com/science/article/pii/S0360319911020192>.

- [21] Frank de Bruijn. The current status of fuel cell technology for mobile and stationary applications. *Green Chemistry*, 7:132–150, 2005.
- [22] M. Schulze and E. Gülzow. Degradation of nickel anodes in alkaline fuel cells. *Journal of Power Sources*, 127(1):252–263, 2004. ISSN 0378-7753. doi: <https://doi.org/10.1016/j.jpowsour.2003.09.021>. URL <http://www.sciencedirect.com/science/article/pii/S0378775303009595>.
- [23] Nagappan Ramaswamy and Sanjeev Mukerjee. Influence of inner- and outer-sphere electron transfer mechanisms during electrocatalysis of oxygen reduction in alkaline media. *Journal of Physical Chemistry C*, 115:18015–18026, 2011. ISSN 1932-7447. doi: 10.1021/jp204680p.
- [24] E. H. Yu, K. Scott, and R. W. Reeve. Electrochemical reduction of oxygen on carbon supported pt and pt/ru fuel cell electrodes in alkaline solutions. *Fuel Cells*, 3(4):169–176, 2004. ISSN 1615-6846. doi: 10.1002/fuce.200330129. URL <https://doi.org/10.1002/fuce.200330129>.
- [25] T. J. Omasta, L. Wang, X. Peng, C. A. Lewis, J. R. Varcoe, and W. E. Mustain. Importance of balancing membrane and electrode water in anion exchange membrane fuel cells. *Journal of Power Sources*, 375, 2018. doi: 10.1016/j.jpowsour.2017.05.006.
- [26] Travis J. Omasta, Andrew M. Park, Jacob M. LaManna, Yufeng Zhang, Xiong Peng, Lianqin Wang, David L. Jacobson, John R. Varcoe, Daniel S. Hussey, Bryan S. Pivovar, and William E. Mustain. Beyond catalysis and membranes: visualizing and solving the challenge of electrode water accumulation and flooding in aemfcs. *Energy & Environmental Science*, 11(3):551–558, 2018. ISSN 1754-5692. doi: 10.1039/C8EE00122G. URL <http://dx.doi.org/10.1039/C8EE00122G>.
- [27] Géraldine Merle, Matthias Wessling, and Kitty Nijmeijer. Anion exchange membranes for alkaline fuel cells: A review. *Journal of Membrane Science*, 377:1–35, 2011. ISSN 0376-7388. doi: 10.1016/j.memsci.2011.04.043.
- [28] Xiang and Chen. Hydrogen and electricity from coal with carbon dioxide separation using chemical looping reactors. *Energy & Fuels*, 21(4):2272–2277, 2007. ISSN 0887-0624. doi: 10.1021/ef060517h. URL <https://doi.org/10.1021/ef060517h>.
- [29] S. Ahmed and M. Krumpelt. Hydrogen from hydrocarbon fuels for fuel cells. *International Journal of Hydrogen Energy*, 26(4):291–301, 2001. ISSN 0360-3199. doi: [https://doi.org/10.1016/S0360-3199\(00\)00097-5](https://doi.org/10.1016/S0360-3199(00)00097-5). URL <https://www.sciencedirect.com/science/article/pii/S0360319900000975>.
- [30] Yohei Akutsu, Dong-Yeol Lee, Yong-Zhi Chi, Yu-You Li, Hideki Harada, and Han-Qing Yu. Thermophilic fermentative hydrogen production from starch-wastewater with bio-granules. *International Journal of Hydrogen Energy*, 34(12):5061–5071, 2009. ISSN 0360-3199. doi: <https://doi.org/10.1016/j.ijhydene.2009.04.024>. URL <https://www.sciencedirect.com/science/article/pii/S0360319909005400>.

- [31] N. Butt, H. L. Beyer, J. R. Bennett, D. Biggs, R. Maggini, M. Mills, A. R. Renwick, L. M. Seabrook, and H. P. Possingham. Biodiversity risks from fossil fuel extraction. *Science*, 342(6157):425, 2013. doi: 10.1126/science.1237261. URL <http://science.sciencemag.org/content/342/6157/425.abstract>.
- [32] Meng Ni, Dennis Y. C. Leung, Michael K. H. Leung, and K. Sumathy. An overview of hydrogen production from biomass. *Fuel Processing Technology*, 87(5):461–472, 2006. ISSN 0378-3820. doi: <https://doi.org/10.1016/j.fuproc.2005.11.003>. URL <https://www.sciencedirect.com/science/article/pii/S0378382005001980>.
- [33] Pierre Millet and Sergey Grigoriev. *Chapter 2: Water Electrolysis Technologies*. Elsevier, 2013.
- [34] Immanuel Vincent and Dmitri Bessarabov. Low cost hydrogen production by anion exchange membrane electrolysis: A review. *Renewable and Sustainable Energy Reviews*, 81: 1690–1704, 2018. ISSN 1364-0321. doi: <https://doi.org/10.1016/j.rser.2017.05.258>. URL <http://www.sciencedirect.com/science/article/pii/S1364032117309127>.
- [35] Marcelo Carmo, David L. Fritz, Jürgen Mergel, and Detlef Stolten. A comprehensive review on pem water electrolysis. *International Journal of Hydrogen Energy*, 38(12):4901–4934, 2013. ISSN 0360-3199. doi: <https://doi.org/10.1016/j.ijhydene.2013.01.151>. URL <https://www.sciencedirect.com/science/article/pii/S0360319913002607>.
- [36] Jason C. Ganley. High temperature and pressure alkaline electrolysis. *International Journal of Hydrogen Energy*, 34(9):3604–3611, 2009. ISSN 0360-3199. doi: <https://doi.org/10.1016/j.ijhydene.2009.02.083>. URL <https://www.sciencedirect.com/science/article/pii/S0360319909003577>.
- [37] A.Sh. Aliyev, R.G. Guseynova, U.M. Gurbanova, D.M. Babanly, V.N. Fateev, I.V. Pushkareva, and D.B. Tagiyev. Electrocatalysts for the electrolysis of water. *Chemical Problems*, 3(16):283–305, 2018.
- [38] Yipu Liu, Xiao Liang, Hui Chen, Ruiqin Gao, Lei Shi, Lan Yang, and Xiaoxin Zou. Iridium-containing water-oxidation catalysts in acidic electrolyte. *Chinese Journal of Catalysis*, 42(7):1054–1077, 2021. ISSN 1872-2067. doi: [https://doi.org/10.1016/S1872-2067\(20\)63722-6](https://doi.org/10.1016/S1872-2067(20)63722-6). URL <https://www.sciencedirect.com/science/article/pii/S1872206720637226>.
- [39] Zi-You Yu, Yu Duan, Xing-Yu Feng, Xingxing Yu, Min-Rui Gao, and Shu-Hong Yu. Clean and affordable hydrogen fuel from alkaline water splitting: Past, recent progress, and future prospects. *Advanced Materials*, n/a(n/a):2007100, 2021. ISSN 0935-9648. doi: <https://doi.org/10.1002/adma.202007100>. URL <https://doi.org/10.1002/adma.202007100>.

- [40] O. Schmidt, A. Gambhir, I. Staffell, A. Hawkes, J. Nelson, and S. Few. Future cost and performance of water electrolysis: An expert elicitation study. *International Journal of Hydrogen Energy*, 42(52):30470–30492, 2017. ISSN 0360-3199. doi: <https://doi.org/10.1016/j.ijhydene.2017.10.045>. URL <https://www.sciencedirect.com/science/article/pii/S0360319917339435>.
- [41] Katherine E. Ayers, Everett B. Anderson, Christopher Capuano, Blake Carter, Luke Dalton, Greg Hanlon, Judith Manco, and Michael Niedzwiecki. Research advances towards low cost, high efficiency pem electrolysis. *ECS Transactions*, 33(1):3–15, 2010.
- [42] Sayed M. Saba, Martin Müller, Martin Robinius, and Detlef Stolten. The investment costs of electrolysis – a comparison of cost studies from the past 30 years. *International Journal of Hydrogen Energy*, 43(3):1209–1223, 2018. ISSN 0360-3199. doi: <https://doi.org/10.1016/j.ijhydene.2017.11.115>. URL <https://www.sciencedirect.com/science/article/pii/S0360319917344956>.
- [43] Dongguo Li, Andrew R. Motz, Chulsung Bae, Cy Fujimoto, Gaoqiang Yang, Feng-Yuan Zhang, Katherine E. Ayers, and Yu Seung Kim. Durability of anion exchange membrane water electrolyzers. *Energy & Environmental Science*, 14(6):3393–3419, 2021. ISSN 1754-5692. doi: 10.1039/D0EE04086J. URL <http://dx.doi.org/10.1039/D0EE04086J>.
- [44] B. Smitha, S. Sridhar, and A. A. Khan. Solid polymer electrolyte membranes for fuel cell applications - a review. *Journal of Membrane Science*, 259:10–26, 2005.
- [45] G. Couture, A. Alaaeddine, F. Boschet, and B. Ameduri. Polymeric materials as anion-exchange membranes for alkaline fuel cells. *Progress in Polymer Science*, 36:15211557, 2011.
- [46] John R. Varcoe, Plamen Atanassov, Dario R. Dekel, Andrew M. Herring, Michael A. Hickner, Paul. A. Kohl, Anthony R. Kucernak, William E. Mustain, Kitty Nijmeijer, Keith Scott, Tongwen Xu, and Lin Zhuang. Anion-exchange membranes in electrochemical energy systems. *Energy & Environmental Science*, 7:3135–3191, 2014. ISSN 1754-5692. doi: 10.1039/C4EE01303D.
- [47] S. Piril Ertem, Tsung Han Tsai, Melissa M. Donahue, Wenxu Zhang, Himanshu Sarode, Ye Liu, Soenke Seifert, Andrew M. Herring, and E. Bryan Coughlin. Photo-cross-linked anion exchange membranes with improved water management and conductivity. *Macromolecules*, 49(1):153–161, 2016. doi: 10.1021/acs.macromol.5b01784.
- [48] Ye Liu, Bingzi Zhang, Corey L. Kinsinger, Yuan Yang, Soenke Seifert, Yushan Yan, C. Mark Maupin, Matthew W. Liberatore, and Andrew M. Herring. Anion exchange membranes composed of a poly(2,6-dimethyl-1,4-phenylene oxide) random copolymer functionalized with a bulky phosphonium cation. *Journal of Membrane Science*, 506:50–59, 2016. doi: 10.1016/j.memsci.2016.01.042.

- [49] Tsung Han Tsai, S. Pırl Ertem, Ashley M. Maes, Soenke Seifert, Andrew M. Herring, and E. Bryan Coughlin. Thermally cross-linked anion exchange membranes from solvent processable isoprene containing ionomers. *Macromolecules*, 2015. ISSN 0024-9297. doi: 10.1021/ma502362a.
- [50] Yifan Li, Ye Liu, Alice M. Savage, Frederick L. Beyer, Soenke Seifert, Andrew M. Herring, and Daniel M. Knauss. Polyethylene-based block copolymers for anion exchange membranes. *Macromolecules*, 48(18):6523–6533, 2015. ISSN 0024-9297. doi: 10.1021/acs.macromol.5b01457. URL <https://doi.org/10.1021/acs.macromol.5b01457>.
- [51] Xueqiang Gao, Hongmei Yu, Jia Jia, Jinkai Hao, Feng Xie, Jun Chi, Bowen Qin, Li Fu, Wei Song, and Zhigang Shao. High performance anion exchange ionomer for anion exchange membrane fuel cells. *RSC Advances*, 7(31):19153–19161, 2017. doi: 10.1039/C7RA01980G. URL <http://dx.doi.org/10.1039/C7RA01980G>.
- [52] Wenxu Zhang, Ye Liu, Aaron C. Jackson, Alice M. Savage, S. Pırl Ertem, Tsung Han Tsai, Soenke Seifert, Frederick L. Beyer, Matthew W. Liberatore, Andrew M. Herring, and E. Bryan Coughlin. Achieving continuous anion transport domains using block copolymers containing phosphonium cations. *Macromolecules*, 2016. ISSN 0024-9297. doi: 10.1021/acs.macromol.6b00653.
- [53] Lisha Liu, John Ahlfield, Andrew Tricker, Deryn Chu, and Paul A. Kohl. Anion conducting multiblock copolymer membranes with partial fluorination and long head-group tethers. *Journal of Materials Chemistry A*, 4:16233, 2016.
- [54] Melissa A. Vandiver, Benjamin R. Caire, Zach Poskin, Yifan Li, Sönke Seifert, Daniel M. Knauss, Andrew M. Herring, and Matthew W. Liberatore. Durability and performance of polystyrene-b-poly(vinylbenzyl trimethylammonium) diblock copolymer and equivalent blend anion exchange membranes. *Journal of Applied Polymer Science*, 132:1–9, 2015. doi: 10.1002/app.41596.
- [55] Lianqin Wang, Emanuele Magliocca, Emma L. Cunningham, William E. Mustain, Simon D. Poynton, Ricardo Escudero-Cid, Mohamed M. Nasef, Julia Ponce-González, Rachida Bance-Souahli, Robert C. T. Slade, Daniel K. Whelligan, and John R. Varcoe. An optimised synthesis of high performance radiation-grafted anion-exchange membranes. *Green Chem.*, 19, 2017. doi: 10.1039/C6GC02526A.
- [56] Lianqin Wang, Jethro J. Brink, Ye Liu, Andrew M. Herring, Julia Ponce-González, Daniel K. Whelligan, and John R. Varcoe. Non-fluorinated pre-irradiation-grafted (peroxidated) ldpe-based anion-exchange membranes with high performance and stability. *Energy & Environmental Science*, 10(10):2154–2167, 2017. ISSN 1754-5692. doi: 10.1039/C7EE02053H. URL <http://dx.doi.org/10.1039/C7EE02053H>.

- [57] Julia Ponce-González, Daniel K. Whelligan, Lianqin Wang, Rachida Bance-Soualhi, Ying Wang, Yanqiu Peng, Hanqing Peng, David C. Apperley, Himanshu N. Sarode, Tara P. Pandey, Ashutosh G. Divekar, Soenke Seifert, Andrew M. Herring, Lin Zhuang, and John R. Varcoe. High performance aliphatic-heterocyclic benzyl-quaternary ammonium radiation-grafted anion-exchange membranes. *Energy & Environmental Science*, 9: 3724–3735, 2016. doi: 10.1039/c6ee01958g.
- [58] Ye Liu, Tara P. Pandey, Himanshu N. Sarode, Mei Chen Kuo, Wenxu Zhang, Rohit Gupta, Samuel Galioto, Amobi G. Ozioko, Soenke Seifert, Matthew W. Liberatore, E. Bryan Coughlin, and Andrew M. Herring. Thin, robust, and chemically stable photo-cross-linked anion exchange membranes based on a polychlorostyrene-b-polycyclooctene-b-polychlorostyrene-aba triblock polymer. *Solid State Ionics*, 316:135–142, 2018. doi: 10.1016/j.ssi.2017.12.031.
- [59] B. Bae, K. Miyatake, and M. Effect Watanabe. Effect of the hydrophobic component on the properties of sulfonated poly(arylene ether sulfone)s. *Macromolecules*, 42:18731880, 2009.
- [60] K. H. Lee, S. Y. Lee, D. W. Shin, C. Wang, S.-H. Ahn, K.-J. Lee, M. D. Guiver, and Y. M. Lee. Structural influence of hydrophobic diamine in sulfonated poly(sulfide sulfone imide) copolymers on medium temperature pem fuel cell. *Polymer*, 55:1317–1326, 2014.
- [61] Xiuhua Li, Qunfang Liu, Yingfeng Yu, and Yuezhong Meng. Quaternized poly(arylene ether) ionomers containing triphenyl methane groups for alkaline anion exchange membranes. *Journal of Materials Chemistry A*, 1(13):4324–4335, 2013. ISSN 2050-7488. doi: 10.1039/C3TA00342F. URL <http://dx.doi.org/10.1039/C3TA00342F>.
- [62] Amaranadh Jasti and Vinod K. Shahi. Multi-block poly(arylene ether)s containing pre-chloromethylated bisphenol: anion conductive ionomers. *Journal of Materials Chemistry A*, 1(20):6134–6137, 2013. ISSN 2050-7488. doi: 10.1039/C3TA10857K. URL <http://dx.doi.org/10.1039/C3TA10857K>.
- [63] Dongyang Chen, Michael A. Hickner, Shuanjin Wang, Jingjing Pan, Min Xiao, and Yuezhong Meng. Synthesis and characterization of quaternary ammonium functionalized fluorene-containing cardo polymers for potential anion exchange membrane water electrolyzer applications. *International Journal of Hydrogen Energy*, 37(21):16168–16176, 2012. ISSN 0360-3199. doi: <https://doi.org/10.1016/j.ijhydene.2012.08.051>. URL <http://www.sciencedirect.com/science/article/pii/S0360319912018538>.
- [64] Xiuhua Li, Yingfeng Yu, and Yuezhong Meng. Novel quaternized poly(arylene ether sulfone)/nano-zro2 composite anion exchange membranes for alkaline fuel cells. *ACS Applied Materials & Interfaces*, 5(4):1414–1422, 2013. ISSN 1944-8244. doi: 10.1021/am302844x. URL <https://doi.org/10.1021/am302844x>.
- [65] Rajeswari Janarthanan, James L. Horan, Benjamin R. Caire, Zachary C. Ziegler, Yuan Yang, Xiaobing Zuo, Matthew W. Liberatore, Michael R. Hibbs, and Andrew M. Herring. Understanding anion transport in an aminated trimethyl polyphenylene with high anionic conductivity. *Journal of Polymer Science Part B: Polymer Physics*, 51(24):1743, 2012.

- [66] Cy Fujimoto, Dae-Sik Kim, Michael Hibbs, Debra Wroblewski, and Yu Seung Kim. Backbone stability of quaternized polyaromatics for alkaline membrane fuel cells. *Journal of Membrane Science*, 423-424:438–449, 2012. ISSN 0376-7388. doi: <https://doi.org/10.1016/j.memsci.2012.08.045>. URL <http://www.sciencedirect.com/science/article/pii/S0376738812006448>.
- [67] Elise E. Switzer, Tim S. Olson, Abhaya K. Datye, Plamen Atanassov, Michael R. Hibbs, Cy Fujimoto, and Christopher J. Cornelius. Novel koh-free anion-exchange membrane fuel cell: Performance comparison of alternative anion-exchange ionomers in catalyst ink. *Electrochimica Acta*, 55(9):3404–3408, 2010. ISSN 0013-4686. doi: <https://doi.org/10.1016/j.electacta.2009.12.073>. URL <http://www.sciencedirect.com/science/article/pii/S0013468610000228>.
- [68] Yifan Li, Aaron C. Jackson, Frederick L. Beyer, and Daniel M. Knauss. Poly(2,6-dimethyl-1,4-phenylene oxide) blended with poly(vinylbenzyl chloride)-b-polystyrene for the formation of anion exchange membranes. *Macromolecules*, 47(19):6757–6767, 2014. ISSN 0024-9297. doi: 10.1021/ma500993s. URL <https://doi.org/10.1021/ma500993s>.
- [69] Ashley M. Maes, Tara P. Pandey, Melissa A. Vandiver, Lauren K. Lundquist, Yuan Yang, James L. Horan, Anastasia Krosovsky, Matthew W. Liberatore, Sönke Seifert, and Andrew M. Herring. Preparation and characterization of an alkaline anion exchange membrane from chlorinated poly(propylene) aminated with branched poly(ethyleneimine). *Electrochimica Acta*, 110:260–266, 2013. ISSN 0013-4686. doi: <https://doi.org/10.1016/j.electacta.2013.04.033>. URL <http://www.sciencedirect.com/science/article/pii/S0013468613006750>.
- [70] Min Zhang, Hyung Kyu Kim, Elena Chalkova, Fedkin Mark, Serguei N. Lvov, and T. C. Mike Chung. New polyethylene based anion exchange membranes (pe-aems) with high ionic conductivity. *Macromolecules*, 44(15):5937–5946, 2011. ISSN 0024-9297. doi: 10.1021/ma200836d. URL <https://pubs.acs.org/doi/abs/10.1021/ma200836d>.
- [71] Henry A. Kostalik, Timothy J. Clark, Nicholas J. Robertson, Paul F. Mutolo, Julie M. Longo, Héctor D. Abruña, and Geoffrey W. Coates. Solvent processable tetraalkylammonium-functionalized polyethylene for use as an alkaline anion exchange membrane. *Macromolecules*, 43(17):7147–7150, 2010. ISSN 0024-9297. doi: 10.1021/ma101172a. URL <https://doi.org/10.1021/ma101172a>.
- [72] Garrett Huang, Mrinmay Mandal, Xiong Peng, Ami C. Yang-Neyerlin, Bryan S. Pivovar, William E. Mustain, and Paul A. Kohl. Composite poly(norbornene) anion conducting membranes for achieving durability, water management and high power (3.4 w/cm<sup>2</sup>) in hydrogen/oxygen alkaline fuel cells. *Journal of the Electrochemical Society*, 166(10):F637, 2019. doi: 10.1149/2.1301910jes. URL <https://doi.org/10.1149/2.1301910jes>.
- [73] Jing Pan, Chen Chen, Lin Zhuang, and Juntao Lu. Designing advanced alkaline polymer electrolytes for fuel cell applications. *Accounts of Chemical Research*, 45(3):473–481, 2012. ISSN 0001-4842. doi: 10.1021/ar200201x. URL <https://doi.org/10.1021/ar200201x>.



- [74] Jing Pan, Juanjuan Han, Liang Zhu, and Michael A. Hickner. Cationic side-chain attachment to poly(phenylene oxide) backbones for chemically stable and conductive anion exchange membranes. *Chemistry of Materials*, 29(12):5321–5330, 2017. ISSN 0897-4756. doi: 10.1021/acs.chemmater.7b01494. URL <https://doi.org/10.1021/acs.chemmater.7b01494>.
- [75] Yating Yang and Daniel M. Knauss. Poly(2,6-dimethyl-1,4-phenylene oxide)-b-poly(vinylbenzyltrimethylammonium) diblock copolymers for highly conductive anion exchange membranes. *Macromolecules*, 48(13):4471–4480, 2015. ISSN 0024-9297. doi: 10.1021/acs.macromol.5b00459. URL <https://doi.org/10.1021/acs.macromol.5b00459>.
- [76] Naoki Yokota, Manai Shimada, Hideaki Ono, Ryo Akiyama, Eriko Nishino, Koichiro Asazawa, Junpei Miyake, Masahiro Watanabe, and Kenji Miyatake. Aromatic copolymers containing ammonium-functionalized oligophenylene moieties as highly anion conductive membranes. *Macromolecules*, 47(23):8238–8246, 2014. ISSN 0024-9297. doi: 10.1021/ma5019878. URL <https://doi.org/10.1021/ma5019878>.
- [77] Ahmed Mohamed Ahmed Mahmoud, Ahmed Mohamed Mohamed Elsaghier, Kanji Otsuji, and Kenji Miyatake. High hydroxide ion conductivity with enhanced alkaline stability of partially fluorinated and quaternized aromatic copolymers as anion exchange membranes. *Macromolecules*, 50(11):4256–4266, 2017. ISSN 0024-9297. doi: 10.1021/acs.macromol.7b00401. URL <https://doi.org/10.1021/acs.macromol.7b00401>.
- [78] Dong Liu, Muzi Xu, Mingliang Fang, Jiale Chen, and Lei Wang. Branched comb-shaped poly(arylene ether sulfone)s containing flexible alkyl imidazolium side chains as anion exchange membranes. *Journal of Materials Chemistry A*, 6(23):10879–10890, 2018. ISSN 2050-7488. doi: 10.1039/C8TA02115E. URL <http://dx.doi.org/10.1039/C8TA02115E>.
- [79] Wenxu Zhang, Ye Liu, Xiaohui Liu, James L. Horan, Ying Jin, Xiaoming Ren, S. Pırl Ertem, Soenke Seifert, Matthew W. Liberatore, Andrew M. Herring, and Edward Bryan Coughlin. Crosslinked anion exchange membranes with connected cations. *Journal of Polymer Science, Part A: Polymer Chemistry*, 2018. doi: 10.1002/pola.28935.
- [80] Patric Jannasch and Eva Annika Weiber. Configuring anion-exchange membranes for high conductivity and alkaline stability by using cationic polymers with tailored side chains. *Macromolecular Chemistry and Physics*, 217(10):1108–1118, 2016. ISSN 1022-1352. doi: 10.1002/macp.201500481. URL <https://doi.org/10.1002/macp.201500481>.
- [81] Jose A. Vega, Casey Chartier, and William E. Mustain. Effect of hydroxide and carbonate alkaline media on anion exchange membranes. *Journal of Power Sources*, 195(21): 7176–7180, 2010. ISSN 0378-7753. doi: <https://doi.org/10.1016/j.jpowsour.2010.05.030>. URL <https://www.sciencedirect.com/science/article/pii/S0378775310008554>.
- [82] Shaji Chempath, Brian R. Einsla, Lawrence R. Pratt, Clay S. Macomber, James M. Boncella, Jonathan A. Rau, and Bryan S. Pivovar. Mechanism of tetraalkylammonium headgroup degradation in alkaline fuel cell membranes. *The Journal of Physical Chemistry C*, 112(9):3179–3182, 2008. ISSN 1932-7447. doi: 10.1021/jp7115577. URL <https://doi.org/10.1021/jp7115577>.

- [83] M. Tomoi, K. Yamaguchi, R. Ando, Y. Kantake, Y. Aosaki, and H. Kubota. Synthesis and thermal stability of novel anion exchange resins with spacer chains. *Journal of Applied Polymer Science*, 64(6):1161–1167, 1997. ISSN 0021-8995. URL [https://doi.org/10.1002/\(SICI\)1097-4628\(19970509\)64:6<1161::AID-APP16>3.0.CO;2-Z](https://doi.org/10.1002/(SICI)1097-4628(19970509)64:6<1161::AID-APP16>3.0.CO;2-Z).
- [84] Ryo Akiyama, Naoki Yokota, Kanji Otsuji, and Kenji Miyatake. Structurally well-defined anion conductive aromatic copolymers: Effect of the side-chain length. *Macromolecules*, 51(9):3394–3404, 2018. ISSN 0024-9297. doi: 10.1021/acs.macromol.8b00284. URL <https://doi.org/10.1021/acs.macromol.8b00284>.
- [85] M. G. Marino and K. D. Kreuer. Alkaline stability of quaternary ammonium cations for alkaline fuel cell membranes and ionic liquids. *ChemSusChem*, 8:513 – 523, 2015. ISSN 1864-564X. doi: 10.1002/cssc.201403022.
- [86] Andrew G. Wright, Thomas Weissbach, and Steven Holdcroft. Poly(phenylene) and m-terphenyl as powerful protecting groups for the preparation of stable organic hydroxides. *Angewandte Chemie International Edition*, 55(15):4818–4821, 2016. ISSN 1433-7851. doi: <https://doi.org/10.1002/anie.201511184>. URL <https://doi.org/10.1002/anie.201511184>.
- [87] Joel S. Olsson, Thanh Huong Pham, and Patric Jannasch. Poly(arylene piperidinium) hydroxide ion exchange membranes: Synthesis, alkaline stability, and conductivity. *Advanced Functional Materials*, 28(2):1702758, 2018. ISSN 1616-301X. doi: <https://doi.org/10.1002/adfm.201702758>. URL <https://doi.org/10.1002/adfm.201702758>.
- [88] Junhua Wang, Yun Zhao, Brian P. Setzler, Santiago Rojas-Carbonell, Chaya Ben Yehuda, Alina Amel, Miles Page, Lan Wang, Keda Hu, Lin Shi, Shimshon Gottesfeld, Bingjun Xu, and Yushan Yan. Poly(aryl piperidinium) membranes and ionomers for hydroxide exchange membrane fuel cells. *Nature Energy*, 4(5):392–398, 2019. ISSN 2058-7546. doi: 10.1038/s41560-019-0372-8. URL <https://doi.org/10.1038/s41560-019-0372-8>.
- [89] Derek J. Strasser, Brendan J. Graziano, and Daniel M. Knauss. Base stable poly(diallylpiperidinium hydroxide) multiblock copolymers for anion exchange membranes. *Journal of Materials Chemistry A*, 5(20):9627–9640, 2017. ISSN 2050-7488. doi: 10.1039/C7TA00905D. URL <http://dx.doi.org/10.1039/C7TA00905D>.
- [90] Ami C. Yang-Neyerlin, Samantha Medina, Kelly M. Meek, Derek J. Strasser, Cheng He, Daniel M. Knauss, William E. Mustain, Svitlana Pylypenko, and Bryan S. Pivovar. Editors’ choice—examining performance and durability of anion exchange membrane fuel cells with novel spirocyclic anion exchange membranes. *Journal of The Electrochemical Society*, 168(4):044525, 2021. ISSN 0013-4651 1945-7111. doi: 10.1149/1945-7111/abf77f. URL <http://dx.doi.org/10.1149/1945-7111/abf77f>.
- [91] Shuang Gu, Rui Cai, Ting Luo, Zhongwei Chen, Minwei Sun, Yan Liu, Gaohong He, and Yushan Yan. A soluble and highly conductive ionomer for high-performance hydroxide exchange membrane fuel cells. *Angewandte Chemie*, 121(35):6621–6624, 2009. ISSN 0044-8249. doi: 10.1002/ange.200806299. URL <https://doi.org/10.1002/ange.200806299>.

- [92] Timothy J. Clark, Nicholas J. Robertson, Henry A. Kostalik Iv, Emil B. Lobkovsky, Paul F. Mutolo, Héctor D. Abruña, and Geoffrey W. Coates. A ring-opening metathesis polymerization route to alkaline anion exchange membranes: Development of hydroxide-conducting thin films from an ammonium-functionalized monomer. *Journal of the American Chemical Society*, 131(36):12888–12889, 2009. ISSN 0002-7863. doi: 10.1021/ja905242r. URL <https://doi.org/10.1021/ja905242r>.
- [93] C. R. Martin, T. A. Rhoades, and J. A. Ferguson. Dissolution of perfluorinated ion-containing polymers. *Analytical Chemistry*, 54(9):1639–1641, 1982.
- [94] M. S. Wilson and S. Gottesfeld. High performance catalyzed membranes of ultra-low pt loadings for polymer electrolyte fuel cells. *Journal of The Electrochemical Society*, 139(2): L28–L30, 1992.
- [95] Vinod M. Jalen and Calvin L. Bushnell. Method of producing highly dispersed catalytic platinum (u.s. patent no. us4136059a), 1977.
- [96] Junfeng Zhou, Krishna Joseph, John M. Ahlfield, Doh-Yeon Park, and Paul A. Kohl. Poly(arylene ether) ionomers with pendant quinuclidium groups and varying molecular weight for alkaline electrodes. *Journal of The Electrochemical Society*, 160(6):F573–F578, 2013. doi: 10.1149/2.077306jes. URL <https://doi.org/10.1149/2.077306jes>.
- [97] Rambabu Gutru, Zarina Turtayeva, Feina Xu, Gaël Maranzana, Brigitte Vigolo, and Alexandre Desforges. A comprehensive review on water management strategies and developments in anion exchange membrane fuel cells. *International Journal of Hydrogen Energy*, 45(38):19642–19663, 2020. ISSN 0360-3199. doi: 10.1016/j.ijhydene.2020.05.026. URL <https://www.sciencedirect.com/science/article/pii/S0360319920317547>.
- [98] Rong Zeng, Jennifer Handsel, Simon D. Poynton, Alexander J. Roberts, Robert C. T. Slade, Henryk Herman, David C. Apperley, and John R. Varcoe. Alkaline ionomer with tuneable water uptakes for electrochemical energy technologies. *Energy & Environmental Science*, 4(12):4925–4928, 2011. ISSN 1754-5692. doi: 10.1039/C1EE02349G. URL <http://dx.doi.org/10.1039/C1EE02349G>.
- [99] Garrett Huang, Mrinmay Mandal, Noor Ul Hassan, Katelyn Groenhout, Alexandra Dobbs, William E. Mustain, and Paul A. Kohl. Ionomer optimization for water uptake and swelling in anion exchange membrane electrolyzer: Hydrogen evolution electrode. *Journal of the Electrochemical Society*, 168:024503, 2021. doi: 10.1149/1945-7111/abde7b. URL <https://doi.org/10.1149/1945-7111/abde7b>.
- [100] Garrett Huang, Mrinmay Mandal, Noor Ul Hassan, Katelyn Groenhout, Alexandra Dobbs, William E. Mustain, and Paul A. Kohl. Ionomer optimization for water uptake and swelling in anion exchange membrane electrolyzer: Oxygen evolution electrode. *Journal of the Electrochemical Society*, 167:164514, 2020. doi: 10.1149/1945-7111/abcde3. URL <https://doi.org/10.1149/1945-7111/abcde3>.

- [101] Mun-Sik Shin, Young-Jun Byun, Young-Woo Choi, Moon-Sung Kang, and Jin-Soo Park. On-site crosslinked quaternized poly(vinyl alcohol) as ionomer binder for solid alkaline fuel cells. *International Journal of Hydrogen Energy*, 39(29):16556–16561, 2014. ISSN 0360-3199. doi: <https://doi.org/10.1016/j.ijhydene.2014.03.181>. URL <http://www.sciencedirect.com/science/article/pii/S0360319914008738>.
- [102] Nora C. Buggy, Yifeng Du, Mei Chen Kuo, Kayla A. Ahrens, Jacob S. Wilkinson, Soenke Seifert, E. Bryan Coughlin, and A. M. Herring. A polyethylene-based triblock copolymer anion exchange membrane with high conductivity and practical mechanical properties. *ACS Applied Polymer Materials*, 2(3):1294–1303, 2020. doi: 10.1021/acsapm.9b01182. URL <https://doi.org/10.1021/acsapm.9b01182>.
- [103] Mun-Sik Shin, Seohee Lim, Jong-Hyeok Park, Hyoung-Juhn Kim, Soryong Chae, and Jin-Soo Park. Thermally crosslinked and quaternized polybenzimidazole ionomer binders for solid alkaline fuel cells. *International Journal of Hydrogen Energy*, 45(20):11773–11783, 2020. ISSN 0360-3199. doi: <https://doi.org/10.1016/j.ijhydene.2020.02.081>. URL <https://www.sciencedirect.com/science/article/pii/S0360319920306455>.
- [104] Xian Liang, Muhammad Aamir Shehzad, Yuan Zhu, Lianqin Wang, Xiaolin Ge, Jianjun Zhang, Zhengjin Yang, Liang Wu, John Robert Varcoe, and Tongwen Xu. Ionomer cross-linking immobilization of catalyst nanoparticles for high performance alkaline membrane fuel cells. *Chemistry of Materials*, 31(19):7812–7820, 2019. ISSN 0897-4756. doi: 10.1021/acs.chemmater.9b00999. URL <https://doi.org/10.1021/acs.chemmater.9b00999>.
- [105] Bencai Lin, Lihua Qiu, Bo Qiu, Yu Peng, and Feng Yan. A soluble and conductive polyfluorene ionomer with pendant imidazolium groups for alkaline fuel cell applications. *Macromolecules*, 44(24):9642–9649, 2011. ISSN 0024-9297. doi: 10.1021/ma202159d. URL <https://doi.org/10.1021/ma202159d>.
- [106] Xiaoming Yan, Shuang Gu, Gaohong He, Xuemei Wu, and Jay Benziger. Imidazolium-functionalized poly(ether ether ketone) as membrane and electrode ionomer for low-temperature alkaline membrane direct methanol fuel cell. *Journal of Power Sources*, 250:90–97, 2014. ISSN 0378-7753. doi: <https://doi.org/10.1016/j.jpowsour.2013.10.140>. URL <http://www.sciencedirect.com/science/article/pii/S0378775313018089>.
- [107] Ziyi Han, Yuki Motoishi, and Tsuyohiko Fujigaya. Alkaline stability of anion-conductive ionomer coated on a carbon surface. *ACS Omega*, 4(17):17134–17139, 2019. ISSN 2470-1343. doi: 10.1021/acsomega.9b01466. URL <https://doi.org/10.1021/acsomega.9b01466>.
- [108] Jin-Soo Park, Seok-Hee Park, Sung-Dae Yim, Young-Gi Yoon, Won-Yong Lee, and Chang-Soo Kim. Performance of solid alkaline fuel cells employing anion-exchange membranes. *Journal of Power Sources*, 178(2):620–626, 2008. ISSN 0378-7753. doi: <https://doi.org/10.1016/j.jpowsour.2007.08.043>. URL <http://www.sciencedirect.com/science/article/pii/S0378775307015972>.

- [109] Jing Pan, Shanfu Lu, Yan Li, Aibin Huang, Lin Zhuang, and Juntao Lu. High-performance alkaline polymer electrolyte for fuel cell applications. *Advanced Functional Materials*, 20(2): 312–319, 2010. ISSN 1616-301X. doi: 10.1002/adfm.200901314. URL <https://doi.org/10.1002/adfm.200901314>.
- [110] Shanfu Lu, Jing Pan, Aibin Huang, Lin Zhuang, and Juntao Lu. Alkaline polymer electrolyte fuel cells completely free from noble metal catalysts. *Proceedings of the National Academy of Sciences*, 105(52):20611, 2008. doi: 10.1073/pnas.0810041106. URL <http://www.pnas.org/content/105/52/20611.abstract>.
- [111] Lu Sun, Junsong Guo, Jie Zhou, Qingming Xu, Deryn Chu, and Rongrong Chen. Novel nanostructured high-performance anion exchange ionomers for anion exchange membrane fuel cells. *Journal of Power Sources*, 202:70–77, 2012. ISSN 0378-7753. doi: 10.1016/j.jpowsour.2011.11.023. URL <http://www.sciencedirect.com/science/article/pii/S0378775311022142>.
- [112] Xin Xu, Sikan Peng, Shanfu Lu, Jian Gong, Jin Zhang, Wanxia Huang, and Yan Xiang. Modulation of the microstructure of the ag/c-based alkaline cathode via the ionomer content for a bipolar membrane fuel cell. *Journal of Power Sources*, 354:92–99, 2017. ISSN 0378-7753. doi: 10.1016/j.jpowsour.2017.04.006. URL <http://www.sciencedirect.com/science/article/pii/S0378775317304834>.
- [113] Junfeng Zhang, Yabiao Pei, Weikang Zhu, Yang Liu, Yan Yin, Yanzhou Qin, and Michael D. Guiver. Ionomer dispersion solvent influence on the microstructure of co-n-c catalyst layers for anion exchange membrane fuel cell. *Journal of Power Sources*, 484: 229259, 2021. ISSN 0378-7753. doi: <https://doi.org/10.1016/j.jpowsour.2020.229259>. URL <https://www.sciencedirect.com/science/article/pii/S0378775320315482>.
- [114] Travis J. Omasta, Xiong Peng, Hamish A. Miller, Francesco Vizza, Lianqin Wang, John R. Varcoe, Dario R. Dekel, and William E. Mustain. Beyond 1.0 w cm<sup>2</sup> performance without platinum: The beginning of a new era in anion exchange membrane fuel cells. *Journal of the Electrochemical Society*, 165:J3039, 2018.
- [115] Noor Ul Hassan, Mrinmay Mandal, Garrett Huang, Horie Adabi Firouzjaie, Paul A. Kohl, and William E. Mustain. Achieving high-performance and 2000 h stability in anion exchange membrane fuel cells by manipulating ionomer properties and electrode optimization. *Advanced Energy Materials*, 10(40):2001986, 2020. ISSN 1614-6832. doi: <https://doi.org/10.1002/aenm.202001986>. URL <https://doi.org/10.1002/aenm.202001986>.
- [116] Alaa Y. Faid, Lin Xie, Alejandro Oyarce Barnett, Frode Seland, Donald Kirk, and Svein Sunde. Effect of anion exchange ionomer content on electrode performance in aem water electrolysis. *International Journal of Hydrogen Energy*, 45(53):28272–28284, 2020. ISSN 0360-3199. doi: <https://doi.org/10.1016/j.ijhydene.2020.07.202>. URL <https://www.sciencedirect.com/science/article/pii/S0360319920328123>.

- [117] Hiroshi Ito, Naoki Miyazaki, Shota Sugiyama, Masayoshi Ishida, Yuka Nakamura, Shinya Iwasaki, Yasuo Hasegawa, and Akihiro Nakano. Investigations on electrode configurations for anion exchange membrane electrolysis. *Journal of Applied Electrochemistry*, 48(3): 305–316, 2018. ISSN 1572-8838. doi: 10.1007/s10800-018-1159-5. URL <https://doi.org/10.1007/s10800-018-1159-5>.
- [118] Ji Eun Park, Sun Young Kang, Seung-Hyeon Oh, Jong Kwan Kim, Myung Su Lim, Chi-Yeong Ahn, Yong-Hun Cho, and Yung-Eun Sung. High-performance anion-exchange membrane water electrolysis. *Electrochimica Acta*, 295:99–106, 2019. ISSN 0013-4686. doi: <https://doi.org/10.1016/j.electacta.2018.10.143>. URL <https://www.sciencedirect.com/science/article/pii/S0013468618323831>.
- [119] Kenji Fukuta, Hiroshi Inoue, Yohei Chikashige, and Hiroyuki Yanagi. Improved maximum power density of alkaline membrane fuel cells (amfcs) by the optimization of mea construction. *ECS Transactions*, 28(30):221–225, 2010.
- [120] Ji E. Chae, So Y. Lee, Sung J. Yoo, Jin Y. Kim, Jong H. Jang, Hee-Young Park, Hyun S. Park, Bora Seo, Dirk Henkensmeier, Kwang H. Song, and Hyoung-Juhn Kim. Polystyrene-based hydroxide-ion-conducting ionomer: Binder characteristics and performance in anion-exchange membrane fuel cells. *Polymers*, 13(5), 2021. ISSN 2073-4360. doi: 10.3390/polym13050690.
- [121] Ana Laura Gonçalves Biancolli, Daniel Herranz, Lianqin Wang, Gabriela Stehlíková, Rachida Bance-Soualhi, Julia Ponce-González, Pilar Ocón, Edson A. Ticianelli, Daniel K. Whelligan, John R. Varcoe, and Elisabete I. Santiago. Etf-based anion-exchange membrane ionomer powders for alkaline membrane fuel cells: a first performance comparison of head-group chemistry. *Journal of Materials Chemistry A*, 6(47):24330–24341, 2018. ISSN 2050-7488. doi: 10.1039/C8TA08309F. URL <http://dx.doi.org/10.1039/C8TA08309F>.
- [122] Shraboni Ghoshal, Bryan S. Pivovar, and Shaun M. Alia. Evaluating the effect of membrane-ionomer combinations and supporting electrolytes on the performance of cobalt nanoparticle anodes in anion exchange membrane electrolyzers. *Journal of Power Sources*, 488:229433, 2021. ISSN 0378-7753. doi: <https://doi.org/10.1016/j.jpowsour.2020.229433>. URL <https://www.sciencedirect.com/science/article/pii/S037877532031716X>.
- [123] Sandip Maurya, Sangtaik Noh, Ivana Matanovic, Eun Joo Park, Claudia Narvaez Villarrubia, Ulises Martinez, Junyoung Han, Chulsung Bae, and Yu Seung Kim. Rational design of polyaromatic ionomers for alkaline membrane fuel cells with >1 w cm<sup>2</sup> power density. *Energy & Environmental Science*, 11(11):3283–3291, 2018. ISSN 1754-5692. doi: 10.1039/C8EE02192A. URL <http://dx.doi.org/10.1039/C8EE02192A>.
- [124] Sung-Dae Yim, Hoon T. Chung, Jerzy Chlistunoff, Dae-Sik Kim, Cy Fujimoto, Tae-Hyun Yang, and Yu Seung Kim. A microelectrode study of interfacial reactions at the platinum-alkaline polymer interface. *Journal of The Electrochemical Society*, 162(6): F499–F506, 2015.

- [125] Ivana Matanovic, Hoon Taek Chung, and Yu Seung Kim. Benzene adsorption: A significant inhibitor for the hydrogen oxidation reaction in alkaline conditions. *Journal of Physical Chemistry Letters*, 2017. doi: 10.1021/acs.jpcllett.7b02228.
- [126] Sandip Maurya, Joseph H. Dumont, Claudia Narvaez Villarrubia, Ivana Matanovic, Dongguo Li, Yu Seung Kim, Sangtaik Noh, Junyoung Han, Chulsung Bae, Hamish A. Miller, Cy H. Fujimoto, and Dario R. Dekel. Surface adsorption affects the performance of alkaline anion-exchange membrane fuel cells. *ACS Catalysis*, 8(10):9429–9439, 2018. doi: 10.1021/acscatal.8b03227. URL <https://doi.org/10.1021/acscatal.8b03227>.
- [127] Sandip Maurya, Cy H. Fujimoto, Michael R. Hibbs, Claudia Narvaez Villarrubia, and Yu Seung Kim. Toward improved alkaline membrane fuel cell performance using quaternized aryl-ether free polyaromatics. *Chemistry of Materials*, 30(7):2188–2192, 2018. ISSN 0897-4756. doi: 10.1021/acs.chemmater.8b00358. URL <https://doi.org/10.1021/acs.chemmater.8b00358>.
- [128] Ivana Matanovic, Sandip Maurya, Eun Joo Park, Jong Yeob Jeon, Chulsung Bae, and Yu Seung Kim. Adsorption of polyaromatic backbone impacts the performance of anion exchange membrane fuel cells. *Chemistry of Materials*, 31(11):4195–4204, 2019. ISSN 0897-4756. doi: 10.1021/acs.chemmater.9b01092. URL <https://doi.org/10.1021/acs.chemmater.9b01092>.
- [129] Eun Joo Park, Sandip Maurya, Albert S. Lee, Daniel P. Leonard, Dongguo Li, Jong Yeob Jeon, Chulsung Bae, and Yu Seung Kim. How does a small structural change of anode ionomer make a big difference in alkaline membrane fuel cell performance? *Journal of Materials Chemistry A*, 7(43):25040–25046, 2019. ISSN 2050-7488. doi: 10.1039/C9TA10157H. URL <http://dx.doi.org/10.1039/C9TA10157H>.
- [130] J. R. Varcoe and R. C. T. Slade. Prospects for alkaline anion-exchange membranes in low temperature fuel cells. *Fuel Cells*, 5(2):187–200, 2005. ISSN 1615-6854. doi: 10.1002/fuce.200400045. URL <http://https://doi.org/10.1002/fuce.200400045>.
- [131] Nenad Markovic, Hubert Gasteiger, and Philip N. Ross. Kinetics of oxygen reduction on pt(hkl) electrodes: Implications for the crystallite size effect with supported pt electrocatalysts. *Journal of The Electrochemical Society*, 144(5):1591–1597, 1997. URL <http://jes.ecsdl.org/content/144/5/1591.abstract>.
- [132] T. J. Schmidt, V. Stamenkovic, Jr P. N. Ross, and N. M. Markovic. Temperature dependent surface electrochemistry on pt single crystals in alkaline electrolyte part 3. the oxygen reduction reaction. *Physical Chemistry Chemical Physics*, 5(2):400–406, 2003. ISSN 1463-9076. doi: 10.1039/B208322A. URL <http://dx.doi.org/10.1039/B208322A>.
- [133] Akiyoshi Kuzume, Enrique Herrero, and Juan M. Feliu. Oxygen reduction on stepped platinum surfaces in acidic media. *Journal of Electroanalytical Chemistry*, 599(2):333–343, 2007. ISSN 1572-6657. doi: <https://doi.org/10.1016/j.jelechem.2006.05.006>. URL <http://www.sciencedirect.com/science/article/pii/S0022072806002555>.

- [134] Hiroshi Yano, Junji Inukai, Hiroyuki Uchida, Masahiro Watanabe, Panakkattu K. Babu, Takeshi Kobayashi, Jong Ho Chung, Eric Oldfield, and Andrzej Wieckowski. Particle-size effect of nanoscale platinum catalysts in oxygen reduction reaction: an electrochemical and  $^{195}\text{Pt}$  ec-nmr study. *Physical Chemistry Chemical Physics*, 8(42):4932–4939, 2006. ISSN 1463-9076. doi: 10.1039/B610573D. URL <http://dx.doi.org/10.1039/B610573D>.
- [135] Fabio H. B. Lima and Edson A. Ticianelli. Oxygen electrocatalysis on ultra-thin porous coating rotating ring/disk platinum and platinum–cobalt electrodes in alkaline media. *Electrochimica Acta*, 49(24):4091–4099, 2004. ISSN 0013-4686. doi: <https://doi.org/10.1016/j.electacta.2004.04.002>. URL <http://www.sciencedirect.com/science/article/pii/S0013468604003500>.
- [136] M. D. Obradović, B. N. Grgur, and Lj M. Vračar. Adsorption of oxygen containing species and their effect on oxygen reduction on  $\text{Pt}_3\text{Co}$  electrode. *Journal of Electroanalytical Chemistry*, 548:69–78, 2003. ISSN 1572-6657. doi: [https://doi.org/10.1016/S0022-0728\(03\)00223-7](https://doi.org/10.1016/S0022-0728(03)00223-7). URL <http://www.sciencedirect.com/science/article/pii/S0022072803002237>.
- [137] Fabio H. B. Lima, M. Janete Giz, and Edson A. Ticianelli. Electrochemical performance of dispersed  $\text{Pt-M}$  ( $\text{M} = \text{V}, \text{Cr}$  and  $\text{Co}$ ) nanoparticles for the oxygen reduction electrocatalysis. *Journal of the Mexican Chemical Society*, 49(2), 2005.
- [138] Marian Chatenet, Marc Aurousseau, Robert Durand, and Françoise Andolfatto. Silver-platinum bimetallic catalysts for oxygen cathodes in chlor-alkali electrolysis: Comparison with pure platinum. *Journal of The Electrochemical Society*, 150(3):D47–D55, 2003. URL <http://jes.ecsdl.org/content/150/3/D47.abstract>.
- [139] T. J. Schmidt, V. Stamenkovic, M. Arenz, N. M. Markovic, and P. N. Ross. Oxygen electrocatalysis in alkaline electrolyte:  $\text{Pt}(\text{hkl})$ ,  $\text{Au}(\text{hkl})$  and the effect of  $\text{Pd}$ -modification. *Electrochimica Acta*, 47(22):3765–3776, 2002. ISSN 0013-4686. doi: [https://doi.org/10.1016/S0013-4686\(02\)00347-X](https://doi.org/10.1016/S0013-4686(02)00347-X). URL <http://www.sciencedirect.com/science/article/pii/S001346860200347X>.
- [140] M. Arenz, T. J. Schmidt, K. Wandelt, P. N. Ross, and N. M. Markovic. The oxygen reduction reaction on thin palladium films supported on a  $\text{Pt}(111)$  electrode. *The Journal of Physical Chemistry B*, 107(36):9813–9819, 2003. ISSN 1520-6106. doi: 10.1021/jp034789m. URL <https://doi.org/10.1021/jp034789m>.
- [141] Y. J. Li, C. C. Chang, and T. C. Wen. A mixture design approach to thermally prepared  $\text{Ir-Pt-Au}$  ternary electrodes for oxygen reduction in alkaline solution. *Journal of Applied Electrochemistry*, 27(2):227–234, 1997. ISSN 1572-8838. doi: 10.1023/A:1018416326922. URL <https://doi.org/10.1023/A:1018416326922>.



- [142] K. V. Ramesh and A. K. Shukla. Carbon-based electrodes carrying platinum-group bimetal catalysts for oxygen reduction in fuel cells with acidic or alkaline electrolytes. *Journal of Power Sources*, 19(4):279–285, 1987. ISSN 0378-7753. doi: [https://doi.org/10.1016/0378-7753\(87\)87004-0](https://doi.org/10.1016/0378-7753(87)87004-0). URL <http://www.sciencedirect.com/science/article/pii/0378775387870040>.
- [143] Jacob S. Spendelow and Andrzej Wieckowski. Electrocatalysis of oxygen reduction and small alcohol oxidation in alkaline media. *Physical Chemistry Chemical Physics*, 9: 2654–2675, 2007. ISSN 1463-9076. doi: 10.1039/b703315j.
- [144] Sally A. Wasileski, Marc T. M. Koper, and Michael J. Weaver. Metal electrode–chemisorbate bonding: General influence of surface bond polarization on field-dependent binding energetics and vibrational frequencies. *The Journal of Chemical Physics*, 115(17):8193–8203, 2001. ISSN 0021-9606. doi: 10.1063/1.1404987. URL <https://doi.org/10.1063/1.1404987>.
- [145] N. M. Marković and P. N. Ross. Surface science studies of model fuel cell electrocatalysts. *Surface Science Reports*, 45(4):117–229, 2002. ISSN 0167-5729. doi: [https://doi.org/10.1016/S0167-5729\(01\)00022-X](https://doi.org/10.1016/S0167-5729(01)00022-X). URL <http://www.sciencedirect.com/science/article/pii/S016757290100022X>.
- [146] Allen J. Bard. Inner-sphere heterogeneous electrode reactions. electrocatalysis and photocatalysis: The challenge. *Journal of the American Chemical Society*, 132(22): 7559–7567, 2010. ISSN 0002-7863. doi: 10.1021/ja101578m. URL <https://doi.org/10.1021/ja101578m>.
- [147] Nagappan Ramaswamy and Sanjeev Mukerjee. Fundamental mechanistic understanding of electrocatalysis of oxygen reduction on pt and non-pt surfaces: Acid versus alkaline media. *Advances in Physical Chemistry*, 2012.
- [148] Nagappan Ramaswamy, Nazih Hakim, and Sanjeev Mukerjee. Degradation mechanism study of perfluorinated proton exchange membrane under fuel cell operating conditions. *Electrochimica Acta*, 53(8):3279–3295, 2008. ISSN 0013-4686. doi: <https://doi.org/10.1016/j.electacta.2007.11.010>. URL <https://www.sciencedirect.com/science/article/pii/S0013468607013758>.
- [149] J. O’M. Bockris Appleby and A. J. *Ch. 3 - Alkaline Fuel Cells (AFCs)*, pages 95–135. Pergamon, 1986. ISBN 978-0-08-033990-0. doi: <https://doi.org/10.1016/B978-0-08-033990-0.50008-3>. URL <https://www.sciencedirect.com/science/article/pii/B9780080339900500083>.
- [150] A. J. Appleby. *FUEL CELLS – OVERVIEW — Introduction*, pages 277–296. Elsevier, Amsterdam, 2009. ISBN 978-0-444-52745-5. doi: <https://doi.org/10.1016/B978-044452745-5.00221-5>. URL <https://www.sciencedirect.com/science/article/pii/B9780444527455002215>.

- [151] Keiichi Okajima, Kenji Nabekura, Takaya Kondoh, and Masao Sudoh. Degradation evaluation of gas-diffusion electrodes for oxygen-depolarization in chlor-alkali membrane cell. *Journal of The Electrochemical Society*, 152(8):D117–D120, 2005. URL <http://jes.ecsdl.org/content/152/8/D117.abstract>.
- [152] M. Chatenet, L. Genies-Bultel, M. Aurousseau, R. Durand, and F. Andolfatto. Oxygen reduction on silver catalysts in solutions containing various concentrations of sodium hydroxide – comparison with platinum. *Journal of Applied Electrochemistry*, 32(10): 1131–1140, 2002. ISSN 1572-8838. doi: 10.1023/A:1021231503922. URL <https://doi.org/10.1023/A:1021231503922>.
- [153] Nagakazu Furuya and Hiroaki Aikawa. Comparative study of oxygen cathodes loaded with ag and pt catalysts in chlor-alkali membrane cells. *Electrochimica Acta*, 45(25):4251–4256, 2000. ISSN 0013-4686. doi: [https://doi.org/10.1016/S0013-4686\(00\)00557-0](https://doi.org/10.1016/S0013-4686(00)00557-0). URL <http://www.sciencedirect.com/science/article/pii/S0013468600005570>.
- [154] D. Šepa, M. Vojnović, and A. Damjanovic. Oxygen reduction at silver electrodes in alkaline solutions. *Electrochimica Acta*, 15(8):1355–1366, 1970. ISSN 0013-4686. doi: [https://doi.org/10.1016/0013-4686\(70\)80055-X](https://doi.org/10.1016/0013-4686(70)80055-X). URL <http://www.sciencedirect.com/science/article/pii/001346867080055X>.
- [155] B. B. Blizanac, P. N. Ross, and N. M. Marković. Oxygen reduction on silver low-index single-crystal surfaces in alkaline solution: rotating ring diskag(hkl) studies. *The Journal of Physical Chemistry B*, 110(10):4735–4741, 2006. ISSN 1520-6106. doi: 10.1021/jp056050d. URL <https://doi.org/10.1021/jp056050d>.
- [156] Platinum price, markets insider, Accessed: 17 June 2021. URL <https://markets.businessinsider.com/commodities/platinum-price>.
- [157] Live silver price charts & historical data, Accessed: 17 June 2021. URL <https://www.apmex.com/spotprices/silver-prices>.
- [158] Endangered elements, american chemical society, Accessed: 23 June 2021. URL <https://www.acs.org/content/acs/en/greenchemistry/research-innovation/endangered-elements.html>.
- [159] A. Fazil and R. Chetty. Synthesis and evaluation of carbon nanotubes supported silver catalyst for alkaline fuel cell. *Electroanalysis*, 26(11):2380–2387, 2014. ISSN 1040-0397. doi: <https://doi.org/10.1002/elan.201400246>. URL <https://doi.org/10.1002/elan.201400246>.
- [160] Gabriel A. Goenaga, Asa L. Roy, Nelly M. Cantillo, Shane Foister, and Thomas A. Zawodzinski. A family of platinum group metal-free catalysts for oxygen reduction in alkaline media. *Journal of Power Sources*, 395:148–157, 2018. ISSN 0378-7753. doi: <https://doi.org/10.1016/j.jpowsour.2018.05.025>. URL <http://www.sciencedirect.com/science/article/pii/S0378775318304865>.

- [161] F. Bidault and A. Kucernak. Cathode development for alkaline fuel cells based on a porous silver membrane. *Journal of Power Sources*, 196(11):4950–4956, 2011. ISSN 0378-7753. doi: <https://doi.org/10.1016/j.jpowsour.2011.02.008>. URL <http://www.sciencedirect.com/science/article/pii/S0378775311003624>.
- [162] A. Kucernak, F. Bidault, and G. Smith. Membrane electrode assemblies based on porous silver electrodes for alkaline anion exchange membrane fuel cells. *Electrochimica Acta*, 82: 284–290, 2012. ISSN 0013-4686. doi: <https://doi.org/10.1016/j.electacta.2012.03.027>. URL <http://www.sciencedirect.com/science/article/pii/S0013468612003660>.
- [163] Iridium price, umicore precious metals management, Accessed: 17 June 2021. URL <https://pmm.umicore.com/en/prices/iridium>.
- [164] Iridium hits all-time high of \$6,000/oz on supply issues, strong demand, 19 March 2021 2021. URL <https://www.spglobal.com/platts/en/market-insights/latest-news/metals/031921-iridium-hits-all-time-high-of-6000oz-on-supply-issues-strong-demand>.
- [165] Gaurav Gupta, Keith Scott, and Mohamed Mamlouk. Performance of polyethylene based radiation grafted anion exchange membrane with polystyrene-b-poly (ethylene/butylene)-b-polystyrene based ionomer using nico2o4 catalyst for water electrolysis. *Journal of Power Sources*, 375:387–396, 2018. ISSN 0378-7753. doi: <https://doi.org/10.1016/j.jpowsour.2017.07.026>. URL <https://www.sciencedirect.com/science/article/pii/S0378775317309084>.
- [166] Emily Cossar, Alejandro Oyarce Barnett, Frode Seland, and Elena A. Baranova. The performance of nickel and nickel-iron catalysts evaluated as anodes in anion exchange membrane water electrolysis. *Catalysts*, 9(10), 2019. ISSN 2073-4344. doi: 10.3390/catal9100814.
- [167] Shannon Klaus, Mary W. Louie, Lena Trotochaud, and Alexis T. Bell. Role of catalyst preparation on the electrocatalytic activity of ni1–xfexooH for the oxygen evolution reaction. *The Journal of Physical Chemistry C*, 119(32):18303–18316, 2015. ISSN 1932-7447. doi: 10.1021/acs.jpcc.5b04776. URL <https://doi.org/10.1021/acs.jpcc.5b04776>.
- [168] Mikaela Görölin, Petko Chernev, Paul Paciok, Cheuk-Wai Tai, Jorge Ferreira de Araújo, Tobias Reier, Marc Heggen, Rafal Dunin-Borkowski, Peter Strasser, and Holger Dau. Formation of unexpectedly active ni–fe oxygen evolution electrocatalysts by physically mixing ni and fe oxyhydroxides. *Chemical Communications*, 55(6):818–821, 2019. ISSN 1359-7345. doi: 10.1039/C8CC06410E. URL <http://dx.doi.org/10.1039/C8CC06410E>.
- [169] Michaela S. Burke, Shihui Zou, Lisa J. Enman, Jaclyn E. Kellon, Christian A. Gabor, Erica Pledger, and Shannon W. Boettcher. Revised oxygen evolution reaction activity trends for first-row transition-metal (oxy)hydroxides in alkaline media. *The Journal of Physical Chemistry Letters*, 6(18):3737–3742, 2015. doi: 10.1021/acs.jpcllett.5b01650. URL <https://doi.org/10.1021/acs.jpcllett.5b01650>.

- [170] Immanuel Vincent, Andries Kruger, and Dmitri Bessarabov. Development of efficient membrane electrode assembly for low cost hydrogen production by anion exchange membrane electrolysis. *International Journal of Hydrogen Energy*, 42(16):10752–10761, 2017. ISSN 0360-3199. doi: <https://doi.org/10.1016/j.ijhydene.2017.03.069>. URL <https://www.sciencedirect.com/science/article/pii/S036031991730993X>.
- [171] Kai Zeng and Dongke Zhang. Recent progress in alkaline water electrolysis for hydrogen production and applications. *Progress in Energy and Combustion Science*, 36(3):307–326, 2010. ISSN 0360-1285. doi: <https://doi.org/10.1016/j.pecs.2009.11.002>. URL <https://www.sciencedirect.com/science/article/pii/S0360128509000598>.
- [172] Yongjun Leng, Guang Chen, Alfonso J. Mendoza, Timothy B. Tighe, Michael A. Hickner, and Chao-Yang Wang. Solid-state water electrolysis with an alkaline membrane. *Journal of the American Chemical Society*, 134(22):9054–9057, 2012. ISSN 0002-7863. doi: 10.1021/ja302439z. URL <https://doi.org/10.1021/ja302439z>.
- [173] M. Z. Iqbal and R. J. Kriek. Silver/nickel oxide (ag/nio) nanocomposites produced via a citrate sol-gel route as electrocatalyst for the oxygen evolution reaction (oer) in alkaline medium. *Electrocatalysis*, 9(3):279–286, 2018. ISSN 1868-5994. doi: 10.1007/s12678-018-0455-5. URL <https://doi.org/10.1007/s12678-018-0455-5>.
- [174] Ruohao Dong, Haoran Du, Yixuan Sun, Kuangfu Huang, Wen Li, and Baoyou Geng. Selective reduction–oxidation strategy to the conductivity-enhancing ag-decorated co-based 2d hydroxides as efficient electrocatalyst in oxygen evolution reaction. *ACS Sustainable Chemistry & Engineering*, 6(10):13420–13426, 2018. doi: 10.1021/acssuschemeng.8b03153. URL <https://doi.org/10.1021/acssuschemeng.8b03153>.
- [175] Wei Wang, Qiang Zhao, Jinxiang Dong, and Jinping Li. A novel silver oxides oxygen evolving catalyst for water splitting. *International Journal of Hydrogen Energy*, 36(13): 7374–7380, 2011. ISSN 0360-3199. doi: <https://doi.org/10.1016/j.ijhydene.2011.03.096>. URL <https://www.sciencedirect.com/science/article/pii/S0360319911006860>.
- [176] Hatem M. A. Amin, Christoph J. Bondue, Santhana Eswara, Ute Kaiser, and Helmut Baltruschat. A carbon-free ag-co<sub>3</sub>o<sub>4</sub> composite as a bifunctional catalyst for oxygen reduction and evolution: Spectroscopic, microscopic and electrochemical characterization. *Electrocatalysis*, 8(6):540–553, 2017. ISSN 1868-5994. doi: 10.1007/s12678-017-0364-z. URL <https://doi.org/10.1007/s12678-017-0364-z>.
- [177] Xing Huang, Minghao Xie, Yihan Chen, Qingshuang Zong, Ziyu Liu, and Yong Jin. Copper–silver oxide nanowires grown on an alloy electrode as an efficient electrocatalyst for water oxidation. *RSC Advances*, 5(33):26150–26156, 2015. doi: 10.1039/C5RA00820D. URL <http://dx.doi.org/10.1039/C5RA00820D>.

- [178] Soressa Abera Chala, Meng-Che Tsai, Wei-Nien Su, Kassa Belay Ibrahim, Alemayehu Dubale Duma, Min-Hsin Yeh, Cheng-Yen Wen, Chia-Hao Yu, Ting-Shan Chan, Hongjie Dai, and Bing-Joe Hwang. Site activity and population engineering of niru-layered double hydroxide nanosheets decorated with silver nanoparticles for oxygen evolution and reduction reactions. *ACS Catalysis*, 9(1):117–129, 2019. doi: 10.1021/acscatal.8b03092. URL <https://doi.org/10.1021/acscatal.8b03092>.
- [179] Anchu Ashok, Anand Kumar, Md Abdul Matin, and Faris Tarlochan. Probing the effect of combustion controlled surface alloying in silver and copper towards orr and oer in alkaline medium. *Journal of Electroanalytical Chemistry*, 844:66–77, 2019. ISSN 1572-6657. doi: <https://doi.org/10.1016/j.jelechem.2019.05.016>. URL <https://www.sciencedirect.com/science/article/pii/S1572665719303662>.
- [180] Ivan S. Filimonenkov, Galina A. Tsirlina, and Elena R. Savinova. Conductive additives for oxide-based oer catalysts: A comparative rrde study of carbon and silver in alkaline medium. *Electrochimica Acta*, 319:227–236, 2019. ISSN 0013-4686. doi: <https://doi.org/10.1016/j.electacta.2019.06.154>. URL <https://www.sciencedirect.com/science/article/pii/S0013468619312976>.
- [181] Michael Hans, Salima Mathews, Frank Mücklich, and Marc Solioz. Physicochemical properties of copper important for its antibacterial activity and development of a unified model. *Biointerphases*, 11(1):018902, 2015. ISSN 1934-8630. doi: 10.1116/1.4935853. URL <https://doi.org/10.1116/1.4935853>.
- [182] M. Lopez-Haro, L. Guétaz, T. Printemps, A. Morin, S. Escribano, P. H. Jouneau, P. Bayle-Guillemaud, F. Chandezon, and G. Gebel. Three-dimensional analysis of nafion layers in fuel cell electrodes. *Nature Communications*, 5(1):5229, 2014. ISSN 2041-1723. doi: 10.1038/ncomms6229. URL <https://doi.org/10.1038/ncomms6229>.
- [183] Pietro G. Santori, Abhishek N. Mondal, Dario R. Dekel, and Frédéric Jaouen. The critical importance of ionomers on the electrochemical activity of platinum and platinum-free catalysts for anion-exchange membrane fuel cells. *Sustainable Energy & Fuels*, 4(7): 3300–3307, 2020. doi: 10.1039/D0SE00483A. URL <http://dx.doi.org/10.1039/D0SE00483A>.
- [184] Devproshad K. Paul, Andrew Fraser, and Kunal Karan. Towards the understanding of proton conduction mechanism in pemfc catalyst layer: Conductivity of adsorbed nafion films. *Electrochemistry Communications*, 13(8):774–777, 2011. ISSN 1388-2481. doi: <https://doi.org/10.1016/j.elecom.2011.04.022>. URL <http://www.sciencedirect.com/science/article/pii/S1388248111001731>.
- [185] Devproshad K. Paul and Kunal Karan. Conductivity and wettability changes of ultrathin nafion films subjected to thermal annealing and liquid water exposure. *The Journal of Physical Chemistry C*, 118(4):1828–1835, 2014. ISSN 1932-7447. doi: 10.1021/jp410510x. URL <https://doi.org/10.1021/jp410510x>.

- [186] Ahmet Kusoglu, Douglas Kushner, Devproshad K. Paul, Kunal Karan, Michael A. Hickner, and Adam Z. Weber. Impact of substrate and processing on confinement of nafion thin films. *Advanced Functional Materials*, 24(30):4763–4774, 2014. ISSN 1616-301X. doi: 10.1002/adfm.201304311. URL <https://doi.org/10.1002/adfm.201304311>.
- [187] Ahmet Kusoglu and Adam Z. Weber. New insights into perfluorinated sulfonic-acid ionomers. *Chemical Reviews*, 117(3):987–1104, 2017. ISSN 0009-2665. doi: 10.1021/acs.chemrev.6b00159. URL <https://doi.org/10.1021/acs.chemrev.6b00159>.
- [188] Steven Holdcroft. Fuel cell catalyst layers: A polymer science perspective. *Chemistry of Materials*, 26(1):381–393, 2014. ISSN 0897-4756. doi: 10.1021/cm401445h. URL <https://doi.org/10.1021/cm401445h>.
- [189] Devproshad K. Paul, Kunal Karan, Aristides Docoslis, Javier B. Giorgi, and Joshua Pearce. Characteristics of self-assembled ultrathin nafion films. *Macromolecules*, 46(9):3461–3475, 2013. ISSN 0024-9297. doi: 10.1021/ma4002319. URL <https://doi.org/10.1021/ma4002319>.
- [190] Devproshad K. Paul, Richard McCreery, and Kunal Karan. Proton transport property in supported nafion nanothin films by electrochemical impedance spectroscopy. *Journal of The Electrochemical Society*, 161(14):F1395–F1402, 2014.
- [191] Anusorn Kongkanand. Interfacial water transport measurements in nafion thin films using a quartz-crystal microbalance. *The Journal of Physical Chemistry C*, 115(22):11318–11325, 2011. ISSN 1932-7447. doi: 10.1021/jp2028214. URL <https://doi.org/10.1021/jp2028214>.
- [192] Miguel A. Modestino, Devproshad K. Paul, Shudipto Dishari, Stephanie A. Petrina, Frances I. Allen, Michael A. Hickner, Kunal Karan, Rachel A. Segalman, and Adam Z. Weber. Self-assembly and transport limitations in confined nafion films. *Macromolecules*, 46(3):867–873, 2013. ISSN 0024-9297. doi: 10.1021/ma301999a. URL <https://doi.org/10.1021/ma301999a>.
- [193] Ahmet Kusoglu, Thomas J. Dursch, and Adam Z. Weber. Nanostructure/swelling relationships of bulk and thin-film pfsa ionomers. *Advanced Functional Materials*, 26(27):4961–4975, 2016. ISSN 1616-301X. doi: <https://doi.org/10.1002/adfm.201600861>. URL <https://doi.org/10.1002/adfm.201600861>.
- [194] Xiao Gao, Kentaro Yamamoto, Tomoyasu Hirai, Tomoki Uchiyama, Noboru Ohta, Naoki Takao, Masashi Matsumoto, Hideto Imai, Seiho Sugawara, Kazuhiko Shinohara, and Yoshiharu Uchimoto. Morphology changes in perfluorosulfonated ionomer from thickness and thermal treatment conditions. *Langmuir*, 36(14):3871–3878, 2020. ISSN 0743-7463. doi: 10.1021/acs.langmuir.9b03564. URL <https://doi.org/10.1021/acs.langmuir.9b03564>.
- [195] Miguel A. Modestino, Ahmet Kusoglu, Alexander Hexemer, Adam Z. Weber, and Rachel A. Segalman. Controlling nafion structure and properties via wetting interactions. *Macromolecules*, 45(11):4681–4688, 2012. ISSN 0024-9297. doi: 10.1021/ma300212f. URL <https://doi.org/10.1021/ma300212f>.

- [196] Joseph A. Dura, Vivek S. Murthi, Michael Hartman, Sushil K. Satija, and Charles F. Majkrzak. Multilamellar interface structures in nafion. *Macromolecules*, 42(13):4769–4774, 2009. ISSN 0024-9297. doi: 10.1021/ma802823j. URL <https://doi.org/10.1021/ma802823j>.
- [197] Douglas I. Kushner, Ahmet Kusoglu, Nikolas J. Podraza, and Michael A. Hickner. Substrate-dependent molecular and nanostructural orientation of nafion thin films. *Advanced Functional Materials*, 29(37):1902699, 2019. ISSN 1616-301X. doi: <https://doi.org/10.1002/adfm.201902699>. URL <https://doi.org/10.1002/adfm.201902699>.
- [198] Graciela C. Abuin, M. Cecilia Fuertes, and Horacio R. Corti. Substrate effect on the swelling and water sorption of nafion nanomembranes. *Journal of Membrane Science*, 428: 507–515, 2013. ISSN 0376-7388. doi: <https://doi.org/10.1016/j.memsci.2012.10.060>. URL <http://www.sciencedirect.com/science/article/pii/S0376738812008216>.
- [199] Hamdy F. M. Mohamed, S. Kuroda, Y. Kobayashi, N. Oshima, R. Suzuki, and A. Ohira. Possible presence of hydrophilic so3h nanoclusters on the surface of dry ultrathin nafion® films: a positron annihilation study. *Physical Chemistry Chemical Physics*, 15(5):1518–1525, 2013. ISSN 1463-9076. doi: 10.1039/C2CP43727A. URL <http://dx.doi.org/10.1039/C2CP43727A>.
- [200] Petr Krtil, Antonín Trojánek, and Zdeněk Samec. Kinetics of water sorption in nafionthin films quartz crystal microbalance study. *The Journal of Physical Chemistry B*, 105(33): 7979–7983, 2001. ISSN 1520-6106. doi: 10.1021/jp004162t. URL <https://doi.org/10.1021/jp004162t>.
- [201] Steffen Hinka, Elena Aleksandrova, and Emil Roduner. Electrochemical afm investigations of proton conducting membranes. *ECS Transactions*, 33(1):57–70, 2010.
- [202] Elena Aleksandrova, Renate Hiesgen, K. Andreas Friedrich, and Emil Roduner. Electrochemical atomic force microscopy study of proton conductivity in a nafion membrane. *Physical Chemistry Chemical Physics*, 9(21):2735–2743, 2007. ISSN 1463-9076. doi: 10.1039/B617516C. URL <http://dx.doi.org/10.1039/B617516C>.
- [203] Elena Aleksandrova, Renate Hiesgen, Dirk Eberhard, K. Andreas Friedrich, Till Kaz, and Emil Roduner. Proton conductivity study of a fuel cell membrane with nanoscale resolution. *ChemPhysChem*, 8(4):519–522, 2007. ISSN 1439-4235. doi: 10.1002/cphc.200600704. URL <https://doi.org/10.1002/cphc.200600704>.
- [204] Osung Kwon, Shijie Wu, and Da-Ming Zhu. Configuration changes of conducting channel network in nafion membranes due to thermal annealing. *The Journal of Physical Chemistry B*, 114(46):14989–14994, 2010. ISSN 1520-6106. doi: 10.1021/jp108163a. URL <https://doi.org/10.1021/jp108163a>.
- [205] Austin M. Barnes and Steven K. Buratto. Imaging channel connectivity in nafion using electrostatic force microscopy. *The Journal of Physical Chemistry B*, 122(3):1289–1295, 2018. ISSN 1520-6106. doi: 10.1021/acs.jpcc.7b08230. URL <https://doi.org/10.1021/acs.jpcc.7b08230>.

- [206] V. J. Bharath, J. Millichamp, T. P. Neville, T. J. Mason, P. R. Shearing, R. J.C. Brown, G. Manos, and D. J.L. Brett. Measurement of water uptake in thin-film nafion and anion alkaline exchange membranes using the quartz crystal microbalance. *Journal of Membrane Science*, 497:229–238, 2016. ISSN 0376-7388. doi: 10.1016/j.memsci.2015.09.027.
- [207] V. J. Bharath, J. R. Jervis, J. J. Bailey, E. Engebretsen, T. P. Neville, J. Millichamp, T. Mason, P. R. Shearing, R. J. C. Brown, G. Manos, and D. J. L. Brett. Effect of humidity on the interaction of co2 with alkaline anion exchange membranes probed using the quartz crystal microbalance. *International Journal of Hydrogen Energy*, 42(38):24301–24307, 2017. ISSN 0360-3199. doi: <https://doi.org/10.1016/j.ijhydene.2017.07.142>. URL <https://www.sciencedirect.com/science/article/pii/S0360319917329774>.
- [208] Douglas I. Kushner, Liang Zhu, Ahmet Kusoglu, and Michael A. Hickner. Side chain influence on the mechanical properties and water uptake of confined comb-shaped cationic polymer thin films. *Macromolecular Chemistry and Physics*, 217:2442–2451, 2016. doi: 10.1002/macp.201600254.
- [209] Udit N. Shrivastava, Avital Zhegur-Khais, Maria Bass, Sapir Willdorf-Cohen, Viatcheslav Freger, Dario R. Dekel, and Kunal Karan. Water content and ionic conductivity of thin films of different anionic forms of anion conducting ionomers. *The Journal of Physical Chemistry C*, 124(43):23469–23478, 2020. ISSN 1932-7447. doi: 10.1021/acs.jpcc.0c04278. URL <https://doi.org/10.1021/acs.jpcc.0c04278>.
- [210] Xiaoyan Luo, Douglas I. Kushner, Jonathan Li, Eun Joo Park, Yu Seung Kim, and Ahmet Kusoglu. Anion exchange ionomers: Impact of chemistry on thin-film properties. *Advanced Functional Materials*, 31(20):2008778, 2021. ISSN 1616-301X. doi: <https://doi.org/10.1002/adfm.202008778>. URL <https://doi.org/10.1002/adfm.202008778>.
- [211] Kenji Kudo, Ryosuke Jinnouchi, and Yu Morimoto. Humidity and temperature dependences of oxygen transport resistance of nafion thin film on platinum electrode. *Electrochimica Acta*, 209:682–690, 2016. ISSN 0013-4686. doi: <https://doi.org/10.1016/j.electacta.2016.04.023>. URL <https://www.sciencedirect.com/science/article/pii/S0013468616308118>.
- [212] Jerzy Chlistunoff. Oxygen permeability of cast ionomer films from chronoamperometry on microelectrodes. *Journal of Power Sources*, 245:203–207, 2014. ISSN 0378-7753. doi: <https://doi.org/10.1016/j.jpowsour.2013.06.128>. URL <http://www.sciencedirect.com/science/article/pii/S037877531301135X>.
- [213] Yutaro Ono and Yuki Nagao. Interfacial structure and proton conductivity of nafion at the pt-deposited surface. *Langmuir*, 32(1):352–358, 2016. ISSN 0743-7463. doi: 10.1021/acs.langmuir.5b02623. URL <https://doi.org/10.1021/acs.langmuir.5b02623>.



- [214] Dan Yao, Tonghui Wei, Lichao Shang, Hui Na, and Chengji Zhao. A comparative study of side-chain-type poly(ether ether ketone) anion exchange membrane functionalized with different hetero-cycloaliphatic quaternary ammonium groups. *RSC Advances*, 9(14): 7975–7983, 2019. doi: 10.1039/C8RA09840A. URL <http://dx.doi.org/10.1039/C8RA09840A>.
- [215] John Ahlfield, Garrett Huang, Lisha Liu, Yuna Kaburagi, Yunbum Kim, and Paul A. Kohl. Anion conducting ionomers for fuel cells and electrolyzers. *Journal of The Electrochemical Society*, 164:F1648–F1653, 2017. doi: 10.1149/2.1341714jes.
- [216] Dongyang Chen, Michael A. Hickner, Ertan Agar, and E. Caglan Kumbur. Selective anion exchange membranes for high coulombic efficiency vanadium redox flow batteries. *Electrochemistry Communications*, 26:37–40, 2013. ISSN 1388-2481. doi: <https://doi.org/10.1016/j.elecom.2012.10.007>. URL <http://www.sciencedirect.com/science/article/pii/S1388248112004304>.
- [217] Tao Luo, Said Abdu, and Matthias Wessling. Selectivity of ion exchange membranes: A review. *Journal of Membrane Science*, 555:429–454, 2018. ISSN 0376-7388. doi: <https://doi.org/10.1016/j.memsci.2018.03.051>. URL <http://www.sciencedirect.com/science/article/pii/S0376738817335779>.
- [218] Ahmed Fuwad, Hyunil Ryu, Noah Malmstadt, Sun Min Kim, and Tae-Joon Jeon. Biomimetic membranes as potential tools for water purification: Preceding and future avenues. *Desalination*, 458:97–115, 2019. ISSN 0011-9164. doi: <https://doi.org/10.1016/j.desal.2019.02.003>. URL <http://www.sciencedirect.com/science/article/pii/S0011916418311664>.
- [219] M Mamlouk, X Wang, K Scott, J A Horsfall, and C Williams. Characterization and application of anion exchange polymer membranes with non-platinum group metals for fuel cells. *Proceedings of the Institution of Mechanical Engineers, Part A: Journal of Power and Energy*, 225(2):152–160, 2011. doi: 10.1177/2041296710394264. URL <https://journals.sagepub.com/doi/abs/10.1177/2041296710394264>.
- [220] Michael A. Hickner, Andrew M. Herring, and E. Bryan Coughlin. Anion exchange membranes: Current status and moving forward. *Journal of Polymer Science Part B: Polymer Physics*, 51(24):1727–1735, 2013. ISSN 0887-6266. doi: 10.1002/polb.23395. URL <https://doi.org/10.1002/polb.23395>.
- [221] Marek Danilczuk, Shulamith Schlick, and Frank D. Coms. Cerium(iii) as a stabilizer of perfluorinated membranes used in fuel cells: In situ detection of early events in the esr resonator. *Macromolecules*, 42(22):8943–8949, 2009. ISSN 0024-9297. doi: 10.1021/ma9017108. URL <https://doi.org/10.1021/ma9017108>.
- [222] Christopher G. Arges and Le Zhang. Anion exchange membranes’ evolution toward high hydroxide ion conductivity and alkaline resiliency. *ACS Applied Energy Materials*, 1: 2991–3012, 2018. doi: 10.1021/acsaem.8b00387.

- [223] Liang Zhu, Jing Pan, Caroline M. Christensen, Bencai Lin, and Michael A. Hickner. Functionalization of poly(2,6-dimethyl-1,4-phenylene oxide)s with hindered fluorene side chains for anion exchange membranes. *Macromolecules*, 49(9):3300–3309, 2016. doi: 10.1021/acs.macromol.6b00578.
- [224] Woo-Hyung Lee, Yu Seung Kim, and Chulsung Bae. Robust hydroxide ion conducting poly(biphenyl alkylene)s for alkaline fuel cell membranes. *ACS Macro Letters*, 4(8):814–818, 2015. doi: 10.1021/acsmacrolett.5b00375. URL <https://doi.org/10.1021/acsmacrolett.5b00375>.
- [225] Thanh Huong Pham, Joel S. Olsson, and Patric Jannasch. N-spirocyclic quaternary ammonium ionenes for anion-exchange membranes. *Journal of the American Chemical Society*, 139(8):2888–2891, 2017. ISSN 0002-7863 1520-5126. doi: 10.1021/jacs.6b12944.
- [226] Xiaomeng Chu, Lei Liu, Yingda Huang, Michael D. Guiver, and Nanwen Li. Practical implementation of bis-six-membered n-cyclic quaternary ammonium cations in advanced anion exchange membranes for fuel cells: Synthesis and durability. *Journal of Membrane Science*, 578:239–250, 2019. ISSN 0376-7388. doi: <https://doi.org/10.1016/j.memsci.2019.02.051>. URL <http://www.sciencedirect.com/science/article/pii/S0376738818335427>.
- [227] Qian Yang, Ling Li, Xue Lang Gao, Hong Yue Wu, Fang Hua Liu, Qiu Gen Zhang, Ai Mei Zhu, Chun Hui Zhao, and Qing Lin Liu. Crown ether bridged anion exchange membranes with robust alkaline durability. *Journal of Membrane Science*, 578:230–238, 2019. ISSN 0376-7388. doi: <https://doi.org/10.1016/j.memsci.2019.02.038>. URL <http://www.sciencedirect.com/science/article/pii/S0376738818333386>.
- [228] Jiantao Fan, Sapir Willdorf-Cohen, Eric M. Schibli, Zoe Paula, Wei Li, Thomas J. G. Skalski, Ania Tersakian Sergeenko, Amelia Hohenadel, Barbara J. Frisken, Emanuele Magliocca, William E. Mustain, Charles E. Diesendruck, Dario R. Dekel, and Steven Holdcroft. Poly(bis-arylimidazoliums) possessing high hydroxide ion exchange capacity and high alkaline stability. *Nature Communications*, 10(1):2306, 2019. ISSN 2041-1723. doi: 10.1038/s41467-019-10292-z. URL <https://doi.org/10.1038/s41467-019-10292-z>.
- [229] Joseph B. Edson, Clay S. Macomber, Bryan S. Pivovar, and James M. Boncella. Hydroxide based decomposition pathways of alkyltrimethylammonium cations. *Journal of Membrane Science*, 399-400:49–59, 2012. ISSN 0376-7388. doi: <https://doi.org/10.1016/j.memsci.2012.01.025>. URL <http://www.sciencedirect.com/science/article/pii/S0376738812000543>.
- [230] Wei You, Elliot Padgett, Samantha N. MacMillan, David A. Muller, and Geoffrey W. Coates. Highly conductive and chemically stable alkaline anion exchange membranes via romp of trans-cyclooctene derivatives. *Proceedings of the National Academy of Sciences of the United States of America*, 116(20):9729, 2019. doi: 10.1073/pnas.1900988116. URL <http://www.pnas.org/content/116/20/9729.abstract>.

- [231] Melissa A. Vandiver, Benjamin R. Caire, Tara P. Pandey, Yifan Li, Sönke Seifert, Ahmet Kusoglu, Daniel M. Knauss, Andrew M. Herring, and Matthew W. Liberatore. Effect of hydration on the mechanical properties and ion conduction in a polyethylene-*b*-poly(vinylbenzyl trimethylammonium) anion exchange membrane. *Journal of Membrane Science*, 497:67–76, 2016. ISSN 0376-7388. doi: <https://doi.org/10.1016/j.memsci.2015.09.034>. URL <http://www.sciencedirect.com/science/article/pii/S0376738815301976>.
- [232] Lianqin Wang, Xiong Peng, William E. Mustain, and John R. Varcoe. Radiation-grafted anion-exchange membranes: the switch from low- to high-density polyethylene leads to remarkably enhanced fuel cell performance. *Energy & Environmental Science*, 12(5): 1575–1579, 2019. ISSN 1754-5692. doi: 10.1039/C9EE00331B. URL <http://dx.doi.org/10.1039/C9EE00331B>.
- [233] G. Gupta, K. Scott, and M. Mamlouk. Soluble polystyrene-*b*-poly(ethylene/butylene)-*b*-polystyrene based ionomer for anion exchange membrane fuel cells operating at 70 °c. *Fuel Cells*, 18:137–147, 2018. doi: 10.1002/fuce.201700176.
- [234] Richard Espiritu, Mohamed Mamlouk, and Keith Scott. Study on the effect of the degree of grafting on the performance of polyethylene-based anion exchange membrane for fuel cell application. *International Journal of Hydrogen Energy*, 41(2):1120–1133, 2016. ISSN 0360-3199. doi: <https://doi.org/10.1016/j.ijhydene.2015.10.108>. URL <http://www.sciencedirect.com/science/article/pii/S0360319915302603>.
- [235] Tauqir A. Sherazi, Joon Yong Sohn, Young Moo Lee, and Michael D. Guiver. Polyethylene-based radiation grafted anion-exchange membranes for alkaline fuel cells. *Journal of Membrane Science*, 441:148–157, 2013. ISSN 0376-7388. doi: <https://doi.org/10.1016/j.memsci.2013.03.053>. URL <http://www.sciencedirect.com/science/article/pii/S0376738813002561>.
- [236] Byungchan Bae, Kenji Miyatake, and Masahiro Watanabe. Effect of the hydrophobic component on the properties of sulfonated poly(arylene ether sulfone)s. *Macromolecules*, 42(6):1873–1880, 2009. ISSN 0024-9297. doi: 10.1021/ma8026518. URL <https://doi.org/10.1021/ma8026518>.
- [237] Himanshu N. Sarode, Yuan Yang, Andrew R. Motz, Yifan Li, Daniel M. Knauss, Soenke Seifert, and Andrew M. Herring. Understanding anion, water, and methanol transport in a polyethylene-*b*-poly(vinylbenzyl trimethylammonium) copolymer anion-exchange membrane for electrochemical applications. *The Journal of Physical Chemistry C*, 121(4):2035–2045, 2017. ISSN 1932-7447. doi: 10.1021/acs.jpcc.6b09205. URL <https://doi.org/10.1021/acs.jpcc.6b09205>.
- [238] Wenxu Zhang. *Synthesis and Characterization of Polymeric Anion Exchange Membranes*. Ph.D. Thesis. Thesis, 2016.

- [239] Joan M. Widin, Adam K. Schmitt, Andrew L. Schmitt, Kyuhyun Im, and Mahesh K. Mahanthappa. Unexpected consequences of block polydispersity on the self-assembly of aba triblock copolymers. *Journal of the American Chemical Society*, 134(8):3834–3844, 2012. ISSN 0002-7863. doi: 10.1021/ja210548e. URL <https://doi.org/10.1021/ja210548e>.
- [240] Andrew L. Schmitt and Mahesh K. Mahanthappa. Polydispersity-driven shift in the lamellar mesophase composition window of peo-pb-peo triblock copolymers. *Soft Matter*, 8(7):2294–2303, 2012. ISSN 1744-683X. doi: 10.1039/C2SM07041C. URL <http://dx.doi.org/10.1039/C2SM07041C>.
- [241] J. Minick, A. Moet, and E. Baer. Morphology of hdpe/ldpe blends with different thermal histories. *Polymer*, 36(10):1923–1932, 1995. ISSN 0032-3861. doi: [https://doi.org/10.1016/0032-3861\(95\)91434-9](https://doi.org/10.1016/0032-3861(95)91434-9). URL <http://www.sciencedirect.com/science/article/pii/0032386195914349>.
- [242] Melissa A. Vandiver, James L. Horan, Yuan Yang, Emily T. Tansey, Söenke Seifert, Matthew W. Liberatore, and Andrew M. Herring. Synthesis and characterization of perfluoro quaternary ammonium anion exchange membranes. *Journal of Polymer Science Part B: Polymer Physics*, 51(24):1761–1769, 2013. ISSN 0887-6266. doi: 10.1002/polb.23171. URL <https://doi.org/10.1002/polb.23171>.
- [243] J Ilavsky and PR Jemian. Irena: tool suite for modeling and analysis of small-angle scattering. *Journal of Applied Crystallography*, 42:347–353, 2009.
- [244] Tara P. Pandey, Himanshu N. Sarode, Yating Yang, Yuan Yang, Keti Vezzù, Vito Di Noto, Soenke Seifert, Daniel M. Knauss, Matthew W. Liberatore, and Andrew M. Herring. A highly hydroxide conductive, chemically stable anion exchange membrane, poly(2,6 dimethyl 1,4 phenylene oxide)- *b*-poly(vinyl benzyl trimethyl ammonium), for electrochemical applications. *Journal of The Electrochemical Society*, 163:H513–H520, 2016. doi: 10.1149/2.0421607jes.
- [245] Tara P. Pandey, Soenke Seifert, Yating Yang, Yuan Yang, Daniel M. Knauss, Matthew W. Liberatore, and Andrew M. Herring. Novel processing of a poly(phenyleneoxide) *b*-poly(vinylbenzyltrimethylammonium) copolymer anion exchange membrane; the effect on mechanical and transport properties. *Electrochimica Acta*, 222:1545–1554, 2016. ISSN 0013-4686. doi: <https://doi.org/10.1016/j.electacta.2016.11.137>. URL <http://www.sciencedirect.com/science/article/pii/S0013468616325002>.
- [246] ChristopherW Bielawski and RobertH Grubbs. Highly efficient ring-opening metathesis polymerization (romp) using new ruthenium catalysts containing n-heterocyclic carbene ligands. *Angewandte Chemie International Edition*, 39(16):2903–2906, 2000. ISSN 1433-7851. doi: 10.1002/1521-3773(20000818)39:16<2903::AID-ANIE2903>>3.0.CO;2-Q. URL [https://doi.org/10.1002/1521-3773\(20000818\)39:16<2903::AID-ANIE2903>>3.0.CO;2-Q](https://doi.org/10.1002/1521-3773(20000818)39:16<2903::AID-ANIE2903>>3.0.CO;2-Q).

- [247] Erik Dümichen, Anne-Kathrin Barthel, Ulrike Braun, Claus G. Bannick, Kathrin Brand, Martin Jekel, and Rainer Senz. Analysis of polyethylene microplastics in environmental samples, using a thermal decomposition method. *Water Research*, 85:451–457, 2015. ISSN 0043-1354. doi: <https://doi.org/10.1016/j.watres.2015.09.002>. URL <http://www.sciencedirect.com/science/article/pii/S0043135415302141>.
- [248] R. Kerber and W. Schnabel. Polymer degradation, principles and practical applications. *Berichte der Bunsengesellschaft für physikalische Chemie*, 87(9):838–839, 1983. ISSN 0005-9021. doi: 10.1002/bbpc.19830870933. URL <https://doi.org/10.1002/bbpc.19830870933>.
- [249] Sergey Vyazovkin. “nothing can hide itself from thy heat”: Understanding polymers via unconventional applications of thermal analysis. *Macromolecular Rapid Communications*, 40(1):1800334, 2019. ISSN 1022-1336. doi: 10.1002/marc.201800334. URL <https://doi.org/10.1002/marc.201800334>.
- [250] Christopher G. Arges, Lihui Wang, Min-suk Jung, and Vijay Ramani. Mechanically stable poly(arylene ether) anion exchange membranes prepared from commercially available polymers for alkaline electrochemical devices. *Journal of the Electrochemical Society*, 162(7):F686–F693, 2015.
- [251] Christopher G. Arges, Javier Parrondo, Graham Johnson, Athrey Nadhan, and Vijay Ramani. Assessing the influence of different cation chemistries on ionic conductivity and alkaline stability of anion exchange membranes. *Journal of Materials Chemistry*, 22(9):3733–3744, 2012. ISSN 0959-9428. doi: 10.1039/C2JM14898F. URL <http://dx.doi.org/10.1039/C2JM14898F>.
- [252] G. Beaucage and D. W. Schaefer. Structural studies of complex systems using small-angle scattering: a unified guinier/power-law approach. *Journal of Non-Crystalline Solids*, 172-174:797–805, 1994. ISSN 0022-3093. doi: [https://doi.org/10.1016/0022-3093\(94\)90581-9](https://doi.org/10.1016/0022-3093(94)90581-9). URL <http://www.sciencedirect.com/science/article/pii/0022309394905819>.
- [253] Randal W. Richards and J. L. Thomason. Small-angle neutron scattering study of block copolymer morphology. *Macromolecules*, 16(6):982–992, 1983. ISSN 0024-9297. doi: 10.1021/ma00240a031. URL <https://doi.org/10.1021/ma00240a031>.
- [254] M. Bevis and E. B. Crellin. The geometry of twinning and phase transformations in crystalline polyethylene. *Polymer*, 12:666–684, 1971. doi: 10.1016/0032-3861(71)90083-8.
- [255] Michael F. Butler, Athene M. Donald, Wim Bras, Geoffrey R. Mant, Gareth E. Derbyshire, and Anthony J. Ryan. A real-time simultaneous small- and wide-angle x-ray scattering study of in-situ deformation of isotropic polyethylene. *Macromolecules*, 28:6383–6393, 1995. ISSN 0024-9297. doi: 10.1021/ma00123a001.

- [256] Surya Subianto, Monica Pica, Mario Casciola, Paula Cojocar, Luca Merlo, Graham Hards, and Deborah J. Jones. Physical and chemical modification routes leading to improved mechanical properties of perfluorosulfonic acid membranes for pem fuel cells. *Journal of Power Sources*, 233:216–230, 2013. ISSN 0378-7753. doi: <https://doi.org/10.1016/j.jpowsour.2012.12.121>. URL <http://www.sciencedirect.com/science/article/pii/S0378775313000712>.
- [257] Marianne P. Rodgers, Leonard J. Bonville, H. Russell Kunz, Darlene K. Slattery, and James M. Fenton. Fuel cell perfluorinated sulfonic acid membrane degradation correlating accelerated stress testing and lifetime. *Chemical Reviews*, 112(11):6075–6103, 2012. ISSN 0009-2665. doi: 10.1021/cr200424d. URL <https://doi.org/10.1021/cr200424d>.
- [258] J. R. MacCallum and C. Vincent. *Polymer Electrolyte Reviews*, volume 2. Elsevier Applied Science, Crown House, Linton Road, Barking, Essex IG11 8JU, England, 1989.
- [259] Tara P. Pandey, Ashley M. Maes, Himanshu N. Sarode, Bethanne D. Peters, Sandra Lavina, Keti Vezzù, Yuan Yang, Simon D. Poynton, John R. Varcoe, Soenke Seifert, Matthew W. Liberatore, Vito Di Noto, and Andrew M. Herring. Interplay between water uptake, ion interactions, and conductivity in an e-beam grafted poly(ethylene-co-tetrafluoroethylene) anion exchange membrane. *Phys. Chem. Chem. Phys.*, 17(6):4367–4378, 2015. ISSN 1463-9076. doi: 10.1039/C4CP05755D.
- [260] K.N. Grew and W.K.S Chiu. A dusty fluid model for predicting hydroxyl anion conductivity in alkaline anion exchange membranes. *Journal of The Electrochemical Society*, 157(3):B327–B337, 2010.
- [261] Javier Parrondo, Min-suk J. Jung, Zhongyang Wang, Christopher G. Arges, and Vijay Ramani. Synthesis and alkaline stability of solubilized anion exchange membrane binders based on poly(phenylene oxide) functionalized with quaternary ammonium groups via a hexyl spacer. *Journal of the Electrochemical Society*, 162:F1236–F1242, 2015.
- [262] Angela D. Mohanty, Steven E. Tignor, Jessica A. Krause, Yoong-Kee Choe, and Chulsung Bae. Systematic alkaline stability study of polymer backbones for anion exchange membrane applications. *Macromolecules*, 49(9):3361–3372, 2016. ISSN 0024-9297. doi: 10.1021/acs.macromol.5b02550. URL <https://doi.org/10.1021/acs.macromol.5b02550>.
- [263] Kristina M. Hugar, Wei You, and Geoffrey W. Coates. Protocol for the quantitative assessment of organic cation stability for polymer electrolytes. *ACS Energy Letters*, 4(7): 1681–1686, 2019. doi: 10.1021/acsenerylett.9b00908. URL <https://doi.org/10.1021/acsenerylett.9b00908>.
- [264] Mrinmay Mandal;, Garrett Huang;, Noor Ul Hassan;, Xiong Peng;, Taoli Gu;, Ahmon H. Brooks-Starks;, Bamdad Bahar;, William E. Mustain;, and Paul A. Kohl;. The importance of water transport in high conductivity and high-power alkaline fuel cells. *Journal of the Electrochemical Society*, 167:054501, 2020.

- [265] C. Richard Desper. Structure and properties of extruded polyethylene film. *Journal of Applied Polymer Science*, 13(1):169–191, 1969. ISSN 0021-8995. doi: 10.1002/app.1969.070130117. URL <https://doi.org/10.1002/app.1969.070130117>.
- [266] Eishun Tsuchida and Hiroyuki Nishide. Polymer-metal complexes and their catalytic activity. *Molecular Properties*, 24:1–87, 1977. doi: <https://doi.org/10.1007/3-540-08124-0.1>.
- [267] U. Divya Madhuri, Jony Saha, and T. P. Radhakrishnan. ‘dip catalysts’ based on polymer-metal nanocomposite thin films: Combining soft-chemical fabrication with efficient application and monitoring. *ChemNanoMat*, 4(12):1191–1201, 2018. ISSN 2199-692X. doi: 10.1002/cnma.201800356. URL <https://doi.org/10.1002/cnma.201800356>.
- [268] Insang You, Minsik Kong, and Unyong Jeong. Block copolymer elastomers for stretchable electronics. *Accounts of Chemical Research*, 52(1):63–72, 2019. ISSN 0001-4842. doi: 10.1021/acs.accounts.8b00488. URL <https://doi.org/10.1021/acs.accounts.8b00488>.
- [269] Nirav Joshi, Takeshi Hayasaka, Yumeng Liu, Huiliang Liu, Osvaldo N. Oliveira, and Liwei Lin. A review on chemiresistive room temperature gas sensors based on metal oxide nanostructures, graphene and 2d transition metal dichalcogenides. *Microchimica Acta*, 185(4):213, 2018. ISSN 1436-5073. doi: 10.1007/s00604-018-2750-5. URL <https://doi.org/10.1007/s00604-018-2750-5>.
- [270] M. Thangamuthu, K.Y. Hsieh, P.V. Kumar, and G.-Y. Chen. Graphene- and graphene oxide-based nanocomposite platforms for electrochemical biosensing applications. *International Journal of Molecular Sciences*, 20(12):2975, 2019.
- [271] Christian Harito, Dmitry V. Bavykin, Brian Yulianto, Hermawan K. Dipojono, and Frank C. Walsh. Polymer nanocomposites having a high filler content: synthesis, structures, properties, and applications. *Nanoscale*, 11(11):4653–4682, 2019. ISSN 2040-3364. doi: 10.1039/C9NR00117D. URL <http://dx.doi.org/10.1039/C9NR00117D>.
- [272] Christoph O. Blattmann and Sotiris E. Pratsinis. Single-step fabrication of polymer nanocomposite films. *Materials*, 11(7):1177, 2018.
- [273] A. Baldan. Adhesively-bonded joints and repairs in metallic alloys, polymers and composite materials: Adhesives, adhesion theories and surface pretreatment. *Journal of Materials Science*, 39(1):1–49, 2004. ISSN 1573-4803. doi: 10.1023/B:JMISC.0000007726.58758.e4. URL <https://doi.org/10.1023/B:JMISC.0000007726.58758.e4>.
- [274] Saviour A. Umoren and Moses M. Solomon. Protective polymeric films for industrial substrates: A critical review on past and recent applications with conducting polymers and polymer composites/nanocomposites. *Progress in Materials Science*, 104:380–450, 2019. ISSN 0079-6425. doi: <https://doi.org/10.1016/j.pmatsci.2019.04.002>. URL <http://www.sciencedirect.com/science/article/pii/S0079642519300398>.

- [275] Xu Zhang, Mark R. Servos, and Juewen Liu. Ultrahigh nanoparticle stability against salt, pH, and solvent with retained surface accessibility via depletion stabilization. *Journal of the American Chemical Society*, 134(24):9910–9913, 2012. ISSN 0002-7863. doi: 10.1021/ja303787e. URL <https://doi.org/10.1021/ja303787e>.
- [276] Nathaniel L. Rosi and Chad A. Mirkin. Nanostructures in biodiagnostics. *Chemical Reviews*, 105(4):1547–1562, 2005. ISSN 0009-2665. doi: 10.1021/cr030067f. URL <https://doi.org/10.1021/cr030067f>.
- [277] Catherine J. Murphy, Tapan K. Sau, Anand M. Gole, Christopher J. Orendorff, Jinxin Gao, Linfeng Gou, Simona E. Hunyadi, and Tan Li. Anisotropic metal nanoparticles: synthesis, assembly, and optical applications. *The Journal of Physical Chemistry B*, 109(29):13857–13870, 2005. ISSN 1520-6106. doi: 10.1021/jp0516846. URL <https://doi.org/10.1021/jp0516846>.
- [278] Prashant V. Kamat. Photophysical, photochemical and photocatalytic aspects of metal nanoparticles. *The Journal of Physical Chemistry B*, 106(32):7729–7744, 2002. ISSN 1520-6106. doi: 10.1021/jp0209289. URL <https://doi.org/10.1021/jp0209289>.
- [279] Ruchi Sharma, Seid Mahdi Jafari, and Somesh Sharma. Antimicrobial bio-nanocomposites and their potential applications in food packaging. *Food Control*, 112:107086, 2020. ISSN 0956-7135. doi: <https://doi.org/10.1016/j.foodcont.2020.107086>. URL <http://www.sciencedirect.com/science/article/pii/S0956713520300025>.
- [280] Dong Chan Kim, Hyung Joon Shim, Woongchan Lee, Ja Hoon Koo, and Dae-Hyeong Kim. Material-based approaches for the fabrication of stretchable electronics. *Advanced Materials*, 32(15):1902743, 2020. ISSN 0935-9648. doi: 10.1002/adma.201902743. URL <https://doi.org/10.1002/adma.201902743>.
- [281] S. Mukherjee and M. Mukherjee. Nitrogen-mediated interaction in polyacrylamide-silver nanocomposites. *Journal of Physics: Condensed Matter*, 18:11233–11242, 2006. ISSN 0953-8984. doi: 10.1088/0953-8984/18/49/015.
- [282] Xinglin Lu, Xunda Feng, Yi Yang, Jin Jiang, Wei Cheng, Caihong Liu, Manesh Gopinadhan, Chinedum O. Osuji, Jun Ma, and Menachem Elimelech. Tuning the permselectivity of polymeric desalination membranes via control of polymer crystallite size. *Nature Communications*, 10(1):2347, 2019. ISSN 2041-1723. doi: 10.1038/s41467-019-10132-0. URL <https://doi.org/10.1038/s41467-019-10132-0>.
- [283] Yao Lu, Xulve Zhang, Xiaobo Yan, Zhaoxia Hu, and Shouwen Chen. The structure–property–performance relationship of disulfonated naphthyl pendants bearing poly(aryl ether)s for polymer electrolyte membrane applications. *Journal of Membrane Science*, 555:45–55, 2018. ISSN 0376-7388. doi: <https://doi.org/10.1016/j.memsci.2018.01.065>. URL <http://www.sciencedirect.com/science/article/pii/S037673881732361X>.



- [284] Esam E. Abdel-Hady, Hamdy F. M. Mohamed, Mohamed Osman Abdel-Hamed, and Mahmoud M. Gomaa. Physical and electrochemical properties of pva/tio<sub>2</sub> nanocomposite membrane. *Advances in Polymer Technology*, 37(8):3842–3853, 2018. ISSN 0730-6679. doi: 10.1002/adv.22167. URL <https://doi.org/10.1002/adv.22167>.
- [285] Maria Bass, Amir Berman, Amarjeet Singh, Oleg Kononov, and Viatcheslav Freger. Surface structure of nafion in vapor and liquid. *The Journal of Physical Chemistry B*, 114(11):3784–3790, 2010. ISSN 1520-6106. doi: 10.1021/jp9113128. URL <https://doi.org/10.1021/jp9113128>.
- [286] Jia-Jun Han, De-Li Liu, and Lin Geng. Studies on the reduction mechanism of oxygen on ag/c catalysts in alkaline solutions. *Journal of Fuel Cell Science and Technology*, 10(6):061004, 2013. ISSN 1550-624X. doi: 10.1115/1.4025055. URL <https://doi.org/10.1115/1.4025055>.
- [287] Cong Zhang, Sijia Liu, Zhongzhang Mao, Xin Liang, and Biaohua Chen. Ag–ni core–shell nanowires with superior electrocatalytic activity for alkaline hydrogen evolution reaction. *Journal of Materials Chemistry A*, 5(32):16646–16652, 2017. ISSN 2050-7488. doi: 10.1039/C7TA04220E. URL <http://dx.doi.org/10.1039/C7TA04220E>.
- [288] Noam Rabag, Meirav Mann-Lahav, Elena S. Davydova, Uri Ash, Reuven Galed, Michael Handl, Renate Hiesgen, Emanuele Magliocca, William Mustain, Jin He, Peixi Cong, Andrew M. Beale, Gideon S. Grader, David Avnir, and Dario R. Dekel. Composite materials with combined electronic and ionic properties. *Matter*, 1(4):959–975, 2019. ISSN 2590-2385. doi: <https://doi.org/10.1016/j.matt.2019.04.007>. URL <http://www.sciencedirect.com/science/article/pii/S2590238519300232>.
- [289] L. Mandelkern. *Crystallization of Polymers*. McGraw-Hill Book Company, 1964. URL <https://books.google.pn/books?id=VTpRAAAAMAAJ>.
- [290] Andrzej Jeziorny. Parameters characterizing the kinetics of the non-isothermal crystallization of poly(ethylene terephthalate) determined by d.s.c. *Polymer*, 19(10):1142–1144, 1978. ISSN 0032-3861. doi: [https://doi.org/10.1016/0032-3861\(78\)90060-5](https://doi.org/10.1016/0032-3861(78)90060-5). URL <http://www.sciencedirect.com/science/article/pii/0032386178900605>.
- [291] A.D. Mohanty, S.E. Tignor, M.R. Sturgeon, H. Long, B.S. Pivovar, and C. Bae. Thermochemical stability study of alkyl-tethered quaternary ammonium cations for anion exchange membrane fuel cells. *Journal of The Electrochemical Society*, 164(13):F1279–F1285, 2017.
- [292] Fang Hua Liu, Chen Xiao Lin, En Ning Hu, Qian Yang, Qiu Gen Zhang, Ai Mei Zhu, and Qing Lin Liu. Anion exchange membranes with well-developed conductive channels: Effect of the functional groups. *Journal of Membrane Science*, 564:298–307, 2018. ISSN 0376-7388. doi: <https://doi.org/10.1016/j.memsci.2018.07.038>. URL <http://www.sciencedirect.com/science/article/pii/S0376738818312663>.

- [293] Charles E. Sing, Jos W. Zwanikken, and Monica Olvera de la Cruz. Electrostatic control of block copolymer morphology. *Nature Materials*, 13(7):694–698, 2014. ISSN 1476-4660. doi: 10.1038/nmat4001. URL <https://doi.org/10.1038/nmat4001>.
- [294] Moon Jeong Park and Nitash P. Balsara. Phase behavior of symmetric sulfonated block copolymers. *Macromolecules*, 41(10):3678–3687, 2008. ISSN 0024-9297. doi: 10.1021/ma702733f. URL <https://doi.org/10.1021/ma702733f>.
- [295] Austin M. Barnes, Yifeng Du, Wenxu Zhang, Soenke Seifert, Steven K. Buratto, and E. Bryan Coughlin. Phosphonium-containing block copolymer anion exchange membranes: Effect of quaternization level on bulk and surface morphologies at hydrated and dehydrated states. *Macromolecules*, 52(16):6097–6106, 2019. ISSN 0024-9297. doi: 10.1021/acs.macromol.9b00665. URL <https://doi.org/10.1021/acs.macromol.9b00665>.
- [296] Vito Di Noto, Rocco Gliubizzi, Enrico Negro, and Giuseppe Pace. Effect of sio2 on relaxation phenomena and mechanism of ion conductivity of [nafion/(sio2)x] composite membranes. *The Journal of Physical Chemistry B*, 110(49):24972–24986, 2006. ISSN 1520-6106. doi: 10.1021/jp0650331. URL <https://doi.org/10.1021/jp0650331>.
- [297] J. L. Koenig. *Spectroscopy of Polymers*. American Chemical Society, Washington, DC, 1992.
- [298] Surya K. Mallapragada and Balaji Narasimhan. Infrared spectroscopy in analysis of polymer crystallinity. *Encyclopedia of Analytical Chemistry*, 2006. ISSN 9780470027318. doi: doi:10.1002/9780470027318.a201210.1002/9780470027318.a2012. URL <https://doi.org/10.1002/9780470027318.a2012>.
- [299] Jianming Zhang, Harumi Sato, Isao Noda, and Yukihiro Ozaki. Conformation rearrangement and molecular dynamics of poly(3-hydroxybutyrate) during the melt-crystallization process investigated by infrared and two-dimensional infrared correlation spectroscopy. *Macromolecules*, 38(10):4274–4281, 2005. ISSN 0024-9297. doi: 10.1021/ma0501343. URL <https://doi.org/10.1021/ma0501343>.
- [300] Kai Zheng, Ruigang Liu, and Yong Huang. A two-dimensional ir correlation spectroscopic study of the conformational changes in syndiotactic polypropylene during crystallization. *Polymer Journal*, 42(1):81–85, 2010. ISSN 1349-0540. doi: 10.1038/pj.2009.304. URL <https://doi.org/10.1038/pj.2009.304>.
- [301] Zachary D. Pozun, Kelly Tran, Anna Shi, Ryan H. Smith, and Graeme Henkelman. Why silver nanoparticles are effective for olefin/paraffin separations. *Journal of Physical Chemistry C*, 115:1811–1818, 2011. doi: 10.1021/jp110579s.
- [302] Ante Bilić, Jeffrey R. Reimers, Noel S. Hush, Rainer C. Hoft, and Michael J. Ford. Adsorption of benzene on copper, silver, and gold surfaces. *Journal of Chemical Theory and Computation*, 2(4):1093–1105, 2006. ISSN 1549-9618. doi: 10.1021/ct050237r. URL <https://doi.org/10.1021/ct050237r>.

- [303] Seok Bin Hong, Seok Jin Hong, Tae-Hyung Kang, Ji Ho Youk, and Woong-Ryeol Yu. Optical and shape memory properties of semicrystalline poly(cyclooctene) upon cold-drawing. *Journal of Polymer Science Part B: Polymer Physics*, 55:1595–1607, 2017. doi: 10.1002/polb.24415.
- [304] Hesham A. Ezzeldin, Allen Apblett, and Gary L. Foutch. Synthesis and properties of anion exchangers derived from chloromethyl styrene codivinylbenzene and their use in water treatment hesham. *International Journal of Polymer Science*, 2010(Article ID 684051):9 pages, 2010.
- [305] John Coates. Interpretation of infrared spectra, a practical approach. *Encyclopedia of Analytical Chemistry*, 2006. ISSN 9780470027318. doi: doi:10.1002/9780470027318.a560610.1002/9780470027318.a5606. URL <https://doi.org/10.1002/9780470027318.a5606>.
- [306] Y.J. Choi, M.S. Kang, J. Cho, and S.H. Moon. Preparation and characterization of ldpe/polyvinylbenzyl trimethyl ammonium salts anion-exchange membrane. *Journal of Membrane Science*, 221(1-2):219–231, 2003.
- [307] Jukka-Pekka Jalkanen and Francesco Zerbetto. Interaction model for the adsorption of organic molecules on the silver surface. *The Journal of Physical Chemistry B*, 110(11): 5595–5601, 2006. ISSN 1520-6106. doi: 10.1021/jp055225g. URL <https://doi.org/10.1021/jp055225g>.
- [308] Yanling Hao and Yan Fang. Piperidine adsorption on two different silver electrodes: A combined surface enhanced raman spectroscopy and density functional theory study. *Journal of Nanoparticle Research*, 9(5):817–824, 2007. ISSN 1572-896X. doi: 10.1007/s11051-006-9122-5. URL <https://doi.org/10.1007/s11051-006-9122-5>.
- [309] David L. Jeanmaire and Richard P. Van Duyne. Surface raman spectroelectrochemistry: Part i. heterocyclic, aromatic, and aliphatic amines adsorbed on the anodized silver electrode. *Journal of Electroanalytical Chemistry and Interfacial Electrochemistry*, 84(1): 1–20, 1977. ISSN 0022-0728. doi: [https://doi.org/10.1016/S0022-0728\(77\)80224-6](https://doi.org/10.1016/S0022-0728(77)80224-6). URL <http://www.sciencedirect.com/science/article/pii/S0022072877802246>.
- [310] S. W. Gaarenstroom and N. Winograd. Initial and final state effects in the esca spectra of cadmium and silver oxides. *The Journal of Chemical Physics*, 67(8):3500–3506, 1977. ISSN 0021-9606. doi: 10.1063/1.435347. URL <https://doi.org/10.1063/1.435347>.
- [311] L. Kundakovic and M. Flytzani-Stephanopoulos. Deep oxidation of methane over zirconia supported ag catalysts. *Applied Catalysis A: General*, 183:35–51, 1999.
- [312] M. Rafiq H. Siddiqui, S.F. Adil, M.E. Assal, Roushown Ali, and A. Al-Warthan. Synthesis and characterization of silver oxide and silver chloride nanoparticles with high thermal stability. *Asian Journal of Chemistry*, 25(6):3405–3409, 2013. doi: 10.14233/ajchem.2013.13874.

- [313] N. García-Huete, J.M. Laza, J.M. Cuevas, J.L. Vilas, E. Bilbao, and L.M. León. Study of the effect of gamma irradiation on a commercial polycyclooctene i. thermal and mechanical properties. *Radiation Physics and Chemistry*, 102:108–116, 2014.
- [314] Ander Reizabala, José Manuel Lazaa, José María Cuevasb, Luis Manuel Leóna, and José Luis Vilas-Vilelaa. Pco-lddpe thermoresponsive shape memory blends. towards a new generation of breathable and waterproof smart membranes. *European Polymer Journal*, 119: 469–476, 2019. doi: doi.org/10.1016/j.eurpolymj.2019.08.013.
- [315] Changdeng Liu, Seung B. Chun, Patrick T. Mather, Lei Zheng, Elisabeth H. Haley, and E. Bryan Coughlin. Chemically cross-linked polycyclooctene: Synthesis, characterization, and shape memory behavior. *Macromolecules*, 35:9868–9874, 2002. ISSN 0024-9297. doi: 10.1021/ma021141j.
- [316] Hatem Abushammala; and Jia Mao;. Impact of the surface properties of cellulose nanocrystals on the crystallization kinetics of poly(butylene succinate). *Crystals*, 10(3):196, 2020. doi: <https://doi.org/10.3390/cryst10030196>.
- [317] Nigel Coburn, Paula Douglas, Derya Kaya, Jaipal Gupta, and Tony McNally. Isothermal and non-isothermal crystallization kinetics of composites of poly(propylene) and mwents. *Advanced Industrial and Engineering Polymer Research*, 1(1):99–110, 2018. ISSN 2542-5048. doi: <https://doi.org/10.1016/j.aiepr.2018.06.001>. URL <http://www.sciencedirect.com/science/article/pii/S2542504818300046>.
- [318] Neil L. A. McFerran, Cecil G. Armstrong, and Tony McNally. Nonisothermal and isothermal crystallization kinetics of nylon-12. *Journal of Applied Polymer Science*, 110(2):1043–1058, 2008. ISSN 0021-8995. doi: 10.1002/app.28696. URL <https://doi.org/10.1002/app.28696>.
- [319] Bernhard Wunderlich. *Chapter VI - The Growth of Crystals*, pages 115–347. Academic Press, 1976. ISBN 978-0-12-765602-1. doi: <https://doi.org/10.1016/B978-0-12-765602-1.50008-2>. URL <http://www.sciencedirect.com/science/article/pii/B9780127656021500082>.
- [320] C. Cazé, E. Devaux, A. Crespy, and J. P. Cavrot. A new method to determine the avrami exponent by d.s.c. studies of non-isothermal crystallization from the molten state. *Polymer*, 38(3):497–502, 1997. ISSN 0032-3861. doi: [https://doi.org/10.1016/S0032-3861\(96\)00552-6](https://doi.org/10.1016/S0032-3861(96)00552-6). URL <http://www.sciencedirect.com/science/article/pii/S0032386196005526>.
- [321] I W Bassi and G Fagherazzi. The triclinic structure of trans-polyoctenamers. *European Polymer Journal*, 4:123–132, 1968.
- [322] G Natta. The monoclinic structure of even trans-polyalkenamers. *European Polymer Journal*, 3:339–352, 1967.

- [323] Adrian Saal, Tino Hagemann, and Ulrich S. Schubert. Polymers for battery applications—active materials, membranes, and binders. *Advanced Energy Materials*, page 2001984, 2020. ISSN 1614-6832. doi: <https://doi.org/10.1002/aenm.202001984>. URL <https://doi.org/10.1002/aenm.202001984>.
- [324] Dario R. Dekel. Review of cell performance in anion exchange membrane fuel cells. *Journal of Power Sources*, 2018. ISSN 0378-7753. doi: 10.1016/j.jpowsour.2017.07.117.
- [325] Zhihang Zhou, Yuanjun Liu, Junhao Zhang, Huan Pang, and Guoxing Zhu. Non-precious nickel-based catalysts for hydrogen oxidation reaction in alkaline electrolyte. *Electrochemistry Communications*, 121:106871, 2020. ISSN 1388-2481. doi: <https://doi.org/10.1016/j.elecom.2020.106871>. URL <https://www.sciencedirect.com/science/article/pii/S1388248120302228>.
- [326] Dong Won Shin, Michael D. Guiver, and Young Moo Lee. Hydrocarbon-based polymer electrolyte membranes: Importance of morphology on ion transport and membrane stability. *Chemical Reviews*, 117(6):4759–4805, 2017.
- [327] Timothy J. Peckham and Steven Holdcroft. Structure-morphology-property relationships of non-perfluorinated proton-conducting membranes. *Advanced Materials*, 22(42):4667–4690, 2010. ISSN 0935-9648. doi: <https://doi.org/10.1002/adma.201001164>. URL <https://doi.org/10.1002/adma.201001164>.
- [328] Yanfang Fan, Mingqiang Zhang, Robert B. Moore, and Chris J. Cornelius. Structure, physical properties, and molecule transport of gas, liquid, and ions within a pentablock copolymer. *Journal of Membrane Science*, 464:179–187, 2014. ISSN 0376-7388. doi: <https://doi.org/10.1016/j.memsci.2014.04.011>. URL <https://www.sciencedirect.com/science/article/pii/S0376738814002919>.
- [329] Sayema K. Tuli, Asa L. Roy, Ramez A. Elgammal, Mengkun Tian, Thomas A. Zawodzinski, and Tomoko Fujiwara. Effect of morphology on anion conductive properties in self-assembled polystyrene-based copolymer membranes. *Journal of Membrane Science*, 565: 213–225, 2018. ISSN 0376-7388. doi: <https://doi.org/10.1016/j.memsci.2018.08.028>. URL <https://www.sciencedirect.com/science/article/pii/S0376738818315370>.
- [330] Charles E. Sing and Monica Olvera de la Cruz. Polyelectrolyte blends and nontrivial behavior in effective flory–huggins parameters. *ACS Macro Letters*, 3(8):698–702, 2014. doi: 10.1021/mz500202n. URL <https://doi.org/10.1021/mz500202n>.
- [331] Rajeev Kumar and M. Muthukumar. Microphase separation in polyelectrolytic diblock copolymer melt: Weak segregation limit. *The Journal of Chemical Physics*, 126(21):214902, 2007. ISSN 0021-9606. doi: 10.1063/1.2737049. URL <https://doi.org/10.1063/1.2737049>.
- [332] Moon Jeong Park, Suhan Kim, Andrew M. Minor, Alexander Hexemer, and Nitash P. Balsara. Control of domain orientation in block copolymer electrolyte membranes at the interface with humid air. *Advanced Materials*, 21(2):203–208, 2009. ISSN 0935-9648. doi: <https://doi.org/10.1002/adma.200801613>. URL <https://doi.org/10.1002/adma.200801613>.

- [333] Jingling Zhang, Xiaoxi Yu, Bingqian Zheng, Jiachun Shen, Surita R. Bhatia, and Nicole S. Sampson. Cationic amphiphilic alternating copolymers with tunable morphology. *Polymer Chemistry*, 11(34):5424–5430, 2020. ISSN 1759-9954. doi: 10.1039/D0PY00782J. URL <http://dx.doi.org/10.1039/D0PY00782J>.
- [334] Charles E. Sing, Jos W. Zwanikken, and Monica Olvera de la Cruz. Theory of melt polyelectrolyte blends and block copolymers: Phase behavior, surface tension, and microphase periodicity. *The Journal of Chemical Physics*, 142(3):034902, 2015. ISSN 0021-9606. doi: 10.1063/1.4905830. URL <https://doi.org/10.1063/1.4905830>.
- [335] Kunal Karan. Pefc catalyst layer: Recent advances in materials, microstructural characterization, and modeling. *Current Opinion in Electrochemistry*, 5(1):27–35, 2017. ISSN 2451-9103. doi: <https://doi.org/10.1016/j.coelec.2017.08.018>. URL <https://www.sciencedirect.com/science/article/pii/S2451910317300406>.
- [336] Julie N. L. Albert and Thomas H. Epps. Self-assembly of block copolymer thin films. *Materials Today*, 13(6):24–33, 2010. ISSN 1369-7021. doi: [https://doi.org/10.1016/S1369-7021\(10\)70106-1](https://doi.org/10.1016/S1369-7021(10)70106-1). URL <https://www.sciencedirect.com/science/article/pii/S1369702110701061>.
- [337] I. W. Hamley. Ordering in thin films of block copolymers: Fundamentals to potential applications. *Progress in Polymer Science*, 34(11):1161–1210, 2009. ISSN 0079-6700. doi: <https://doi.org/10.1016/j.progpolymsci.2009.06.003>. URL <https://www.sciencedirect.com/science/article/pii/S0079670009000641>.
- [338] M. Pourbaix. Atlas of electrochemical equilibria in aqueous solution. *NACE*, 307, 1974. URL <https://ci.nii.ac.jp/naid/10011714604/en/>.
- [339] Emilia Morallón, José Luis Vázquez, and Antonio Aldaz. Electrochemical behaviour of pt(111) in alkaline media. effect of specific adsorption of anions. *Journal of Electroanalytical Chemistry*, 334(1):323–338, 1992. ISSN 1572-6657. doi: [https://doi.org/10.1016/0022-0728\(92\)80581-N](https://doi.org/10.1016/0022-0728(92)80581-N). URL <https://www.sciencedirect.com/science/article/pii/002207289280581N>.
- [340] Heine A. Hansen, Jan Rossmeisl, and Jens K. Nørskov. Surface pourbaix diagrams and oxygen reduction activity of pt, ag and ni(111) surfaces studied by dft. *Physical Chemistry Chemical Physics*, 10(25):3722–3730, 2008. ISSN 1463-9076. doi: 10.1039/B803956A. URL <http://dx.doi.org/10.1039/B803956A>.
- [341] Adnan Qaseem, Fuyi Chen, Xiaoqiang Wu, and Roy L. Johnston. Pt-free silver nanoalloy electrocatalysts for oxygen reduction reaction in alkaline media. *Catalysis Science & Technology*, 6(10):3317–3340, 2016. ISSN 2044-4753. doi: 10.1039/C5CY02270C. URL <http://dx.doi.org/10.1039/C5CY02270C>.

- [342] Zhi-Peng Wu, Dominic T. Caracciolo, Yazan Maswadeh, Jianguo Wen, Zhijie Kong, Shiyao Shan, Jorge A. Vargas, Shan Yan, Emma Hopkins, Keonwoo Park, Anju Sharma, Yang Ren, Valeri Petkov, Lichang Wang, and Chuan-Jian Zhong. Alloying–realloying enabled high durability for pt–pd-3d-transition metal nanoparticle fuel cell catalysts. *Nature Communications*, 12(1):859, 2021. ISSN 2041-1723. doi: 10.1038/s41467-021-21017-6. URL <https://doi.org/10.1038/s41467-021-21017-6>.
- [343] Xinlong Tian, Xiao Zhao, Ya-Qiong Su, Lijuan Wang, Hongming Wang, Dai Dang, Bin Chi, Hongfang Liu, Emiel J. M. Hensen, Xiong Wen Lou, and Bao Yu Xia. Engineering bunched pt-ni alloy nanocages for efficient oxygen reduction in practical fuel cells. *Science*, 366(6467):850, 2019. doi: 10.1126/science.aaw7493. URL <http://science.sciencemag.org/content/366/6467/850.abstract>.
- [344] Yeongun Ko, Stephanie Christau, Regine von Klitzing, and Jan Genzer. Charge density gradients of polymer thin film by gaseous phase quaternization. *ACS Macro Letters*, 9(2): 158–162, 2020. doi: 10.1021/acsmacrolett.9b00930. URL <https://doi.org/10.1021/acsmacrolett.9b00930>.
- [345] Tsung Han Tsai, Ashley M. Maes, Melissa A. Vandiver, Craig Versek, Sönke Seifert, Mark Tuominen, Matthew W. Liberatore, Andrew M. Herring, and E. Bryan Coughlin. Synthesis and structure-conductivity relationship of polystyrene-block- poly(vinyl benzyl trimethylammonium) for alkaline anion exchange membrane fuel cells. *Journal of Polymer Science, Part B: Polymer Physics*, 51:1751–1760, 2013. ISSN 1099-0488. doi: 10.1002/polb.23170.
- [346] G. Odian. *Principles of Polymerization*. John Wiley & Sons, Ltd, 2004.
- [347] Sébastien Perrier. 50th anniversary perspective: Raft polymerization—a user guide. *Macromolecules*, 50(19):7433–7447, 2017. ISSN 0024-9297. doi: 10.1021/acs.macromol.7b00767. URL <https://doi.org/10.1021/acs.macromol.7b00767>.
- [348] J. B.; Sanderson R. D. Bowes, A.; Mcleary. Ab and aba type butyl acrylate and styrene block copolymers via raft-mediated miniemulsion polymerization. *J. Polym. Sci. Part A Polym. Chem.*, 45(4):588–604, 2007.
- [349] Ian W. Hamley and Valeria Castelletto. Small-angle scattering of block copolymers: in the melt, solution and crystal states. *Progress in Polymer Science*, 29(9):909–948, 2004. ISSN 0079-6700. doi: <https://doi.org/10.1016/j.progpolymsci.2004.06.001>. URL <https://www.sciencedirect.com/science/article/pii/S0079670004000681>.
- [350] Hirokazu Hasegawa and Takeji Hashimoto. Morphology of block polymers near a free surface. *Macromolecules*, 18(3):589–590, 1985. ISSN 0024-9297. doi: 10.1021/ma00145a051. URL <https://doi.org/10.1021/ma00145a051>.

- [351] V. Khanna, E. W. Cochran, A. Hexemer, G. E. Stein, G. H. Fredrickson, E. J. Kramer, X. Li, J. Wang, and S. F. Hahn. Effect of chain architecture and surface energies on the ordering behavior of lamellar and cylinder forming block copolymers. *Macromolecules*, 39(26):9346–9356, 2006. ISSN 0024-9297. doi: 10.1021/ma0609228. URL <https://doi.org/10.1021/ma0609228>.
- [352] Kazem D. Safa and Mirzaagha Babazadeh. Glass transition temperature modification of acrylic and dienic type copolymers of 4-chloromethyl styrene with incorporation of (me3si)3c- groups. *European Polymer Journal*, 40(8):1659–1669, 2004. ISSN 0014-3057. doi: <https://doi.org/10.1016/j.eurpolymj.2004.04.005>. URL <https://www.sciencedirect.com/science/article/pii/S0014305704001405>.
- [353] Mingdi Yan and Olof Ramstrom. *Molecularly Imprinted Materials: Science and Technology*. Boca Raton, FL, 2004.
- [354] S. K. Sinha, E. B. Sirota, S. Garoff, and H. B. Stanley. X-ray and neutron scattering from rough surfaces. *Physical Review B*, 38(4):2297–2311, 1988. doi: 10.1103/PhysRevB.38.2297. URL <https://link.aps.org/doi/10.1103/PhysRevB.38.2297>.
- [355] M. Rauscher, T. Salditt, and H. Spohn. Small-angle x-ray scattering under grazing incidence: The cross section in the distorted-wave born approximation. *Physical Review B*, 52(23):16855–16863, 1995. doi: 10.1103/PhysRevB.52.16855. URL <https://link.aps.org/doi/10.1103/PhysRevB.52.16855>.
- [356] P. Busch, M. Rauscher, D.-M. Smilgies, D. Posselt, and C. M. Papadakis. Grazing-incidence small-angle x-ray scattering from thin polymer films with lamellar structures - the scattering cross section in the distorted-wave born approximation. *Journal of Applied Crystallography*, 39(3):433–442, 2006. ISSN 0021-8898. doi: [doi:10.1107/S0021889806012337](https://doi.org/10.1107/S0021889806012337). URL <https://doi.org/10.1107/S0021889806012337>.
- [357] S. Lenz, M. Bonini, S. K. Nett, M. C. Lechmann, S. G. J. Emmerling, R. S. Kappes, M. Memesa, A. Timmann, S. V. Roth, and J. S. Gutmann. Global scattering functions: a tool for grazing incidence small angle x-ray scattering (gisaxs) data analysis of low correlated lateral structures. *The European Physical Journal - Applied Physics*, 51(1):10601, 2010. ISSN 1286-0042. doi: 10.1051/epjap/2010064.
- [358] Boualem Hammouda. Analysis of the beaucage model. *Journal of Applied Crystallography*, 43(6):1474–1478, 2010. ISSN 0021-8898. doi: [doi:10.1107/S0021889810033856](https://doi.org/10.1107/S0021889810033856). URL <https://doi.org/10.1107/S0021889810033856>.
- [359] Scott A. Eastman, Sangcheol Kim, Kirt A. Page, Brandon W. Rowe, Shuhui Kang, Christopher L. Soles, and Kevin G. Yager. Effect of confinement on structure, water solubility, and water transport in nafion thin films. *Macromolecules*, 45(19):7920–7930, 2012. ISSN 0024-9297. doi: 10.1021/ma301289v. URL <https://doi.org/10.1021/ma301289v>.



- [360] Andrew M Herring, E. Bryan Coughlin, Mathew W. Liberatorre, Tara P Pandey, Himanshu N Sarode, Ye Liu, Vito Di Noto, and Ketì Vezzù. The implications of cation clustering in anion exchange membranes on conductivity and mechanical properties. *ECS Transactions*, 75(14):945, 2016.
- [361] Katherine Ayers, Nemanja Danilovic, Ryan Ouimet, Marcelo Carmo, Bryan Pivovar, and Marius Bornstein. Perspectives on low-temperature electrolysis and potential for renewable hydrogen at scale. *Annual Review of Chemical and Biomolecular Engineering*, 10(1): 219–239, 2019. ISSN 1947-5438. doi: 10.1146/annurev-chembioeng-060718-030241. URL <https://doi.org/10.1146/annurev-chembioeng-060718-030241>.
- [362] Claudiu C. Pavel, Franco Cecconi, Chiara Emiliani, Serena Santiccioli, Adriana Scaffidi, Stefano Catanorchi, and Massimiliano Comotti. Highly efficient platinum group metal free based membrane-electrode assembly for anion exchange membrane water electrolysis. *Angewandte Chemie International Edition*, 53(5):1378–1381, 2014. ISSN 1433-7851. doi: <https://doi.org/10.1002/anie.201308099>. URL <https://doi.org/10.1002/anie.201308099>.
- [363] Sang Hyun Ahn, Byung-Seok Lee, Insoo Choi, Sung Jong Yoo, Hyoung-Juhn Kim, EunAe Cho, Dirk Henkensmeier, Suk Woo Nam, Soo-Kil Kim, and Jong Hyun Jang. Development of a membrane electrode assembly for alkaline water electrolysis by direct electrodeposition of nickel on carbon papers. *Applied Catalysis B: Environmental*, 154-155:197–205, 2014. ISSN 0926-3373. doi: <https://doi.org/10.1016/j.apcatb.2014.02.021>. URL <https://www.sciencedirect.com/science/article/pii/S0926337314001143>.
- [364] L. Zeng and T. S. Zhao. Integrated inorganic membrane electrode assembly with layered double hydroxides as ionic conductors for anion exchange membrane water electrolysis. *Nano Energy*, 11:110–118, 2015. ISSN 2211-2855. doi: <https://doi.org/10.1016/j.nanoen.2014.10.019>. URL <https://www.sciencedirect.com/science/article/pii/S2211285514202199>.
- [365] Pengzuo Chen, Kun Xu, Tianpei Zhou, Yun Tong, Junchi Wu, Han Cheng, Xiuli Lu, Hui Ding, Changzheng Wu, and Yi Xie. Strong-coupled cobalt borate nanosheets/graphene hybrid as electrocatalyst for water oxidation under both alkaline and neutral conditions. *Angewandte Chemie International Edition*, 55(7):2488–2492, 2016. ISSN 1433-7851. doi: <https://doi.org/10.1002/anie.201511032>. URL <https://doi.org/10.1002/anie.201511032>.
- [366] Zhu-Ping Nie, De-Kun Ma, Guo-Yong Fang, Wei Chen, and Shao-Ming Huang. Concave bi2wo6 nanoplates with oxygen vacancies achieving enhanced electrocatalytic oxygen evolution in near-neutral water. *Journal of Materials Chemistry A*, 4(7):2438–2444, 2016. ISSN 2050-7488. doi: 10.1039/C5TA09536K. URL <http://dx.doi.org/10.1039/C5TA09536K>.
- [367] Yanzhi Sun, Chunxiang Liu, Linying Zhang, Pingyu Wan, Shuxian Zhuang, Yang Tang, Yongmei Chen, and Junqing Pan. Ultrafast electrodeposition of nife hydroxide nanosheets on nickel foam as oxygen evolution anode for energy-saving electrolysis of na2co3/nahco3. *ChemElectroChem*, 4(5):1044–1050, 2017. ISSN 2196-0216. doi: <https://doi.org/10.1002/celc.201600713>. URL <https://doi.org/10.1002/celc.201600713>.

- [368] Hiroshi Ito, Natsuki Kawaguchi, Satoshi Someya, Tetsuo Munakata, Naoki Miyazaki, Masayoshi Ishida, and Akihiro Nakano. Experimental investigation of electrolytic solution for anion exchange membrane water electrolysis. *International Journal of Hydrogen Energy*, 43(36):17030–17039, 2018. ISSN 0360-3199. doi: <https://doi.org/10.1016/j.ijhydene.2018.07.143>. URL <https://www.sciencedirect.com/science/article/pii/S036031991832367X>.
- [369] Jiangjin Liu, Zhenye Kang, Dongguo Li, Magnolia Pak, Shaun M. Alia, Cy Fujimoto, Guido Bender, Yu Seung Kim, and Adam Z. Weber. Elucidating the role of hydroxide electrolyte on anion-exchange-membrane water electrolyzer performance. *Journal of The Electrochemical Society*, 168(5):054522, 2021. ISSN 0013-4651 1945-7111. doi: 10.1149/1945-7111/ac0019. URL <http://dx.doi.org/10.1149/1945-7111/ac0019>.
- [370] Xinzhi Cao, David Novitski, and Steven Holdcroft. Visualization of hydroxide ion formation upon electrolytic water splitting in an anion exchange membrane. *ACS Materials Letters*, 1(3):362–366, 2019. doi: 10.1021/acsmaterialslett.9b00195. URL <https://doi.org/10.1021/acsmaterialslett.9b00195>.
- [371] Noga Ziv and Dario R. Dekel. A practical method for measuring the true hydroxide conductivity of anion exchange membranes. *Electrochemistry Communications*, 2018. doi: 10.1016/j.elecom.2018.01.021.
- [372] Ulrike Krewer, Christine Weinzierl, Noga Ziv, and Dario R. Dekel. Impact of carbonation processes in anion exchange membrane fuel cells. *Electrochimica Acta*, 263:433–446, 2018. ISSN 0013-4686. doi: <https://doi.org/10.1016/j.electacta.2017.12.093>. URL <https://www.sciencedirect.com/science/article/pii/S0013468617326531>.
- [373] Samuel St John, Robert W. Atkinson, Asa Roy, Raymond R. Unocic, Alexander B. Papandrew, and Thomas A. Zawodzinski. The effect of carbonate and ph on hydrogen oxidation and oxygen reduction on pt-based electrocatalysts in alkaline media. *Journal of The Electrochemical Society*, 163(3):F291–F295, 2016. ISSN 0013-4651 1945-7111. doi: 10.1149/2.1071603jes. URL <http://dx.doi.org/10.1149/2.1071603jes>.
- [374] Huong Doan, Jenna Malley, Tanner Jankins, Christopher Lin, Asel Primbetova, and Sanjeev Mukerjee. Catalytic and mass transport effects of carbonate ions at an anion exchange membrane interface (pgm vs. non-pgm) for a practical and efficient water splitting cell. In *ECS Meeting Abstracts*, volume MA2017-01. The Electrochemical Society. ISBN 2151-2043. doi: 10.1149/ma2017-01/30/1414. URL <http://dx.doi.org/10.1149/MA2017-01/30/1414>.
- [375] S. Stucki, A. Schuler, and M. Constantinescu. Coupled co2 recovery from the atmosphere and water electrolysis: Feasibility of a new process for hydrogen storage. *International Journal of Hydrogen Energy*, 20(8):653–663, 1995. ISSN 0360-3199. doi: [https://doi.org/10.1016/0360-3199\(95\)00007-Z](https://doi.org/10.1016/0360-3199(95)00007-Z). URL <https://www.sciencedirect.com/science/article/pii/036031999500007Z>.

- [376] I. T. McCrum, M. A. Hickner, and M. J. Janik. Quaternary ammonium cation specific adsorption on platinum electrodes: A combined experimental and density functional theory study. *Journal of The Electrochemical Society*, 165(2):F114–F121, 2018. ISSN 0013-4651 1945-7111. doi: 10.1149/2.1351802jes. URL <http://dx.doi.org/10.1149/2.1351802jes>.
- [377] Kensaku Kodama, Kenta Motobayashi, Akihiro Shinohara, Naoki Hasegawa, Kenji Kudo, Ryosuke Jinnouchi, Masatoshi Osawa, and Yu Morimoto. Effect of the side-chain structure of perfluoro-sulfonic acid ionomers on the oxygen reduction reaction on the surface of pt. *ACS Catalysis*, 2018. doi: 10.1021/acscatal.7b03571.
- [378] Sladjana Martens, Ludwig Asen, Giorgio Ercolano, Fabio Dionigi, Chris Zalitis, Alex Hawkins, Alejandro Martinez Bonastre, Lukas Seidl, Alois C. Knoll, Jonathan Sharman, Peter Strasser, Deborah Jones, and Oliver Schneider. A comparison of rotating disc electrode, floating electrode technique and membrane electrode assembly measurements for catalyst testing. *Journal of Power Sources*, 392:274–284, 2018. ISSN 0378-7753. doi: <https://doi.org/10.1016/j.jpowsour.2018.04.084>. URL <https://www.sciencedirect.com/science/article/pii/S0378775318304336>.
- [379] Jason Tai Hong Kwan, Arman Bonakdarpour, Greg Afonso, and David P. Wilkinson. Bridging fundamental electrochemistry with applied fuel cell testing: A novel and economical rotating disk electrode tip for electrochemical assessment of catalyst-coated membranes. *Electrochimica Acta*, 258:208–219, 2017. ISSN 0013-4686. doi: <https://doi.org/10.1016/j.electacta.2017.10.087>. URL <https://www.sciencedirect.com/science/article/pii/S0013468617322090>.
- [380] Rameshwori Loukrakpam, Bruna Ferreira Gomes, Tintula Kottakkat, and Christina Roth. A bird’s eye perspective of the measurement of oxygen reduction reaction in gas diffusion electrode half-cell set-ups for pt electrocatalysts in acidic media. *Journal of Physics: Materials*, 4(4):044004, 2021. ISSN 2515-7639. doi: 10.1088/2515-7639/ac0319. URL <http://dx.doi.org/10.1088/2515-7639/ac0319>.
- [381] Peter Mardle, Gnanavel Thirunavukkarasu, Shaoliang Guan, Yu-Lung Chiu, and Shangfeng Du. Comparative study of ptni nanowire array electrodes toward oxygen reduction reaction by half-cell measurement and pemfc test. *ACS Applied Materials & Interfaces*, 12(38): 42832–42841, 2020. ISSN 1944-8244. doi: 10.1021/acsami.0c11531. URL <https://doi.org/10.1021/acsami.0c11531>.
- [382] Beata Dembinska, Agnieszka Zlotorowicz, Magdalena Modzelewska, Krzysztof Miecznikowski, Iwona A. Rutkowska, Leszek Stobinski, Artur Malolepszy, Maciej Krzywiecki, Jerzy Zak, Enrico Negro, Vito Di Noto, and Pawel J. Kulesza. Low-noble-metal-loading hybrid catalytic system for oxygen reduction utilizing reduced-graphene-oxide-supported platinum aligned with carbon-nanotube-supported iridium. *Catalysts*, 10(6), 2020. ISSN 2073-4344. doi: 10.3390/catal10060689.

- [383] David Franzen, Barbara Ellendorff, Melanie C. Paulisch, André Hilger, Markus Osenberg, Ingo Manke, and Thomas Turek. Influence of binder content in silver-based gas diffusion electrodes on pore system and electrochemical performance. *Journal of Applied Electrochemistry*, 49(7):705–713, 2019. ISSN 1572-8838. doi: 10.1007/s10800-019-01311-4. URL <https://doi.org/10.1007/s10800-019-01311-4>.
- [384] N. Bogolowski, O. Ngaleu, M. Sakthivel, and J. F. Drillet. Long-life bifunctional basrcofeo<sub>3</sub>/c gas diffusion electrode. *Carbon*, 119:511–518, 2017. ISSN 0008-6223. doi: <https://doi.org/10.1016/j.carbon.2017.04.051>. URL <https://www.sciencedirect.com/science/article/pii/S0008622317304177>.
- [385] Foteini M. Sapountzi, Elena D. Orlova, Juliana P. S. Sousa, Laura M. Salonen, Oleg I. Lebedev, Georgios Zafeiropoulos, Mihalis N. Tsampas, Hans J. W. Niemantsverdriet, and Yury V. Kolen'ko. Fep nanocatalyst with preferential [010] orientation boosts the hydrogen evolution reaction in polymer-electrolyte membrane electrolyzer. *Energy & Fuels*, 34(5): 6423–6429, 2020. ISSN 0887-0624. doi: 10.1021/acs.energyfuels.0c00793. URL <https://doi.org/10.1021/acs.energyfuels.0c00793>.
- [386] John Banhart. Manufacture, characterisation and application of cellular metals and metal foams. *Progress in Materials Science*, 46(6):559–632, 2001. ISSN 0079-6425. doi: [https://doi.org/10.1016/S0079-6425\(00\)00002-5](https://doi.org/10.1016/S0079-6425(00)00002-5). URL <https://www.sciencedirect.com/science/article/pii/S0079642500000025>.
- [387] Guan-Qun Han, Yan-Ru Liu, Wen-Hui Hu, Bin Dong, Xiao Li, Xiao Shang, Yong-Ming Chai, Yun-Qi Liu, and Chen-Guang Liu. Three dimensional nickel oxides/nickel structure by in situ electro-oxidation of nickel foam as robust electrocatalyst for oxygen evolution reaction. *Applied Surface Science*, 359:172–176, 2015. ISSN 0169-4332. doi: <https://doi.org/10.1016/j.apsusc.2015.10.097>. URL <https://www.sciencedirect.com/science/article/pii/S0169433215025167>.
- [388] Kai-Li Yan, Xiao Shang, Wen-Kun Gao, Bin Dong, Xiao Li, Jing-Qi Chi, Yan-Ru Liu, Yong-Ming Chai, and Chen-Guang Liu. Ternary mno<sub>2</sub>/nico<sub>2</sub>o<sub>4</sub>/nf with hierarchical structure and synergistic interaction as efficient electrocatalysts for oxygen evolution reaction. *Journal of Alloys and Compounds*, 719:314–321, 2017. ISSN 0925-8388. doi: <https://doi.org/10.1016/j.jallcom.2017.05.207>. URL <https://www.sciencedirect.com/science/article/pii/S0925838817318248>.
- [389] Julia van Druenen, Brandy K. Pilapil, Yoseif Makonnen, Diane Beauchemin, Byron D. Gates, and Gregory Jerkiewicz. Electrochemically active nickel foams as support materials for nanoscopic platinum electrocatalysts. *ACS Applied Materials & Interfaces*, 6(15): 12046–12061, 2014. ISSN 1944-8244. doi: 10.1021/am501097t. URL <https://doi.org/10.1021/am501097t>.

- [390] Arumugam Sivanantham and Sangaraju Shanmugam. Nickel selenide supported on nickel foam as an efficient and durable non-precious electrocatalyst for the alkaline water electrolysis. *Applied Catalysis B: Environmental*, 203:485–493, 2017. ISSN 0926-3373. doi: <https://doi.org/10.1016/j.apcatb.2016.10.050>. URL <https://www.sciencedirect.com/science/article/pii/S0926337316308141>.
- [391] Boguslaw Pirozynski, Tomasz Mikolajczyk, Mateusz Luba, and Alireza Zolfaghari. Kinetics of oxygen evolution reaction on nickel foam and platinum-modified nickel foam materials in alkaline solution. *Journal of Electroanalytical Chemistry*, 847:113194, 2019. ISSN 1572-6657. doi: <https://doi.org/10.1016/j.jelechem.2019.113194>. URL <https://www.sciencedirect.com/science/article/pii/S1572665719304540>.
- [392] Chenchen Li, Jun Chen, Yu Wu, Weiyi Cao, Shangbin Sang, Qiumei Wu, Hongtao Liu, and Kaiyu Liu. Enhanced oxygen evolution reaction activity of nife layered double hydroxide on nickel foam- reduced graphene oxide interfaces. *International Journal of Hydrogen Energy*, 44(5):2656–2663, 2019. ISSN 0360-3199. doi: <https://doi.org/10.1016/j.ijhydene.2018.11.167>. URL <https://www.sciencedirect.com/science/article/pii/S0360319918337996>.
- [393] V. Vij, S. Sultan, A. M. Harzandi, A. Meena, J. N. Tiwari, W. G. Lee, T. Yoon, and K. S. Kim. Nickel-based electrocatalysts for energy-related applications: Oxygen reduction, oxygen evolution, and hydrogen evolution reactions. *ACS Catalysis*, 7(10):7196–7225, 2017. ISSN 2155-5435. doi: [10.1021/acscatal.7b01800](https://doi.org/10.1021/acscatal.7b01800).
- [394] Y. P. Chen, K. Rui, J. X. Zhu, S. X. Dou, and W. P. Sun. Recent progress on nickel-based oxide/(oxy)hydroxide electrocatalysts for the oxygen evolution reaction. *Chemistry- A European Journal*, 25(3):703–713, 2019. ISSN 0947-6539 1521-3765. doi: [10.1002/chem.201802068](https://doi.org/10.1002/chem.201802068).
- [395] Nora C. Buggy, Yifeng Du, Mei-Chen Kuo, Ryan J. Gasvoda, Soenke Seifert, Sumit Agarwal, E. Bryan Coughlin, and Andrew M. Herring. Investigating silver nanoparticle interactions with quaternary ammonium functionalized triblock copolymers and their effect on midblock crystallinity. *ACS Applied Polymer Materials*, 2(11):4914–4923, 2020. doi: [10.1021/acscapm.0c00819](https://doi.org/10.1021/acscapm.0c00819). URL <https://doi.org/10.1021/acscapm.0c00819>.
- [396] Nora C. Buggy, Yifeng Du, Mei-Chen Kuo, Soenke Seifert, Ryan J. Gasvoda, Sumit Agarwal, E. Bryan Coughlin, and Andrew M. Herring. Designing anion exchange ionomers with oriented nanoscale phase separation at a silver interface. *Unpublished results, in review*, 2021.
- [397] Kenneth S. W. Sing. *7 - Assessment of Surface Area by Gas Adsorption*, pages 237–268. Academic Press, Oxford, 2014. ISBN 978-0-08-097035-6. doi: <https://doi.org/10.1016/B978-0-08-097035-6.00007-3>. URL <https://www.sciencedirect.com/science/article/pii/B9780080970356000073>.
- [398] Allen J. Bard and Larry R. Faulkner. *Electrochemical Methods: Fundamentals and Applications, 2nd Edition*. John Wiley & Sons, Inc., New York, 2000. ISBN 978-0-471-04372-0.

- [399] Weiran Zheng, Mengjie Liu, and Lawrence Yoon Suk Lee. Best practices in using foam-type electrodes for electrocatalytic performance benchmark. *ACS Energy Letters*, 5(10): 3260–3264, 2020. doi: 10.1021/acsenerylett.0c01958. URL <https://doi.org/10.1021/acsenerylett.0c01958>.
- [400] Tatsuya Shinagawa, Angel T. Garcia-Esparza, and Kazuhiro Takanabe. Insight on tafel slopes from a microkinetic analysis of aqueous electrocatalysis for energy conversion. *Scientific Reports*, 5(1):13801, 2015. ISSN 2045-2322. doi: 10.1038/srep13801. URL <https://doi.org/10.1038/srep13801>.
- [401] J. Ponce, J. L. Rehspringer, G. Poillerat, and J. L. Gautier. Electrochemical study of nickel–aluminium–manganese spinel  $\text{NiAl}_2\text{Mn}_2\text{O}_4$ . electrocatalytical properties for the oxygen evolution reaction and oxygen reduction reaction in alkaline media. *Electrochimica Acta*, 46(22):3373–3380, 2001. ISSN 0013-4686. doi: [https://doi.org/10.1016/S0013-4686\(01\)00530-8](https://doi.org/10.1016/S0013-4686(01)00530-8). URL <https://www.sciencedirect.com/science/article/pii/S0013468601005308>.
- [402] Junming Zhang, Hua Bing Tao, Min Kuang, Hong Bin Yang, Weizheng Cai, Qingyu Yan, Qing Mao, and Bin Liu. Advances in thermodynamic-kinetic model for analyzing the oxygen evolution reaction. *ACS Catalysis*, 10(15):8597–8610, 2020. doi: 10.1021/acscatal.0c01906. URL <https://doi.org/10.1021/acscatal.0c01906>.
- [403] Ya-Hui Fang and Zhi-Pan Liu. Tafel kinetics of electrocatalytic reactions: From experiment to first-principles. *ACS Catalysis*, 4(12):4364–4376, 2014. doi: 10.1021/cs501312v. URL <https://doi.org/10.1021/cs501312v>.
- [404] Justus Masa, Stefan Barwe, Corina Andronescu, Ilya Sinev, Adrian Ruff, Kolleboyina Jayaramulu, Karina Elumeeva, Bharathi Konkena, Beatriz Roldan Cuenya, and Wolfgang Schuhmann. Low overpotential water splitting using cobalt–cobalt phosphide nanoparticles supported on nickel foam. *ACS Energy Letters*, 1(6):1192–1198, 2016. doi: 10.1021/acsenerylett.6b00532. URL <https://doi.org/10.1021/acsenerylett.6b00532>.
- [405] Chi Zhang, Zhuohong Xie, Yi Liang, Dingding Meng, Zheng Wang, Xin He, Weiye Qiu, Mei Chen, Ping Liang, and Zhonghua Zhang. Morphological and compositional modification of  $\text{-Ni(OH)}_2$  nanoplates by ferrihydrite for enhanced oxygen evolution reaction. *International Journal of Hydrogen Energy*, 46(34):17720–17730, 2021. ISSN 0360-3199. doi: <https://doi.org/10.1016/j.ijhydene.2021.02.173>. URL <https://www.sciencedirect.com/science/article/pii/S0360319921007473>.
- [406] R. A. Marcus. Chemical and electrochemical electron-transfer theory. *Annual Review of Physical Chemistry*, 15(1):155–196, 1964. ISSN 0066-426X. doi: 10.1146/annurev.pc.15.100164.001103. URL <https://doi.org/10.1146/annurev.pc.15.100164.001103>.
- [407] Wolfgang Schmickler and Elizabeth Santos. *Interfacial Electrochemistry, 2nd Edition*. Springer-Verlag Berlin Heidelberg, London, New York, 2010.


- [408] Tianyi Kou, Shanwen Wang, Jesse L. Hauser, Mingpeng Chen, Scott R. J. Oliver, Yifan Ye, Jinghua Guo, and Yat Li. Ni foam-supported Fe-doped Ni(OH)<sub>2</sub> nanosheets show ultralow overpotential for oxygen evolution reaction. *ACS Energy Letters*, 4(3):622–628, 2019. doi: 10.1021/acsenerylett.9b00047. URL <https://doi.org/10.1021/acsenerylett.9b00047>.
- [409] Ana Soutelo-Maria, Jean-Luc Dubois, Jean-Luc Couturier, Magali Brebion, and Giancarlo Cravotto. Regeneration of Raney®-nickel catalyst for the synthesis of high-value amino-ester renewable monomers. *Catalysts*, 10(2), 2020. ISSN 2073-4344. doi: 10.3390/catal10020229.
- [410] Haibin Jiang, Shuliang Lu, Xiaohong Zhang, Wei Dai, and Jinliang Qiao. Polymer-supported Raney nickel catalysts for sustainable reduction reactions. *Molecules (Basel, Switzerland)*, 21(7):833, 2016. ISSN 1420-3049. doi: 10.3390/molecules21070833. URL <https://pubmed.ncbi.nlm.nih.gov/27347922><https://www.ncbi.nlm.nih.gov/pmc/articles/PMC6273563/>.
- [411] S. Basaveni, N. V. Kuchkina, Z. B. Shifrina, M. Pal, and M. Rajadurai. Ni nanoparticles on polyaromatic hyperbranched polymer support as a mild, tunable, and sustainable catalyst for catalytic transfer hydrogenation. *Journal of Nanoparticle Research*, 21(5):91, 2019. ISSN 1572-896X. doi: 10.1007/s11051-019-4533-2. URL <https://doi.org/10.1007/s11051-019-4533-2>.
- [412] H. Rachapudy, G. G. Smith, V. R. Raju, and W. W. Graessley. Properties of amorphous and crystallizable hydrocarbon polymers. iii. studies of the hydrogenation of polybutadiene. *Journal of Polymer Science: Polymer Physics Edition*, 17(7):1211–1222, 1979. ISSN 0098-1273. doi: <https://doi.org/10.1002/pol.1979.180170706>. URL <https://doi.org/10.1002/pol.1979.180170706>.
- [413] W. H. Tsai, J. T. Young, F. J. Boerio, and P. P. Hong. Characterization of model polyimide/silver interphases using surface-enhanced Raman scattering. *Langmuir*, 7(4): 745–754, 1991. ISSN 0743-7463. doi: 10.1021/la00052a024. URL <https://doi.org/10.1021/la00052a024>.
- [414] Yu Seung Kim. Polymer electrolytes with high ionic concentration for fuel cells and electrolyzers. *ACS Applied Polymer Materials*, 3(3):1250–1270, 2021. doi: 10.1021/acsapm.0c01405. URL <https://doi.org/10.1021/acsapm.0c01405>.
- [415] Benjamin Chu and Benjamin S. Hsiao. Small-angle x-ray scattering of polymers. *Chemical Reviews*, 101(6):1727–1762, 2001. ISSN 0009-2665. doi: 10.1021/cr9900376. URL <https://doi.org/10.1021/cr9900376>.
- [416] Xiangping Min, Yan Shi, Zhuoxin Lu, Lisha Shen, Taiwo Oladapo Ogundipe, Pralhad Gupta, Chi Wang, Changqing Guo, Zhida Wang, Hongyi Tan, Sanjeev Mukerjee, and Changfeng Yan. High performance and cost-effective supported iron catalyst for proton exchange membrane water electrolysis. *Electrochimica Acta*, 385:138391, 2021. ISSN 0013-4686. doi: <https://doi.org/10.1016/j.electacta.2021.138391>. URL <https://www.sciencedirect.com/science/article/pii/S0013468621006812>.

- [417] Y. Dong and S. Komarneni. Strategies to develop earth-abundant heterogeneous oxygen evolution reaction catalysts for ph-neutral or ph-near-neutral electrolytes. *Small Methods*, 5(1), 2021. ISSN 2366-9608. doi: 10.1002/smtd.202000719.
- [418] Nanjun Chen and Young Moo Lee. Anion exchange polyelectrolytes for membranes and ionomers. *Progress in Polymer Science*, 113:101345, 2021. ISSN 0079-6700. doi: <https://doi.org/10.1016/j.progpolymsci.2020.101345>. URL <https://www.sciencedirect.com/science/article/pii/S0079670020301386>.
- [419] Dirk Henkensmeier, Malukah Najibah, Corinna Harms, Jan Žitka, Jaromír Hnát, and Karel Bouzek. Overview: State-of-the art commercial membranes for anion exchange membrane water electrolysis. *Journal of Electrochemical Energy Conversion and Storage*, 18(2), 2020. ISSN 2381-6872. doi: 10.1115/1.4047963. URL <https://doi.org/10.1115/1.4047963>.
- [420] Dorte Posselt, Jianqi Zhang, Detlef-M. Smilgies, Anatoly V. Berezkin, Igor I. Potemkin, and Christine M. Papadakis. Restructuring in block copolymer thin films: In situ gisaxs investigations during solvent vapor annealing. *Progress in Polymer Science*, 66:80–115, 2017. ISSN 0079-6700. doi: <https://doi.org/10.1016/j.progpolymsci.2016.09.009>. URL <https://www.sciencedirect.com/science/article/pii/S0079670016300727>.



## APPENDIX

### COPYRIGHT PERMISSIONS



**Polymeric materials as anion-exchange membranes for alkaline fuel cells**

**Author:** Guillaume Couture, Ali Alaaeddine, Frédéric Boschet, Bruno Ameduri

**Publication:** Progress in Polymer Science

**Publisher:** Elsevier

**Date:** November 2011

Copyright © 2011 Elsevier Ltd. All rights reserved.

**Order Completed**

Thank you for your order.

This Agreement between Ms. Nora Buggy ("You") and Elsevier ("Elsevier") consists of your license details and the terms and conditions provided by Elsevier and Copyright Clearance Center.

Your confirmation email will contain your order number for future reference.

<b>License Number</b>	5110370067691	<a href="#">Printable Details</a>
<b>License date</b>	Jul 15, 2021	

**📄 Licensed Content**

<b>Licensed Content Publisher</b>	Elsevier
<b>Licensed Content Publication</b>	Progress in Polymer Science
<b>Licensed Content Title</b>	Polymeric materials as anion-exchange membranes for alkaline fuel cells
<b>Licensed Content Author</b>	Guillaume Couture, Ali Alaaeddine, Frédéric Boschet, Bruno Ameduri
<b>Licensed Content Date</b>	Nov 1, 2011
<b>Licensed Content Volume</b>	36
<b>Licensed Content Issue</b>	11
<b>Licensed Content Pages</b>	37

**📄 Order Details**

<b>Type of Use</b>	reuse in a thesis/dissertation
<b>Portion</b>	figures/tables/illustrations
<b>Number of figures/tables/illustrations</b>	1
<b>Format</b>	both print and electronic
<b>Are you the author of this Elsevier article?</b>	No
<b>Will you be translating?</b>	No

**📄 About Your Work**

<b>Title</b>	Investigating interfaces for Electrochemical Devices Using Tunable Block Copolymer Electrolytes
<b>Institution name</b>	Colorado School of Mines
<b>Expected presentation date</b>	Aug 2021

**📄 Additional Data**

<b>Order reference number</b>	1
<b>Portions</b>	Figure 2

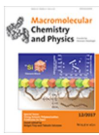
**📍 Requestor Location**

<b>Requestor Location</b>	Ms. Nora Buggy 14330 Fairview Ln  GOLDEN, CO 80401 United States Attn: Ms. Nora Buggy
---------------------------	--

**📄 Tax Details**

<b>Publisher Tax ID</b>	98-0397604
-------------------------	------------

Figure A.1 Permission to reproduce Figure 1.7 from [45].



**Configuring Anion-Exchange Membranes for High Conductivity and Alkaline Stability by Using Cationic Polymers with Tailored Side Chains**

**Author:** Patric Jannasch, Eva Annika Weiber  
**Publication:** Macromolecular Chemistry and Physics  
**Publisher:** John Wiley and Sons  
**Date:** Feb 29, 2016

© 2016 WILEY-VCH Verlag GmbH & Co. KGaA, Weinheim

**Order Completed**

Thank you for your order.

This Agreement between Ms. Nora Buggy ("You") and John Wiley and Sons ("John Wiley and Sons") consists of your license details and the terms and conditions provided by John Wiley and Sons and Copyright Clearance Center.

Your confirmation email will contain your order number for future reference.

License Number	5110370368092	<a href="#">Printable Details</a>
License date	Jul 15, 2021	

<p><b>Licensed Content</b></p> <table style="width: 100%; border-collapse: collapse;"> <tr> <td style="width: 30%;">Licensed Content Publisher</td> <td>John Wiley and Sons</td> </tr> <tr> <td>Licensed Content Publication</td> <td>Macromolecular Chemistry and Physics</td> </tr> <tr> <td>Licensed Content Title</td> <td>Configuring Anion-Exchange Membranes for High Conductivity and Alkaline Stability by Using Cationic Polymers with Tailored Side Chains</td> </tr> <tr> <td>Licensed Content Author</td> <td>Patric Jannasch, Eva Annika Weiber</td> </tr> <tr> <td>Licensed Content Date</td> <td>Feb 29, 2016</td> </tr> <tr> <td>Licensed Content Volume</td> <td>217</td> </tr> <tr> <td>Licensed Content Issue</td> <td>10</td> </tr> <tr> <td>Licensed Content Pages</td> <td>11</td> </tr> </table>	Licensed Content Publisher	John Wiley and Sons	Licensed Content Publication	Macromolecular Chemistry and Physics	Licensed Content Title	Configuring Anion-Exchange Membranes for High Conductivity and Alkaline Stability by Using Cationic Polymers with Tailored Side Chains	Licensed Content Author	Patric Jannasch, Eva Annika Weiber	Licensed Content Date	Feb 29, 2016	Licensed Content Volume	217	Licensed Content Issue	10	Licensed Content Pages	11	<p><b>Order Details</b></p> <table style="width: 100%; border-collapse: collapse;"> <tr> <td style="width: 30%;">Type of use</td> <td>Dissertation/Thesis</td> </tr> <tr> <td>Requestor type</td> <td>University/Academic</td> </tr> <tr> <td>Format</td> <td>Print and electronic</td> </tr> <tr> <td>Portion</td> <td>Figure/table</td> </tr> <tr> <td>Number of figures/tables</td> <td>1</td> </tr> <tr> <td>Will you be translating?</td> <td>No</td> </tr> </table>	Type of use	Dissertation/Thesis	Requestor type	University/Academic	Format	Print and electronic	Portion	Figure/table	Number of figures/tables	1	Will you be translating?	No
Licensed Content Publisher	John Wiley and Sons																												
Licensed Content Publication	Macromolecular Chemistry and Physics																												
Licensed Content Title	Configuring Anion-Exchange Membranes for High Conductivity and Alkaline Stability by Using Cationic Polymers with Tailored Side Chains																												
Licensed Content Author	Patric Jannasch, Eva Annika Weiber																												
Licensed Content Date	Feb 29, 2016																												
Licensed Content Volume	217																												
Licensed Content Issue	10																												
Licensed Content Pages	11																												
Type of use	Dissertation/Thesis																												
Requestor type	University/Academic																												
Format	Print and electronic																												
Portion	Figure/table																												
Number of figures/tables	1																												
Will you be translating?	No																												

<p><b>About Your Work</b></p> <table style="width: 100%; border-collapse: collapse;"> <tr> <td style="width: 30%;">Title</td> <td>Investigating Interfaces for Electrochemical Devices Using Tunable Block Copolymer Electrolytes</td> </tr> <tr> <td>Institution name</td> <td>Colorado School of Mines</td> </tr> <tr> <td>Expected presentation date</td> <td>Aug 2021</td> </tr> </table>	Title	Investigating Interfaces for Electrochemical Devices Using Tunable Block Copolymer Electrolytes	Institution name	Colorado School of Mines	Expected presentation date	Aug 2021	<p><b>Additional Data</b></p> <table style="width: 100%; border-collapse: collapse;"> <tr> <td style="width: 30%;">Order reference number</td> <td>2</td> </tr> <tr> <td>Portions</td> <td>Scheme 2</td> </tr> </table>	Order reference number	2	Portions	Scheme 2
Title	Investigating Interfaces for Electrochemical Devices Using Tunable Block Copolymer Electrolytes										
Institution name	Colorado School of Mines										
Expected presentation date	Aug 2021										
Order reference number	2										
Portions	Scheme 2										

<p><b>Requestor Location</b></p> <table style="width: 100%; border-collapse: collapse;"> <tr> <td style="width: 30%;">Requestor Location</td> <td>Ms. Nora Buggy 14330 Fairview Ln  GOLDEN, CO 80401 United States Attn: Ms. Nora Buggy</td> </tr> </table>	Requestor Location	Ms. Nora Buggy 14330 Fairview Ln  GOLDEN, CO 80401 United States Attn: Ms. Nora Buggy	<p><b>Tax Details</b></p> <table style="width: 100%; border-collapse: collapse;"> <tr> <td style="width: 30%;">Publisher Tax ID</td> <td>EU826007151</td> </tr> </table>	Publisher Tax ID	EU826007151
Requestor Location	Ms. Nora Buggy 14330 Fairview Ln  GOLDEN, CO 80401 United States Attn: Ms. Nora Buggy				
Publisher Tax ID	EU826007151				

Figure A.2 Permission to reproduce Figure 1.8 from [78].



### Physicochemical properties of copper important for its antibacterial activity and development of a unified model

Author: Michael Hans, Salima Mathews, Frank Mücklich, et al

Publication: Biointerphases

Publisher: American Vacuum Society

Date: Mar 1, 2016

Rights managed by AIP Publishing.

#### Order Completed

Thank you for your order.

This Agreement between Ms. Nora Buggy ("You") and AIP Publishing ("AIP Publishing") consists of your license details and the terms and conditions provided by AIP Publishing and Copyright Clearance Center.

Your confirmation email will contain your order number for future reference.

License Number 5110370615054

[Printable Details](#)

License date Jul 15, 2021

#### Licensed Content

Licensed Content Publisher American Vacuum Society  
Licensed Content Publication Biointerphases  
Licensed Content Title Physicochemical properties of copper important for its antibacterial activity and development of a unified model  
Licensed Content Author Michael Hans, Salima Mathews, Frank Mücklich, et al  
Licensed Content Date Mar 1, 2016  
Licensed Content Volume 11  
Licensed Content Issue 1

#### Order Details

Type of Use Thesis/Dissertation  
Requestor type Student  
Format Print and electronic  
Portion Figure/Table  
Number of figures/tables 1  
Will you be translating? No

#### About Your Work

Title Investigating Interfaces for Electrochemical Devices Using Tunable Block Copolymer Electrolytes  
Institution name Colorado School of Mines  
Expected presentation date Aug 2021

#### Additional Data

Order reference number 3  
Portions Figure 4

#### Requestor Location

Ms. Nora Buggy  
14330 Fairview Ln

#### Tax Details

Requestor Location GOLDEN, CO 80401  
United States  
Attn: Ms. Nora Buggy

Figure A.3 Permission to reproduce Figure 1.11 from [165].

**Characteristics of Self-Assembled Ultrathin Nafion Films**

**Author:** Devproshad K. Paul, Kunal Karan, Aristides Docoslis, et al  
**Publication:** Macromolecules  
**Publisher:** American Chemical Society  
**Date:** May 1, 2013

*Copyright © 2013, American Chemical Society*

**ACSPublications**  
Most Trusted. Most Cited. Most Read.

**PERMISSION/LICENSE IS GRANTED FOR YOUR ORDER AT NO CHARGE**

This type of permission/license, instead of the standard Terms and Conditions, is sent to you because no fee is being charged for your order. Please note the following:

- Permission is granted for your request in both print and electronic formats, and translations.
- If figures and/or tables were requested, they may be adapted or used in part.
- Please print this page for your records and send a copy of it to your publisher/graduate school.
- Appropriate credit for the requested material should be given as follows: "Reprinted (adapted) with permission from {COMPLETE REFERENCE CITATION}. Copyright (YEAR) American Chemical Society." Insert appropriate information in place of the capitalized words.
- One-time permission is granted only for the use specified in your RightsLink request. No additional uses are granted (such as derivative works or other editions). For any uses, please submit a new request.

If credit is given to another source for the material you requested from RightsLink, permission must be obtained from that source.

[BACK](#) [CLOSE WINDOW](#)

Figure A.4 Permission to reproduce Figure 1.12 from [189].

**A Polyethylene-Based Triblock Copolymer Anion Exchange Membrane with High Conductivity and Practical Mechanical Properties**

**Author:** Nora C. Buggy, Yifeng Du, Mei-Chen Kuo, et al  
**Publication:** ACS Applied Polymer Materials  
**Publisher:** American Chemical Society  
**Date:** Mar 1, 2020

*Copyright © 2020, American Chemical Society*

**ACSPublications**  
Most Trusted. Most Cited. Most Read.

**PERMISSION/LICENSE IS GRANTED FOR YOUR ORDER AT NO CHARGE**

This type of permission/license, instead of the standard Terms and Conditions, is sent to you because no fee is being charged for your order. Please note the following:

- Permission is granted for your request in both print and electronic formats, and translations.
- If figures and/or tables were requested, they may be adapted or used in part.
- Please print this page for your records and send a copy of it to your publisher/graduate school.
- Appropriate credit for the requested material should be given as follows: "Reprinted (adapted) with permission from {COMPLETE REFERENCE CITATION}. Copyright (YEAR) American Chemical Society." Insert appropriate information in place of the capitalized words.
- One-time permission is granted only for the use specified in your RightsLink request. No additional uses are granted (such as derivative works or other editions). For any uses, please submit a new request.

If credit is given to another source for the material you requested from RightsLink, permission must be obtained from that source.

[BACK](#) [CLOSE WINDOW](#)

Figure A.5 Permission to reproduce Chapter 2 from [102].

**Investigating Silver Nanoparticle Interactions with Quaternary Ammonium Functionalized Triblock Copolymers and Their Effect on Midblock Crystallinity**

Author: Nora C. Buggy, Yifeng Du, Mei-Chen Kuo, et al  
 Publication: ACS Applied Polymer Materials  
 Publisher: American Chemical Society  
 Date: Nov 1, 2020

ACS Publications  
 Most Trusted. Most Cited. Most Read.

Copyright © 2020, American Chemical Society

---

**PERMISSION/LICENSE IS GRANTED FOR YOUR ORDER AT NO CHARGE**

This type of permission/license, instead of the standard Terms and Conditions, is sent to you because no fee is being charged for your order. Please note the following:

- Permission is granted for your request in both print and electronic formats, and translations.
- If figures and/or tables were requested, they may be adapted or used in part.
- Please print this page for your records and send a copy of it to your publisher/graduate school.
- Appropriate credit for the requested material should be given as follows: "Reprinted (adapted) with permission from {COMPLETE REFERENCE CITATION}. Copyright {YEAR} American Chemical Society." Insert appropriate information in place of the capitalized words.
- One-time permission is granted only for the use specified in your RightsLink request. No additional uses are granted (such as derivative works or other editions). For any uses, please submit a new request.

If credit is given to another source for the material you requested from RightsLink, permission must be obtained from that source.

[BACK](#) [CLOSE WINDOW](#)

Figure A.6 Permission to reproduce Chapter 3 from [395].

**Nora Buggy** <nbuggy@myemail.mines.edu>  
 to Yifeng ▾  
 Dr. Yifeng Du,

Do you give me permission to reproduce the following in my thesis?

Co-authored published articles:

- A POLYETHYLENE-BASED TRIBLOCK COPOLYMER ANION EXCHANGE MEMBRANE WITH HIGH CONDUCTIVITY AND PRACTICAL MECHANICAL PROPERTIES, ACS Applied Polymer Materials, 2020, DOI: 10.1021/acsapm.9b01182
- INVESTIGATING SILVER NANOPARTICLE INTERACTIONS WITH QUATERNARY AM-MONIUM FUNCTIONALIZED TRIBLOCK COPOLYMERS AND THEIR EFFECT ON MIDBLOCK CRYSTALLINITY, ACS Applied Polymer Materials, 2020, DOI: 10.1021/acsapm.0c00819

Co-authored publications in review:

- DESIGNING ANION EXCHANGE IONOMERS WITH ORIENTED NANOSCALE PHASE SEPARATION AT A SILVER INTERFACE, in review for publication in the Journal of Physical Chemistry C
- EVALUATING THE EFFECT OF IONOMER CHEMICAL COMPOSITION IN SILVER-IONOMER CATALYST INKS TOWARD THE OXYGEN EVOLUTION REACTION BY HALF-CELL MEASUREMENTS AND WATER ELECTROLYSIS, in review for publication in Electrochimica Acta.

Please reply yes if you agree to reproduce this material in my thesis.

Best,  
 Nora

---

**Yifeng Du**  
 to me ▾  
 Doctor Nora Buggy,

Absolutely Yes -- my great honor! :)

Will be looking forward to seeing your thesis online as well!

-Yifeng

Figure A.7 Permission received to reproduce co-authored journal articles, either published or in review, from Yifeng Du.

**Nora Buggy** <nbuggy@mymail.mines.edu>

to Mei ▾

Mei-Chen Kuo,

Do you give me permission to reproduce the following in my thesis?

Co-authored published articles:

- A POLYETHYLENE-BASED TRIBLOCK COPOLYMER ANION EXCHANGE MEMBRANE WITH HIGH CONDUCTIVITY AND PRACTICAL MECHANICAL PROPERTIES, ACS Applied Polymer Materials, 2020, DOI: 10.1021/acsapm.9b01182  
- INVESTIGATING SILVER NANOPARTICLE INTERACTIONS WITH QUATERNARY AM-MONIUM FUNCTIONALIZED TRIBLOCK COPOLYMERS AND THEIR EFFECT ON MIDBLOCK CRYSTALLINITY, ACS Applied Polymer Materials, 2020, DOI: 10.1021/acsapm.0c00819

Co-authored publications in review:

- DESIGNING ANION EXCHANGE IONOMERS WITH ORIENTED NANOSCALE PHASE SEPARATION AT A SILVER INTERFACE, in review for publication in the Journal of Physical Chemistry C  
- EVALUATING THE EFFECT OF IONOMER CHEMICAL COMPOSITION IN SILVER-IONOMER CATALYST INKS TOWARD THE OXYGEN EVOLUTION REACTION BY HALF-CELL MEASUREMENTS AND WATER ELECTROLYSIS, in review for publication in Electrochimica Acta.

Please reply **yes** if you agree to reproduce this material in my thesis.

Best,

Nora

--

Nora C. Buggy, PhD

*She/Her/Hers*

Chemical and Biological Engineering | Herring Group

COLORADOSCHOOLOFMINES

---

**Mei Kuo** <mkuo@mines.edu>

to me ▾

Yes.

Mei-Chen Kuo

Figure A.8 Permission received to reproduce co-authored journal articles, either published or in review, from Mei-Chen Kuo.

**Nora Buggy** <nbuggy@mymail.mines.edu>

to jawilkin ▾

Jacob S. Wilkinson,

Do you give me permission to reproduce the following in my thesis?

Co-authored published articles:

- A POLYETHYLENE-BASED TRIBLOCK COPOLYMER ANION EXCHANGE MEMBRANE WITH HIGH CONDUCTIVITY AND PRACTICAL MECHANICAL PROPERTIES, ACS Applied Polymer Materials, 2020, DOI: 10.1021/acsapm.9b01182

Please reply **yes** if you agree to reproduce this material in my thesis.

Best,

Nora

--

Nora C. Buggy, PhD

*She/Her/Hers*

Chemical and Biological Engineering | Herring Group

COLORADOSCHOOLOFMINES

---

**Jacob Wilkinson**

to me ▾

Yes

Figure A.9 Permission received to reproduce co-authored journal articles, either published or in review, from Jacob S. Wilkinson.

**Nora Buggy** <nbuggy@mymail.mines.edu>

to Ivy ▾

Ivy Wu,

Do you give me permission to reproduce the following in my thesis?

Co-authored publications in review:

- EVALUATING THE EFFECT OF IONOMER CHEMICAL COMPOSITION IN SILVER-IONOMER CATALYST INKS TOWARD THE OXYGEN EVOLUTION REACTION BY HALF-CELL MEASUREMENTS AND WATER ELECTROLYSIS, in review for publication in *Electrochimica Acta*.

Please reply **yes** if you agree to reproduce this material in my thesis.

Best,

Nora

--

Nora C. Buggy, PhD

*She/Her/Hers*

Chemical and Biological Engineering | Herring Group

COLORADOSCHOOLOFMINES

---

**Ivy Wu**

to me ▾

Yes

Figure A.10 Permission received to reproduce co-authored journal articles, either published or in review, from Ivy Wu.

**Nora Buggy** <nbuggy@mymail.mines.edu>

to kahrens ▾

Kayla A. Ahrens,

Do you give me permission to reproduce the following in my thesis?

Co-authored published articles:

- A POLYETHYLENE-BASED TRIBLOCK COPOLYMER ANION EXCHANGE MEMBRANE WITH HIGH CONDUCTIVITY AND PRACTICAL MECHANICAL PROPERTIES, *ACS Applied Polymer Materials*, 2020, DOI: 10.1021/acsapm.9b01182

Please reply **yes** if you agree to reproduce this material in my thesis.

Best,

Nora

--

Nora C. Buggy, PhD

*She/Her/Hers*

Chemical and Biological Engineering | Herring Group

COLORADOSCHOOLOFMINES

---

**Kayla Ahrens**

to me ▾

Yes.

Thanks,

Kayla

Figure A.11 Permission received to reproduce co-authored journal articles, either published or in review, from Kayla A. Ahrens.

**Nora Buggy** <nbuggy@mymail.mines.edu>

to ryan.gasvoda ▾

Dr. Ryan Gasvoda,

Do you give me permission to reproduce the following in my thesis?

Co-authored published articles:

- INVESTIGATING SILVER NANOPARTICLE INTERACTIONS WITH QUATERNARY AM-MONIUM FUNCTIONALIZED TRIBLOCK COPOLYMERS AND THEIR EFFECT ON MIDBLOCK CRYSTALLINITY, ACS Applied Polymer Materials, 2020, DOI: 10.1021/acsapm.0c00819

Co-authored publications in review:

- DESIGNING ANION EXCHANGE IONOMERS WITH ORIENTED NANOSCALE PHASE SEPARATION AT A SILVER INTERFACE, in review for publication in the Journal of Physical Chemistry C

Please reply **yes** if you agree to reproduce this material in my thesis.

Best,

Nora

--

Nora C. Buggy, PhD

*She/Her/Hers*

Chemical and Biological Engineering | Herring Group

COLORADOSCHOOLOFMINES

---

**Ryan.Gasvoda@lamresearch.com**

to me ▾

Hi Nora,

Yes, go ahead! Congrats!

Thanks,

*Ryan J. Gasvoda, Ph.D*

Process Engineer 3 | Deposition Products Group

Figure A.12 Permission received to reproduce co-authored journal articles, either published or in review, from Ryan J. Gasvoda.



**Nora Buggy** <nbuggy@mymail.mines.edu>

to James ▾

James M. Crawford,

Do you give me permission to reproduce the following in my thesis?

Co-authored publications in review:

- EVALUATING THE EFFECT OF IONOMER CHEMICAL COMPOSITION IN SILVER-IONOMER CATALYST INKS TOWARD THE OXYGEN EVOLUTION REACTION BY HALF-CELL MEASUREMENTS AND WATER ELECTROLYSIS, in review for publication in *Electrochimica Acta*.

Please reply **yes** if you agree to reproduce this material in my thesis.

Best,

Nora

--

Nora C. Buggy, PhD

*She/Her/Hers*

Chemical and Biological Engineering | Herring Group

COLORADO SCHOOL OF MINES

---

**James Crawford** <jcrawford@mines.edu>

to me ▾

Yes.

Figure A.13 Permission received to reproduce co-authored journal articles, either published or in review, from James M. Crawford.

**Nora Buggy** <nbuggy@mymail.mines.edu>

to Ria ▾

Ria Ghosh,

Do you give me permission to reproduce the following in my thesis?

Co-authored publications in review:

- EVALUATING THE EFFECT OF IONOMER CHEMICAL COMPOSITION IN SILVER-IONOMER CATALYST INKS TOWARD THE OXYGEN EVOLUTION REACTION BY HALF-CELL MEASUREMENTS AND WATER ELECTROLYSIS, in review for publication in *Electrochimica Acta*.

Please reply **yes** if you agree to reproduce this material in my thesis.

Best,

Nora

--

Nora C. Buggy, PhD

*She/Her/Hers*

Chemical and Biological Engineering | Herring Group

COLORADOSCHOOLOFMINES

---

**Ria Ghosh**

to me ▾

Hello Nora,

Yes I approve.

Ria

Figure A.14 Permission received to reproduce co-authored journal articles, either published or in review, from Ria Ghosh.

**Nora Buggy** <nbuggy@mymail.mines.edu>

to Morgan ▾

Morgan S. Ezell,

Do you give me permission to reproduce the following in my thesis?

Co-authored publications in review:

- EVALUATING THE EFFECT OF IONOMER CHEMICAL COMPOSITION IN SILVER-IONOMER CATALYST INKS TOWARD THE OXYGEN EVOLUTION REACTION BY HALF-CELL MEASUREMENTS AND WATER ELECTROLYSIS, in review for publication in *Electrochimica Acta*.

Please reply **yes** if you agree to reproduce this material in my thesis.

Best,

Nora

--

Nora C. Buggy, PhD

*She/Her/Hers*

Chemical and Biological Engineering | Herring Group

COLORADOSCHOOLOFMINES

---

**Morgan Ezell**

to me ▾

yes

Figure A.15 Permission received to reproduce co-authored journal articles, either published or in review, from Morgan S. Ezell.

**Nora Buggy** <nbuggy@mymail.mines.edu>

to Sumit ▾

Dr. Sumit Agarwal,

Do you give me permission to reproduce the following in my thesis?

Co-authored published articles:

- INVESTIGATING SILVER NANOPARTICLE INTERACTIONS WITH QUATERNARY AM-MONIUM FUNCTIONALIZED TRIBLOCK COPOLYMERS AND THEIR EFFECT ON MIBLOCK CRYSTALLINITY, ACS Applied Polymer Materials, 2020, DOI: 10.1021/acsapm.0c00819

Co-authored publications in review:

- DESIGNING ANION EXCHANGE IONOMERS WITH ORIENTED NANOSCALE PHASE SEPARATION AT A SILVER INTERFACE, in review for publication in the Journal of Physical Chemistry C

Please reply **yes** if you agree to reproduce this material in my thesis.

Best,

Nora

--

Nora C. Buggy, PhD

*She/Her/Hers*

Chemical and Biological Engineering | Herring Group

COLORADOSCHOOLOFMINES

---

**Sumit Agarwal** <sagarwal@mines.edu>

to me ▾

Yes.

Figure A.16 Permission received to reproduce co-authored journal articles, either published or in review, from Sumit Agarwal.

**Nora Buggy** <nbuggy@mymail.mines.edu>  
to Moises ▾

Dr. Moises A. Carreon,

Do you give me permission to reproduce the following in my thesis?

Co-authored publications in review:

- EVALUATING THE EFFECT OF IONOMER CHEMICAL COMPOSITION IN  
SILVER-IONOMER CATALYST INKS TOWARD THE OXYGEN EVOLUTION REACTION  
BY HALF-CELL MEASUREMENTS AND WATER ELECTROLYSIS, in review for publication in *Electrochimica Acta*.

Please reply **yes** if you agree to reproduce this material in my thesis.

Best,  
Nora  
--

Nora C. Buggy, PhD  
*She/Her/Hers*  
Chemical and Biological Engineering | Herring Group  
COLORADOSCHOOLOFMINES

---

**Moises Carreon** <mcarreon@mines.edu>  
to me ▾

yes

Figure A.17 Permission received to reproduce co-authored journal articles, either published or in review, from Moises A. Carreon.

**Nora Buggy** <nbuggy@mymail.mines.edu>

to Soenke ▾

Dr. Soenke Seifert,

Do you give me permission to reproduce the following in my thesis?

Co-authored published articles:

- A POLYETHYLENE-BASED TRIBLOCK COPOLYMER ANION EXCHANGE MEMBRANE WITH HIGH CONDUCTIVITY AND PRACTICAL MECHANICAL PROPERTIES, ACS Applied Polymer Materials, 2020, DOI: 10.1021/acsapm.9b01182  
- INVESTIGATING SILVER NANOPARTICLE INTERACTIONS WITH QUATERNARY AM-MONIUM FUNCTIONALIZED TRIBLOCK COPOLYMERS AND THEIR EFFECT ON MIDBLOCK CRYSTALLINITY, ACS Applied Polymer Materials, 2020, DOI: 10.1021/acsapm.0c00819

Co-authored publications in review:

- DESIGNING ANION EXCHANGE IONOMERS WITH ORIENTED NANOSCALE PHASE SEPARATION AT A SILVER INTERFACE, in review for publication in the Journal of Physical Chemistry C  
- EVALUATING THE EFFECT OF IONOMER CHEMICAL COMPOSITION IN SILVER-IONOMER CATALYST INKS TOWARD THE OXYGEN EVOLUTION REACTION BY HALF-CELL MEASUREMENTS AND WATER ELECTROLYSIS, in review for publication in Electrochimica Acta.

Please reply **yes** if you agree to reproduce this material in my thesis.

Best,  
Nora  
--

Nora C. Buggy, PhD  
*She/Her/ Hers*  
Chemical and Biological Engineering | Herring Group  
COLORADOSCHOOLOFMINES

---

**Seifert, Soenke**

to me ▾

yes

Figure A.18 Permission received to reproduce co-authored journal articles, either published or in review, from Soenke Seifert.

**Nora Buggy** <nbuggy@myemail.mines.edu>

to Bryan ▾

Dr. E. Bryan Coughlin,

Do you give me permission to reproduce the following in my thesis?

Co-authored published articles:

- A POLYETHYLENE-BASED TRIBLOCK COPOLYMER ANION EXCHANGE MEMBRANE WITH HIGH CONDUCTIVITY AND PRACTICAL MECHANICAL PROPERTIES, ACS Applied Polymer Materials, 2020, DOI: 10.1021/acscapm.9b01182  
- INVESTIGATING SILVER NANOPARTICLE INTERACTIONS WITH QUATERNARY AM-MONIUM FUNCTIONALIZED TRIBLOCK COPOLYMERS AND THEIR EFFECT ON MIBBLOCK CRYSTALLINITY, ACS Applied Polymer Materials, 2020, DOI: 10.1021/acscapm.0c00819

Co-authored publications in review:

- DESIGNING ANION EXCHANGE IONOMERS WITH ORIENTED NANOSCALE PHASE SEPARATION AT A SILVER INTERFACE, in review for publication in the Journal of Physical Chemistry C  
- EVALUATING THE EFFECT OF IONOMER CHEMICAL COMPOSITION IN SILVER-IONOMER CATALYST INKS TOWARD THE OXYGEN EVOLUTION REACTION BY HALF-CELL MEASUREMENTS AND WATER ELECTROLYSIS, in review for publication in Electrochimica Acta.

Please reply **yes** if you agree to reproduce this material in my thesis.

Best,

Nora

--

Nora C. Buggy, PhD

*She/Her/Her*

Chemical and Biological Engineering | Herring Group

COLORADOSCHOOLOFMINES

---

**Bryan Coughlin**

to me ▾

Hello Dr. Buggy,

YES.

--Bryan

Figure A.19 Permission received to reproduce co-authored journal articles, either published or in review, from E. Bryan Coughlin.